Ion camera development for real–time acquisition of localised pH responses using the CMOS based 64×64–pixel ISFET sensor array technology

A thesis submitted to the
Department of Electronics and Electrical Engineering
School of Engineering
University of Glasgow
in fulfilment of the requirements
for the Degree of
Doctor of Philosophy

Balázs Németh
April 2012

Abstract

This thesis presents the development and test of an integrated ion camera chip for monitoring highly localised ion fluxes of electrochemical processes using an ion sensitive sensor array. Ionic concentration fluctuations are shown to travel across the sensor array as a result of citric acid injection and the BZ–reaction. The imaging capability of non–equilibrium chemical activities is also demonstrated monitoring self–assembling micrometre sized polyoxometalate tubular and membranous architectures. The sufficient spatial resolution for the visualisation of the 10–60 µm wide growing trajectories is provided by the dense sensor array containing 64×64 pixels. In the case of citric acid injection and the BZ–reaction the ion camera chip is shown to be able to resolve pH differences with resolution as low as the area of one pixel. As a result of the transient and volatile ionic fluxes high time resolution is required, thus the signal capturing can be performed in real–time at the maximum sampling rate of 40 µs per pixel, 10.2 ms per array. The extracted sensor data are reconstructed into ionic images and thus the ionic activities can be displayed as individual figures as well as continuous video recordings. This chip is the first prototype in the envisioned establishment of a fully automated CMOS based ion camera system which would be able to image the invisible activity of ions using a single microchip.

In addition the capability of detecting ultra–low level pH oscillations in the extracellular space is demonstrated using cells of the slime mould organism. The detected pH oscillations with extent of ~0.022 pH furthermore raise the potential for observing fluctuations of ion currents in cell based tissue environments. The intrinsic noise of the sensor devices are measured to observe noise effect on the detected low level signals. It is experimentally shown that the used ion sensitive circuits, similarly to CMOS, also demonstrate 1/f noise. In addition the reference bias and pH sensitivity of the measured noise is confirmed. Corresponding to the measurement results the noise contribution is approximated with a 28.2 µV peak–to–peak level and related to the 450 µV ± 70 µV peak–to–peak oscillations amplitudes of the slime mould. Thus a maximum intrinsic noise contribution of 6.2 ± 1.2 % is calculated. A H^+ flickering hypothesis is also presented that correlates the pH fluctuations on the surface of the device with the intrinsic 1/f noise.

The ion camera chip was fabricated in an unmodified 4–metal 0.35 µm CMOS process and the ionic imaging technology was based on a 64×64–pixel ion sensitive field effect transistor (ISFET) array. The high–speed and synchronous operation of the 4096 ISFET sensors occupying 715.8×715.8 µm space provided a spatial resolution as low as one pixel. Each pixel contained 4 transistors with 10.2×10.2 µm layout dimensions and the pixels were separated by a 1 µm separation gap. The ion sensitive silicon nitride based passivation layer was in contact with the floating gates of the ISFET sensors. It allowed the capacitive measurements of localised changes in the ionic concentrations, e.g. pH, pNa, on the surface of the chip. The device showed an average ionic sensitivity of 20 mV/pH and 9 mV/pNa. The packaging and encapsulation was carried out using PGA–100 chip carriers and two–component epoxies. Custom designed printed circuit boards (PCBs) were used to provide interface between the ISFET array chip and the data acquisition system. The data acquisition and extraction part of the developed software system was based on LabVIEW, the data processing was carried out on Matlab platform.

Declaration and Copyright

Declaration

The content of this thesis is my independent and own work which has been performed at the Electronics Design Centre, School of Engineering, University of Glasgow, Glasgow, UK. Clear reference is provided at each stages where I used any work or information from others.

Balázs Németh

Copyright

Acknowledgements

I would like to acknowledge the great help of people which was essential to finish the work for this thesis. I thank my supervisor, Prof. David R. S. Cumming, his continuous support, hints and advices as well as his patience for keeping me on the right track during my PhD. His encouraging comments helped me a lot with getting new ideas, realising the mistakes or pointing out the way forward. I also thank Dr. Mathis O. Riehle for being my second supervisor and Dr. Diego Barrettino for the initial 9 months of my doctoral studies. This work could not have been brought to such a successful end without the active chemical/biological cooperation with Prof. Lee Cronin, Dr. Mark D. Symes, Dr. Christoph Busche, Dr. Soichiro Tsuda and Antoine G. Boulay.

I pay special thanks to Dr. Gábor Mezősi, for his help, ideas and the highly entertaining conversations, Dr. James Grant for proofreading my thesis, publications and for the regular "good quality chats". Also special thanks to Dr. Anne Bernassau for the ultrasound cooperation and her friendship. I thank all members of the MST group as well for the enjoyable time. Although he cannot be with us anymore, I pay gratitude to Dr. Simon Triger for being a climbing partner and such a cheerful person, it was great to have known you...

I would like to thank my whole family for their constant support and encouragement throughout my journey in Glasgow.

Contents

List of Figures

List of Tables

Glossary of Symbols

A	Ampere
α	Sensitivity parameter
α_H	Hooge coefficient
c(t)	Autocorrelation function
C_D	Depletion capacitance
C_{GC}	Gouy–Chapman capacitance
C_H	Helmholtz capacitance
C_I	Inversion capacitance
C_{IT}	Interface capacitance
C_{OX}	Oxide capacitance
C_T	Transfer capacitance
f	Frequency
F	Faraday constant
φ_{int}	Potential across the electrolyte–insulator interface
Φ_M, Φ_{Si}	Work functions of the gate terminal and the semiconductor
Φ_F	Fermi potential
G	Available free energy
g_m	Transconductance
GND	Ground potential
χ_{sol}	Dipole potential of water molecules
Hz	Hertz
I_D	Drain current
k	Boltzmann constant
L	Gate length of the applied transistors
MET 1/2/3/4	Interconnection metal 1/2/3/4
mm	Millimetres
ms	Millisecond
mV	Millivolt
µA	Microampere
μ_{eff}	Effective mobility of the charge carriers
µm	Micrometre
µs	Microsecond
N	Number of mobile charge carriers
$p_0(t)$	Probability measure for not making a transition between specified times
$p_1(t)$	Probability measure for making a transition between specified times
$P_{11}(t)$	Probability measure for even number of transitions
$P_{10}(t)$	Probability measure for odd number of transitions
pH	Measure for the activity of hydrogen ions in aqueous solutions
pH_{pzc}	Point of zero charge
pK	Measure for the activity of potassium ions in aqueous solutions
pNa	Measure for the activity of sodium ions in aqueous solutions

ψ_S	Surface potential
q	Coulomb charge of an electron
Q_D	Depletion charge
Q_I	Inversion charge
Q_{IT}, Q_{ss}	Fast interface state charge
Q_{OX}	Oxide charge
R	Resistance
ρ	Charge density
S_I	Drain current spectral density
S_V	Gate voltage spectral density
T	Absolute temperature
τ_e, τ_1	Time constant of electron emission
τ_c, τ_0	Time constant for electron capturing
UV	Ultra violet
V	Volt
VDS	Drain–source voltage
V_{FB}	Flat–band voltage
V_{DD}	Power potential
V_G	Gate voltage
V_{GS}	Gate–source voltage
V_{IHP}	Voltage drop at the Inner Helmholtz Plane
V_{OHP}	Voltage drop at the Outer Helmholtz Plane
V_{REF}	Reference electrode voltage
V_T	Threshold voltage
W	Gate width of the applied transistors
z	Valence of ions

List of Acronyms

AMIS	Accumulation Method Ion Sensors
ASIC	Application Specific Integrated Circuit
BZ	Belousov–Zhabotinsky
CAD	Computer Aided Design
CCD	Charge Coupled Device
CMOS	Complementary Metal Oxide Semiconductor
DI	Deionised
DIP	N,N´–bis (5–phenanthridinium–5–yl–ethyl chloride)octane–1,8–diamine dihydrochloride
DNA	Deoxyribonucleic acid
DRC	Design Rule Check
DSA	Dynamic Signal Analyser
EIS	Electrolyte–Insulator–Semiconductor
EMI	Electromagnetic Interference
FPS	Frame per second
EXT	Netlist extraction
G–R	Generation–recombination
IC	Integrated Circuit
ISFET	Ion sensitive field effect transistor
LoC	Lab-on-a-Chip
LPCVD	Low pressure chemical vapour deposition
LVS	Layout versus schematic
MOSFET	Metal oxide semiconductor field effect transistor
MPW	Multi Project Wafer
µTAS	Miniaturized Total Chemical Analysis System
PCB	Printed Circuit Board
POM	Polyoxometalate
PSD	Power spectral density
PRE/qRE	Pseudo/Quasi Reference Electrode
PXI	PCI eXtensions for Instrumentation
RCX	RC extraction
RTS	Random Telegraph Signal
RT–target	Real–time target
SMPS	Switching mode power supply
SNR	Signal to noise ratio
TDMS	Technical Data Management Streaming
VLSI	Very Large Scale Integrated

Publications

A. Papers

Peer–reviewed journal papers

1. **Balazs Nemeth**, Mark D. Symes, Antoine G. Boulay, Christoph Busche, Geoffrey J. T. Cooper, David R. S. Cumming & Leroy Cronin: *Real–Time Ion–Flux Imaging in the Growth of Micron–Scale Structures and Membranes,* Advanced Materials, Volume 24, Issue 9, p. 1238–1242, 2012

2. **B. Nemeth**, S. Tsuda, C. Busche, L. Cronin and D. R. S. Cumming: *An ISFET sensor system for real–time detection of extracellular pH oscillations in slime mould*, Electronics Letters, Volume 48, Issue 3, p.144–146, 2012, ***featured publication in the front article of journal issue***, Electronics Letters, Volume 48, Issue 3, p.135–136, 2012

3. **Balazs Nemeth**, Christoph Busche, Soichiro Tsuda, Leroy Cronin and David R. S. Cumming: *Imaging the Belousov–Zhabotinsky reaction in real time using an ion sensitive array*, Chemical Communications, Vol. 48, pp. 5085-5087, 2012

4. **Balazs Nemeth**, David R. S. Cumming: *High–resolution real–time ion–camera system using a CMOS–based chemical sensor array for proton imaging*, Sensors and Actuators B: Chemical, Volumes 171–172, pp. 747–752, 2012

5. Peter Shields, **Balazs Nemeth**, Richard B. Green, Mathis O. Riehle, David R. S. Cumming: *High–speed imaging of 2–D ionic diffusion using a 16x16–pixel CMOS ISFET array on the microfluidic scale*, IEEE Sensors Journal, Vol. 12, No. 9, pp. 2744–2749, 2012

Conference Paper

1. Cumming, D. R. S. ; Shields, P. N. ; Piechocinski, M. S. ; **Nemeth, B.**: *High speed sensing using ion sensitive field effect transistors*, 4th IEEE International Workshop on Advances in Sensors and Interfaces (IWASI), pp.57–59 2011

B. Oral Presentations

1. **B. Nemeth**, M. Symes, A. G. Boulay, C. Busche, L. Cronin, D. R. S. Cumming: ***Invited talk*,** *Imaging ions in chemistry and biology*, Imaging Network Seminars, University of Glasgow, Oct 2011
2. **B. Nemeth**, D. R. S. Cumming: *Ion camera development for real–time acquisition of localised pH responses using the CMOS–based 64×64–pixel ISFET sensor array technology*, Bioengineering11, Queen Mary University of London, Sept 2011
3. A. L. Bernassau, Y. Ma, **B. Nemeth**, P. MacPherson, C. Courtney, D. R. S. Cumming, M. Riehle, B. W. Drinkwater: *pH Sensor Integration in an Octagon ultrasonic cell and its applications*, University of Southampton, Aug 2011
4. A. L. Bernassau, Y. Ma, **B. Nemeth**, P. MacPherson, C. Courtney, M. Riehle, B. W. Drinkwater, D. R. S. Cumming: *Octagon and Heptagon ultrasonic cell: strength, weakness and their application*, University of Southampton, Feb 2011

C. Poster Presentations

1. A. L. Bernassau, **B. Nemeth**, Y. Ma, C. Courtney, D. R. S. Cumming, M. Riehle, B. W. Drinkwater: *Integration of acoustic tweezers and ISFET–pH sensor*, University of Southampton, Feb 2011
2. **B. Nemeth**: *Development and evaluation of a 64×64–pixel ISFET pH sensor array using standard 0.35µm CMOS technology*, Postgraduate Conference, University of Glasgow

E. Media

1. **BBC**: *Glasgow University microchip 'speeds up DNA analysis'* – My development is included in the video available from website

F. Industry

1. **National Instruments Case Study**
   Balazs Nemeth, David R. S. Cumming: *Real–time acquisition and visualisation of ion fluxes using an ion camera microchip*, *http://sine.ni.com/cs/app/doc/p/id/cs-14703*

G. Reviewer

1. **Sensor Letters**, American Scientific Publishers
   http://www.aspbs.com/sensorlett.html
2. **Electronic Letters**, Institution of Engineering and Technology
   http://www.theiet.org/resources/journals/eletters/index.cfm

1. Introduction

1.1. Motivation

"I can use your MOSFETs. Bring them here, but don't bring the gate metal." [1] – said P. Bergveld from University of Twente to Prof. O.W. Memelink from Philips in 1967. This comment proved to be the first big milestone in the research of ion sensitive sensor devices. The initial devices invented by Bergveld were included in brain based electrophysiological characterisation research to study the tremor phenomenon of Parkinson's disease. In addition the electrolyte and cells were in direct contact with the gate oxide of the sensors. The developed ion sensing devices were termed as ion sensitive field effect transistors (ISFETs) and were observed to change their drain current with respect to specific ionic concentration levels in the applied electrolytes and extracellular space. Since the initial invention, over the past approximately 45 years, several additional applications have been discovered for MOSFET based ion–sensitive transistors including food and medical sciences, biochemistry and electrochemistry.

The range of applications for ISFETs is very broad because ISFETs are ion sensors and the measurement of pH, pH fluctuations and other additional ionic species, is important in various industrial and medical fields. Besides the ionic species of interest, ISFET devices also vary in terms of size. They can be included in desktop or handheld devices mostly as a pH meter however ISFETs are also used in or as a part of microelectronic circuits as well. The size of ion sensors included in integrated circuits usually varies from a few micrometres up to some hundreds of micrometres. One of the main advantages of ISFETs is that they enable the monitoring of ionic activity in biochemical or electrochemical systems. This is significant because on the one hand ions are cardinal elementary units of chemical processes that develop by releasing or taking up electrons by redox reactions. On the other hand the micrometre–scale size of ISFET sensors can find applicability in fields where robust desktop or hand–held devices cannot be used, e.g. implantable sensors. Thus the link between electrochemical, biochemical processes and microelectronic circuits became established with the application of ISFET transistors.

The fabrication of ISFET transistors was initially carried out using adapted CMOS processes where the gate metal was removed to provide a direct interface between the transistor gate and the electrolyte. It was shown later [2] that ISFETs could also be

fabricated in sub–micron unmodified CMOS processes. The usage of unmodified CMOS processes simplified the sensor design and fabrication, reduced the overall costs and standardised the fabrication steps. In addition it enabled the automated integration of ISFET sensors into VLSI circuitries which facilitated the downscaling of complex ion sensor technologies. The fabrication methods of integrated ISFET devices also significantly influenced the applicability of the sensors since the default passivation layer over the chip deposited by the manufacturer could be used as the ion sensing layer.

Silicon nitride is common to use in most CMOS processes as part of the passivation layer and it is responsive to several ion species. This multiple ionic sensitivity makes it difficult to observe specific ion currents of a liquid or a biological tissue. Thus, if necessary, ionic specificity is usually achieved on the one hand by depositing an additional ion sensing layer with very selective responsiveness onto the chip surface which completely seals the passivation. On the other hand the careful selection of the applied specimen and chemical substances can ensure that the reacting system delivers only one time and space varying ionic flux. However, despite the various possible ion specific measurements, in the majority of cases ISFET devices are used as proton sensors. Hence the concentration fluctuations of hydrogen ions are detected in several elements, e.g. the electrolyte bulk, the extracellular space of living tissues or the interior of organs and intestines in particular [3].

Both voltage and current sensor output signals are commonly measured for evaluating the response of the devices to the occurring ionic flux. Depending on the strength of the induced change in the ionic concentration and the used reacting substances the voltage outputs of the ISFET sensors adapt with appropriate rise or fall. The extent of the signal fluctuations are also determined by the sensitivity rates of the ion sensing layers to the ionic species in question that often follow a linear function over a broad logarithmic range. Besides the sensitivity the long term output signal stability of the ISFET sensors usually is a critical parameter especially in the field of medical devices. The ion sensors with expected long–term and continuous operation require robust sensor structures and a settled response to reliably analyse quantities, e.g. pH of blood.

However, the short term and rapid responses of ion sensors are also important to investigate recording only the transient ionic behaviour and thus voltage signal fluctuations without consideration of absolute values. Transient events, e.g. fast pH change, or dynamic processes, e.g. periodical concentration fluctuations in chemical and biological systems usually occur in the millisecond time period and are often followed by the development of

equilibrium. The narrow temporal margins also limit the required operation and observation time. As a consequence, the acquisition of the rapidly changing and relative sensor data implies the possibility of monitoring the dynamic behaviour of electrochemical systems. Thus focusing on only short term and rapid events enables the observation of highly volatile occurrences including the mixing process of chemical substances, localised chemical reactions or even the flow and location of a specific ionic current of a biological tissue.

In the literature the output signals of ISFET sensors were mostly utilised and classified as simple data traces that corresponded to the fluctuations of the ionic concentrations in liquids. Furthermore it was common practice to consider systems which retrieved the data by using individual ion sensors either for pH or for additional ionic species. Thus on the one hand it indicates that the opportunity of improved data representation with colours was not part of the main stream of ISFET research. The assignment of different colours to different parts of the data value range is important because it can facilitate the visual distinction between separate parts of the data traces. On the other hand bundles of ion sensors of the same type can also deliver valuable information in terms of the localisation of the occurring chemical reactions. The arrangement of ion sensors in an array structure enables the comparison of the activity of neighbouring sensors and can potentially reveal localised reactions over the sensor surface.

Hence the limited time focus and fast data capturing as well as the array structuring of ion sensors provide the chance to record the behaviour of dynamic and moving chemical or biological processes at technology dependent spatial resolution. In addition the consideration of the sensor array data as whole and combining it with the suggested colour coding it becomes possible to achieve the visualising of the mobile ionic behaviour as developing images of the transient ionic transport events. As a consequence, the ionic transport can be imaged even as continuous video recordings by concatenating the series of developed images. It indicates the achievement of a monolithic and ISFET–based ion camera system that can provide high time resolution due to the fast data acquisition and high spatial resolution because of the dense sensor array and the number of participating ISFET pixels. Ionic imaging is a relatively novel field in ionic research and certainly innovative in the sector of ISFETs to date. In addition it is expected that ion camera microchips can potentially replace heavy machineries in the future and contribute to the analysis of chemical and biological systems.

This thesis introduces the development of an integrated ion camera system that is based on the 64×64–pixel ISFET array technology. The innovative ion camera chips were fabricated in an unmodified 4–metal 0.35 µm CMOS process from austriamicrosystems. It is shown in the subsequent chapters that the chip, with an overall extent of 4.2×4.3 mm, was able to image localised concentration fluctuations of H^+ and Na^+ using the 715.8×715.8 µm large ISFET sensor array containing 4096 sensors. The spatial resolution of the demonstrated ionic imaging approach is shown to be as low as the size of one ISFET pixel, 10.2×10.2 µm. Besides mixing acidic and alkaline substances the visualisation of ionic activity was also tested using advanced chemical substances and the slime mould biological exemplar. The results showed that the ion camera chip detected spontaneous chemically induced pH fluctuations, synchronised ultra–low level pH oscillations and the growth of micrometre–sized polyoxometalate tubular and membranous structures. Because of the fast decaying reactions real–time data acquisition was utilized using the hardware–timed synchronised functionalities of the measurement cards. A maximum rate of 40 µs per pixel, 10.2 ms per array, data capturing speed was achieved which corresponded to a ~100 frame per second device scanning rate. The developed and discussed semiconductor chip is the first ion camera prototype that is built on the 64×64–pixel ISFET sensor array technology.

1.2. Objectives

The presented research work was carried out at the Electronics Design Centre, University of Glasgow. This thesis presents the scientific achievements in ISFET based ionic imaging using an unmodified 0.35µm CMOS fabrication approach. In particular, the presented work was carried out following the objectives below:

- Development of a dense and high–resolution ISFET sensor array with multifunctional pixel circuits using an unmodified CMOS fabrication process, thus silicon nitride is the ion sensitive layer.
- Development of a fast and hardware–timed data acquisition system that provides sufficiently high time resolution to follow the chemical reactions and development of software algorithms to efficiently exploit the high spatial resolution information provided by the ISFET sensor array.
- Measurement of localised concentration fluctuations of ionic species that the silicon nitride is responsive to including H^+ and Na^+ as well as the expectedly arising intrinsic noise of the sensor pixels.

- The output data set of the complete ISFET sensor array is considered and taken for imaging purpose therefore the short term and rapid ionic concentration fluctuations are of interest. The responses of single pixels are also considered for evaluation of 1/f noise.
- Testing the system with advanced chemistry and biology related experiments that by nature provide localised ionic activity or are characterisable with ionic specificity from the considered range of ionic species.

The following chapters discuss the research work carried out alongside the demonstrated list of objectives. The tests with moving chemical trajectories were performed using live optical video recording. It demonstrated the excellent correlation between the ion camera and optical microscope images and furthermore showed that in special cases the ion camera could "see" more than the optical microscope devices.

1.3. Organisation of the chapters

The succeeding sections of this thesis are organised as follows:

Chapter 2 reviews the corresponding literature to show the development of ISFET devices and to give an insight into the existing approaches in ionic imaging to date. The potential intrinsic noise sources and lab–on–a–chip systems are also discussed.

Chapter 3 summarises firstly the theory on 1/f noise discussing the widely known number and mobility fluctuation theories. The RTS noise phenomenon is demonstrated showing the probability distribution of RTS occurrences and the calculated Lorentzian power spectrum. Secondly the chapter delivers an introduction on redox reactions and describes the electrochemical background of the sensor–electrolyte interface. The reference electrodes used are demonstrated and the principles of ISFET transistors are discussed.

Chapter 4 discusses the architecture of the system approaching from the structure of a single ISFET pixel towards the topology of the complete system with schematic and layout representations. This chapter also discusses the applied packaging and encapsulation methods as well as the utilised real–time data acquisition system and data extraction algorithm.

Chapter 5 presents the experimental results on measured noise showing its bias and pH dependence in ion–sensitive devices. The H^+ flickering hypothesis is introduced in the

analogy with the random telegraph signal noise correlating electrochemical processes and the measureable intrinsic noise of ISFET circuits. In addition the chapter discusses the measurement work showing the ability to detect the ultra–low level pH oscillations of cell based biological specimens.

Chapter 6 demonstrates that the ion camera chip is able to visualise ionic activity of induced and spontaneous reactions. The ions move as a wave front across the surface of the sensor array in the case of citric acid injection and the BZ–reaction. The growth of nearly nanometre–sized tubular and membranous polyoxometalate architectures is also imaged at high spatial and temporal resolution. In addition it is shown that the ion camera device is able to monitor the growth of the chemical structures when the view of the optical microscope was obstructed.

Chapter 7 summarises the work discussed and presenting the conclusions of the results. The chapter also outlines the plans for future improvements for the following prototypes of the chip.

The thesis includes 2 appendices that contain on the one hand the schematic circuit diagrams of the chip on the other hand snippets from the separate software modules.

2. Literature review

2.1. Ion sensitive field–effect transistors

The ion sensitive field–effect transistor (ISFET) concept was initially introduced by Bergveld in 1970 [4] to match ion sensitive electrodes with solid state electronics. In his experiments he used p–type MOSFET (metal–oxide–semiconductor field–effect transistor) transistor structures with thermally grown SiO_2 without a gate metal terminal. Increasing drain current has been measured proportional to the increasing molarity of NaCl in the applied solution at constant pH and drain–source voltage. One of the novelties mentioned was the capability of performing electrochemical experiments without the need of incorporating reference electrodes to measure the surface charge with the device. The significance of ISFETs in terms of electrophysiology was reported in his subsequent publication [5] associating the device with additional amplification electronics. It was shown by plotting drain current against the concentration fluctuation of NaCl, KCl, $CaCl_2$ and $MgCl_2$ that the hydrated surface of thermally grown SiO_2 was sensitive to the key ionic species in cell–based biological tissues.

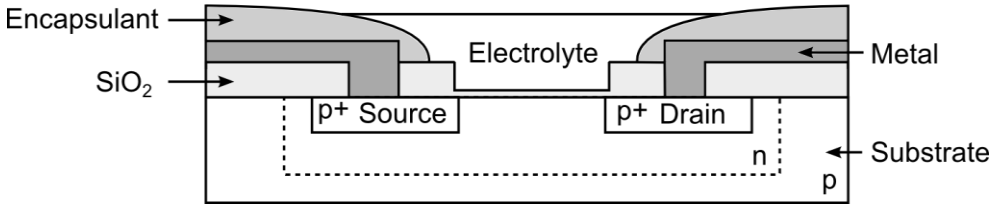

Figure 2.1 Structure of a SiO_2 gate ISFET

As an improvement of Bergveld's initial concept Matsuo *et al.* [6] performed experiments using Si_3N_4 and SiO_2 dual layers as ion–sensitive gate dielectric and saturated calomel electrode to reference potential of electrolyte. The MOSFET circuit connected in a source–follower configuration was insulated by a 1 µm thick deposited silicon dioxide save for the gate window sensory area. The device was reported to show low pNa and pK sensitivities although the slope pH sensitivity was shown to closely agree with theoretical glass electrode results.

ISFET devices were also designed to target specific ions showing their importance as chemical sensors. The potassium sensor by Moss *et al.* [7] used a similar Si_3N_4 – SiO_2 dual layer approach with removed gate metal and additional deposited valinomycin–based ion–sensitive membrane. The authors emphasized the necessity of preconditioning the ISFET

devices and the usage of Si_3N_4 because of its resistance to hydration thus reducing gate current leakage. In addition, the application of a reference electrode was also considered to be essential – disputing Bergveld's observations. The properties of ISFETs for detection of $H^+/K^+/Ca^{2+}$ concentration changes with replaced gate metals were discussed by McBride *et al.* [8]. They indicated the different stability and life time of sensors depending on the type of deposited ion–selective membrane. A MOS–based fabrication process was described by Esashi *et al.* [9] to establish a technology for fabrication of ISFET sensors. H^+ and Na^+ sensitive ISFETs were integrated on the same device accommodating the ion–sensitive area to the tip of the probe. The microprobe was also used as an in–vivo intracranial pH and pNa sensor in a rabbit. The device measured the drop of [H+] and [Na+] as a result of temporary termination of the artificial respiration.

Several inorganic materials have been reported to be compatible for ion–sensitive type measurements in the literature. The membrane deposition onto the top of the ISFET gates seemed to be a common practice either with or without gate metal. Table 2.1 summarises the materials that have been reported to have appreciable pH sensitivity and were applied as ion–sensitive membranes.

Material of membrane	**Range** pH	**Sensitivity** [mV/pH]	**References**
SiO_2	4–10	25–35	[10]
Si_3N_4	1–13	46–56	[7]
Al_2O_3	1–13	52–58	[7]
Ta_2O_5	2–9	59.3	[11]
BN	1.8–10	50–59	[12]
ZrO_2	1–8.5	58	[13]
RuO_2	2–10	52.1	[14]
TiN	4–10	57	[15]
Pt	1–5	25.1	[16]
IrO_x	1.5–12.1	57.1–57.6	[17]
HfO_2	2–8	55	[18]

Table 2.1 Materials used for detection of pH fluctuation in the literature

Silicon dioxide (SiO_2) was initially used for measuring the fluctuations in proton concentration however some time later silicon nitride (Si_3N_4) and aluminium oxide (Al_2O_3) were also found to deliver excellent pH response as well. The application of tantalum oxide (Ta_2O_5) showed that it is possible to deposit diverse materials as [H^+] sensitive membrane, even unusual ones like for instance borazon (BN), zirconium oxide (ZrO_2) and

ruthenium oxide (RuO_2). Titanium nitride and platinum coatings have also been found suitable as well as iridium oxide (IrO_x) and hafnium oxide (HfO_2) based technologies.

The ion–sensitive field effect transistor concept has also been used to target additional ionic species extending the scope of applicability. Ion–sensitive membranes selective to K^+, Na^+, even Co^{2+} and Cu^{2+} ions have been reported. The membrane materials are listed in Table 2.2.

Membrane material	**Ion species X**	**Observed range of concentration [pX]**	**Sensitivity [mV/pX]**	**References**
RTV silicon rubber	K^+	1.5–4.5	56	[19]
Sodium aluminosilicate	Na^+	0–2	56–58	[20]
Calix[4]arene	Na^+	1.5–3	59.2	[21]
Calix[8]arene	Co^{2+}	1–2.5	22.3	[21]
TCNQ	Cu^{2+}	2–5	30	[22]

Table 2.2 Specific ion sensitive membrane materials

The development of MOSFET–based microelectronic systems using CMOS (complementary metal–oxide–semiconductor) fabrication processes facilitated the progression towards a common structure for ISFET sensors. Initial research on developing chemical sensor devices in several hundreds of micrometres dimension range focused mostly on using CMOS processes with appropriate modifications on the ISFET side. In the 2 µm feature size CMOS technology of Bousse *et al.* [23] MOS and ISFET transistors were built in close proximity on silicon and shared similar fabrication steps until the completion of the metallisation. Tungsten silicide was applied as interconnection metal because of its resistance to high temperatures that occurred throughout the deposition processes. The deposition of an undoped silicon dioxide layer was followed by a photolithographic window opening above the ISFET gate and the SiO_2 was subsequently etched away up to the preserved polycrystalline silicon (polysilicon) gate. Silicon nitride was then deposited onto the chip surface as passivation and pH sensitive layer which was followed by the fabrication of an on–chip silver/silverchloride (Ag/AgCl) reference electrode. According to the authors' comments, the Si_3N_4 could have been exchanged to Al_2O_3 or Ta_2O_5 as well considering the freedom for high temperature and proven pH–sensitivity. Wong *et al.* [24] reported a different CMOS–ISFET process where the ion–sensitive devices were located in a separate n–well to provide p–n junction isolation. The

polysilicon and the gate oxide were wet etched which was followed by the growth of an approximately 150 Å thick SiO_2 layer. Si_3N_4 and Ta_2O_5 were deposited onto the surfaces along with photolithographic patterning and annealing to oxidise the Si_3N_4/ SiO_2 to $SiO_xN_y/Si_3N_4/SiO_2$. In the final step of the fabrication process a thick Ta_2O_5 layer was sputtered to encapsulate the chip, save for the ISFET gates. The pH sensitivity for the tantalum gate was measured to be 58–59 mV/pH and the nitrided gate showed a sensitivity of 18–20 mV/pH that was ideal for their measurement purposes. In the following years similar research has been conducted following the path of simplified MOS processes and investigating the compatibility of ISFET and MOS technologies as discussed in the publication of Cané *et al.* [25]. The aim for performing the complete fabrication flow and integration in one single CMOS process has been articulated by Yeow *et al.* [26] emphasizing its practicability and cost efficiency. The produced 15×16 array of ISFET–comparator blocks used ISFETs with an etched gate, regrown gate oxide and deposited Si_3N_4 resulted in a pH sensitivity of 57 mV/pH.

The work of Bausells *et al.* [27] presented important developments on the flow of ISFET fabrication achieving its complete integration into commercial CMOS fabrication. A two–metal CMOS process was selected and the polysilicon gates of the ISFET transistors were connected to the Si_3N_4/SiO_2 passivation layer through the intermediate metal layers and vias as shown in Figure 2.2. As a consequence the pH sensitive passivation layer with sensitivity of 47 mV/pH was in contact with the electrolyte and the gate voltage of the ISFETs was capacitively perturbed through the ion–sensitive membrane. The core significances of unmodified CMOS process based microelectronic designs were on the one hand the chance to use pre–developed library components that vastly decrease the invested time in the system design. On the other hand the chip manufacturing simplified to fitted computer design using special foundry parameters provided by appropriate external companies who also accomplish the fabrication with dedicated machinery, as discussed in Section 4.1.

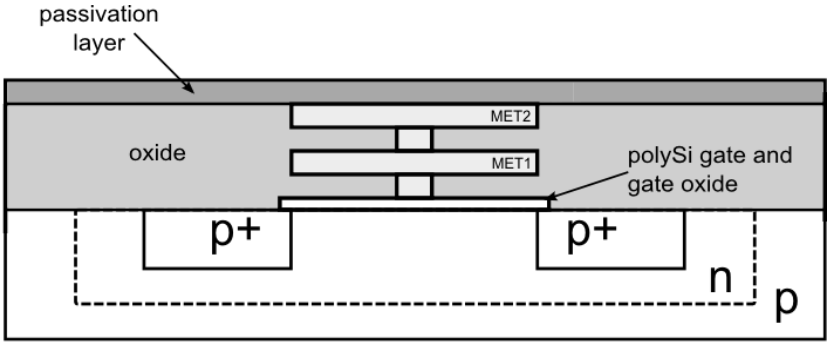

Figure 2.2 ISFET transistor fabricated in a two–metal CMOS process [27].

2.2. Noise sources

Noise is an important factor to consider when designing very large scale integrated (VLSI) circuits due to its impact on the quality of the signal recorded. The undesired random or periodical perturbation of the useful signal by the intrinsic noise might compromise the signal–to–noise (SNR) ratio. Due to the extensive number of potential noise sources in electronics only the class of intrinsic sources in semiconductors are reviewed in this work. The following sections give a brief overview on these noise sources focusing specifically on the field of low voltage and current fluctuations in semiconductors.

2.2.1. Thermal noise

The thermal noise originates from the random and thermally agitated motion of charge carriers in metal and semiconductor materials. The thermal noise is often referred as Johnson or Nyquist noise, referring to the scientists who reported the phenomenon (Johnson, [28]) and verified it theoretically (Nyquist, [29]) from Bell Laboratories. This type of noise exists without any application of a bias voltage and is considered as white–noise because of its flat shaped power spectral density (PSD). The expressions for the fluctuating current and voltage was defined as [30]

$$I^2_{noise} = \frac{4kT\Delta f}{R} \tag{2.1}$$

$$V^2_{noise} = 4kTR\Delta f \tag{2.2}$$

where R is the resistance of the material, T is the temperature, k is the Boltzmann–coefficient and Δf is the bandwidth. Considering that the velocity and direction of the scattered electrons are random, the amplitude and the sign of the resulting current are random as well. As a consequence the measured average net current over a sufficiently long time is zero. The thermal noise is an essential phenomenon in circuits containing resistive parts and is often an integral part of other types of noise therefore limits the precision of measurements.

2.2.2. Shot noise

The shot noise, or as also referred to as Schottky noise, stems from the quantised nature of the flow of charge carriers over a potential barrier, i.e. a p–n junction. The variation in

value of the DC current across a diode relates to the fluctuation in the number of electrons holding charge level q over a period of time. The occurrence of this type of signal inconsistency, first described by W. Schottky [31], follows a Poisson distribution if the number of travelling electrons is random and the charge carriers are assumed to act independently. The average noise current value is defined as [32]

$$I_{n\,noise}^2 = 2qI_{DC}\Delta f \tag{2.3}$$

where q denotes the $1.6\times10^{-19}C$ charge, I_{DC} is the considered DC current and Δf is the bandwidth. Depending on the observed range of current and bandwidth the role of the shot noise might be dominant. Taking the expressive example of [33], if a ~57nA fluctuating RMS current is considered around a 1A DC current at 10 kHz bandwidth, the ratio of the current fluctuation is approx. 0.000006%. Meanwhile if a sensitive measurement had to be performed at a DC current level of 1µA and bandwidth of 10 kHz, the average noise current would be ~56 pA which is approx. 0.006% of the DC value. Following these principles lowering the considered DC current to 1pA we would receive a current fluctuation of about 6%. The shot noise is categorized as white noise and consequently it is inseparable from the thermal noise in semiconductor systems.

2.2.3. Generation–recombination noise

The generation–recombination (g–r) noise is observable in semiconductor devices and relates to the characteristic random trapping and detrapping phenomenon of electrons that in turn impacts the transport of charge carriers. If an electron is captured in an electronic state in the forbidden gap (traps) at a time constant of τ_c it is unable to participate in the electronic conduction until its release from the trap in τ_e time. Traps, i.e. energy states in the band gap, can originate from various sources as for example lattice defects due to impurity atoms, improper Si/SiO_2, nonidealities from fabrication. The generation–recombination noise is generally introduced using only τ_e and τ_c time constants showing movements of electrons however it should be noted that the phenomenon could be explained with holes as well. The number of free charge carriers in the conduction band fluctuates due to constant generation and recombination mechanisms of the traps available in the oxide and at the Si/SiO_2 interface. Therefore it is worth describing it in frequency domain including Poisson statistics of many uniform trapping/detrapping events with same characteristic time constant. The description of Jones [34] based on Kirton *et al.* [35] and

Machlup [36] shows that the spectral representation of the fluctuation of free charge carriers is Lorentzian (calculation is shown in Section 3.1.3):

$$\frac{S_N(\omega)}{N^2} = 4 \cdot \frac{\overline{\Delta N}^2}{N^2} \cdot \frac{\tau_0}{1+(\omega\tau_0)^2} \tag{2.4}$$

In the equation τ_0 is the time constant and $\overline{\Delta N}^2$ is the variance of N which denotes the number of free charge carriers.

2.2.4. Random Telegraph Signal noise

The random telegraph signal (RTS) noise is a particular type of the g–r noise that accounts for the effect of only a few number of traps. The RTS noise is usually characterised by the measurable current fluctuation switching values between two or three states. Ralls *et al.* [37] demonstrated the random switching events with fabricated $\frac{W}{L} = \frac{0.15\mu m}{1\mu m}$ MOSFET structures on p–type silicon. The observation that RTS noise mainly originates from interfacial trap region at the silicon/silicon–dioxide interface was confirmed along with its produced Lorentzian spectrum. The RTS noise induced drain current fluctuations of an nMOS transistor with effective width and length dimension of 1.2 µm and 0.35 µm respectively are shown in Figure 2.3. The RTS noise phenomenon is further discussed in Section 3.1.3

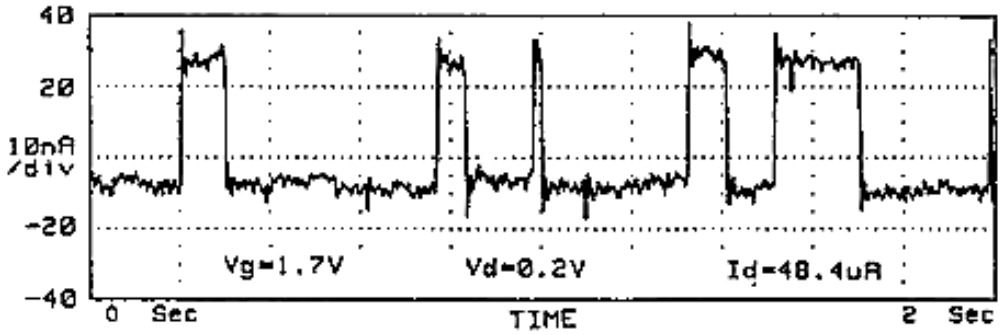

Figure 2.3 RTS noise induced drain current fluctuations. Image reproduced from [38]

2.2.5. 1/f noise

The 1/f noise, or flicker noise, is present in all semiconductor and metal structures, making it essential to observe and study in physics and electronics. The characteristic behaviour of the flicker noise was first described by Johnson [39]. It usually is approximated by the

$K\frac{1}{f^{\eta}}$ formula [40] [41] where η is a constant between 1.2 and 0.7, although its value is often chosen to 1 to be practical in calculations. The origin of flicker noise has been subject to a long term debate discussing whether the phenomenon comes from the fluctuation in the number of mobile charge carriers (McWhorther, [42]) or from the fluctuation of electron mobility (Hooge, [43]). Dutta *et al.* [44], Weissmann [45] and Kirton *et al.* [35] found that traps like the defects in the oxide lattice some nanometres away from the Si/SiO_2 interface and other impurities have an influence on the electron transport, i.e. on the drain current of MOSFET devices. It was shown that the trapping and detrapping of charge carriers had an effect on both the number of carriers and the channel mobility in the considered small area semiconductor devices. It was furthermore ascertained that in small area devices these occurrences introducing random current noise could be characterised by Lorentzian spectra showing $1/f^2$ properties [30] and that the superposition of independent Lorentzian spectras resulted in a 1/f–type roll–off. Hooge *et al.* [46] showed with a pure mathematical approach excluding mobility or number fluctuation and considering only traps and relaxation times that the summation of Lorentzians yield a 1/f spectrum mainly if the relaxation processes of the various τ time constants are isolated which indicates that these random processes are expected to act independently and no transitions are allowed between them. The noise characteristic resulting from the several RTS processes is shown in Figure 2.4.

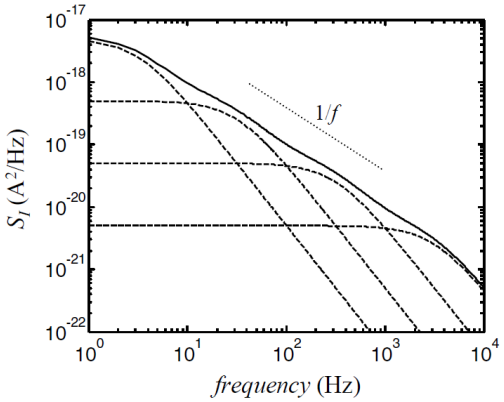

Figure 2.4 Noise showing 1/f roll–off as result of superposition of independent RTS processes. Image reproduced from [30]

It is apparent that the isolated RTS events with different time constants demonstrate $1/f^2$ type relaxation meanwhile the envelope function emerging from the summation of RTS responses displays 1/f behaviour.

The 1/f noise is discussed in Chapter 3.1 chapter in greater detail introducing the mobility and number of fluctuation theories by Hooge and McWhorther, respectively. The RTS phenomenon is discussed in Section 5.6 in correlation with the pixel circuits of the ion camera system.

2.3. Lab–on–a–chip systems

Measurement toolkits and methods were subject to continuous development over the past two decades in material science, particularly in the fields of chemistry and biology. The focus of the experimental and analytical work gradually drifted from manually controlled machineries towards automatised compact–sized and mixed–signal sensor systems. The trends to expand research knowledge of synthetic and organic materials at low molecular levels required the shrinkage of the sensor size in terms of both the surface and volume. The structural modifications to reduce the sensitive area of signal translators demanded reestablishment of the principles regarding interfaces between test and measurement devices. The miniaturisation of microsystems imposed increasingly strict limitations in the sensor design making the highest possible integration substantially important. Thus the highly integrated combinations of sensing and actuating components and compatible building blocks have emerged to be a leading priority. As a consequence, the transition from macroscopic to microscopic scaled sensory implementations advanced the structures of interconnecting electronic circuitries and instrumentation.

Following the general development path of electronics based research from early stages to the current modern industrial solutions there are three generic categories to classify levels of system integration:

- *Machinery level*. The macroscopic machinery level is interpreted as an extensive assembly of bulky electrical instruments that is built by human or hydraulic power around the test bench. This category typically assumed to incorporate thick cable interconnections and to require substantial room space.
- *Board level*. The mesoscopic system size in terms of integration is defined as board level in correlation with its reduced dimensions. The characteristic core of this tier is the printed circuit board (PCB) that is mostly laminated epoxy of several layers, i.e. FR–4. The relevant soldered physical connections between on–board and integrated circuit (IC) blocks usually are in the range of millimetres and hundreds of micrometres regarding length and width respectively.

- *VLSI level*. The degree of coherence between signal and structure is delivered at the highest rate in the VLSI class indicating the composition of sensory and supplementary electronics monolithically on a single piece of semiconductor. Feature sizes as small as tens of nanometres are lithographically defined onto a single chip producing extremely compact systems. Noise sensitivity is often reduced by performing all relevant tasks locally on–device and only signals ready for acquisition are supplied at output terminals.

Sensor devices are applied to transduce the characteristic signal of an object or substance into a measurable quantity that is in correlation with the static or dynamic properties of the original system. The application of electrochemical or organic sensors is essential for measuring and transforming the fluctuation of material parameters of the surrounding aqueous or gaseous environment into electronic signals. Multidisciplinary system concepts are therefore required on the one hand to interface the external environment with internal circuitry through sensory objects. On the other hand it is vital to perform measurement, analysis and assessment, and maintain control feedback mechanisms if necessary.

An abstract level hypothesis expressing needs and considerations from analytical chemistry was introduced by Manz *et al.* [47] who proposed to call the still theoretical device as a miniaturized total chemical analysis system (μTAS). A μTAS was believed to replace common laboratory equipment avoiding time consuming processes. It was additionally envisioned that it was going to reduce the demand for qualified technician personnel. μTAS devices were in addition expected to demonstrate great potential in analytical methods, e.g. chromatography, electrophoresis and flow–injection analysis. The suggested research directives of down–scaling and merging functionality on the same device has resulted in further technological developments. Besides μTAS, the communicated technical term *Lab-on-a-Chip (LoC)*has also gradually arisen in the literature as well.

The following sections introduce samples of the evolution of LoC systems that interface electronics, chemistry and biology. The focus of the review is narrowed due to several existing strategies in terms of implementation of LoC devices, i.e. glass and polymer materials, surface and bulk micromachining, MEMS and bioMEMS, electronics, etc. [48]. System–on–a–Chip (SoC), Lab–on–a–Pill (LoP), System–in–Package (SiP) and Lab–on–a–Chip approaches are often referred as synonyms in the literature concerning the combination of electronics with aqueous environmental experimentation. Due to the scope of this thesis the Lab–on–a–Chip term is preferred throughout this work and only LoC–

type microsystems are favoured that were designed and fabricated on unmodified CMOS platforms. Thus ones that connect integrated sensors with complex on–chip electronic circuitry and might undergo subsequent post–processing techniques.

2.4. Unmodified CMOS LoCs

The general system principles of an LoC device built in a standard CMOS process is shown in Figure 2.5. The dynamic interactions between sensors of the fabricated CMOS chip and the applied chemical compounds or biological tissues induce respective voltage or current output changes that are detected and further processed with supplementary electronics.

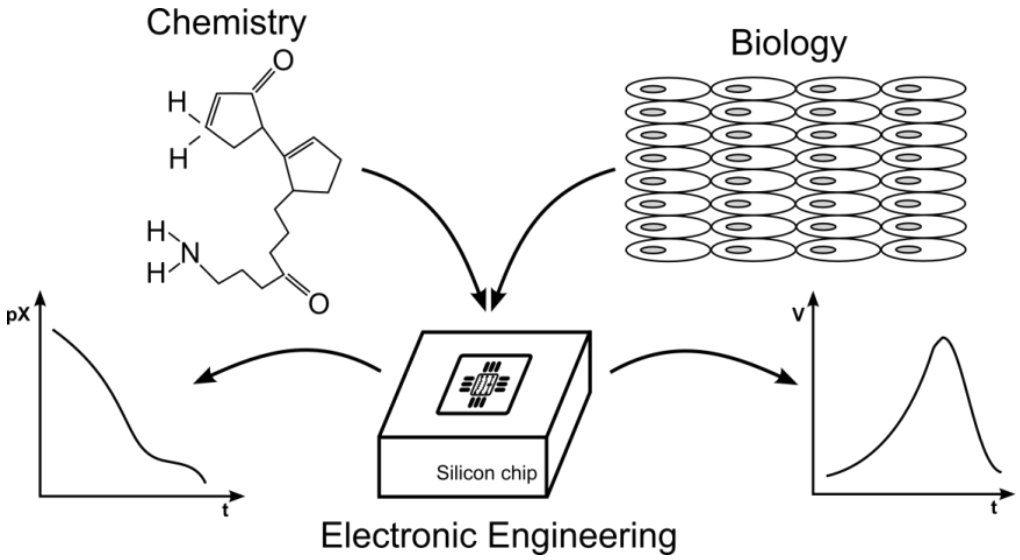

Figure 2.5 General system principles of standard CMOS process based Lab–on–a–Chip devices

LoC inventions of multidimensional complexity were strongly limited to the resource availabilities of the respective research organisations in the late 1980's since technological costs were one of the main obstacles in the design and fabrication cycles. Sensory systems based on semiconductor electronics inevitably required self–developed sets of design libraries, masks and cleanroom recipes for manufacturing. The approach by Bausells *et al.* [27] had considerable impact on the development of highly integrated biosensor microsystems. The opportunity of standardised implementations offered by various foundries enabled researchers to focus innovation on the design and supplementary post–processing. The sensitivity of ISFET devices showed inconsistency in the literature, 54–58 mV/pH [49], 45 mV/pH [50] and even 25 mV/pH [51] where the authors concluded that the pH sensitivity could be dependent on the technology of the foundries. The work of Ravezzi *et al.* [52] demonstrated that application–specific integrated circuits (ASICs) could

be embedded as vital part of LoC systems. A differential circuit was developed as well as switched capacitor arrangements with non–overlapping clock signals were implemented to improve performance and to cancel DC–offset. The NMOS W/L=800 µm/20 µm transistors were placed into a p–well for separation purposes and the circuitry was fabricated in a submicron CMOS process (Thesys/AMS 0.8 µm 5V CMOS). The ion–sensitive passivation of ISFETs was the standard Si_3N_4/SiO_2 dual layer though a buffered hydrogel layer was deposited above the reference FETs to make them ion–insensitive. The device was aimed to be used in evaluation of water pollution and biomedical diagnostics. Its 56 mV/pH sensitivity was published only later [53]. Many developed LoC devices have shown potential to be used for clinical purposes, e.g. the multifunctional sensor chip of Lauwers *et al.* [54]. Eight sensors and interface circuits ensured the monitoring of various vital parameters, i.e. pH, pO_2, pCO_2, as well as enabling on–chip four–point measurements and temperature control. The standard 1.2 µm 5V CMOS process was followed by post–processing to shape the sensors and to deposit the ion–selective membranes for the on–chip amperometric, conductometric and K^+–selective ISFET measurements. Tang *et al.* [55] envisioned an approach for in–situ measurements throughout the human gastrointestinal (GI) tract by encapsulating a multi–sensor chip for ingestion and wireless continuous monitoring. The fabricated system prototype consisted of two pieces of 5×5 mm^2 silicon dies for the sensor array and one 4.5×4.5 mm^2 ASIC for analogue signal conditioning, multiplexing and data conversion. An unmodified 3.3V 0.6 µm CMOS fabrication process was chosen for device implementation. The oxygen sensor was designed to characterise intra–intestinal aerobic bacteria meanwhile the pH sensor, of 23.4 mV/pH sensitivity, was responsible for measuring gastric acidity. Dual electrode conductivity sensors performed an indirect estimation of intestinal content and a PN junction silicon diode compensated the temperature dependence of the surrounding detectors. The entire in–situ GI endoscope capsule was demonstrated later in [56] as shown in Figure 2.6. The telemetry system was in wireless connection with a wearable base station that could catch and process the transmitted data in real–time. Although this system was an assembly of many components it is still referred as LoC because of its interconnecting on–chip sensory elements. The concept of utilizing fabricated semiconductor devices with bio–related science products induced several developments in ISFET research. Simulation and modelling [57] work demonstrated applicability of an alternative, Al_2O_3, ion–sensitive membrane and standard n–type ISFETs were demonstrated to be applicable in enzyme detection [58]. Commercial ISFET sensors were also applied to monitor the quality of drinking water and the pollution of suburban rivers [59] where the sensors were coupled with a custom designed data

processor. The ultimate aim of the CMOS ASIC was to be the driving core of a handheld pH meter that collects and administers the signals of the industrial Si_3N_4 and Al_2O_3 ISFETs.

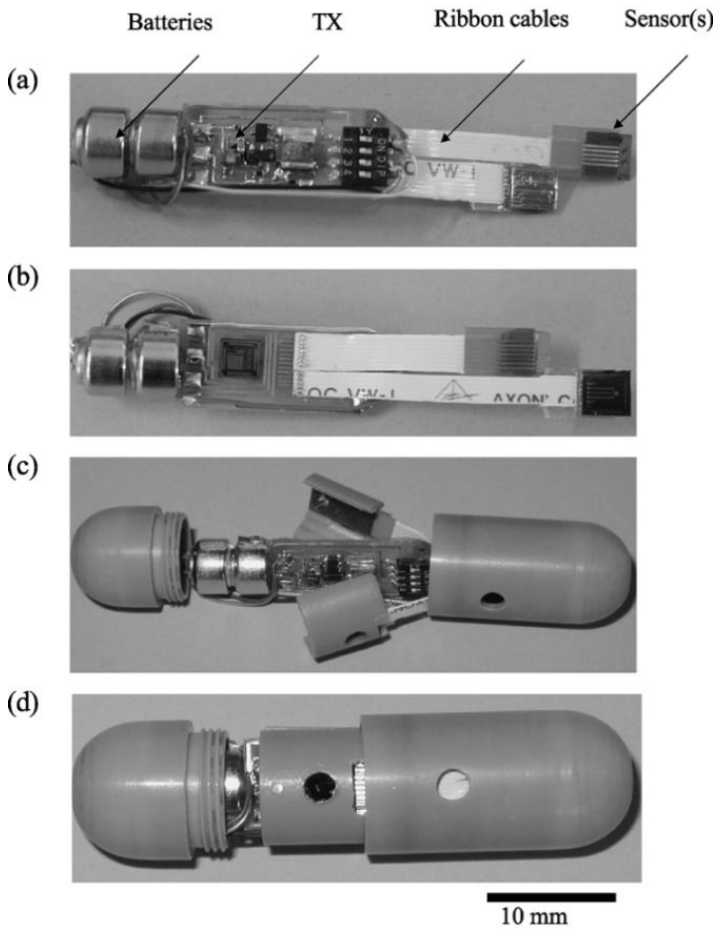

Figure 2.6 In–situ GI endoscope capsule with sensors, circuitry, batteries and shielding. (a) and (b) show the sensor system from the front and rear views respectively, (c) and (d) display the embedding and enclosing procedure of the system. Image reproduced from [56].

The compact single–chip pH measurement system by Hammond *et al.* [60] fabricated in the AMS 3.3V 0.6 µm CMOS process could be classified as the next level of integrated LoC sensor devices. The pH measurements were carried out by applying the differential detection principles and an on–chip quasi–reference electrode (qRE) to bias the ion–sensitive and reference transistors. The operation, scheduling and wireless data transmission was controlled by the laid out Motorola 6805 microcontroller unit (MCU) and SRAM memory components. The consideration of the trapped charge in the silicon nitride/silicon dioxide passivation layer contributed to the novelty of Hammond's work. The trapped charge induced by for example improper Si/SiO_2 interface, damage or dislocations in the material lattice, embedded impurity atoms or ions, etc. was perturbed by direct ultraviolet (UV) illumination exposure as described in [61]. The threshold voltage of

the ISFET transistors was modified by continuous UV irradiation mobilising the space charge present in the passivation. The UV beams elevated the energy level of charge carriers over the potential barrier of the passivation layer enabling them to tunnel towards MET4 as shown in Figure 2.7.

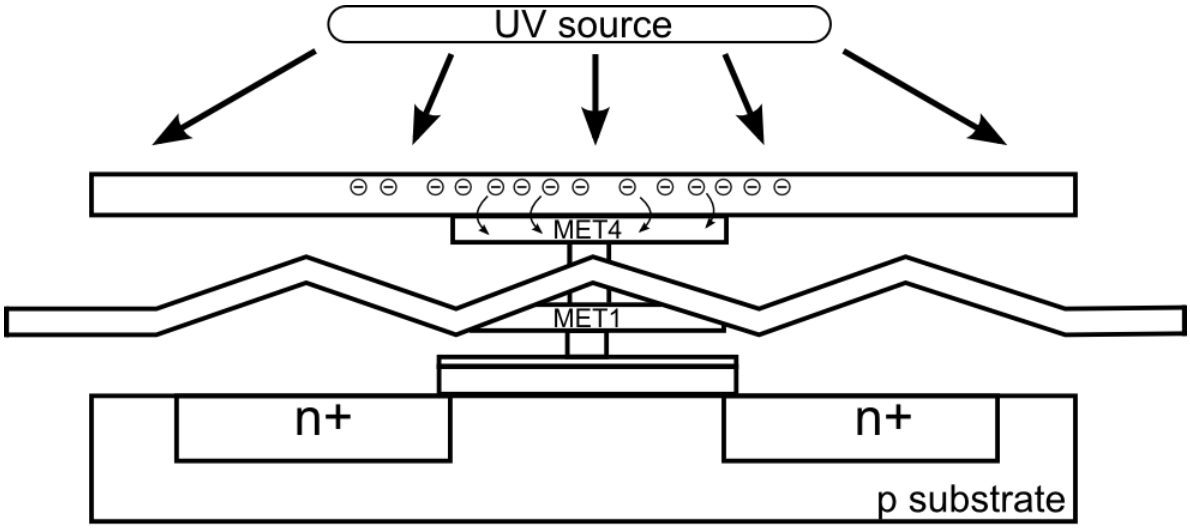

Figure 2.7 Cross–sectional view of an n–type ISFET demonstrating the physical effect of the UV irradiation

ISFET based LoC systems have been researched for invasive medical applications in the field of blood glucose disassembly analysis. Georgiou *et al.* [62] presented a silicon beta cell approach that modelled the physiological activity of human pancreatic beta cells inducing burst signals in correlation with the concentration of glucose. The ultimate goal of this LoC device was to establish the technology to develop an artificial pancreas including the silicon beta cell as a core building block which was expected to be an aid for diabetics keeping insulin balance monitored. Beta cells of the Langerhans islet in the human pancreas control the glucose metabolism by eliciting synchronised and repetitive depolarisations, bursts of action potentials, as stimulus for insulin release [63]. A glucose oxidise enzyme was immobilised on the surface of the sensor circuitry fabricated in a 0.25 µm UMC CMOS process. The capability was shown to generate glucose concentration dependent burst responses with adjustable width for plateau phase. The authors classified their work to be subject of extensive further research in terms of interactions with beta cell clusters and generated burst patterns. The work of Li *et al.* [64] further demonstrated the chemical applicability of ion–sensitive devices. Standard fabricated p–type ISFETs were subject to an additional two–step wet etch post–processing. The polysilicon gate and the intermediate metal layers were removed by piranha etchant and KOH to have the ~70 Å gate oxide layer exposed. The transistor surface was then functionalised by 3–aminopropyltriethoxysilane to make the device sensitive to dopamine. Based on its

sensitivity to femtomolar ranged dopamine concentration differences in the used electrolyte the applied technology was expected to have future potential in the treatment of Parkinson's disease.

The compact size and flexibility of standard CMOS based ion sensitive sensors and sensor networks are key factors for integration into multidisciplinary systems. The potentiometric, amperometric and even frequency–based [65] interactions cover a broad range of future application fields from biological and electrochemical equipment to long–term oceanographic underwater measurements [66]. Due to MPW (Multi Project Wafer) manufacturing opportunities at semiconductor foundries the design and fabrication became generally available for research and low volume production purposes.

2.5. Ion–sensitive sensor arrays

The application of standard fabricated CMOS sensor devices in biomedical and electrochemical research supported the micro–scaled investigations of specific ion concentration fluctuations in custom assays and electrolytes. The broader availability of fabrication processes allowed the development of various circuit structures based on clusters of sensors. A typical application of LoC systems with multiple integrated ion–sensitive transistors is either distributed or centred in terms of sensor locations. Devices of distributed type usually contain several separate detectors on–chip performing different monitoring functionalities as discussed in e.g. [67]. Centred type systems are on the contrary designed around one cluster of interconnecting sensor devices implementing identical operation with spatiotemporal differences, e.g. Eversmann *et al.* [68]. The discussion of ion–sensitive arrays in this work is focused to ion sensing devices built on unmodified CMOS platforms with eventual post–processing steps are considered

The Cell Monitoring System (CNS) by Baumann *et al.* [49] and Lehmann *et al.* [69] is in principle considered as the first array of ion, oxygen, enzyme and temperature sensors built on unmodified CMOS platform. The standard CMOS fabrication of various sized transistors was in the first instance followed by deposition of thick thermal SiO_2, Si_3N_4/SiO_2 and Al_2O_3/SiO_2 to test the performance of different ion–sensitive layers. Al_2O_3 gates with W/L=100 µm/4 µm transistors were preferred in the second case (Lehmann *et al.*). The experimentation was carried out using a flow–through type measurement setup with regular pumping of fresh media into the chamber of various cell cultures. The behaviour of the cells was tested by injection of iodoacetate as well. The pH fluctuations as

a result of the acidification of the media around the grown cells were shown to follow the pumping period, demonstrating the use of an ISFET as a flow–sensor. Besides the demonstrated opportunity of profiting from flow monitoring, the low–scaled spatial resolution information in cell–based biological measurements could be concluded as key outcome of the CNS experiments. Iodoacetate is an enzyme inhibitor in glycolysis and its addition resulted in the accumulation of lactic acid around the cells. Upon addition of iodoacetate response was observed to the acidic changes in the extracellular pH only at sensors underneath cells demonstrating localised pH detection with CMOS based sensor arrays.

The scalable array architectures of ion–sensitive field–effect transistors based on an unmodified 0.35 µm CMOS platform were introduced by Milgrew *et al.* They developed 2×2 [70] and 16×16 [71] pixel large sensor arrays as displayed in Figure 2.8.

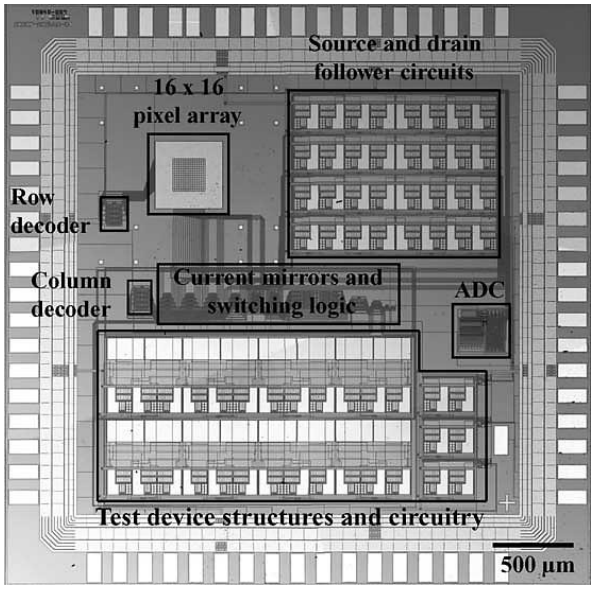

Figure 2.8 Micrograph of a 16×16 ISFET array device. Image reproduced from [71]

The differential and single ISFET operation modes provided sufficient flexibility in terms of data readout as well as the on–chip pseudo reference electrode (PRE) and the Ag/AgCl reference electrodes. The 400 mV drain–source voltage was held constant across the ISFET sensors in a source–drain follower configuration by sourcing and sinking 20 µA current with cascode current mirrors. The Si_3N_4 passivation layer acted as the ion–sensitive membrane during the measurements and 57 and 46 mV/pH sensitivity rates were reported. The challenges of packaging were overcome by the deposition and processing of multiple layers of SU–8 photoresist. SU–8 was used on the one hand to seal off the surface of the chip around the sensor arrays and on the other hand it was required to encapsulate the bond wires. This applied encapsulant was furthermore preferred by its biocompatibility that was

of substantial importance to enable cell culturing on the top of the devices. Later on cultured Madin–Darby canine kidney (MDCK) cells were subject to injection of 200 µl of growth medium with 1mM iodoacetate that was shown to trigger the discussed pH response with a 0.39 pH difference [72].

A scalable array structure designed to perform multiple tasks with one single chip was reported by Hassibi *et al.* [73]. The 0.18 µm CMOS chip was shown to have adjustable operation modes to carry out ion–sensitive, impedance, amperometric and voltammetric measurements. The 5×10 pixels of the fabricated device were equipped with on–chip working, counter and reference electrodes and instrumentation amplifier connected configurable pixel circuits underneath. Despite the short 12 hours predicted life time of the sensor chip it was expected to have considerable impact on biochemical detection methods, e.g. DNA hybridisation.

The DNA sequencer chip shown in Figure 2.9 and associated instrumentation by Rothberg *et al.* [74] are among the most recent developments in the field of LoC ion–sensitive sensor arrays.

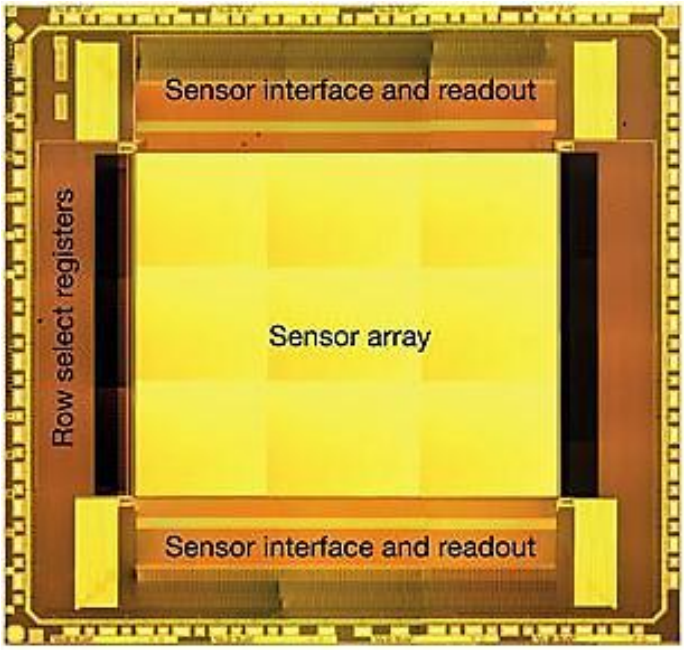

Figure 2.9 DNA sequencer. Image reproduced from [74]

Tantalum–oxide was used as a proton sensitive membrane for the standard 0.35 µm CMOS fabricated microchip. The multiple production cycles of the ion chip is shown in Table 2.3. It is apparent that at first the number of sensors was increased followed by the increase of density in the placement of the detectors reducing the number of sensors underneath the wells from three to two. Each well with a diameter of 3.5 µm is large enough to

accommodate one bead equipped with appropriately bonded and prepared DNA fragments. The beads loaded onto the surface of the chip were rinsed into the individual wells by spinning it in a centrifuge. Fluctuations in the proton concentrations of approximately

Production cycles	Number of ISFETs [$\times 10^6$]	Number of accessible sensors [$\times 10^6$]	Center–to–center pitch size [mm]	Chip surface size [mm^2]
1	1.5	1.2	5.1	115.54
2	7.2	6.1	5.1	306.25
3	13	11	3.8	306.25

Table 2.3 Fabrication cycle parameters of the DNA sequencer chip.

0.02 pH were detected in each well during the course of 4 seconds which was followed by a wash to remove beads from the wells and prepared the chip surface for the continuation of the measurements. The chip was used also to sequence and analyse the complete genome of a previously selected test person and the sequencing procedure was based on a physical model and signal filters to discard the reads with low accuracy. The authors demonstrated the possibility to apply ion–sensitive transistors based Lab–on–a–Chip systems in genomic research. It was furthermore shown that this fully automatised solution could significantly decrease sequencing time to hours while maintaining similar accuracy.

2.6. Ionic imaging

Ion sensitive field effect devices translate ionic concentration fluctuations in chemical substances into time domain voltage or current output signal variations. Besides the LoCs that investigate outputs of separate sensors each with sensitivity to different ionic species, an assembly of electrochemical sensors or transducers measuring identical class of parameters could be considered as an improvement. Array arrangement of ion sensitive sensors with identical physical configurations provides fine–resolution spatial information of an electrolyte thus enables the monitoring of localised chemical properties and reactions. The observation of reactions in a spatially confined manner could deliver indications to, for example, fluid dynamical quantities of diffusion, laminar flow or quality of homogeneous mixing of liquids.

For the case when output signals in the sensor array remain relatively consistent throughout the measurements and the signal values are in a common range, images are possible to be developed by assigning colour bands to the individual parts of the output

range. The methodology is also described in Section 6.1. Time–domain recording of the responses of the clustered ion sensors leads to a series of matrices where each matrix contains the data set belonging to the same time slots during the data acquisition. The colour coded visualisation of the series of data matrixes derived from the raw measurement results is termed *ionic imaging* or *ionic mapping* [75] therefore allows visualising the dynamic behaviour of substances demonstrating localised changes in the measurement values that are directly linked to the physical localised ionic concentration changes on the surface of the respective sensors. The initial series of silicon–based microscopic ion imagers were presented by Sawada *et al.* in [76] and [77] following the charge coupled device (CCD) technique.

The purpose of these prototypes was to demonstrate that the accumulation method ion sensors (AMISs) delivered considerably larger pH sensitivity than ISFET sensors depending on the number of used operation cycles. The cross–sectional view of an AMIS and its sensing methodology is shown in Figure 2.10.

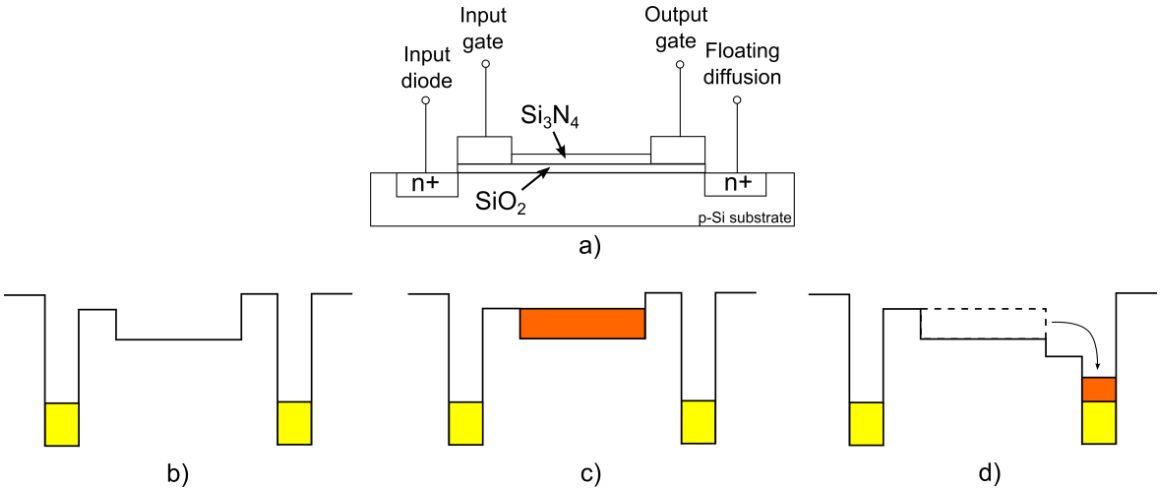

Figure 2.10 (a) Cross–sectional view and operation principles (b, c, d) of the CCD technique based AMIS devices. Image reproduced after [77].

The sensors were fabricated in a CCD process with SiO_2 and Si_3N_4 layers as ion–sensitive passivation using membrane dimensions of 100 µm × 80 µm and a channel length of 50 µm. An AMIS device, Figure 2.10a, consisted of four terminals (input diode, input gate, output gate and floating diffusion) and the passivation layer. A pH dependent potential well was expected to develop underneath the ion–sensitive layer showing growth with increasing acidity. The operation of the CCD–type sensor started by turning off the output gate separating the floating diffusion and channel area, displayed in Figure 2.10b. The input diode was then triggered, shown in Figure 2.10c, with one voltage pulse that forward biased the input diode and charged the potential well. The accumulated charge was

subsequently transferred to the floating diffusion potential well by triggering the output gate terminal as seen in Figure 2.10d. The floating diffusion region was in connection with a voltage follower circuit for signal readout that is not present in Figure 2.10. The output gate was furthermore clocked at 1 kHz and the complete displayed process was repeated five times in a cycle. This cyclic and integrating data readout provided the reported total 450 mV/pH sensitivity. Hizawa *et al.* applied similar principles to design and fabricate 10×10 [78] and 32×32 [79] pixel large CCD–type imager cells in a single metal – single poly CMOS process. It was demonstrated that the sensor arrays were capable to construct images of the mixing of acids and neutral buffers as well as acid diffusions in alkaline buffers.

The separate stages of DNA detection were imaged by Nakazato *et al.* [80] using the developed 16×16–pixel extended–gate electrode ISFET sensor array. The array chip shown in Figure 2.11a was fabricated in an unmodified 1.2 µm CMOS technology and extended metal gates were developed by deposition of 20 nm Ti and 50 nm Au during post–processing above all extended–gate electrode ISFET sensors [81].

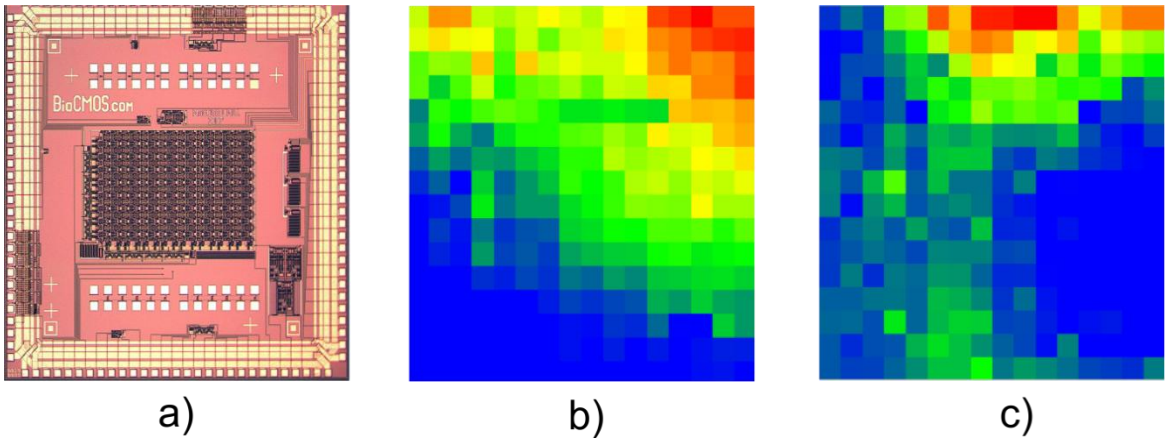

Figure 2.11 (a) 16× 16–pixel ISFET array with extended gates, 2D visualisation of DNA (b) immobilisation and (c) hybridisation. Images were reproduced and assembled from [80]

5'–thiol–modified oligonucleotides were immobilised on the extended gates of the 105.3 µm × 81.4 µm large pixels and hybridised with their complementary oligonucleotides. Figure 2.11b and c show the responses of the chip to the DNA immobilisation and hybridisation delivering evidence for the detection of 2D DNA distributions with ISFET sensors. Although the ISFETs were kept in the same operation point by the source–drain follower type pixel circuit, the output responses were found to be non–uniform which was attributed to non–laminar fluid flow and an imperfect interface between electrodes and electrolyte.

3. Theory

3.1. 1/f noise

The presence of noise or auxiliary uncertainties is an important factor to consider in complex system arrangements as well as the eventual applicable reduction techniques. Uncontrolled disturbances may have a significant impact on the overall performance with superimposed compromising signal values on the useful signal or decreasing the signal–to–noise ratio. The potentially diminishing signal qualities therefore might result in fatal errors as for example data loss or systematic failure. It is vital to identify the origin of the disruption and develop methods to eliminate the physical root of the problem or compensate its effect.

In semiconductor material based monolithic technologies the noise around the sensor devices as well as in the blocks of the supplementary application specific integrated circuitry (ASIC) appear as current or voltage fluctuations in the vast majority of the cases. The measured noise is usually random and sensitive to the influences of the parameter fluctuations in the surrounding environment of the test device, i.e. temperature, humidity, intensity of light, etc. In addition the characteristic shape of the noise phenomenon depends on its nature and frequency range. Both high and low frequency noise types can give rise to potential instability in the system if no compensation is present. The phenomenon of flicker noise is among the most discussed low frequency noise types and is often modelled as the consequence and aggregate of an extensive group of regularly occurring events in the charge carrier transport. The flicker noise is also called 1/f noise [82] in the literature and has been subject to an extensive debate over several decades in terms of its origin, e.g. number of fluctuations, mobility fluctuations and random telegraph signals. There have been many attempts to develop techniques to regulate the level of added intrinsic noise in the measured signal as for example the chopper–stabilisation [83], various averaging procedures [84], or even the cyclic switching method between accumulation and inversion [85].

The present main section in the first instance discusses the number fluctuation and mobility fluctuation models as well as the characteristics of the RTS noise to provide an introduction on the most dominant 1/f noise theories. It is followed by discussing the measurement results and introducing a hypothesis on the contribution of H^+ flickering to

the overall 1/f noise. It is demonstrated that the measured flicker noise had dependency on the applied bias voltage and settled pH values of the electrolyte.

3.1.1. Number fluctuation

The number fluctuation of free charge carriers is one of the leading models on the origin of 1/f noise in semiconductors. The basic concepts of trapping/detrapping were published by McWhorter [42] observing the noise phenomenon in germanium filaments. In his theory the noise origin was attributed to electron capture and release through slow surface states with relaxation time constants in the range of seconds and minutes. It was assumed that the τ time constants of the slow surface states varied at a distribution rate of $1/\tau$ and were located at the germanium–germanium oxide interface and electrons tunnel from and into them. The number fluctuation model was implemented by several authors contributing with improvements, i.e. the trapping and detrapping tunnel mechanism into fast surface states (interface states) and slow surface states (oxide traps) described by Fu *et al.* [86].

The quantitative approach for the number fluctuation model by Ghibaudo [87] described the effect of dynamic exchange of free charge carriers in relation to drain current and flat–band voltage. The initial consideration was to describe the drain current spectral density in terms of fluctuating voltages since $S_I = g_m^2 \cdot S_V$ where S_V is the input gate voltage spectral density. Furthermore it is assumed that electrons are captured from and released to the inversion layer and this charge carrier exchange takes place in the oxide at the semiconductor interface. Thus for the case of a constant V_G gate voltage applied to the semiconductor device the drain current fluctuates although the gate voltage should in theory keep the drain current fixed (power supply noises are not considered). The trapped or released charge carriers modulate the interfacial oxide charge that is considered as a δQ_{OX} fluctuation in the overall oxide charge. The gate voltage is defined as [87]

$$V_G = V_{FB} + \psi_S - \frac{Q_I + Q_D + Q_{IT}}{C_{OX}} \tag{3.1}$$

where V_G is the gate voltage, V_{FB} is the flat–band voltage, ψ_S is surface potential and Q_I, Q_D, Q_{IT} are inversion, depletion and fast interface state charge, respectively. Equation (3.1) shows a gate voltage dependency on the flat–band voltage thus the drain current fluctuation is related to the gate voltage level as well as the changes in the flat–band

voltage. Considering only differential changes as the result of the fluctuation in the number of free charge carriers the fluctuation in the oxide charge, for NMOS, can be expressed as

$$\delta V_{FB} = -\delta Q_{OX} / C_{OX} \tag{3.2}$$

where C_{OX} is the gate–oxide capacitance. Due to the capacitive relationship Equation (3.3) between the oxide charge and the inversion charge the modulation in the oxide charge and therefore in the flat–band voltage induces fluctuations in the inversion charge as well.

$$\delta Q_I = \frac{C_I}{C_{OX} + C_D + C_{IT} + C_I} \delta Q_{OX} = \frac{C_I}{C_{OX} + C_D + C_{IT} + C_I} \left(C_{OX} \delta V_{FB} \right) \tag{3.3}$$

where

$$C_D = -\partial Q_D / \partial \psi_S \quad C_{IT} = -\partial Q_{IT} / \partial \psi_S \quad C_I = -\partial Q_I / \partial \psi_S$$

In the linear region the inversion charge fluctuation can be described as a differential variation in the I_D drain current

$$\delta I_D = \frac{\partial I_D}{\partial Q_I} \delta Q_I = \frac{\partial I_D}{\partial V_G} \frac{\partial V_G}{\partial \psi_S} \frac{\partial \psi_S}{\partial Q_I} \delta Q_I \tag{3.4}$$

Equation (3.4) demonstrates that the incorporation of the $g_m = \delta I_D / \delta V_G$ transconductance and consideration of (3.2) enables the approximation of the drain current as

$$\delta I_D = -g_m \delta V_{FB} = -g_m \frac{\delta Q_{OX}}{C_{OX}} \tag{3.5}$$

As a consequence, shown in Equation (3.6), the spectral density of the drain current is proportional to the spectral density of the flat–band voltage and the spectral density of the oxide charge[87], [88].

$$S_{I_D^2} = g_m^2 S_{V_{FB}^2} = g_m^2 \frac{S_{Q_{OX}^2}}{WLC_{OX}^2} \tag{3.6}$$

It is thus shown that the drain current of semiconductor devices can vary even though the applied gate voltage is constant, not considering power supply noise. The drain current

fluctuation can consequently be attributed to oxide charge modulation by trapping and detrapping free charge carriers. For the last term of Equation (3.6) the charge spectral density and C_{OX} were expressed per unit area in terms of the W and L dimensions of the device in question.

The number fluctuation model is often extended with the investigation of the effective mobility of the inversion layer [89]. The mobility of the charge carriers depends on the inversion layer charge that is influenced by the Q_{OX} oxide charge, therefore it is assumed that the number fluctuation can induce additional fluctuations in the channel mobility and hence results in an additional fluctuation in the drain current. Following Ghibaudo [89] the modified, unified, number fluctuation model is thus obtained as

$$\delta I_D = \delta V_{FB} \left.\frac{\partial I_D}{\partial V_{FB}}\right|_{\mu_{eff}=const} + \delta\mu_{eff} \left.\frac{\partial I_D}{\partial \mu_{eff}}\right|_{V_{FB}=const} \tag{3.7}$$

where μ_{eff} denotes the effective mobility of the charge carriers in the inversion layer. Considering the symmetry between I_D and μ_{eff} and defining the $\alpha = \frac{1}{\mu_{eff}^2}\frac{\partial \mu_{eff}}{\partial Q_{OX}}$ coupling parameter [30] the compensated drain current fluctuation is obtained as

$$\delta I_D = -g_m \delta V_{FB} - \alpha \mu_{eff} I_D C_{OX} \delta V_{FB} \tag{3.8}$$

that results in the power spectral density

$$S_{I_D^2} = \left(1 + \frac{\alpha \mu_{eff} C_{OX}}{g_m}\right)^2 g_m^2 S_{V_{FB}^2} \tag{3.9}$$

The model thus quantifies the impact of the tunnelling based trapping and detrapping of free charge carriers on the drain current while the gate voltage is held constant. The second term of the model incorporates the fluctuation in the effective channel mobility in the inversion layer as a result of the fluctuation in the oxide charge.

3.1.2. Mobility fluctuation

The mobility fluctuation model was first proposed by Hooge [43] [90] introducing the origin of 1/f noise as a fluctuation in mobility in the bulk materials. The Hooge model was developed based on empirical work observing homogeneous metal samples and defined as

$$\frac{S_R}{R^2} = \frac{\alpha_H}{Nf} \tag{3.10}$$

where the empirical α_H Hooge coefficient was supposed to be a dimensionless constant with value of 2×10^{-3}, R is resistance, N is the number of mobile charge carriers and f is frequency.

It was later on discussed that the α_H is rather a material dependent constant that was found in terms of silicon in the range of 5×10^{-6} and 2×10^{-3} [91]. As a consequence the expression for the Hooge coefficient has been revised as

$$\alpha_H = \alpha_{latt}\left(\frac{\mu}{\mu_{latt}}\right)^2 \tag{3.11}$$

where α_{latt} is constant with an approximate value of 2×10^{-3}, μ is the mobility of mobile carriers and μ_{latt} is incorporated due to lattice scattering. The mobility fluctuation theory was later adapted to MOSFETs as well to allow noise modelling in integrated circuits. The expression for the linear operation region was calculated by Hooge *et al.* [91] [92] as

$$S_{V_G}(f) = \frac{q}{C_{OX}}\frac{\alpha_H}{WLf}(V_{GS} - V_T) \tag{3.12}$$

3.1.3. RTS noise

The random telegraph signal noise is a well–studied phenomenon that arises in both n and p channel MOS transistor devices as measureable amplitude fluctuations in the output current. Discrete switching events in single electron traps were observed by Ralls *et al.* [37] showing traces of the oscillating phenomenon between two current levels. It was furthermore demonstrated that the superposition of multiple event sequences propagates responses with additional switching levels that result in indistinguishable trap activity. Ohata *et al.* [93] measured various RTS sequences where the RTSs acted independently and others which contained traps with correlating interactions. The temperature dependence of RTSs [94] and dependence of its pulse width on the applied bias voltage [95] was also shown by Uren *et al.*

3.1.3.1. Probability distribution of RTS events

It is important to analyse the theory of the RTS phenomenon to develop a method to characterise the process. Uren *et al.* [96] modelled the random trapping and detrapping events using the explanation by Machlup [36] extracting the average statistical properties of the events. The modelling approach was based on probability calculations considering the RTS as a Poisson process assuming independent instantaneous transitions. The transitions were assumed between two possible physical states 0 and 1 that symbolise the low and high current states, respectively. Furthermore the probability of physical switching was characterised by $1/\tau_0$ for the $0 \to 1$ transitions while the $1 \to 0$ ones were approximated by $1/\tau_1$. Consider $A(t)$ the probability of not having made a transition until time *t* and $1/\tau_1$ the probability of making a transition to state 0 at time *t*. Thus the equation for probability $p_1(t)$ making a transition between times only *t* and $t+dt$ is derived as

$$p_1(t) = A(t)/\overline{\tau_1} \tag{3.13}$$

Equation (3.14) similarly shows the probability of not having a transition at time $t+dt$ which corresponds to not having made transition until time *t*, $A(t)$, and not making transition between *t* and dt, $(1-dt/\overline{\tau_1})$.

$$\begin{gathered} A(t+dt) = A(t)(1-dt/\overline{\tau_1}) \\ \Downarrow \\ \frac{dA(t)}{dt} = -\frac{A(t)}{\overline{\tau_1}} \end{gathered} \tag{3.14}$$

Integrating both sides, $A(t) = \exp\left(-t/\overline{\tau_1}\right)$, and applying $A(0) = 1$ to the equation the expressions for $p_1(t)$ and $p_0(t)$ are calculated as

$$\begin{aligned} p_1(t) &= \frac{1}{\overline{\tau_1}} \exp\left(-\frac{t}{\overline{\tau_1}}\right) \\ p_0(t) &= \frac{1}{\overline{\tau_0}} \exp\left(-\frac{t}{\overline{\tau_0}}\right) \end{aligned} \tag{3.15}$$

The result demonstrates the exponential distribution rate of the RTS time constants that complies with the applied Poisson process principles.

3.1.3.2. Power spectrum of the RTS noise

The RTS noise results in Lorentzian spectra and delivers a 1/f noise spectrum for the case of interaction with several RTS sequences as discussed in Section 2.2.3. The spectrum of RTSs is often derived using the Wiener–Khintchine Theorem [97] which states that the Fourier transformed autocorrelation function of a random process equals the power spectral density of the process. Therefore the autocorrelation function of the investigated Poisson process needs to be obtained [96]. The amplitude and probability values are chosen as $x_0 = 0$ and $\overline{\tau_0}/\left(\overline{\tau_0}+\overline{\tau_1}\right)$ for state 0 and $x_1 = \Delta I$, $\overline{\tau_1}/\left(\overline{\tau_0}+\overline{\tau_1}\right)$ for state 1. The autocorrelation function of a signal is usually derived by correlating the function to itself multiple times. $P_{11}(t)$ is defined as the probability for an even number of transitions and $P_{10}(t)$ as the probability for an odd number of transitions thus $P_{11}(t)+P_{10}(t)=1$ and both start from state 1. The autocorrelation of an RTS is for $P_{11}(t)$ is thus given as

$$\begin{aligned} c(t) &= \left\langle x(s)+x(s+t)\right\rangle = \\ &= x_1 x_1 \times \left\{x(s)=\Delta I\right\} \times \left\{x(s+t)=\Delta I\right\} = \\ &= (\Delta I)^2 \frac{\overline{\tau_1}}{\overline{\tau_0}+\overline{\tau_1}} P_{11}(t) \end{aligned} \qquad (3.16)$$

which expresses the probability for the system to be in state 1 until the start and for even number of events at time *t*. Using the definitions above the probability of even number of transitions at time $t+dt$ can be defined as well, shown in Equation (3.17). The definition of the probability of even transitions at time $t+dt$ is expressed as the probability of the odd number of transitions in time *t*, $P_{10}(t)$, and one transition at time dt, $\frac{dt}{\overline{\tau_0}}$; and the probability of an even number of transitions in time *t*, $P_{11}(t)$,and no transition at time dt, $\left(1-\frac{dt}{\overline{\tau_1}}\right)$.

$$P_{11}(t+dt) = P_{10}(t)\frac{dt}{\overline{\tau_0}} + P_{11}(t)\left(1-\frac{dt}{\overline{\tau_1}}\right) \quad and \quad dt \to 0$$
$$\Downarrow \tag{3.17}$$
$$\frac{dP_{11}(t)}{dt} + P_{11}(t)\left(\frac{1}{\overline{\tau_0}}+\frac{1}{\overline{\tau_1}}\right) = \frac{1}{\overline{\tau_0}}$$

The equation is solved using the integration factor $IF = e^{\int \frac{1}{\overline{\tau_0}}+\frac{1}{\overline{\tau_1}}dt} = e^{\left(\frac{1}{\overline{\tau_0}}+\frac{1}{\overline{\tau_1}}\right)t}$

$$P_{11}(t) = \frac{\overline{\tau_1}}{\overline{\tau_0}+\overline{\tau_1}} + \frac{\overline{\tau_0}}{\overline{\tau_0}+\overline{\tau_1}} e^{-\left(\frac{1}{\overline{\tau_0}}+\frac{1}{\overline{\tau_1}}\right)t} \tag{3.18}$$

The result calculated by substituting Equation (3.16) into Equation (3.18) and using the Wiener–Kintchine theorem $S(\omega) = 4\int c(\tau)\cos(\omega\tau)d\tau$ the power spectral density of an RTS can be calculated as

$$S(f) = \frac{4(\Delta I)^2}{\left(\overline{\tau_0}+\overline{\tau_1}\right)\left[\left(\frac{1}{\overline{\tau_0}}+\frac{1}{\overline{\tau_1}}\right)^2 + \left(2\pi f\right)^2\right]} \tag{3.19}$$

Assuming the symmetrical conditions of $\overline{\tau_0} = \overline{\tau_1} = \tau$, the result simplifies to the following function

$$S(f) = \frac{2(\Delta I)^2 \overline{\tau}}{4+\left(2\pi f \overline{\tau}\right)^2} \tag{3.20}$$

which delivers Lorentzian spectra that can account for 1/f noise in the case of interconnecting trap activities shown in Section 2.2.3.

The present chapter discusses the results of the accomplished noise measurements with ISFET circuits. The *proof–of–concept* investigations demonstrated that the level of intrinsic 1/f noise could be influenced using its sensitivity to

- Bias voltage
- pH level

The 1/f noise is considered between 4 and 200 Hz in this work. The auto–scaled settings of the SignalExpress software were used from a laptop computer for noise measurements due to the automatic range selection functionality of the NI PXI–4461 measurement card. The data acquisitions occurred at 2 kHz continuous sampling rate taking 1000 data points and averaging the results with continuous RMS averaging 3000 times. The measured and averaged results were stored as default snapshots in the SignalExpress software and were exported later on into native text files which were further processed on Matlab platform.

3.2. Ion–sensitive transistors

Ion–sensitive field–effect transistors are ion sensor devices that are applicable for multiple purposes, e.g. genomic analysis, therapeutical treatments, etc. The sensors need to be adapted to the specific applications for example by depositing a suitable sensing layer to achieve the desired ionic sensitivity and selectivity. Thus the appropriate selection of a sensing material also enables ion–specific experiments to be performed. The 64×64–pixel ISFET sensor array utilised silicon nitride as a sensory layer, the nitride deposition was performed by the manufacturer in the chosen CMOS fabrication process. The Si_3N_4 is known to be responsive to various ionic species besides H^+ and OH^-. Therefore although its usage reduces the fabrication and design costs, it is often challenging to fit the technology to living cell based applications or to identify the effects of individual ion species. However, the multiple selectivity provides the functionality of monitoring the overall result of aggregate ionic transport. The ionic selectivity can also be influenced by controlling the investigated biological or electrochemical processes to ensure that only the ion of interest is subject to change.

This chapter delivers a theoretical description on the electrochemical background of ionic measurements with ISFETs. Hence at first the principles of redox reactions are elucidated which is followed by the explanation of the sensor–electrolyte interface introducing the respective double layer models as well. The electrochemical interface between the surface of the passivation layer and the applied electrolyte is shown by the site–binding model. The control effect of the reference electrode on the electrochemical cell and the underlying electronics is also demonstrated. In addition the types of reference electrodes and the fabrication method used for the micro reference electrode are introduced. This is followed by discussing the electronics background of ISFET devices and its connection with CMOS showing the dependence of the electronic response on pH.

3.2.1. Electrochemical interactions

Ionic experiments are strongly dependent on the transport of protons and electrons under a stable external bias potential or current control [98] [99]. Electrochemical reactions that are coupled with semiconductor based ion–sensitive devices are typically characterised by electron or ion exchange at the solid phase–liquid phase interface. The manifestations of the charge transfers throughout the electrochemical system are considered to take place in the form of reduction–oxidation processes. This implies therefore that one part of the electrochemical redox system releases and the other part takes up electrons. Hence the redox reaction in general form is described as

$$\begin{aligned} &oxidised + ne \rightleftarrows reduced \\ &\upsilon_O O + ne \rightleftarrows \upsilon_R R \end{aligned} \tag{3.21}$$

where *ne* denotes the number of transferred charge units and υ_O, υ_R are the respective reaction rates because every reaction takes place within a finite time range. These reactions occur rapidly and quickly reach the thermodynamic equilibrium. The redox reactions in the electrochemical system are likely to occur at the interface region. Therefore the oxidants or reductants need to be transported to the local proximity of interfaces to trigger the electron–exchange reactions. The move of charged particles is considered to occur by various mass transfer methods including [98]

- Migration–that is the motion of positive or negative charged ions across the solution by the electrostatic force of electrodes that are in contact with the electrolyte
- Diffusion–that is the random movement of ions between areas of low and high ionic concentrations. The diffusion occurs in three dimension and the concentration differences can establish a gradient for the ionic flow.

The ion sensitive system is considered as an electrochemical cell in this work consisting of two independent half–reactions at the electrode–electrolyte and the electrolyte–insulator interface. Corresponding to Equation (3.21) the equilibrium of an electrode in terms of ion exchange when dipped into electrolyte can be described as [98]

$$M^{n+} + ne \rightleftarrows M \tag{3.22}$$

where M is the interacting ion species. Equation (3.22) delivers an important quantitative and intuitive explanation to the understanding of redox processes. The development of 1 mole *M* requires the reduction of 1 mole of M^{2+} by n faradays (*F*) which indicate the amount of coulomb electron charge per mole. The transfer of $n \cdot F$ induces a voltage fluctuation of *E* volts therefore the overall consumed energy of the reaction is $n \cdot E \cdot F$. It thus implies that the total energy of the electrochemical system is decreased by $n \cdot E \cdot F$ joule at constant pressure and temperature. Hence that much less free energy is available in the system to develop redox reactions. Therefore

$$\begin{aligned} \Delta G &= -nEF \\ \Delta G_0 &= -nE_0F \end{aligned} \tag{3.23}$$

where $\Delta G, \Delta G_0$ are the available free energy and the standard free energy as well as correspondingly E, E_0 denote the induced voltage difference and the standard electrode potential. The van't Hoff equation is applied for the electrode redox reactions that quantifies the variation of free energy for chemical processes

$$\Delta G = \Delta G_0 + RT \ln\left(\frac{a_M}{a_{M^{n+}}}\right) \tag{3.24}$$

where $a_M, a_{M^{n+}}$ are the activities of the ions in the chemical interaction. Combining Equation (3.23) and Equation (3.24) we get

$$\begin{aligned} -nEF &= -nE_0F + RT \ln\left(\frac{a_M}{a_{M^{n+}}}\right) \\ E &= E_0 + \frac{RT}{nF} \ln\left(\frac{a_M}{a_{M^{n+}}}\right) \end{aligned} \tag{3.25}$$

Based on the discussed equations the expression is generalised as

$$E = E_0 + \frac{RT}{nF} \ln\left(\frac{[Oxidant]}{[Reductant]}\right) \tag{3.26}$$

which is the *Nernst–equation* that establishes the link between applied electrode potential and activities and concentrations of interacting ionic species in the case of stable equilibrium. An electrode or a chemical process is frequently referred to as nernstian if it is reversible and obeys the Nernst–equation.

3.2.2. Sensor–electrolyte interface

The analysis of the interface between the electrode and electrolyte is vital because the effects of variations in chemical quantities, e.g. concentration fluctuations of substances, are translated into electronic signals across this interface. The electrochemical interaction between the solid and liquid phases implies charge redistribution at the interface region until chemical equilibrium occurs [100]. Under equilibrium conditions charge carriers from both sites are expected to accumulate at the surfaces of electrode and electrolyte. Thus the differences between the developed electrochemical potentials establish an electric field across the interface [101]. This potential can usually be detected by differential voltage measurements between a working electrode and a reference electrode with a known electrochemical surface potential. The development of the electric field is the result of electrostatic interactions because of the lack of removal path of excess charges in the system, thus no DC current flows across the structure ignoring potential leakage currents.

The mechanism of the electrochemical interactions between electrode and electrolyte has been described by various surface charge distribution models [102]. The common point of the existing theories is the representation of the electrostatically accumulated charge distribution as an ionic double–layer with opposite ion polarities between the electrode–electrolyte interface sites. The first description of the double layer model by Helmholtz [103] is shown in Figure 3.1a. It demonstrates the electrochemical system containing either only positive or negative charges on the sides of the interface. Thus the ions are either attracted to or repelled from the interface region. In the model positive charges are assigned to negative ones developing a tight double layer not considering ionic interactions from neither other ions nor in the bulk electrolyte. The Helmholtz model therefore describes the charge distribution with a similar approach to a capacitor. The one plate is the electrode surface and the other plate would be the layer of charge from the electrolyte with opposite polarity. The charges are treated as point charges and hence the distance between charge and electrode is approximated by the x_H ionic radius. The C_H capacitance of the double layer is then calculated as

$$C_H = \frac{\varepsilon_R \varepsilon_0}{x_H} \tag{3.27}$$

where ε_R is the relative permittivity, ε_0 is the vacuum permittivity. The model thus considers only a surface layer of ions and disregards any potential concentration change of ions.

The compact Helmholtz double layer model was revised independently by Gouy [104] and Chapman [105] indicating the varying thickness of the interface layer in the liquid phase. The improved model incorporated considerations on the relationship between the capacity of the double layer and the ionic concentration in the electrolyte shown in Figure 3.1b.

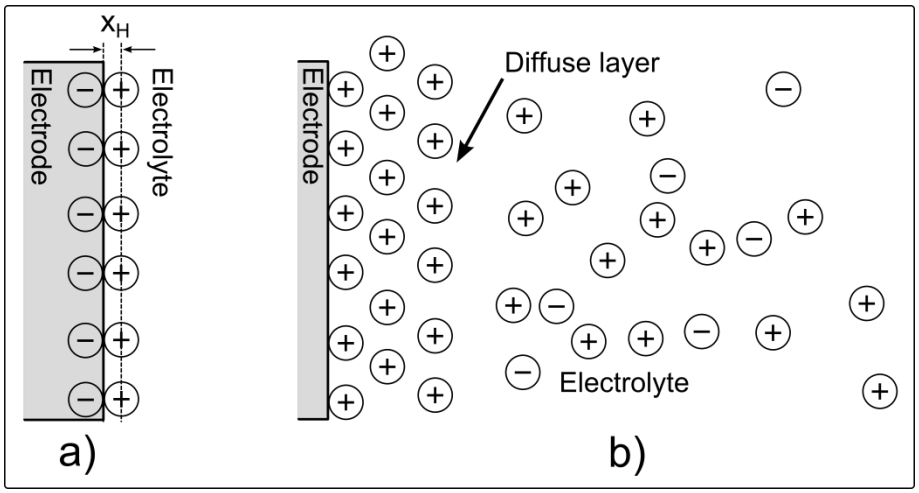

Figure 3.1 The image shows the (a) Helmholtz and (b) Gouy–Chapman models for the development of electrical double layers

Multiple layers of ionic charges were expected in the proximity of the interface and diffuse charge carrier movements in the electrolyte bulk further away from the interface region [101]. A non–linear voltage drop was implied across the variable double layer and the electrolyte regions. The allocation of ionic charges followed the Boltzmann distribution in the Gouy–Chapman model [102] [106] therefore the probability of finding charges in a certain distance from the electrode surface is calculated as

$$n_i = n_i^0 \exp\left(\frac{-z_i e\varphi}{kT}\right) \qquad (3.28)$$

where n_i^0 is the number density of the respective ions in the electrolyte, z the valence of the ions, e is the electron charge, φ is the voltage value at the exact location, k is the Boltzmann constant and T is the temperature. The determination of the ionic distribution allowed the assumption that the spread of the charge density will follow a similar profile. Hence a distance x is considered in the electrolyte from the electrode which is divided into dx thin pieces thus the ρ charge density is

$$\rho(x) = \sum_i n_i z_i e = \sum_i n_i^0 z_i e \exp\left(\frac{-z_i e\varphi}{kT}\right) \qquad (3.29)$$

The gradient of the charge distribution from the electrode surface is approximated by the Poisson law

$$\nabla^2\varphi(x) = -\frac{\rho(x)}{\varepsilon_a} \qquad (3.30)$$

The description of the electrostatic interactions of layers of ionic charges and their statistical distribution as well as the combination of Equation (3.29) and Equation (3.30) leads to the Poisson–Boltzmann equation

$$\nabla^2\varphi(x) = -\frac{e}{\varepsilon_a}\sum_i n_i^0 z_i \exp\left(\frac{-z_i e\varphi}{kT}\right) \qquad (3.31)$$

The charge density and capacitance of the double layer is obtained by solving the differential equation as indicated in { [102] – Equations (3.24–26) }.

The Gouy–Chapman theory was later combined with the Helmholtz model by Stern [107] to give a better explanation of the electrochemical charge distribution at the electrode–electrolyte interface. The Stern model on the one hand represents the interface double layer as a compact layer of ions at the electrode surface which indicates that charges cannot approach the electrode closer than their ionic radii. On the other hand the rigid surface layer of ions is extended with a diffuse layer into the electrode bulk according to the model. The boundary between the surface and the diffuse layer is termed as outer Helmholtz plane (OHP). The Stern model thus also gives an approximation on the overall double layer capacity as well. The capacity of the surface charge layer can be represented as a capacitor and the capacity of the Gouy–Chapman diffuse layer. The overall capacity of the two layers is modelled as a series connection of the Helmholtz, C_H, and Gouy–Chapman, C_{GC}, capacitances, therefore

$$\frac{1}{C_S} = \frac{1}{C_H} + \frac{1}{C_{GC}} \qquad (3.32)$$

This Stern model was then extended by Grahame [108] indicating that the surface should be divided into three separate sections. The improved model postulated the existence of a surface layer where specifically adsorbed ions were located in the very near vicinity of the electrode surface. According to the Grahame model this layer contained the ions that lost

their solvation to the electrolyte and bound strong to the surface. It also contained charges of either positive or negative polarity on the surface. This layer of specifically adsorbed ions was called inner Helmholtz plane (IHP). The OHP was the region of solvated ions and the diffuse layer expanded from the OHP into the electrolyte bulk. The common characteristic of both Stern and Grahame models was a linear potential distribution until the OHP boundary, at which the potential dropped off exponentially.

The concepts of the Grahame model were enhanced by Bockris *et al.* [109] suggesting the arrangement shown in Figure 3.2.

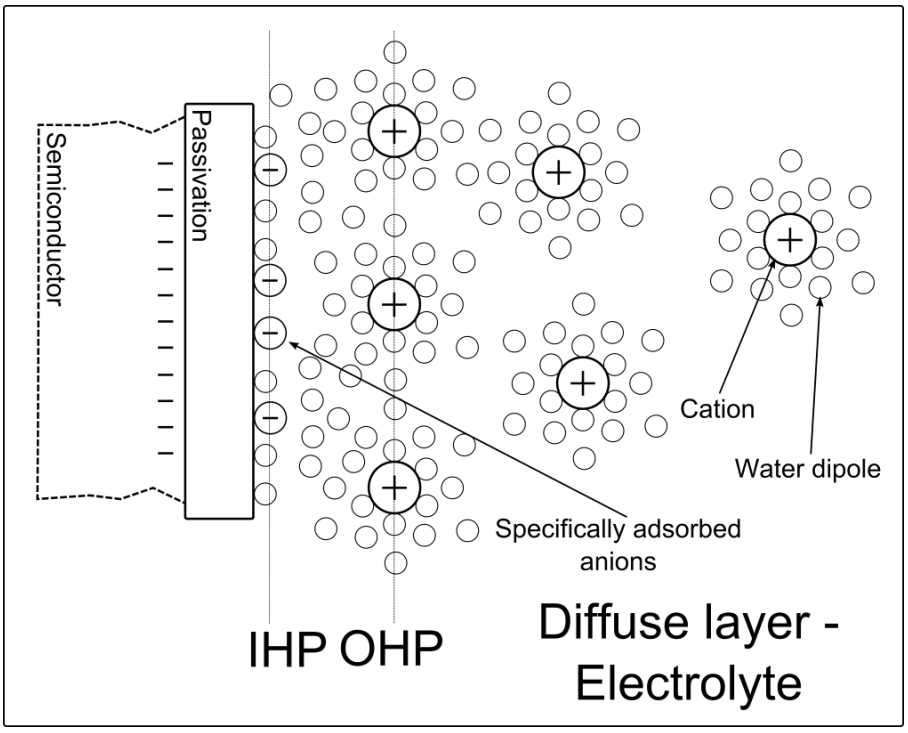

Figure 3.2 The double layer model of Bockris *et al.* [109]

The Bockris–Devanathan–Müller model took into account that the solute material is in aqueous dipolar solvent (water) and that the concentration of the solvent dominates the reactions. The dipolar water molecules were supposed to form a surface layer with orientated in correlation with the local electrode surface sites. Specifically adsorbed charged molecules, as in the Grahame model, were supposed to reside in the near proximity of the interface surface. The dipole layer inside the IHP region was also assumed to include the specifically adsorbed ions. The solvated ions were located in the OHP region and the diffuse layer was defined as being further from the electrode than the OHP layer. Similarly to the Stern model the electrostatic potential distribution was taken as linear up to the OHP region.

Surface charge modelling is an important part of understanding the behaviour of ISFET devices. The ISFETs are also in explicit contact with aqueous electrolyte solutions through their passivation layers. The use of the theoretical charge arrangements described above are of particular significance in case of software modelling of ISFETs.

3.2.3. Site–binding model

The response of sensor devices and the developing total charge at their interface regions is dependent on the physical parameters of the applied sensing materials used [100]. The surface charge distribution models discussed describe the electrostatic interactions at the sensor surface and in the electrolyte bulk [101]. However these theories ignore the fact that the surface of the sensing material undergoes hydration when it is brought into contact with aqueous solutions.

There are two general approaches that explain the phenomenon of hydration, the (a) gel–layer and the (b) site–binding model. The main principle of the gel–layer theory is the confluent hydration of the sensor surface. It is thus expected that a layer of the sensing material hydrates some nanometres thick causing the surface region to develop a double layer and thus a capacitive interface to the underlying electronics. The alternative approach, the site–binding model, was first introduced by Yates *et al.* [110] and gave a feasible approximation to the chemical interactions and surface charging between the sensing material and the electrolyte. The site–binding model represents the surface of the sensor as a series of diverse chemical sites that can accommodate the charged molecules from the electrolyte. Charge binding places of the sites can have a range of origins, e. g. unsatisfied bonds or chemical transformations, hydrolysis. As the charge–binding sites can interact with both H^+ and OH^-, the pH will determine the majority ion species binding to the surface. The example of silicon dioxide hydration demonstrates the process of ionic exchange between solid and aqueous phases at the amphoteric sites [100]

$$\begin{aligned} SiOH_2^+ &\rightleftarrows SiOH + H^+ \\ SiOH &\rightleftarrows SiO^- + H^+ \end{aligned} \qquad (3.33)$$

Equation (3.33) shows that the surface of the silicon-dioxide hydrolyses into silanol groups in case of a SiO_2 – aqueous electrolyte contact. Due to this hydrolysis the protons bind to the silanol groups rather than to SiO_2. The site–binding model was preferred throughout this work because on the one hand the site binding model quantitatively explains the

chemical interactions. On the other hand it enables the theoretical description of the activity of ISFET devices in terms of sensor arrays as well. In Chapters 5 and 6 the capability of ISFET arrays for measuring localised pH and pNa responses is demonstrated. The ISFET sensor chip was fabricated in an unmodified CMOS process and as a consequence the transistors interacted with the electrolyte across the insulating passivation layer. The solvation of the silicon nitride, Si_3N_4, passivation is expected to develop amphoteric and basic surface sites. In Si_3N_4 each nitrogen connects to three silicon atoms and has a lone electron pair for hydrolysis [111]. The reactions between water and the nitride layer is described as [111] [112]

$$\begin{aligned} Si_3N + H_2O &\rightleftharpoons Si_2NH + SiOH \\ Si_2NH + H_2O &\rightleftharpoons SiNH_2 + SiOH \\ SiNH_2 + H^+ &\rightleftharpoons SiNH_3^+ \\ SiOH + H^+ &\rightleftharpoons SiOH_2^+ \\ SiOH &\rightleftharpoons SiO^- + H^+ \end{aligned} \qquad (3.34)$$

A graphical description of the site–binding model is presented in Figure 3.3. It is shown that the expected surface sites develop at the surface of the passivation layer, binding and releasing charged ions into the electrolyte. The chemical equations (3.34) describe the developments of amphoteric and basic sites when the silicon nitride is in contact with an aqueous solution.

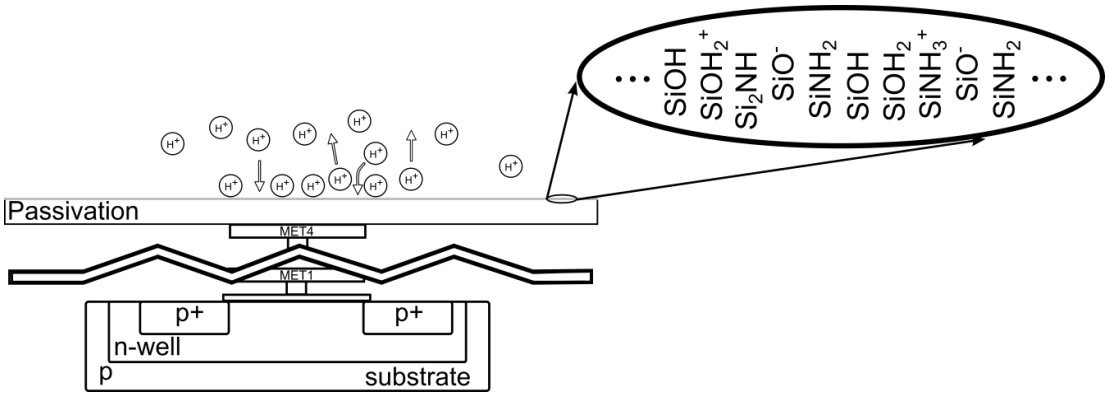

Figure 3.3 Site – binding model for the silicon nitride passivation layer of ISFET devices

However we can find the same results using an intuitive approach. It was shown that the silicon nitride can oxidise at high temperatures producing additional silicon oxynitride and silicon dioxide layers at the surface [113]. Low pressure chemical vapour deposition (LPCVD) is typically used for depositing silicon nitride layers and is performed at approximately 800 degrees Celsius temperature. Therefore it can be assumed that some

nanometres thick oxide and oxynitride layers develop on the surface of the silicon nitride at increased temperature and that the aqueous solution hydrolyses first these surface layers and then the silicon nitride.

3.2.4. Reference electrodes and fabrication

The potential sources or arising electrical potentials have to be under stable control while performing electrochemical measurements. The characteristics of the occurring reactions might change depending on the applied voltage across the electrochemical cell and number of electrodes immersed into the electrolyte solution. In general the setting and measurement of electrochemical potentials require a rather simple setup structure where semiconductor based sensor devices are concerned. Corresponding to the description in Section 3.2.1 the considered electrochemical cell consists of a reference electrode, the electrolyte and the insulator at the top of the ISFET sensor chip. The reference electrode maintains a constant bias potential to the sensor electronics across the insulator which is the passivation layer in the CMOS process. As a consequence the applied reference potential is distributed across the complete sensor structure of the EIS system.

The profile of the potential drop is important to consider since it indicates that the effect of the reference voltage is a function of intermediate potential entities [114]. The reference electrode potential is treated here as constant. Due to the capacitive link between the applied reference electrode potential (V_{ref}) and the gate potential of the sensing CMOS device (V_g), V_g follows the changes of V_{ref}. The demonstration of the decay of the electrostatic potential is shown in Figure 3.4.

The EIS system shown in Figure 3.4 is required to satisfy the charge neutrality equation assuming that there is no current flowing through the structure. In this case the charge neutrality could be defined as [100]

$$\sigma_e + \sigma_{el} + \sigma_{diff} + \sigma_i + \sigma_s = 0 \qquad (3.35)$$

where σ_e, σ_{el}, σ_i, and σ_s are the charge density at the electrode interface, electrolyte bulk, electrolyte–insulator interface and the surface of the semiconductor, respectively. Corresponding to Equation (3.35) the continuity of electrostatic potentials of the system is expressed as

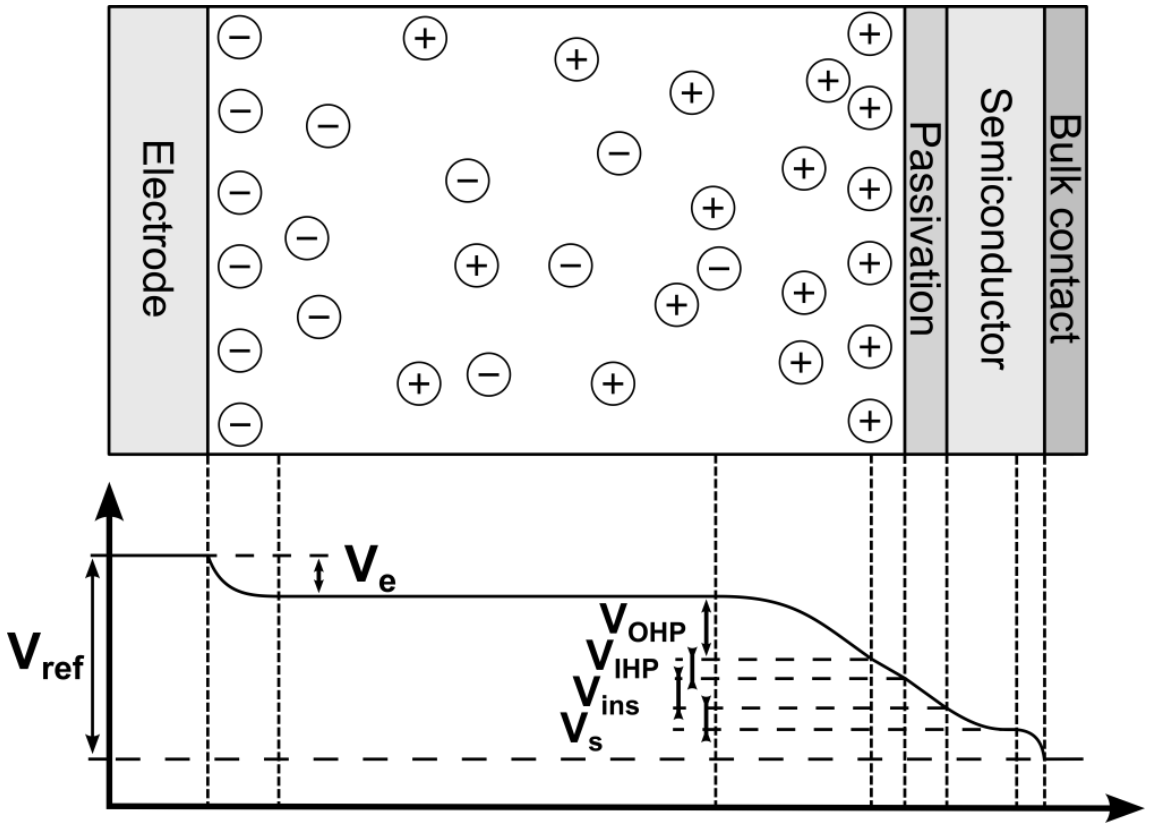

Figure 3.4 The characteristics of the potential drop across the EIS structure is demonstrated where V_e, V_{OHP}, V_{IHP}, V_{ins}, V_s denote the potential drops at the electrode interface, outer Helmholtz plane, inner Helmholtz plane, insulator and the semiconductor. The image is not to scale [101].

$$V_{ref} + (V_e - V_{ref}) + (V_{OHP} - V_e) + (V_{IHP} - V_{OHP}) + (V_{ins} - V_{IHP}) + (V_s - V_{ins}) - V_s = 0 \qquad (3.36)$$

and corresponding to the Gouy–Chapman–Stern (GCS) model

$$\sigma_i = \frac{V_{ins} - V_{IHP}}{C_H} \qquad (3.37)$$

$$\sigma_{diff} = \frac{V_{OHP} - V_e}{C_{GC}} \qquad (3.38)$$

C_H and C_{GC} are the capacitances indicated in the GCS model. These results are important in the field of modelling the behaviour of ISFET structures. Equation (3.37) and Equation (3.38) establish the connection between arising interfacial charges, electrostatic potential drops and hypothetical model capacitances.

The reference electrodes are usually selected with respect to their robustness, life time and stability in terms of interface potentials. The interface potential is considerably influenced by the materials used and the continuous interfacial ionic transfer when the reference electrode is immersed into an electrolyte. In addition, external contaminations or drying

out can also substantially shorten the life time of the electrode or even destroy it. The optimal bias points of the chip devices varied with their usage, therefore the optimal applied bias potential was determined each time before using the circuit.

Two distinct types of reference electrodes were used for the ISFET experimentations discussed in Section 6. On the one hand commercial BASi RE–6 glass electrodes were utilised. On the other hand micro Ag/AgCl electrodes were fabricated to suit the requirements of the live video recorded ISFET measurements. The reference electrodes used as well as the fabrication method of the micro electrode are shown in Figure 3.5a and b. The BASi RE–6, shown in Figure 3.5a, is a widely favoured reference electrode for general application purposes. The 6 mm thick and 3 cm long reference electrode is manufactured from glass and contains an Ag/AgCl metal electrode fitted in the middle of the glass body. The cylindrical transparent glass cover encapsulates a chamber around the metal electrode that is filled by 3M NaCl gel material. The ionic connection between the electrolyte and the enclosed salty gel to the external environment is provided by a porous ceramic frit that is fitted to the end of the electrode body. Thus in a purely aqueous environment it would imply a continuous Na^+, Cl^-, H^+ and OH^- ionic exchange at the porous interface. The RE–6 was stored in 3M NaCl solution in agreement with the prescription of the manufacturer to avoid drying out and contamination by interfacial ionic exchange.

The BASi RE–6 reference electrodes were necessary to replace for the electrochemical applications discussed in Section 6.2 and Section 6.3 and the plastic chamber on the chip carrier was also changed as shown in 4.5. The requirements of live video recording excluded the applicability of the BASi RE–6 on the one hand because of its extensive size. In the case of inserting the RE–6 into the smaller plastic chamber, the body of the glass electrode completely covered the chip surface thus making it impossible to observe the device. On the other hand the glassy surface of the RE–6 electrostatically attracted the surrounding water molecules. The water accumulated at the glass surface after insertion of the RE–6 into the larger plastic container which made the recorded pictures strongly blurred. Therefore micro reference electrode was fabricated using a plain silver wire as base material following the three electrode cell procedure [115]. The fabrication setup of the Ag/AgCl reference electrode, working electrode and silver wire counter electrode wire is demonstrated in Figure 3.5b. The electrolyte used was 0.1 M KCl residing in a glass beaker and the electrodes were manually placed into the electrolyte. The oxidation was carried out in potentiometric manner as shown in Figure 3.5b.

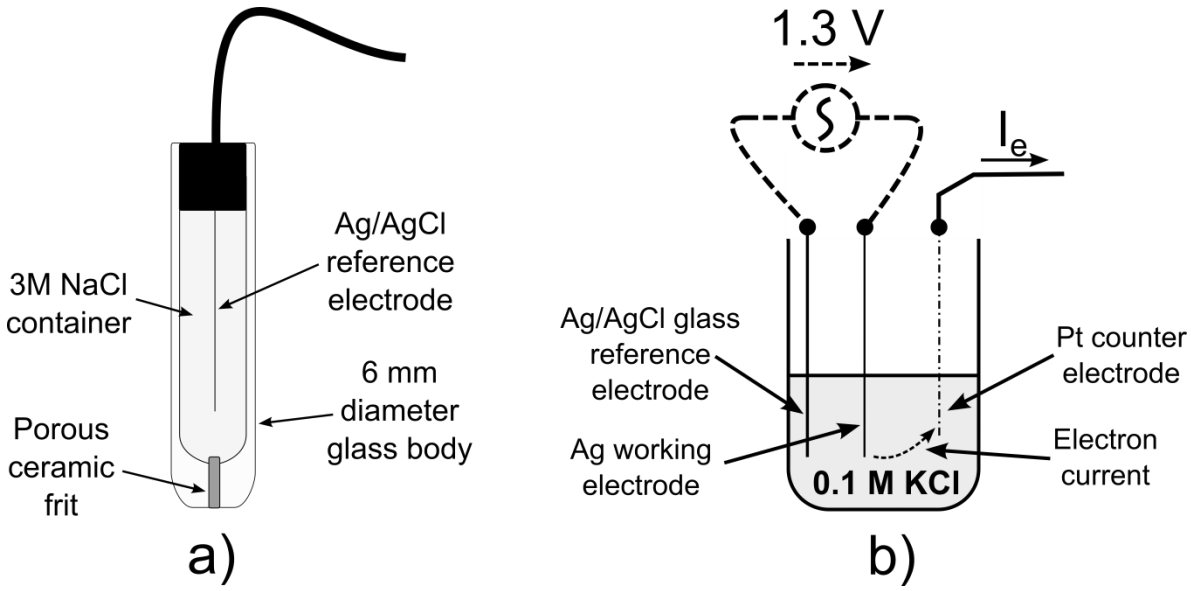

Figure 3.5 The image demonstrates the applied reference electrodes for the ion sensitive measurements. (a) shows a BASi RE–6 glass reference electrode and (b) shows the fabrication method of the Ag/AgCl micro reference electrode.

The oxidation of the deposited silver layer was performed using potentiostatic methods in a three–electrode configuration. Stable 1.3 V voltage was delivered to the working electrode relative to the glass covered reference electrode and a lower potential to the counter electrode. This maintained a continuous potential difference between the working and counter electrodes which in turn induced an ionic current throughout the electrolyte collected by the counter electrode. The potential of the counter electrode was automatically adjusted upon the detection of ionic current to ensure the direction of the current. The average duration of the oxidation processes applied was 1 minute. As final step of the oxidation the resulting Ag–AgCl reference electrode was rinsed in DI water and left to dry.

The prepared reference electrodes showed great applicability in terms of live video recording and potential referencing with respect to the common ground point of the electronic system. They demonstrated excellent flexibility which was critically important because the electrode was manually positioned around the silicon chamber on the surface of the chip device (Figure 4.9). These Ag/AgCl electrodes were furthermore thin enough to facilitate the image acquisition without any disturbing effects as the result of electrostatic interactions. The fabricated reference electrodes demonstrated fairly short life time and sensitivity to light. The utilised DIP solutions, discussed later, and various acids often dissolved the AgCl from the silver wire. Despite these disadvantages the micro Ag/AgCl reference electrodes proved to be an efficient and suitable tool for controlling the gate voltages of the ISFET transistors during the experiments.

3.2.5. Ion–sensitive field effect transistor

The ion–sensitive field effect transistors as mentioned earlier are ion sensor devices that are identical in structure to the CMOS transistors [116]. Besides CMOS components the wide availability of sub–micron fabrication processes from various manufacturers facilitated the integration of ISFET devices as well. The fabrication of CMOS electronics and ISFET sensors furthermore provided the significant advantage of reducing the overall cost of the development process. The design of ISFET sensors are different to on–chip VLSI electronics since the gates of ISFETs are floating due to being connected to the passivation layer across intermediate vias and metal layers as displayed in Figure 3.6a. The passivation layer of commercially fabricated ISFETs usually comprises a dual layer of Si_3N_4 and SiO_2. The silicon nitride demonstrates considerable resistance to hydration although the thickness of the deposited layer, approximately 1 µm, might lead to deficiencies, e.g. in case of using highly acidic or basic substances. In normal operation the silicon dioxide layer with thickness of nearly 1 µm insulates the Si_3N_4 from the underlying top–metal layer. It thus also blocks the path of eventual leakage currents across the passivation towards the electronics.

The CMOS fabricated ISFET circuit components are modelled using the approach of Figure 3.6b based on the discussions of Section 3.2.2, Section 3.2.3 and Section 3.2.4. The ISFET system model is described by identifying three different parts, capacitances C_{GC}, C_H and C_T as well as the source of the reference potential and the transistor. C_{GC} is the Gouy–Chapman capacitance and the C_H is the Helmholtz capacitance corresponding to the Stern–model. C_T is called the transfer capacitance that aims to account for the capacitive coupling from the top–metal layer to the MOS channel thus including the gate capacitance as well. Therefore $V_{REF,}$ the reference electrode voltage, is considered to perturb the floating gate and the drain current of the ISFET transistor by the multiple capacitive relationship. The identical structure of ISFETs with CMOS devices also implies that the physical parameters are characterisable using similar considerations. Hence the drain current of ISFET transistors in the linear operation region is defined as [116]

$$I_D = C_{OX}\mu\frac{W}{L}\left[\left(V_{GS}-V_T\right)V_{DS}-\frac{V_{DS}^2}{2}\right] \qquad (3.39)$$

where the C_{OX}, μ, W, L are physical constants and are the gate oxide capacitance, channel electron mobility, the width and length of the transistor, respectively. V_{DS}, V_{GS} and V_T are

drain–source voltage, gate–source voltage and the threshold voltage, respectively. The parameters of Equation (3.39) are all well controlled quantities in a CMOS process that might be used to characterise the ionic sensitivity of ISFET devices. Traditionally the threshold voltage is taken to describe the ion–sensitive processes because it by definition provides a link between surface potentials, charges and capacitances. The threshold voltage of the CMOS transistors can be expressed as

$$V_T = \frac{\Phi_M - \Phi_{Si}}{q} - \frac{Q_{OX} + Q_{SS} + Q_D}{C_{OX}} + 2\Phi_F \qquad (3.40)$$

where Φ_M and Φ_{Si} are the work functions of the gate terminal and the semiconductor bulk, Q_{OX} is the trapped charge in the gate oxide, Q_{SS} is the charge at the SiO_2–Si interface and Q_D is the depletion charge in the semiconductor bulk.

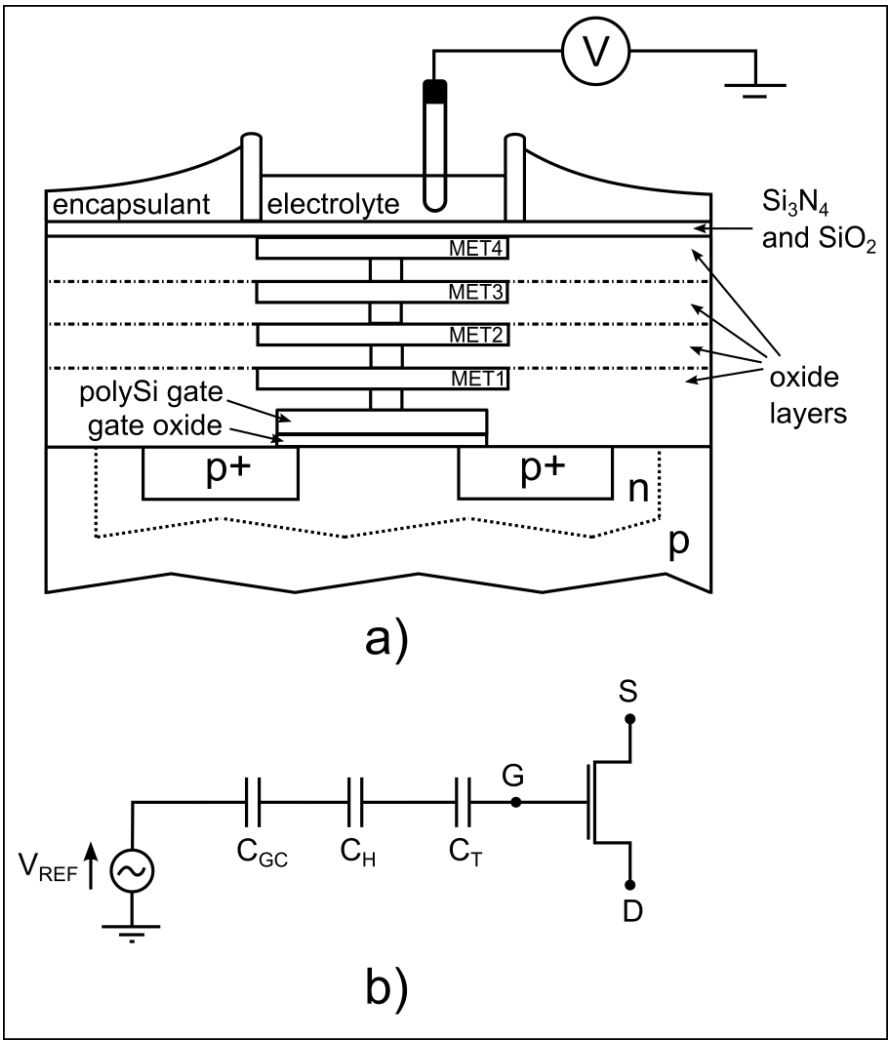

Figure 3.6 (a) General structure and (b) macromodel for ISFET devices as they are considered in this work.

The first term of Equation (3.40) gives the potential difference between the gate terminal and the semiconductor surface and the second term describes the charge distribution dependent potential which arises across the transistor. The equilibrium electrostatic potential Φ_F (Fermi–potential) of the semiconductor establishes the connection between the threshold voltage, the surface semiconductor potential and the number of charge carriers. The exact origin of the factor of 2 under strong inversion condition is shown elsewhere ([117] – Equation 2.3.1–20). For the case of ISFET transistors the formula of Equation (3.40) is adapted. The gate of an ISFET is floating, in contrast to CMOS devices where the voltage drop at the gate terminal is well defined by connecting metal tracks to nodes of the surrounding electronics. In the case of ISFETs therefore the reference electrode is considered as the gate terminal and the Φ_M component is then transformed as

$$V_T = V_{ref} - \varphi_{int} + \chi_{sol} - \frac{\Phi_{Si}}{q} - \frac{Q_{OX} + Q_{SS} + Q_D}{C_{OX}} + 2\Phi_F \qquad (3.41)$$

where V_{ref} is the DC reference electrode potential, φ_{int} is the potential across the electrolyte–insulator interface and χ_{sol} is the dipole potential of water molecules in the solvent. φ_{int} is dependent on the pH value of the electrolyte thus the threshold voltage of the ISFET device also correlates to the actual pH value. As a consequence the substitution of Equation (3.41) into Equation (3.39) would show that the fluctuation of the electrolyte pH explicitly affects the drain current of the ISFET sensors as well as the measured gate–source and drain–source voltages.

The pH sensitivity of ISFETs was modelled by van Hal [118] showing the $\Delta\varphi_{int}$ electrostatic potential changes across the electrode–electrolyte interface and defined the α dimensionless sensitivity parameter as

$$\Delta\varphi_{int} = -2.3\alpha\frac{kT}{q}\left(pH_{pzc} - pH\right) \qquad (3.42)$$

$$\alpha = \frac{1}{\left(2.3kTC_{int}/q^2\beta_{int}\right)+1} \qquad (3.43)$$

where pH_{pzc} is the point of zero charge, the pH value at which the interface region is electrically neutral. C_{int} is the differential capacitance across the interface and β_{int} is the buffer capacity parameter at the surface of the silicon nitride. The equations indicate that

the value of the sensitivity parameter is in the range of 0–1 and therefore the sensor device delivers the maximum performance, 58.2 mV/pH for silicon nitride, if this parameter is 1. If α is between 0 and 1, then the response is called sub–Nernstian. As discussed in Section 2.1, the physical measurements demonstrate that the pH sensitivity sometimes varies substantially. At the time of writing this thesis, the phenomenon of varying pH sensitivity is attributed on the one hand to the potentially varying parameters of nitride deposition, on the other hand to the development of SiO_2 on the nitride surface. The exact identification of the source of the differences is subject to future investigations.

3.3. Summary

This chapter outlined the theoretical background of the intrinsic 1/f noise measured in semiconductor devices. In the first instance the physical models for noise origin, number and mobility fluctuation, were introduced taking a practical and intuitive approach for the number fluctuation. The RTS noise was elucidated showing its probability distribution for the separate trapped and detrapped states and its Lorentzian power spectrum that can develop 1/f spectra in case of several RTS responses.

The present chapter also provided a detailed discussion on the main theoretical principles of detection of ion concentration fluctuations with ion sensitive field–effect transistors. The chapter part of ion–sensitive devices started with introducing the essential background of electrochemical interactions and redox processes. The discussion was continued by elucidating theoretical models on the structure and operation of the electrolyte–sensory material interface. The chemical interactions between the electrolyte and the silicon nitride passivation layer were introduced using the principles of the well–known site–binding model. The electrochemical description was followed by explaining the theoretical electrostatic charge distribution across the electrochemical cell as well as describing the used reference electrodes and fabrication methods. The theoretical aspects of ion–sensitive transistors were additionally discussed and an interpretation for the threshold voltage change and ionic sensitivity were given.

4. System, packaging and data acquisition

Design processes of sensor network based electronic systems usually require elaborating abstract models or methods to develop a basic platform to build the complex structure on as first step in the project cycle. The applied standard bottom–up development approach is often used for integrating separately designed components constructing larger building blocks towards the interconnected and distributed system architecture. The use of complex design systems is essential in semiconductor based electronics containing sensor array modules because on the one hand they rely on the integration of several supplementary circuit elements performing specific tasks, e.g. amplification, sensor selection, signal conversion, interface control. On the other hand they aid to analyse series of synchronisation events in the network of component blocks and time constrained signal transfers to handle repetitive occurrences, e.g. pixel addressing.

This chapter primarily demonstrates the system level development of the 64×64–pixel ISFET array device by elucidating the general guidelines of design software and foundries as well as describing the developed on– and off–chip circuit components. The explanation follows with a detailed discussion on the bonding, packaging and encapsulation of the fabricated silicon die. The structure of the developed real–time data acquisition system is described which was able to acquire the analog voltage signals at high temporal and spatial resolution. The method of useful data extraction is furthermore presented as well as its multi–dimensional representation approaches.

4.1. CAD systems and foundries

The application of multifunctional design software that calculate using either ideal parameters or close estimates of the real physical constants facilitate the modelling of electronic elements. This class of software are generally referred as computer aided design (CAD) systems and a possible generic iterative workflow is presented in Figure 4.1. The high–level designs often use ideal values, e.g. voltage and current sources, to aid the modelling work and incorporate the logical interconnections of circuitries called schematics. In a sensor development flow the schematics are simulated at first to verify the functionalities and capabilities of the developed on– or off–chip components. The high–level schematic configuration of the circuitry is translated into the layout representation with matching element topology and logical connections. The layout design level is a vital

step in both the bottom–up and top–down development flows because the physical description and structure of sensors, transistors and additional on–chip devices are defined at this stage. The decisions whether transistors are in the same or in separate wells, whether blocks are connected on first or fourth metal layer, whether guard–ring is placed around the elements, etc., can still critically influence the operation of the circuit.

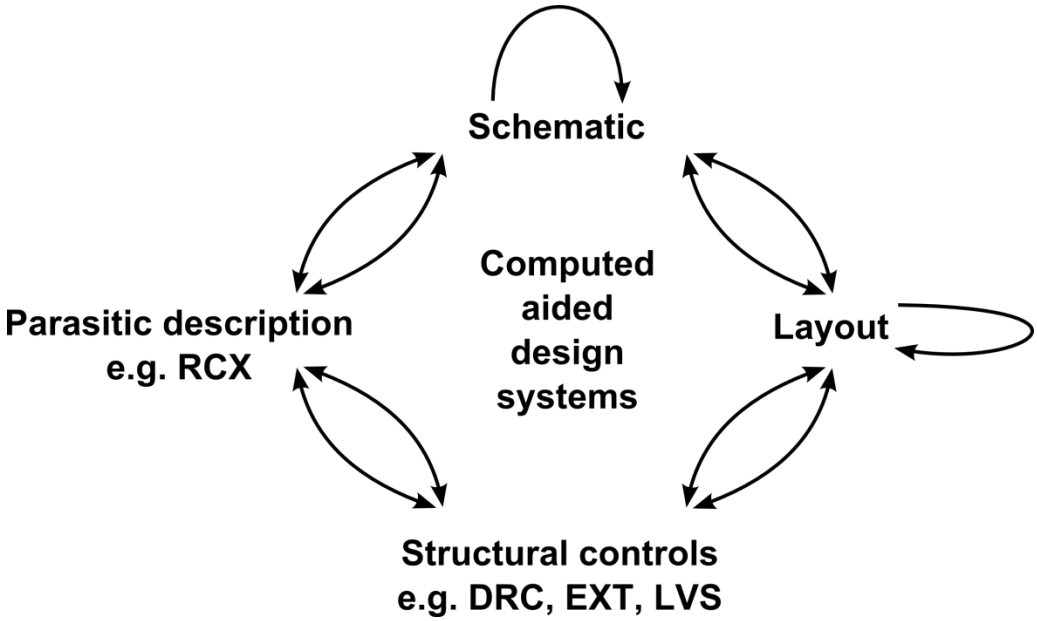

Figure 4.1 General description on the iterative design flow of very large scale integrated (VLSI) electronic devices

Despite the matching placement of instances with the logical circuit structure the appropriate selection of physical parameters is essential. Layout design software furthermore check the topology and dimensions of the instances against a set of predefined rules which is called device rule check (DRC). It is usually followed by the netlist extraction (EXT) based on the physical device connections. The analogous architecture of the circuitry between schematic and layout level, EXT format, is ensured by a separate tool called layout–versus–schematic (LVS). The LVS is required to locate any short–circuits or other anomalies in the arrangement. It is also vital to explore the behaviour of the developed device or circuit component using solely real estimations of coefficients. The post–layout simulation is essential to be performed upon success of the LVS, to indicate any signal losses, crosstalk or eventual disruption in the signal integrity. The post–layout simulations are rendered applying RC extraction (RCX) or parasitic extraction based on the netlist of the schematic. The parasitic extraction fits resistances and capacitances to the topology of laid out instances allowing the emulation of the genuine operation of the circuitries. The place and quality of RC component fitting is dependent on the applied CAD software and algorithm. It is shown in Figure 4.1 that the design of VLSI circuits is

an iterative process because the chance is weak that the topology and parameters are selected to achieve the best trade–off at the first time. There usually are several simulation attempts required to tune the parameters to a satisfactory level which enables stepping one stage further in the design cycle. Due to the iterative nature of the CAD based device developments it is eventually required to return to the initial highest design level if simulations at lower design levels deliver insufficient results, e.g. schematics ↔ RCX deliver incompatible results.

The vendors of CAD systems, e.g. Cadence Design Systems, Mentor Graphics, etc., usually provide a software framework to complete the development flow without the exact definitions of design rules or material specifications. It indicates the flexibility of CAD systems with various technologies and feature sizes and therefore a CAD software is usually adaptable to substantial sets of requirements. The groups of consistent DRC rules, LVS rules, RCX rules, etc. are supplied externally and fitted to the delivered technology and specific fabrication needs. The specifications of used materials are integrated and in most cases published in confidential documents by the foundry. The selected foundry for the 64×64–pixel ISFET sensor array device was the austriamicrosystems AG providing the CMOS process with the HIT–Kit v3.70 design kit. The used C35B4 technology was a CMOS process with 4 metal layers and 0.35µm feature size as shown in Figure 4.2.

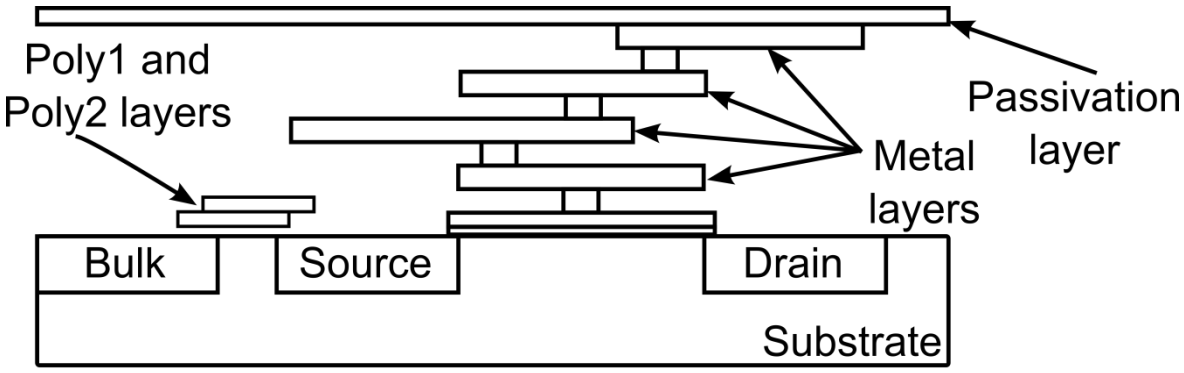

Figure 4.2 Structural description of the AMS 0.35µ C35B4 technology. Image is not to scale.

It is demonstrated in the structural description of the chosen technology, Figure 4.2, that the separate alloy metal layers are connected with vias of tungsten base. The CMOS structure is split into different levels that are insulated by oxide layers. The resistor design or even wiring is achievable on two additional polysilicon layers at the cost of higher sheet resistance comparing to metal leads. The fabricated devices are sealed by the passivation layer to prevent the environment from external damage or influence.

The developed ISFET array chip prototypes were fabricated in the Multi–Project Wafer service of Europractice. The design was submitted to the Fraunhofer Institute for Integrated Circuits, Erlangen, Germany and was placed on the same silicon wafer together with other developments. The fabricated devices were cleaved by the manufacturer and were delivered to the University of Glasgow.

4.2. Operation modes

The flexible operation was one of the priorities during the design of the ISFET sensor array chip to ensure reusability and the potential of further adjustability and scalability. From the logical planning phase of the system the initial expectation was the development of a sensor circuitry which is variable between different parameter configurations only by supplying the respective digital inputs on–chip. The flexible behaviour thus provides the opportunity to conduct measurements at several levels in terms of frequency, number of cooperating electronic components and types of controls. Besides the various control methods the flexible operation conditions maintain certain protection against malfunctioning parts due to for example fabrication or design issues by the ability of deliberately omitting components upon demand.

Although there were 4 distinct operation modes, discussed below, which were outlined, elaborated and designed for, only the external mode was set throughout the ion sensory measurements. The application of the additional digital input configurations for the non–external modes was intentionally missed. The internal signals for pixel addressing, modulations and signal filtering originating from on–chip ring oscillators were difficult to synchronise with the external data acquisition, thus the approach of fully external control was preferred.

4.2.1. Standard

The standard mode was planned as default operation mode having the vast majority of functionalities controlled internally. The operation of the chip was primarily based on the four independent on–chip ring oscillators with two separately adjustable power potential inputs for each oscillator. The first and second oscillators were responsible for fast and slow internal addressing where the difference in output frequencies was guaranteed by the unequal frequency divisions in the output signal of the oscillators. The third oscillator controlled the modulations and demodulations of the input and output signals, respectively.

The fourth oscillator provided the control signals for on–chip switched capacitor filters through a non–overlapping clock generator. The standard mode was designed to provide signals on the 2×16 output terminals simultaneously.

4.2.2. Fast

The fast mode of the 64×64 sensor array was designed to perform rapid measurement cycles to enable the readout of the complete sensor frame in a short time range. This operation mode was based on the bypassing of on–chip modules that were not essential or suitable for the fast operation. This configuration guaranteed that only the first ring oscillator was active and the supplementary services were either bypassed or deactivated. The output frequency of the oscillator block and therefore the base frequency for addressing were set to 250 kHz by adjusting the voltages at the respective analog input terminals. This would have implied a read out sensor frame in each 1.2 ms time slot. The primary aim of introducing the fast mode was the intention of universally using the ISFET array device in cell–, diffusion– and ionic–imaging application where the speed of data acquisition is a critical parameter.

4.2.3. Semi–external

The semi–external method was introduced on the one hand to provide a supplementary externally–perturbed internal addressing capability. A specific I/O pad was dedicated as access point to the addressing module while the parameters of the fast operation mode were set at the digital inputs. Thus it implemented support and protection for the case of a dysfunctional on–chip ring oscillator. On the other hand the semi–external mode was useful because it delivered an on–chip approach for enabling the deliberate control over the pixel addressing speed. The used I/O pad connected to the entry point of the internal addressing blocks and therefore the rate of pixel addressing could be influenced by using an external arbitrary waveform generator and disabling the on–chip oscillator.

4.2.4. External

The external mode provided complete control over the ISFET array chip and this mode was used throughout the physical measurements. In external mode the chip was switched into the fast configuration and all oscillators and additional circuitries were disabled, only the sensor array, bias supply, buffers and addressing were active. The access point and thus

the frequency dividers of the semi–external mode were also bypassed, therefore the inputs of the addressing decoder connected directly to 6 I/O pads in the padring. The digital inputs at the pads were supplied externally and the analog voltages were acquired synchronously on multiple channels at the same time as discussed in Section 4.6. Hence each component and signal path was regulated and synchronised by off–chip sources.

4.3. 64×64–pixel ISFET array chip

The 64×64–pixel ISFET sensor array chip was structured to be an interactive and capacitively coupled environment between the sensors and the aqueous electrolyte across the foundry default passivation layer. The selected 0.35 µm CMOS process from austriamicrosystems enabled the integration and linking of the 4096 ion–sensitive pixels with required complexity on 4 metal layers. Modular hierarchy was prioritised for design of the ISFET array device with intention of potential scaling improvements to map and visualise the dynamic activity of chemical substances using the highest resolution.

The following sections describe the units and modules of the ISFET array chip. It is essential to note that only the components are analysed that were intrinsic parts of the system during 1/f and ISFET measurements. Therefore the functionalities of the pixels, addressing modules and the ISFET array are described.

4.3.1. Pixel

The elementary unit of the 64×64–pixel sensor device is a pixel that is replicated multiple times across the ISFET array. The schematic and layout representation of the developed ISFET pixel circuit is shown in Figure 4.3. Figure 4.3a demonstrates that a pixel circuit consists of four transistors: P1 PMOS transistor, P2 p–type ISFET transistor and the transmission gate circuit of P3 and N1 PMOS and NMOS transistors. The $W_{P1}/L_{P1} = 2\mu m/1\mu m$ P1 transistor performs multiple functionalities during the activated time period of the sensor pixel. On the one hand it delivers approximately 16 µA current thus acts as a load transistor, as an in–pixel current source during the pixel readout. On the other hand the P1 transistor implements the in–pixel row addressing as well because its V_{row} gate voltage is alternated between 1.2 V and the power potential. The $W_{P2}/L_{P2} = 5\mu m/0.35\mu m$ P2 p–type ISFET transistor is used to detect the concentration differences for H^+ and Na^+ ions in the electrolyte. It is shown in Figure 4.3b that the gate of the ISFET transistor is connected to a central point of the pixel on Poly 1 and this point is

connected further to the patterned MET4 top metal layer using intermediate vias and metal layers. As the patterned MET4 structure is in direct connection with the passivation layer it is ensured that the voltage fluctuations across the passivation perturb the gate potential of P2.

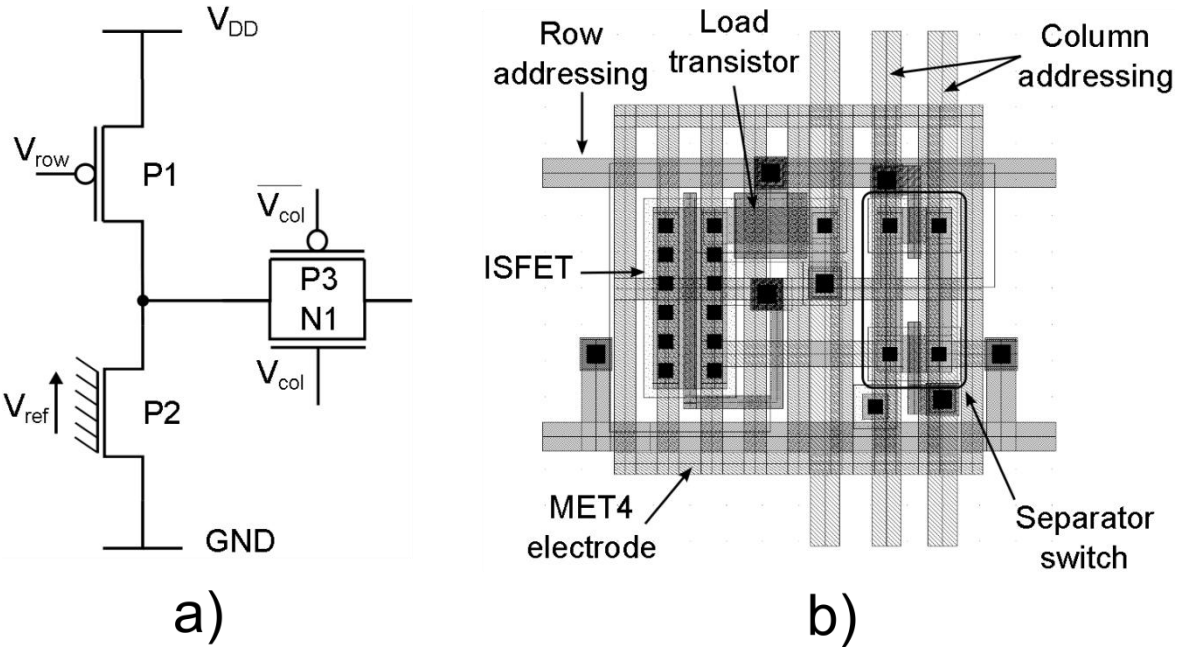

Figure 4.3 Schematic (a) and layout (b) representation of an ISFET pixel circuit.

The $W_{P3,N1}/L_{P3,N1} = 1\mu m/0.35\mu m$ transmission gate circuit separates the source–follower ISFET circuit from the analog output channels and guarantees that charge sharing between pixels on the same output channel is prevented. Due to the complementary transistors in the transmission gate circuit the signals for opening or closing is provided simultaneously with opposite logical states using inverter circuits outside the sensor array.

4.3.2. Decoder, Multiplexers, Demultiplexers

The external control of the sensor chip is driven by a tightly regulated addressing protocol on VLSI level. The procedure of sensor selection is implemented using decoders, multiplexers and demultiplexers, Figure 4.4. Their displayed input digital code is varied uniformly and the actual code is provided in each data readout cycle before the analog reading. The vertical addressing was performed using a 6/64 decoder circuit shown in Figure 4.4a. The 6/64 decoder component received the supplied 6–bit digital code and selected the respective column of the ISFET array by connecting the potential of the chosen output terminal to GND. The binary input digital code is increased by binary 1 from 000000 to 111111 in equal time steps hence each column address from 0 to 63 is

resolved sequentially. The 4/1 multiplexer shown in Figure 4.4b is used in the data readout of the selected row from the ISFET array.

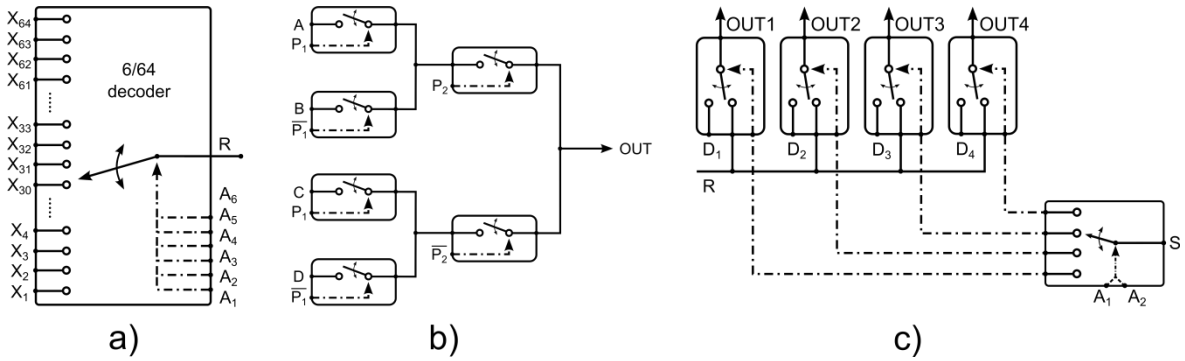

Figure 4.4 The on–chip digital components, (a) 6/64 decoder, (b) 4/1 multiplexer and (c) 1/4 demultiplexer, are demonstrated that were used to implement the sensor selection/addressing.

The multiplexer connects specific rows with the output buffer amplifiers and keeps the same state as long as the 6/64 decoder finishes the actual sequence from 0 to 63. The demultiplexer component, Figure 4.4c, receives the same digital row addressing code that is supplied to the multiplexers as well. Therefore the demultiplexer block containing switches and a 2/4 decoder cooperates with the multiplexer by activating the selected line while the multiplexer directs its read out analog voltage values to the output buffer.

4.3.3. ISFET array

The 64×64–pixel ISFET sensor array is a modular device which makes it suitable for high–speed operation. The 4096 sensors of the ISFET array were designed and fabricated by systematic replication of a single pixel. The replicated pixels were arranged into an array shape that was vertically divided into 16 separate sectors as demonstrated in Figure 4.5a. The sectorial division of the array into 16 pieces of 4–row blocks was essential because it accelerated the data readout by enabling the parallelisation of tasks on several data channels discussed in Section 4.6.

Each 4–row block is an independent part of the array that contains 4×64 = 256 ISFET sensors. All four matrix rows of a 4–row block connect to a demultiplexer and a multiplexer, thus there are 16 demultiplexers and 16 multiplexers implemented on the sides of the array. The gate terminals of the P1 transistors of pixels, Figure 4.3a, are connected which are located in the same array row and these control lines are connected to the respective output terminals of the demultiplexers. Thus a demultiplexer activates a complete row at once by changing the control potential of each P1 transistor in the same

row to 1.2 V. The output terminals of the pixels of the same row are connected in a similar manner to an output line which is in direct connection with an input of a multiplexer. The output lines of the ISFET array are connected to the output channels depending on the supplied row address. The fabricated sensor array, the MET4 ring around the ISFET array, GND and V_{DD} paths as well as row addressing and output lines are displayed in Figure 4.5b which was taken by optical microscope. The image verifies the discussed 715.8×715.8 µm size and the square shape of the 64×64–pixel sensor array. In the scanning electron microscope images in Figure 4.5b also demonstrate the patterned style of the top metal of each pixel. The initial aim of patterning the MET4 was to clean the silicon nitride in the passivation layer from trapped charges by exposing the chip to direct ultraviolet (UV) radiation. Although several UV exposure tests were carried out prior to the ionic measurements, the application of the method was discontinued because of the lacking observable improvements.

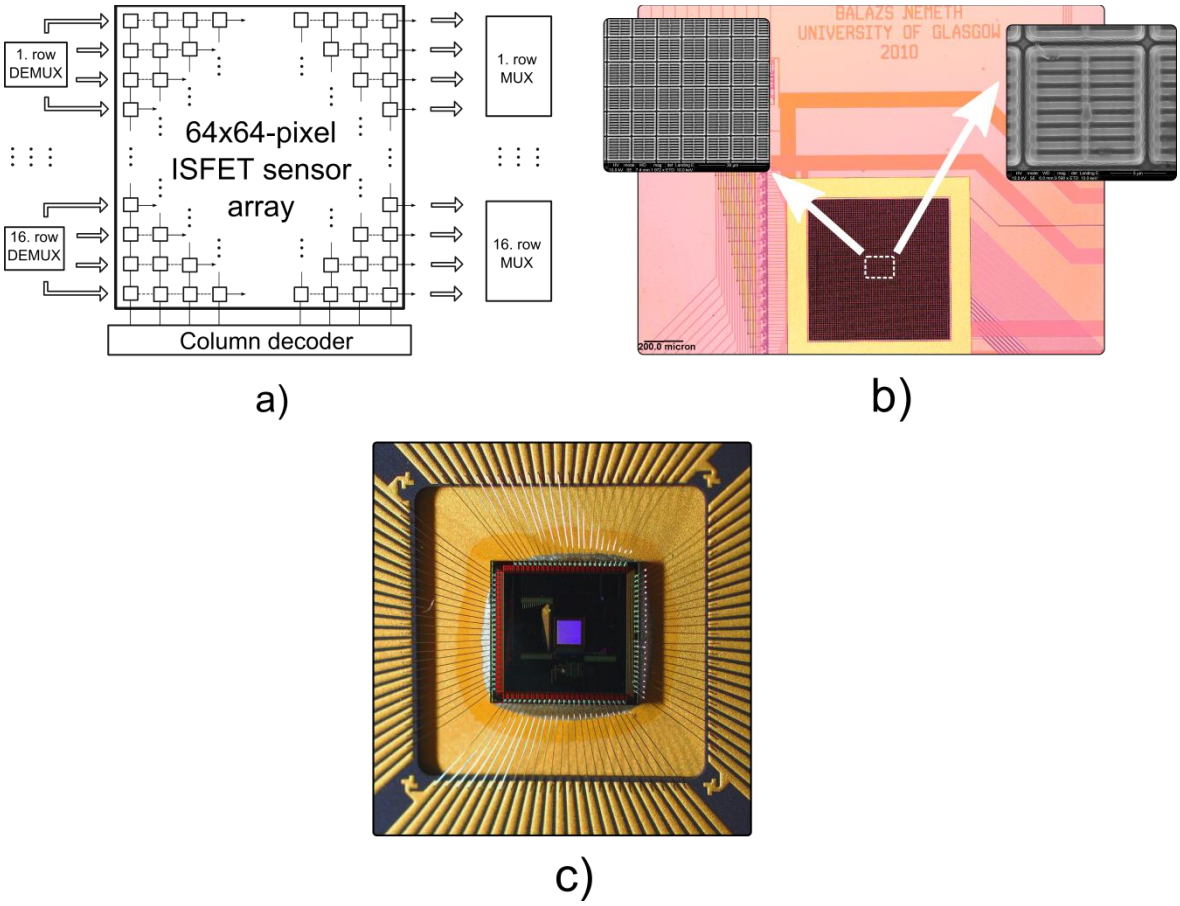

Figure 4.5 (a) system–level description of the operation of the ISFET array, (b) the fabricated ISFET array and (c) the fabricated, packaged and bonded chip is demonstrated.

The 100× magnified optical microscope image of the complete fabricated, bonded and packaged chip is shown in Figure 4.5c. It is demonstrated that the sensor array was located in the geometrical centre of the chip to suit the requirements of the encapsulation process,

discussed later. The chip shown in Figure 4.5c was packaged and bonded by the manufacturer company, further bondings were carried out at the Physics Department of the University of Glasgow.

4.4. Chip layout and off–chip electronics

The layout of the ISFET sensor array chip was developed using the design environment of the Cadence, Inc. and the HIT–Kit v3.70 design kit from austriamicrosystems. The Assura layout tool was utilized throughout the physical design in accordance with the preconditions of the manufacturer. The complete layout architecture of the developed 64×64–pixel ISFET sensor array chip is shown in Figure 4.6.

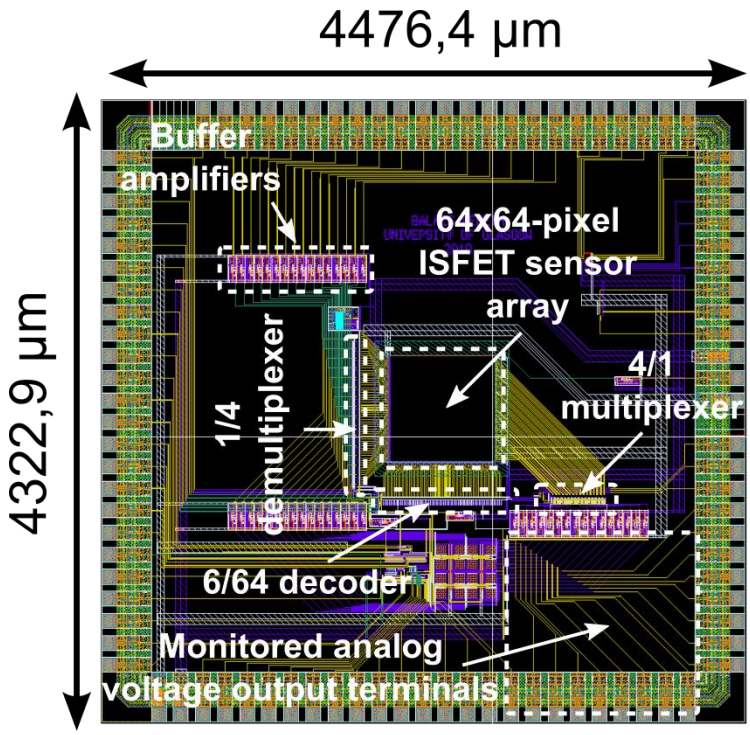

Figure 4.6 Physical layout of the 64×64–pixel ISFET array chip

It is demonstrated in Figure 4.6 that on the one hand the chip required an approximate space of 4.4×4.3 mm on silicon. On the other hand it is shown that the fabricated device is a pad–limited design incorporating 95 I/O pads in the 3–bus padring recommended by austriamicrosystems. The chip was developed with double power and double ground terminals delivering the signals on 75 µm wide tracks on MET1 and MET2 layers. The power and ground pads were connected to provide flexibility in biasing and to ensure that there are two powering points in the case one would be dysfunctional. The structure of components discussed in Section 4.3.2, buffer amplifiers and the ISFET array are shown in Figure 4.6. The ISFET array is displayed as a black square because of the insufficient

resolution of the layout tool when showing fine details with the complete chip layout in scope. The 16 analog output terminals are also marked where the signals were acquired from during the data acquisition.

The connection between the chip and the computer was essential to establish to maintain external control over the ISFET device. An interface board was therefore designed that integrated the chip socket and the access points of the data acquisition hardware as well as the ground and power potentials. The layout and the fabricated printed circuit board (PCB) are demonstrated in Figure 4.7.

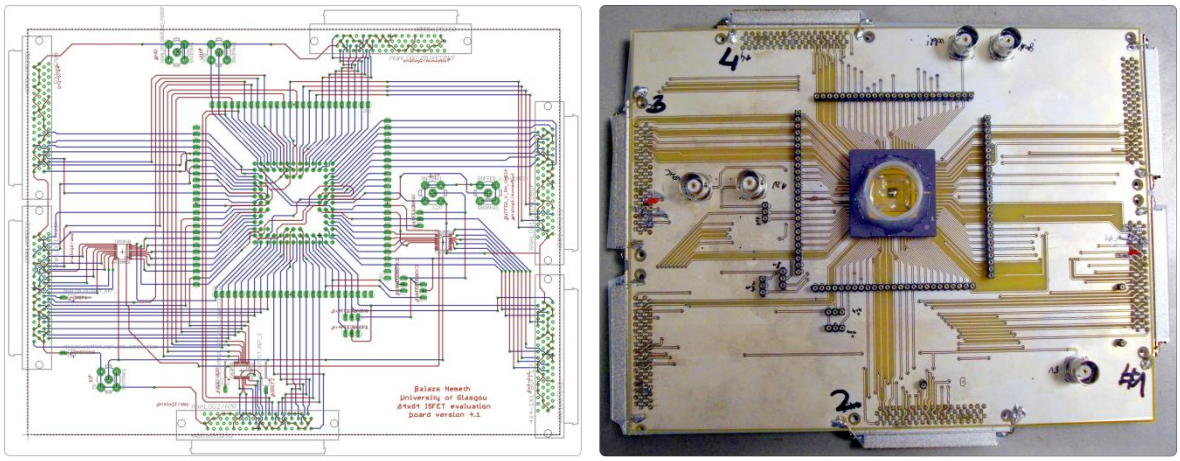

Figure 4.7 The image demonstrates the (a) layout and (b) external fabricated interface board.

It was critically important that the grounding was balanced between the measurement hardware, interface board and the chip device because the measurements could only be taken with respect to a common reference point. Thus at first a common ground point was developed by connecting the ground terminals of all involved instruments and cables. As a consequence the ground potential of the interface board was supplied by the common ground point through the internal noise shielding ground cover of the BNC cables. The data acquisition hardware received its main ground from the electricity network, though it was insufficient because specific analog ground potential was required to provide for the differential measurements. It is shown in Figure 4.7b that the frames of the default male Small Computer System Interface (SCSI) connectors were attached to the PCB board by soldering. Additional aluminium wires were soldered from the metal male SCSI frames to the ground plane of the board. These ground connections were vital since the outer metal cover of the female SCSI connectors of the cables from the measurement device were in connection with the male SCSI frame. Thus it was ensured that the analog input ground of the measurement cards was supplied by the common ground point of the overall system.

Voltage level incompatibility issues usually arise when performing the task of pixel addressing using an external signal source. The source of incompatibility is that the external control instrument normally delivers the pre–set digital output at TTL signal levels (0 – 5 V) meanwhile the semiconductor chip accepts CMOS levels (0 – 3.3 V). According to the specifications from the chip manufacturer the + 5 V applied gate voltage is the upper extreme of the safe operation environment for the fabricated CMOS transistors. Thus a long term cyclic operation at TTL voltage levels would potentially lead to irreversible damage in the circuit structure. Avoiding eventual damage in the sensor topology, three MAX3001 voltage level translator ICs, Figure 4.7a, were incorporated in the off–chip electronic design shifting the level of the digital signal from TTL to CMOS. The locations of the MAX3001 ICs are visible in Figure 4.7b as well although it shows the other side of the board.

The several versions of the PCB interface board were fabricated in the PCB express service of the PCB Train – Newbury Electronics Ltd. The 2 layer fabrication was supplied using 1 oz. copper with silver immersion finish and the minimum track gap was 0.2 mm.

4.5. Packaging and encapsulation

The packaging and encapsulation terms are often used interchangeable in the overall preparation process of the semiconductor chip for measurement purposes although they are treated separately in this work. Finding a suitable package for the developed chip is often complicated task because it depends on several parameters in terms of chip accessibility, applied bonding method, number of on–chip I/O pads, socket availability and material of the chip carrier. Devices for research purposes are usually packaged in open cavity carriers to fit the later often adjusted encapsulation methods. The number of used I/O pads is also important because above a typical limit of 100–120 pads mostly flip–chip or through–hole packages are available and this ought to be considered while designing the PCB interface board. The use of packages with high pin numbers and the need of frequent device exchange usually require the soldering of fitting sockets that provide connections to the data acquisition hardware.

The selection of a stable encapsulation method is of absolute importance for ISFET array devices because it needs to prevent the contact between bonding wires and the aqueous environment. The potential short circuits between bonding wires are likely to result in serious damage in the device structure or complete dysfunction of the chip. The deposition

and curing technique of the encapsulant and the quality of the encapsulation material is also critical point in the sealing process. The deposition of an overly fluid epoxy on and around the bonding wires without extra care can cause fatal consequences for the chip device which means that the epoxy overruns the chip surface and thus the ISFET array device. Using some type of epoxy as encapsulant the deposition technique is empirically recommended to be multi–layered for practical reasons, e.g. more stable sealing and better protection against potential leaking current from electrolyte through the encapsulant.

The initial depositions were carried out using a general purpose RS Components 851-044 two–component epoxy on a FR–4 PCB board having the I/O pads of the chip straight bonded to the copper tracks on the board as shown in Figure 4.8a. The chip device was located in a 600 µm deep 5×5 mm recess that was milled in the centre of the board. A cut part of a circular acrylic tube was used as container for the applied electrolyte and the used

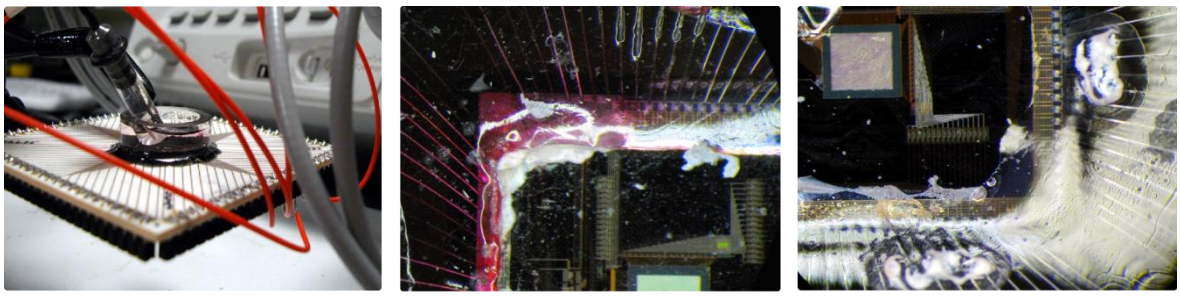

Figure 4.8 Initial bonding attempt (a) having the pads bonded to the copper tracks on PCB. (b) demonstrates long–term damage of salt residue and (c) shows short circuit through the RS Components general purpose potting epoxy.

BASi RE–6 reference electrode. The reference electrode was stored in 3M NaCl solution following the advice of the manufacturer and the epoxy components were mixed in 50% – 50% ratio. Although this general purpose epoxy was easy to use, cure and dispense with a dispenser gun, it did not prove to deliver great stability in the long–term. The experienced damages are shown in Figure 4.8b and c with intentionally dried chip surface which was necessary for taking the photographs. Figure 4.8b demonstrates that the epoxy sometimes delaminated from the chip surface where it was thin, even if it was multi–layered. In case the reference electrode was not washed properly before measurements, a salty residue remained on the surface after multiple use which is visible under the delaminated part of the epoxy in Figure 4.8b. The top–right corner and middle–bottom part of Figure 4.8c show the resulting stains of a developed short circuit between bonding wires across the electrolyte. The phenomenon occurred after 2 deposition runs and between two spots with

different thickness of covering encapsulant. The spot in the middle was covered by a thinner layer of epoxy while the other one had a stable and thick cover. Therefore the consequence was taken that the material structure of the epoxy might be the reason that caused this instability. This type of short circuit resulted in irreversible damage in the electronics for the chips it happened to.

The strategy of encapsulation was subsequently amended with additional epoxy materials in focus. The Epotek OE145 semi–transparent and two–component epoxy was selected as improvement in the isolation process as shown in Figure 4.9a. The transparency was an important factor during the covering because of the manual deposition technique, thus the snap or displacement of bonding wires were essential to be discovered and the data readout was adjusted upon occurrence. The viscosity of the Epotek OE145 strongly depended on the mixing ratio of the base material and its solvent. It was possible to deposit and cure the material on many layers without experiencing delamination or eventual material disruption causing short circuit across the electrolyte. The electrolyte liquid evaporation prevented by using a 25 ml Corning centrifuge tube with screw cap, the tube was cut manually by a Rotax tube cutter. Although the mixed OE145 proved to be a stable substance, anomalies were experienced in the course of its curing process. The epoxy was deposited around the chips and bonding wires and it was left to dry for at least 24 hours and thereafter the chips were placed into the oven to harden at 80 Celsius degrees for 12–24 hours. It was unfortunately observed that the epoxy overran the chip surfaces for only some devices, others remained intact and the encapsulant hardened. In each specific encapsulation run the packaging, deposition technique and used epoxy mixture was identical for all involved chip devices and the number of affected chips by the discussed anomalies followed irregular pattern for each run. Thus further improvements were essential to implement to avoid the anomaly with the epoxy.

The final encapsulation approach is demonstrated in Figure 4.9b and c that delivered a safe and repeatable solution for the ionic imaging measurement series. The applied sealant was exchanged to the Epotek 302–3M that is a low viscosity, colorless and two–component epoxy with a short curing period. The complete transparency of the sealant material was an important advantage during the deposition. An on–chip barrier was essential to establish preventing the very fluid epoxy to compromise or damage the chip surface. General purpose silicon rubber sealant (Geocel Ltd., UK) was taken onto the surface of the silicon nitride in square shape around the sensor array. The chip carrier was placed on a hotplate that heated the carrier to approximately 80 Celsius degrees.

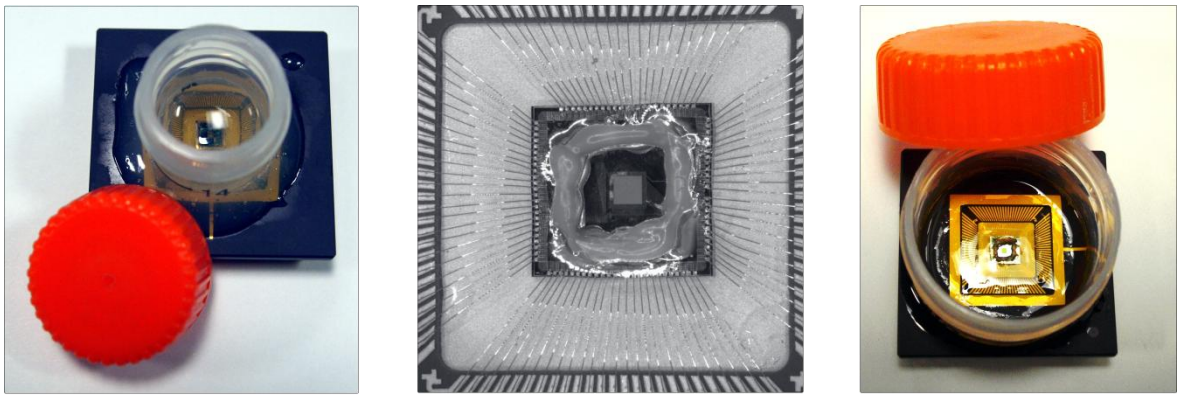

Figure 4.9 (a) shows the encapsulated chip with Epotek OE145, (b) and (c) demonstrate the improved sealing methodology with Epotek 302–3M

The silicon rubber was dispensed in two layers onto the chip surface to create a silicon chamber around the ISFET array with sufficiently high waterproof walls. The silicon layers were dispensed with an approximate 30 minutes delay each time to allow the rubber to dry and harden up properly. The Epotek 302–3M was mixed with its solvent in almost 40% – 60% ratio that resulted in a highly fluidic compound which was then carefully flown onto the hot chip carrier using plastic pipettes. The maintenance of the high temperature was advantageous on the one hand because the prepared epoxy compound ran smoother around the chip with silicon chamber and bonding wires in the open cavity of the chip carrier. On the other hand the epoxy dried out significantly faster which shortened the preparation time of the multi–layered encapsulations. The Epotek 302–3M was usually taken to the surface on 4 layers giving each layer 3–5 hours time for drying; the exact drying time strongly depended on the quality of the epoxy mixture.

4.6. Real–time data acquisition

Several data acquisition methods, e.g. oscilloscope, microcontroller based, etc., were attempted to read out the analog voltage response of each pixel in a uniform and fast manner. The applied methods were necessary to reconsider because the chemical environment of the monolithic, semiconductor chip based ion camera system implied strong limitations in terms of data readout speed. The planned measurements for visualising the transport of protons and sodium ions on the surface of the silicon nitride required a strict time schedule for the data acquisition that was suitable to electrochemical processes. Therefore a real–time data acquisition system was developed with appropriate task priority considerations.

Multi–tasking operating systems are not suitable to perform real–time task management because the CPU time is shared among several processes. In addition it cannot be guaranteed that a process has continuous access to hardware resources, if another high–priority process, e.g. anti–virus, firewall, etc., requires immediate intervention. The shortest time unit of a multi–tasking operating system, e.g. Microsoft Windows, is characteristically in the 1 ms range which is disproportionate to the need of chemical mechanisms. In general the real–time systems are applicable for fast measurement purposes because of their dedicated software architecture. The real–time capable devices usually carry out only a very few amount of tasks using predefined protocols with respect to a set of priorities and the repetitive process cycles are driven by the hardware clock of the system. Thus the hardware clocking enables the required reliable and timely accurate task management without unexpected interruptions.

The VLSI level flow of the data acquisition method is displayed in Figure 4.10. As discussed before, the sensor array is horizontally divided into 16 pieces of 4–row blocks and each 4–row block is connected to an individual multiplexer and demultiplexer. The outputs of the multiplexers are linked to the buffer amplifiers which are bound to the I/O pads of the ISFET array chip. The paths from the multiplexer outputs to the I/O pads are considered as output channels. Corresponding to the number of available multiplexers 16 analog output channels were used during the experimentation and their data was transmitted over network for storage and further data processing. The identical row addresses at both sides provided the synchronous row activation and data readout while the pixels were sampled through the line using the decoder. The possible crosstalk between pixels and output channels is reduced by immediate setting of the inactive lines to either analog ground or power rails.

The uniformly changing and constant digital codes as well as the analog voltage acquisition were achieved using two NI PXIe–6358 measurement cards that were placed into a PXIe–1073 5–slot chassis. The pixels were sampled at a maximum data acquisition rate of 40 µs per pixel, 10.2 ms per sensor array, thus the sampling frequency was 25 kHz and ~100 frame–per–seconds (fps). Although the applied sampling frequency was securely below the maximum achievable 1.25 MS/s/channel, higher rates were not considered because of the stability of the simultaneous operated analog input and digital output terminals.

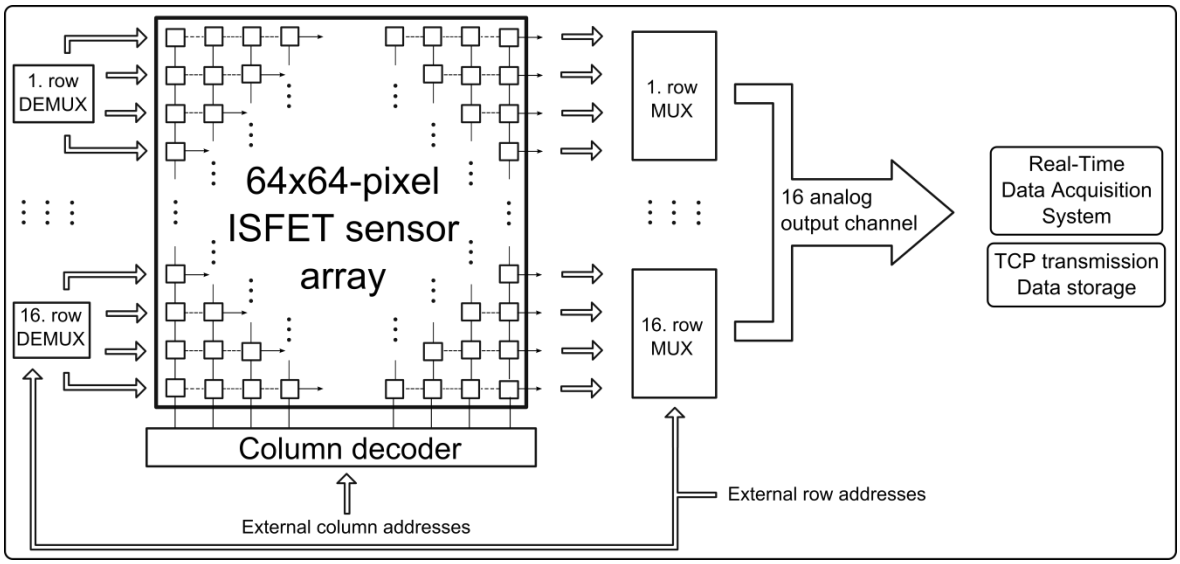

Figure 4.10 Description of the on–chip data acquisition principles

The 40 µs per pixel, 10.2 ms per sensor frame data recording speed implies that a row in the array could be read out in 64×40 µs = 2.56 ms and therefore the read out time of a 4–row block was 4×2.56 ms = 10.2 ms. Since the acquisition of the pixel information was carried out on 16 analog channels simultaneously the required time for the data readout of the complete sensor array equalled the time required for one 4–row block.

The pipelined system level flow of the data acquisition process is demonstrated in Figure 4.11. It is shown that the data recording procedure was a composition of multiple independent processes that communicated in a handshake–like manner to guarantee the acknowledged information stream. Figure 4.11 additionally shows that the data acquisition system consisted of a desktop–PC (host), another desktop PC (RT–target), the PXIe–6358 measurement cards with the PXIe–1073 5–slot chassis and the 64×64–pixel ISFET sensor array with the interface board.

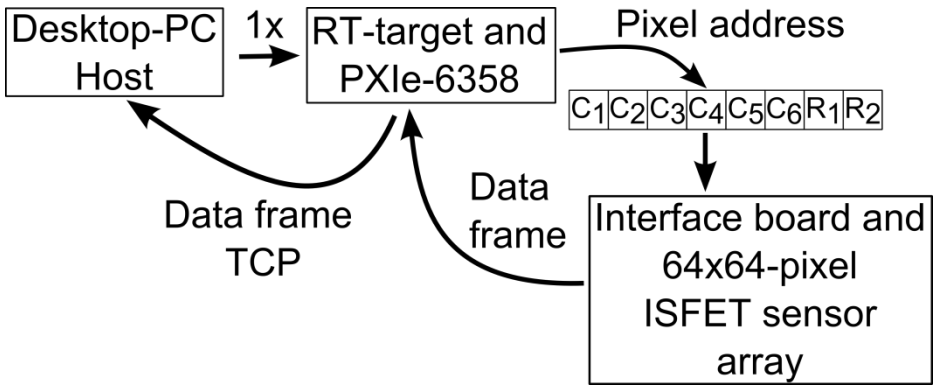

Figure 4.11 System–level description of the pipelined data acquisition flow.

The host computer was used to control the overall process running the LabVIEW 2009 environment on Windows XP platform. By launching the developed distributed software

system the host computer downloaded the real–time software part to the RT–target through network using the file transfer protocol (FTP) as the first step in the mechanism. The host side software then downloaded a prepared list of consecutive binary codes to the RT–target. Each item in the list of binary codes was a 14 bits long address word that combined pixel addresses with the respective digital constants to force the ISFET array chip into the desired operation mode. The download was followed by the automatic launch of the developed real–time software on the RT–target. The measurement cards selected the appropriate 14–bit address code and delivered it to the preferred digital output port. The digital input was divided into three separate pieces by the on–chip electronics. 6 bits maintained the mode conditions and the remaining 8 bits contained the pixel addressing information. 6 bits of the addressing code were wired to the 6/64 decoder and the other 2 bits were bound to the multiplexers and demultiplexers. The hardware–timed pixel addresses selected one pixel from each 4–row blocks simultaneously thus every sent pixel address activated 16 pixels in the ISFET array at once corresponding to the available 16 analog output channels.

The analog voltage readings of 16 pixels at once were synchronised by the PXIe–6358 measurement cards after supplying the digital input for the chip using the ‘hardware–timed single point’ functionality of the system. The hardware–timed single point mode provides readily–controlled bufferless continuous hardware timing for data acquisition or signal generation purposes. Using this functionality a single reading supplying one data point was performed per pixel which resulted in a 16 data point long vector at single–type precision, 4 bytes, each time. The data of the 16×256 readings of the 4–row blocks was concatenated into a vector of 1×4096 dimensions which was the data set of the complete sensor frame per time slot. The size of a data frame containing single–type data points was 16 Kbyte. The data frames were then internally transferred from the high–priority synchronous real–time data acquisition process to the non–deterministic network process that sent it to the host computer asynchronously. The network process was qualified as non–deterministic because the TCP protocol generally does not guarantee the regular transfer and access to network resources within a strict margin error.

The pipelined continuous high–density data transfer on 16 analog output channels resulted in large data streams of 1.56 Mbyte/second (93.75Mbyte/min) at the maximal 40 µs per pixel, 10.2 ms per frame sampling speed. This amount of data was essential to be immediately saved for further offline data processing. The acquired signals were streamed into hierarchical measurement files using the National Instruments standard Technical Data

Management Streaming (TDMS) data format. The data frames of the 64×64–pixel ISA were important to be separated while reading the continuous data stream, therefore each received 16384 bytes generated a user event that recovered the data vectors from byte code and stored them as 1×4096–long channels. Depending on the length of the data acquisition the TDMS files could quickly reach or exceed the 10 000 channel amount.

In addition the described data acquisition process shows that the system is capable of monitoring arbitrary sections of the sensor array thus allowing flexible detection for the user. The pixel addresses need to be calculated in advance to achieve the desired smaller data coverage. The calculated pixel addresses then need to be listed and downloaded to the RT–target which delivers them to the chip device.

4.7. Data extraction

The extraction of the useful signal from the acquired raw measurement data was necessary for visualising the low–level difference signal originating from the ionic concentration fluctuations in the electrolyte on the top of the chip. The hierarchical data streaming into TDMS format was primarily followed by data analysis investigating only the response of a selected pixel to gain a general estimate of the quality and course of the data and measurement. The timing information, e.g. time slot of injection or liquid deposition, were possible to determine from the estimated results which were essential for the signal visualisation and analysis purposes.

Figure 4.12 presents the visualisation methodology of the detection of ionic transport signal and localised fluctuations in ionic concentrations over the 64×64–pixel ISFET array which was implemented in LabVIEW. The chosen TDMS file containing the measurement data was processed by a sub–routine performing cyclic readout by consecutively selecting the 1x4096 long channels and hence the data frames. A limit for the extent of the investigated data range was set and a reference data frame was chosen prior to the launch of the cyclic reading based on the results of the initially performed estimation. The reference frame was chosen manually and its index was determined so that its location in the data set preceded any event, e.g. injection, diffusion, that was aimed to be visualised. The relative signal of the ionic motion was then extracted as the difference between the raw reference signals. Therefore the reference frame was subtracted from each subsequent data frames until the limit of the prescribed range. The subtraction was followed by the

transfer of the difference data set to the appropriate LabVIEW chart or graph components to draw the curve of ionic signals or to showcase a 2D or 3D videos of the extracted data.

The developed method was analogous for 1, 2 or 3 dimensional data representations in terms of mechanism. Only the parameters of the algorithm needed to be adjusted to fit the different dimension requirements. Although the data could be demonstrated in all three dimensions it is important to note that the data extraction was in reality a two–dimensional approach. The ISFET sensor array measured the ionic concentration fluctuations *on the surface* of the chip. The 1 dimensional results were gained by considering the results of only specific pixels.

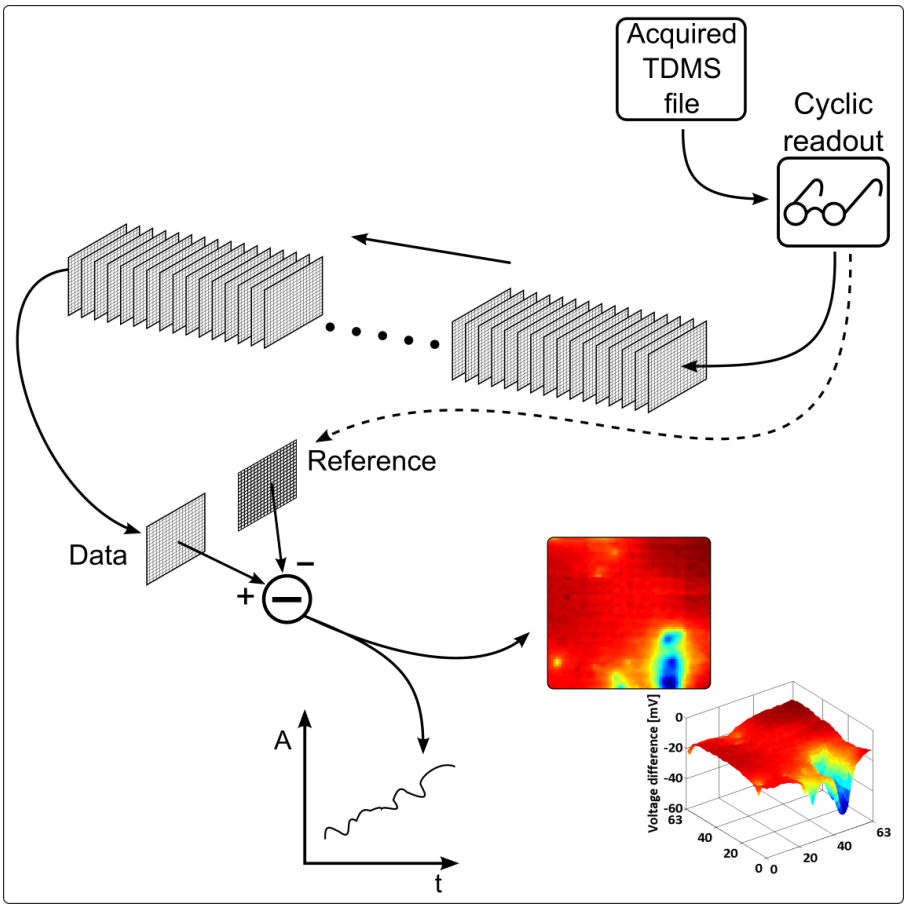

Figure 4.12 Description of the data extraction method for video and diagram class results

4.8. Summary

A 64×64–pixel ISFET sensor array was developed which was fabricated in the 0.35 µm four–metal CMOS process using HIT–Kit v3.70, both from the austriamicrosystems AG, in the MPW service of the Europractice. The fabrication was carried out by the Fraunhofer Institute for Integrated Circuits, Erlangen, Germany. The general design flow of on–chip microelectronic circuits was discussed demonstrating the cyclic design approach of CAD

systems from the schematic diagram to the laid–out end product. The multi–parameter considerations for flexible operations and the operation modes were introduced that were aimed to suit diverse measurement purposes. The architecture of the ISFET sensor array was discussed showing the interactions of the on–chip components. The complete physical chip layout was presented with dimension parameters and marked locations of the utilised design components as well as the interface board with the off–chip electronics. The development stages of the packaging and encapsulation procedure of the ISFET array device was presented showing the path of achieving a reliable and repeatable solution of encapsulation. The structure and operation of the real–time data acquisition system was shown and it was discussed that ~100 fps (40 µs per pixel, 10.2 ms per sensor array) hardware–timed data capturing rate was achieved. The method of data extraction was also investigated presenting the method of visualising the signals of ionic concentration fluctuations in 1, 2, 3 dimensions.

5. High sensitivity measurements using single pixels

ISFETs are electrochemical sensors that transform the signals of ion concentration fluctuations into voltage changes. Hence the expected fluctuations of the useful signals at the output of the ISFET pixels were expected to be low. The measurements of low level signals require complex considerations in terms of applied methods and environment. On the one hand it is important to separate the useful signal from the acquired raw data and on the other hand the level of noise often needs to be decreased to obtain a clear response signal. Therefore the ability of performing highly sensitive measurements detecting ultra–low level pH signals had to be confirmed. In addition it was essential to show whether the arising intrinsic noise of the ISFET devices affected the measured signal.

The demonstration of the ultra–low level pH detection was carried out using a cell based biological specimen that provided periodical oscillation in the extracellular pH. Furthermore in order to prevent the modulation effect of external noise including the electricity network, surrounding wireless networks and parasitic couplings the measurement setup for intrinsic noise was sealed off from its environment. The noise experiments were therefore conducted in a Faraday cage which was the echoless RF chamber of the University of Glasgow.

This chapter discusses at first the ionic sensitivity of the chip to protons and sodium ions. It is followed by the identification of internal noise sources and the required operation range. The measurement data of the noise experiments show that the measured noise demonstrated sensitivity to changes in bias voltage and pH. It is also shown that the surrounding instrumentation influenced the measured 1/f noise signal. In addition an RTS noise analogous H^+ flickering hypothesis is introduced correlating the electrochemical experimentation with the intrinsic noise of the ISFET devices. It is furthermore demonstrated that the ISFET array device was able to observe ultra–low level pH oscillations in the range of 0.022 pH using the slime mould biological exemplar. This low level pH responsiveness is imperative to date for ion–sensor devices fabricated in a sub–micron and unmodified CMOS process.

5.1. Ionic sensitivities

The sensor chip was characterised before the implemented measurement series to evaluate the sensitivity of the chip to H^+ and Na^+. The test solutions containing various

concentrations of either protons or sodium ions were produced in advance. The sodium ion containing substances were prepared by mixing NaCl and deionised (DI) water creating 10^{-4} M, 10^{-3} M, 10^{-2} M, 10^{-1} M and 1 M solutions. Substances with pH in the range of 1 to 13 were prepared to measure pH sensitivity. pH 1 and pH 13 were standard 0.1 M hydrochloric acid and 0.1 M sodium hydroxide solutions, respectively. pH 12 and pH 2 substances were produced by diluting the 0.1 M HCl and 0.1M NaOH solutions by DI water at rate of 1:10. pH 11 and pH 3 were made by further dilution of pH 12 and pH 2 using the same dilution rate. pH 10, pH 7 and pH 4 were commercial pH buffer solutions.

The pH and pNa sensitivity of the silicon nitride was tested by depositing the respective substances onto the surface of the packaged and encapsulated ISFET array chip. The sensitivity measurements were carried out in a predefined order to ensure the consistency of the measurement results. The pH solutions were deposited onto the silicon nitride surface and were left to equilibrate on average for 1.5 minutes and then the measurements were taken as indicated in Figure 5.1.

The equilibration time was slightly different in case of the pNa solutions where the resting time of the substances was on average 2 minutes. The chip surface and the polypropylene chamber, discussed in Section 4.5, were thoroughly washed with DI water between the depositions of each pH and pNa substance.

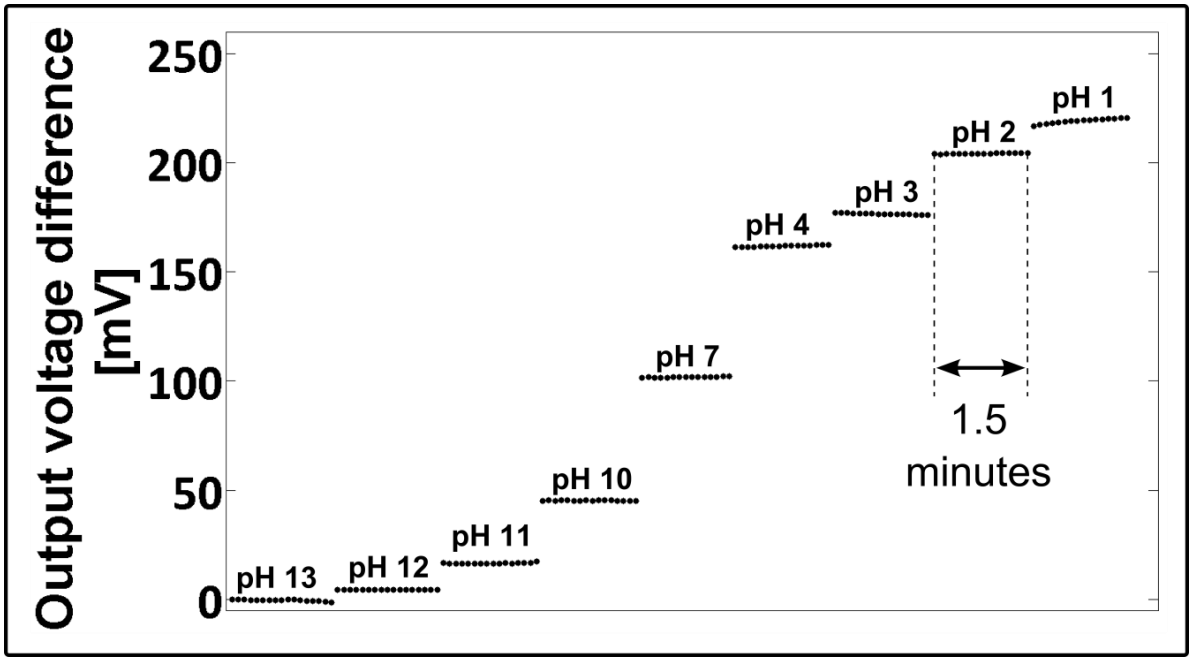

Figure 5.1 Differential voltage response data of the pH test measurements.

In case of pH solutions the substances were deposited in decreasing pH order, thus from

alkali towards acidic liquids. The pNa solutions were applied to the chip surface in increasing concentration sequence thus from 10^{-4} M NaCl towards 1 M NaCl. The data of the pH responses were evaluated for 10 pixels of the ISFET array that were spatially separated on the sensor array device. The respective measurement results were collected, averaged and plotted against pH and pNa levels. The results demonstrated approximately 20 mV/pH and 9 mV/pNa ionic sensitivities as displayed in Figure 5.2.

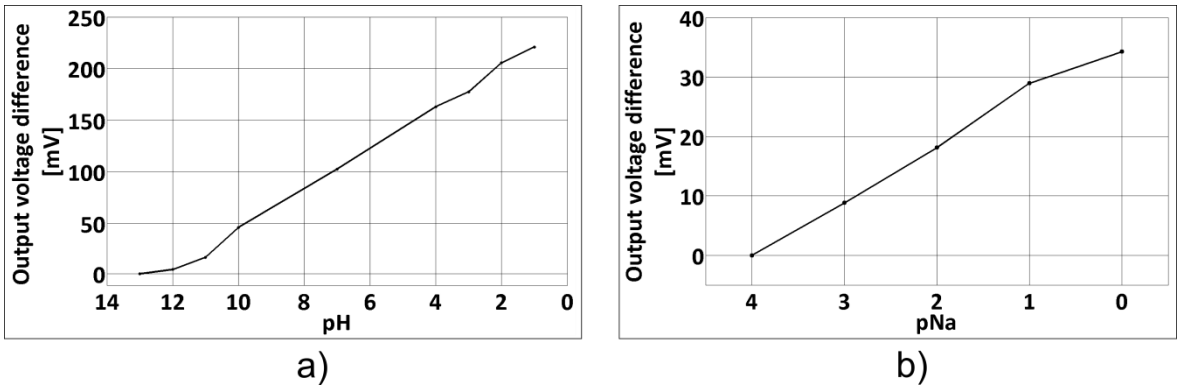

Figure 5.2 The charts show the sensitivities of the ISFET sensors to (a) protons and (b) sodium ions[1].

5.2. Sources of disturbances

The structural description of the noise measurement setup and interconnections are displayed in Figure 5.3. It is shown that the fluctuating output voltage of a pixel is measured in the chamber using an NI PXI–4461 dynamic signal analyser (DSA) card while transistors were under controlled biasing. Due to the anechoic RF test chamber the setup was sealed against external noises although it did not provide protection against internal sources. The measurement setup consisted of two Agilent E3631A Triple Output Power Supplies, one Hewlett–Packard 3458A digital multimeter, one NI PXI–1073 chassis with the discussed measurement card and one laptop of Sony Vaio type. The used instruments needed to be in the $x \leq 2$ metres proximity of the devices under test because of the structure of the RF chamber and available hardware resources.

It was therefore initially expected that the instruments contribute additional noise to the measured 1/f signal as shown in Figure 5.4. Four main internal noise sources were identified and their combination was assumed to have influenced the 1/f signal as displayed in Figure 5.4:

[1] Data extracted by Dr. Mark D. Symes and reproduced with permission.

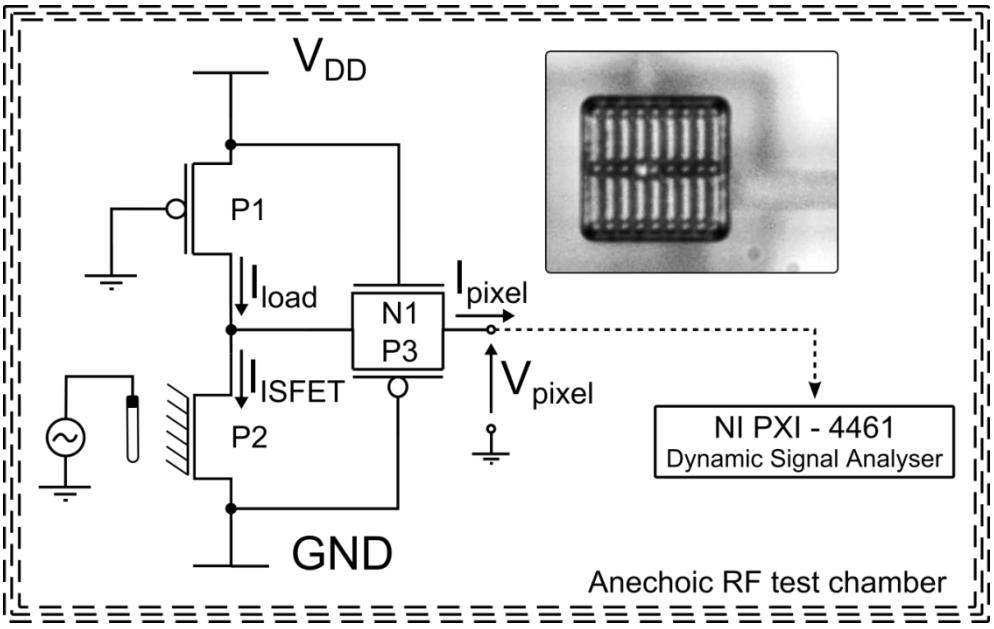

Figure 5.3 Structural description of the measurement setup used for 1/f noise experiments.

- Laptop computer
- DC power supply
- Common ground point
- Interconnections

As shown in Figure 5.4 the acquired noise signal contained frequency components that followed the displayed pattern which in turn indicated the presence of a wide range noise source. The investigation was carried out by turning on only specific instruments one by one to prevent the simultaneous noise contribution of multiple devices. The laptop computer and the DSA card as well as its PXI–1073 chassis were operated continuously to perform the data acquisition.

The spectral components of the noise of the Agilent Power Supplies were measured by setting the output voltage to 3.3 V on Output 1 (0 to +6 V range) and connecting it to the input of the DSA card. The frequency components of the ground signal were measured by connecting the common ground point and the input of the DSA card. The measurements were carried out using AC coupling and the applied shielded coaxial cable reduced the interaction of the measured signal with its environment.

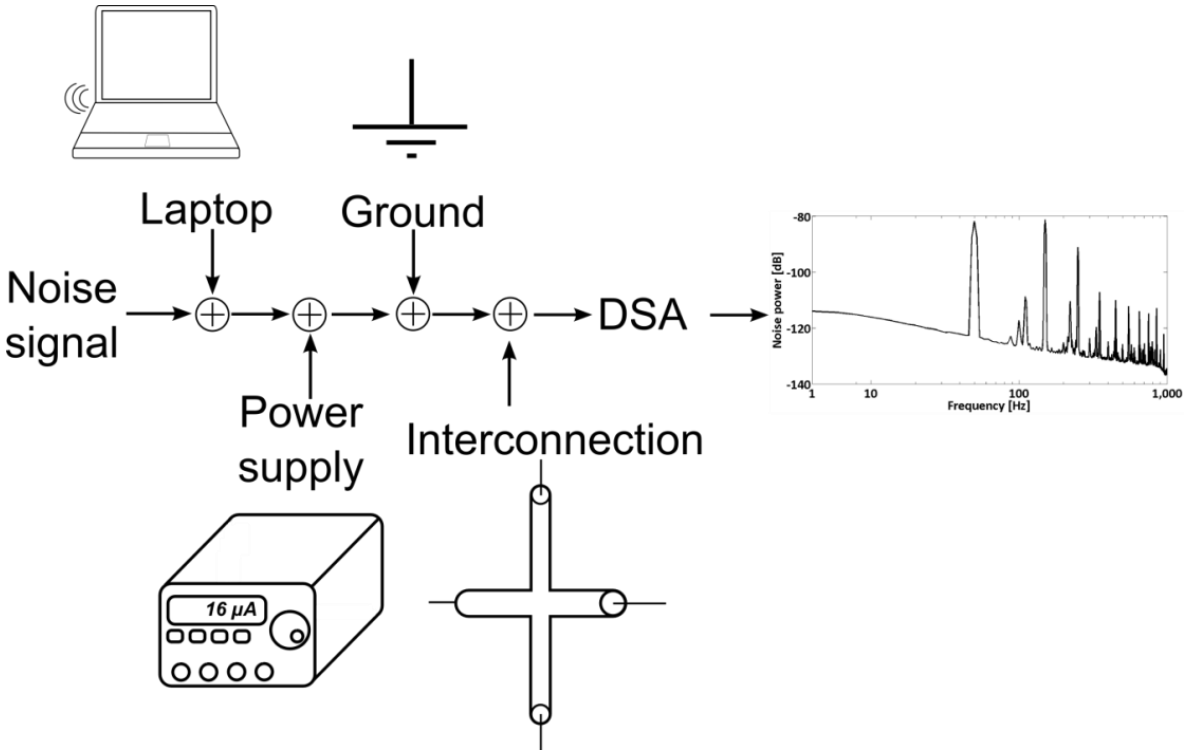

Figure 5.4 Internal noise sources in the RF test chamber.

The measured results are shown for the 10 Hz to 1 kHz span in logarithmic–logarithmic representation in Figure 5.5. It is apparent from the result of Figure 5.5a that the measured noise signal of the DC power supply decreased more steeply than 1/f. A signal drop of $1/f^{1.4}$ was observed using Matlab. It is demonstrated that the amplitude of the noise of Figure 5.5 stayed securely below –69 dB ≅ 355 µV RMS which complies with the < 0.35 mV RMS expected noise level specified by the manufacturer. The noise on the ground signal dropped at an even higher slope rate shown in Figure 5.5b. The noise of the common ground point followed $1/f^2$ characteristics. The results show that the noise of the supplied power signal and ground potential dominantly contained low frequency components. The noise remained under the –100 dB ($10^{-\frac{100}{20}} = 10$ µV) level above ~500 Hz and 40 Hz in case of the power potential and ground, respectively. The particular source of the frequency domain spikes shown in Figure 5.4 was suspected to be the AC power unit of the laptop computer. The AC power unit containing a switching mode power supply (SMPS) is a potential origin of electromagnetic interference (EMI) which could be responsible for the wide range noise experienced in the acquired signals. The laptop computer needed to be in the same room with the PXI–1073 chassis because the devices were connected with an approximately 2 metres long shielded cable using a PXI–ExpressCard8360 interface.

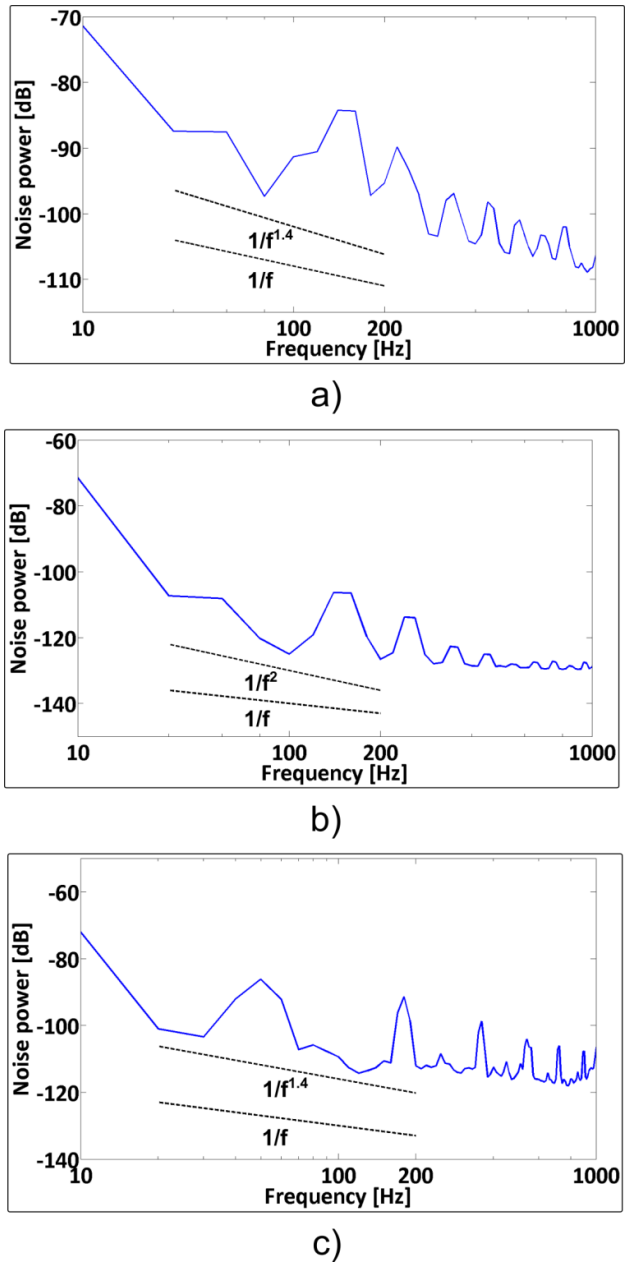

Figure 5.5 Measured noise contribution of (a) the DC power supply and (b) the common ground point (c) the laptop computer in logarithmic–logarithmic format. An unshielded cable was used to act as an antenna receiving the surrounding electromagnetic disturbances for the measurement of (c). Results are in dBV.

The measurement instruments could not be placed outside the RF chamber either because the closure its thick door was essential to provide sealing against external noise that in turn would have broken the electric cables. The laptop computer was necessarily operated from the built–in AC supply due to its dysfunctional power electronics and battery.

The noise contribution of the laptop computer was measured by connecting a nearly 10 cm long unshielded piece of cable to the DSA card with a shielded crocodile–clips coaxial cable. The unshielded cable acted as an antenna receiving the surrounding electromagnetic waves. This observation was important because on the one hand the short unshielded

cables were used as bridges between PCB board with semiconductor chip and the dynamic signal analyser. Thus each connected unshielded cable was expected to receive the same amount of disturbance. On the other hand the laptop computer could be identified as the dominant source of the internal noise sources as shown in Figure 5.5c. The spikes of Figure 5.4 appeared in the acquired signal while only the computer and the DSA card were in operation, other instruments were switched off. It is visible in Figure 5.5c that the overall noise performance between 10 and 200 Hz demonstrated a nearly $1/f^{1.4}$ fall and the noise level securely remained under the –80 dB thus 100 µV level.

The discussed internal noise sources were identified prior to the measurement and their contribution was considered. Sections 5.4, 5.5 demonstrate that the added noise did not completely compromise the 1/f signals. Although the presence of internal noise sources and intrinsic noise is shown, neither of them could reach a voltage level that could significantly influence the quality of ionic imaging as discussed in Chapter 6.

5.3. Pixel operation range

The operation range for the investigated ISFET pixels was determined prior to the measurements. The operation point was expected to be shifted because of the trapped charge in the nitride and oxide layers. Hence the initial experiments to identify the operation ranges of the ISFET pixels were carried out over a broad bias voltage range. The operation point of the ISFET transistor was only measureable with consideration of the additional transistors due to the pixel structure shown in Figure 5.6a. Figure 5.6a displays that the I_{load} load current of the pixel is provided by the P1 PMOS transistor which therefore acts as an in–pixel current source.

The flicker noise analysis was conceived by using the minimum number of instruments and wires to introduce the least possible amount of added noise to the 1/f signal. Corresponding to the intention of simplifying the setup, a $V_{row} = 0\,\mathrm{V}$ bias voltage was applied by connecting the gate of P1 to the ground terminal which saved the usage of one additional DC power supply. The 0 V bias voltage was measured to have resulted in a higher $I_{load} = 53 - 54\,\mu\mathrm{A}$ load current. The chip with the pixels under test was placed into a PGA–100 open cavity ceramic chip carrier that was attached to a dedicated PCB board. The bonding and encapsulation method used is described in Section 4.5. The gate voltage of the ISFET transistor was controlled using a BASi RE–6 reference electrode that was

placed into the respective pH solutions. Specific values of I_{pixel} pixel output current were recorded by systematically changing the bias voltage at the input terminal of the reference electrode. As a consequence of the structure of the pixel the results were considered inversely compared to conventional I_D/V_{DS} operation point evaluations. The measured I_{pixel} reached its maximum value if the P2 p–type ISFET transistor was switched off because under these circumstances the P2 behaved as a large resistance. Similarly, I_{pixel} was considered to be at its minimum value if P2 was switched on because the flowing I_{ISFET} reduced the pixel output current with respect to the equation $I_{pixel} = I_{load} - I_{ISFET}$.

The current response of an ISFET pixel is displayed in Figure 5.6b showing the subthreshold and linear operation regions. The presented values were measured using a Hewlett–Packard 3458A digital multimeter.

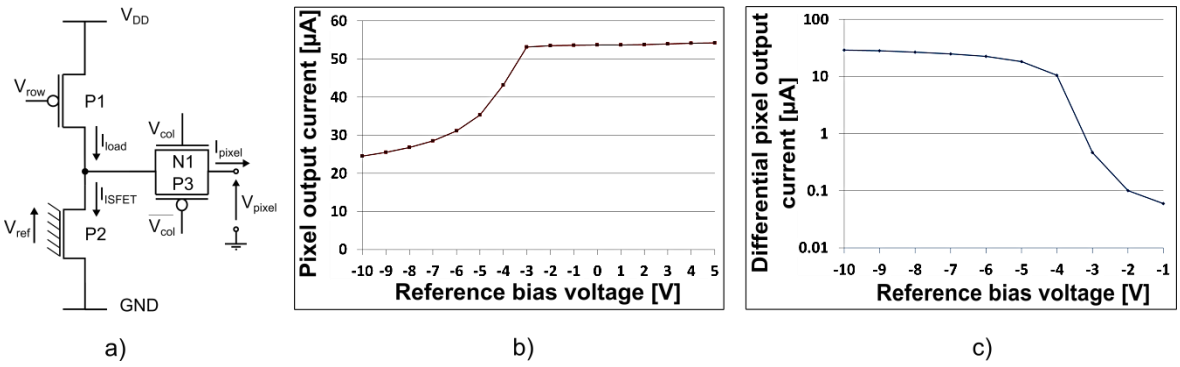

Figure 5.6 The image shows (a) the pixel structure, (b) current output of an ISFET pixel and (c) the differential pixel output current relative to the data of 0 V.

A reference voltage sequence from +5 V to –10 V with 1 V steps was applied to the reference electrode and thus indirectly to the gate of the ISFET transistor. As demonstrated in Figure 5.6b, the ISFET remained in the subthreshold regime can be attributed to the [–3 V; +5 V] interval. In this region the decrease in the pixel output current value was limited. The linear operation region of the pixel was considered over the [–3V; –5V] range where the measured I_{pixel} dropped by slightly more than 20 µA indicating the activity of the ISFET transistor. The range below –5 V was considered as the inversion operation region since the slope of the gradient in the output current value turned into a decreasing trend. Figure 5.6c demonstrates a differential current data representation derived from Figure 5.6b where the data interval of [0 V; –10 V] is represented relative to the data of 0V. The data is shown in logarithmic scale in order to visualise the current change in the subthreshold region as well.

5.4. Bias dependence

The measured noise of the ISFET pixels was found to be sensitive to the applied bias voltage. The varying noise response of one ISFET pixel is shown in Figure 5.7 using logarithmic–linear (Figure 5.7a) and logarithmic–logarithmic (Figure 5.7b) data scaling over the 4–1 kHz frequency span.

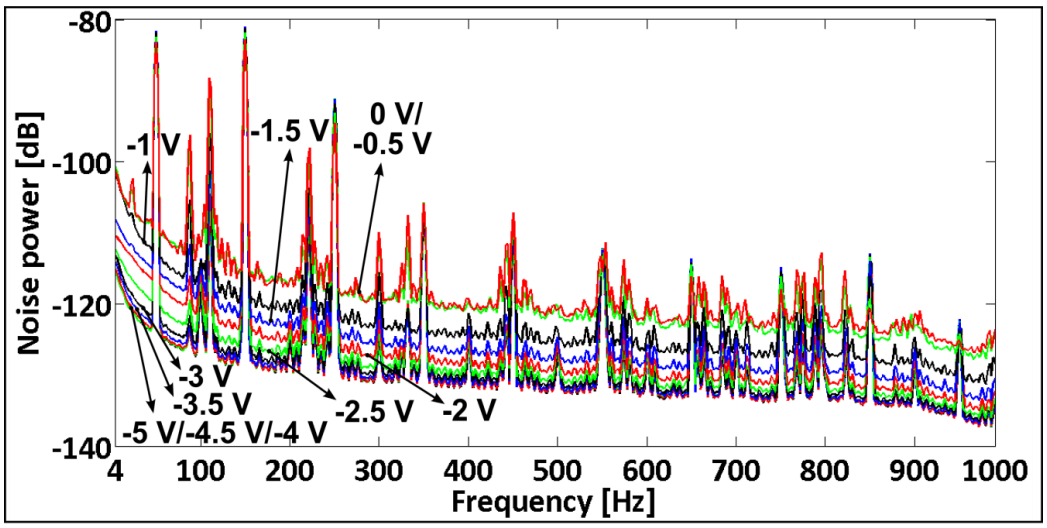

a)

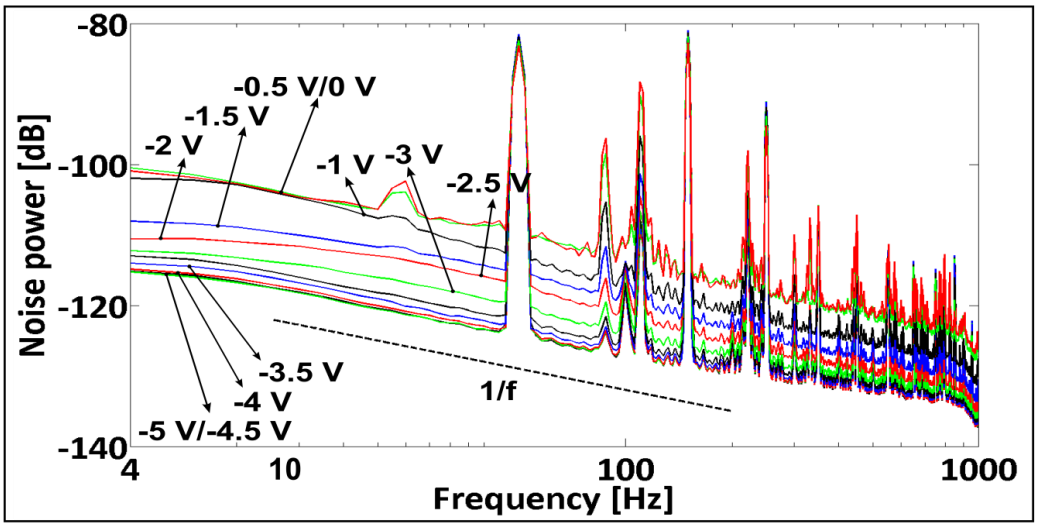

b)

Figure 5.7 The bias dependence of the 1/f noise in an ISFET pixel is shown in (a) a logarithmic–linear and (b) in logarithmic–logarithmic scale. Results are in dBV.

The previously discussed broad range noise superimposed on the 1/f signals is also presented. An estimation on the quality of the noise signals is presented in Figure 5.7b, it is demonstrated that the course of the noise signal shows good correlation with the fitted 1/f

function on the 10–200 Hz range. The results show that, corresponding to Figures 5.6b and c, the bias voltages were applied between 0 V and –5 V with –0.5 V steps starting from 0 V. The data demonstrated the expected separation between noise levels throughout the complete investigated frequency range. It is noticeable from the results of Figure 5.7 that the 1/f–type data traces appear between 4 and 200 Hz and the noise is subject to a characteristically decreasing trend at frequencies over 200 Hz.The measured noise voltage results showed separation from –1 V DC bias and the separation trend continued until approximately –3.5 V DC. As a consequence of the pixel structure the *effect* of the activity of the ISFET transistor could be measured. The noise contribution of all four in–pixel transistors was considered since CMOS transistors are generally subject to arising intrinsic noise phenomenon, e.g. 1/f noise. The P1, P3 and N1 transistors in Figure 5.6a were constant noise sources because they received fixed bias voltages during the operation. The ISFET transistor could therefore influence the overall measureable noise of the pixel circuit. The opening of the ISFET sensor altered the output current of the pixel circuit which in turn was followed by the measureable noise level. Thus the changes in the noise level of the pixel dominantly show bias dependency since the characteristics of the noise traces remain with DC value shift.

The noise responses focussed on the 1/f part between 4 and 200 Hz frequencies are shown in Figure 5.8 in logarithmic–logarithmic scale. Figure 5.8 demonstrates that the acquired noise data are in good correlation with the 1/f characteristics over the 4–200 Hz range.

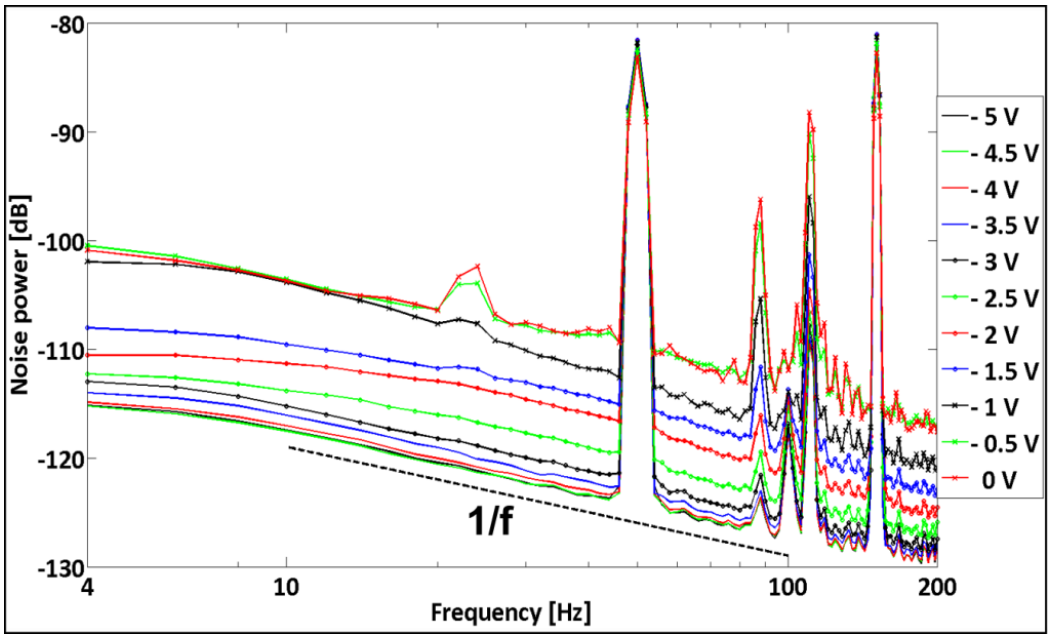

Figure 5.8 Bias dependence of the 1/f noise in an ISFET pixel in the 4–200 Hz range. The results are shown in logarithmic–logarithmic scale. Results are in dBV.

The noise value differences extracted from the data of Figure 5.7 are shown in Figure 5.9 as a function of bias voltage at given frequencies. Each acquired data trace was sampled at the frequencies of 10, 20, 70, 170, 390, 520, 730 and 990 Hz. It displays that the most difference occurred at the lower frequency slots thus in the region of 1/f noise which also corresponds to Figure 5.7. The data traces of 10 Hz and 20 Hz show an approximate 13.5 dB difference in the noise power over the [–1 V; –5V] bias range that corresponds to ~8 µV rms. Data traces of higher frequencies, e.g. 990 Hz, demonstrate less sensitivity to the bias change. The data trace of 10 Hz allows the assumption that another noise source, apart from 1/f noise and thermal noise, could be also present since the noise curves were similar demonstrating DC shift. A current dependent noise type was expected which acted together with the additional intrinsic noise species. Thus it was concluded that noise species, e.g shot noise and number fluctuation, could contribute to the overall measured noise signal of the ISFET pixel.

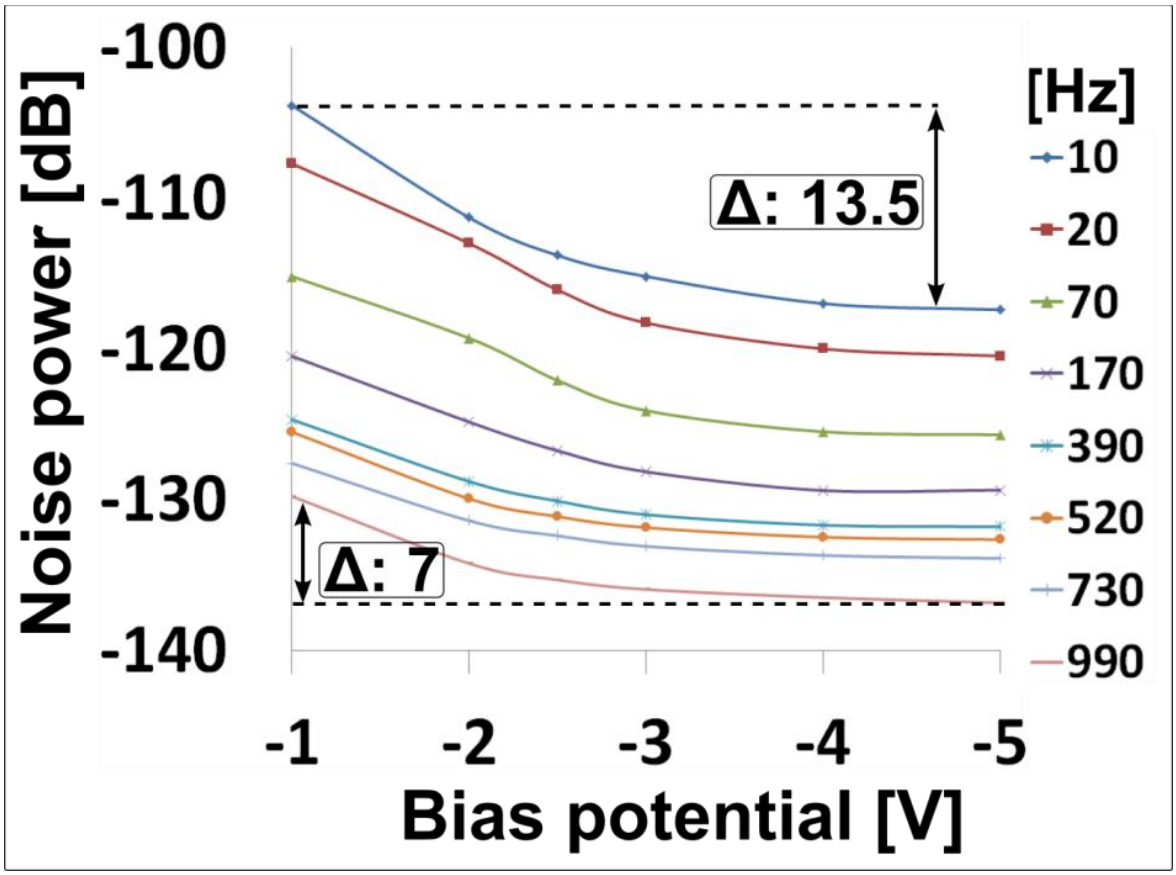

Figure 5.9 (a) 1/f noise with slightly different falls were measured at the separate bias voltage levels (b) demonstrates the similar differences in noise values at given bias voltages and frequencies. Results in dBV.

5.5. pH dependence

The measured noise of the ISFET pixels was found to demonstrate pH sensitivity while depositing different electrolytes into the container on the ceramic chip carrier. Standard solutions of 0.1 M sodium hydroxide, pH 13, and 0.1 M hydrogen chloride, pH 1, were applied as electrolyte. The pH of the aqueous solutions was increased and decreased by 1:10 dilutions with deionised water (DI water). The pH 11 and pH 3 values were produced by diluting the pH 13 and pH 1 solutions twice. The dilutions were carried out by mixing 2.5 ml of the substance with 22.5 ml DI water in a 25 ml glass vial. The surface of the silicon nitride was thoroughly washed by DI water prior to the deposition of the chemical substances to avoid any remaining liquids influencing the data acquisition.

The pH sensitivity of the recorded noise is presented in Figure 5.10a and b in the range of 4 Hz to 1000 Hz under –3 V DC bias conditions. Similar to the bias dependent results it was observable that the 1/f noise appeared over the 4 Hz–200 Hz range. Figure 5.10b demonstrates correlation to the fitted 1/f function over the 4–200 Hz frequency range. The acquired data shows that the noise signal showed pH sensitivity and remained under the –110 dB limit. The measured pH sensitive 1/f noise responses of the ISFET pixels were also experienced to demonstrate sensitivity to the strength of the liquids. The responses of pH 1 and pH 13 were pronounced and separated however the responses of pH 3 and pH 11 would not fit a linear pH sensitivity function. Thus the 1/f noise signals of pH 3 and pH 11 were considerably closer to each other as it would be expected assuming linear pH sensitivity. The trace of the DI water diluted version of pH 7 was not measureable because of its very low 10^{-7} M molarity. Several attempts were made to produce the required pH 3, pH 7 and pH 11 solutions by mixing a suitable amount of 10^{-1} M NaOH and 10^{-1} M HCl. The mixing was also attempted with larger volume substances. Due to the logarithmic nature of pH and hence its titration curve the setting of the desired pH values proved to be difficult, thus only diluted substances were used during the experiments.

The pH sensitivity of the 1/f noise is shown in Figure 5.11 for the 4–200 Hz range. Figure 5.11 demonstrates that despite the sensitivity to the strength of the liquids the noise responses adequately separate at the different pH levels. The results of Figure 5.11 show that the noise power difference between the pH 1 and pH 13 was 5.7 dB at 10 Hz frequency and 6.9 dB at 30 Hz frequency which remained relatively stable for the whole frequency span.

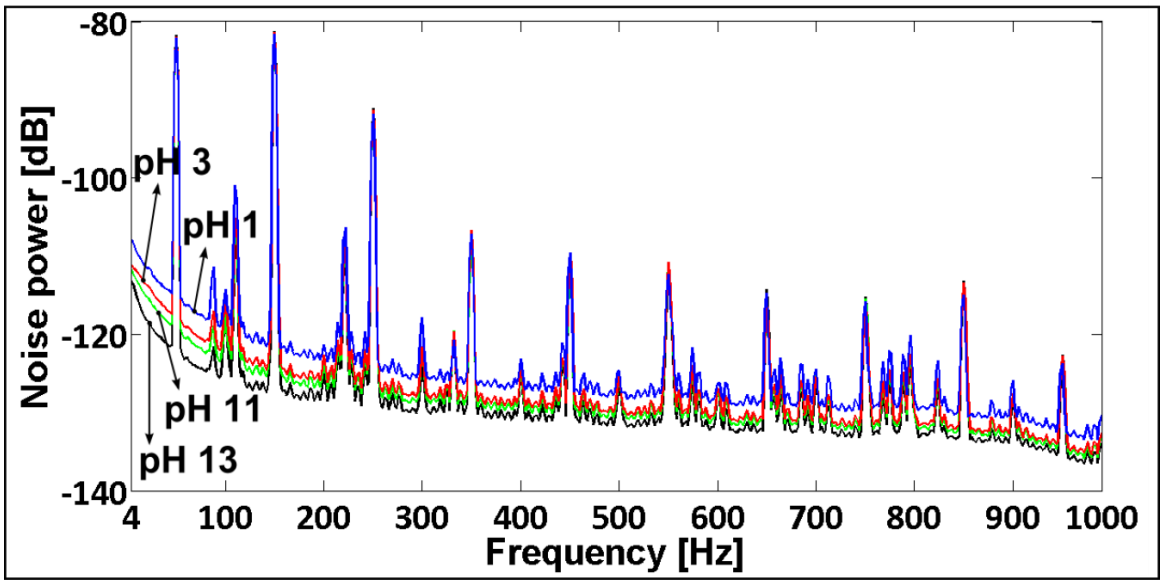

a)

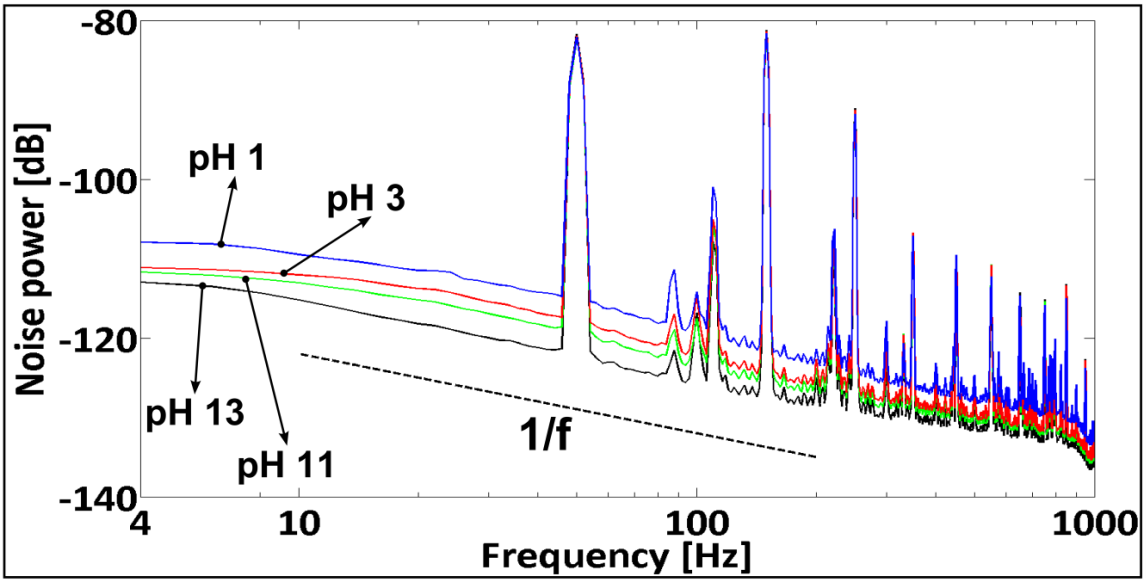

b)

Figure 5.10 The pH sensitivity of the measured flicker noise is presented in (a) logarithmic–linear and (b) logarithmic–logarithmic representations. Results are in dBV.

The demonstrated results of Figure 5.10b were sampled at 10 Hz, 20 Hz, 70Hz, 170 Hz, 390 Hz, 520 Hz, 730 Hz and 990 Hz frequencies to show the characteristic of the measured noise. Figure 5.12 shows that the characteristics of the data at the separate frequencies remained similar although the differences between extremes of the noise traces showed decrease at higher frequencies. The most significant value differences, e.g. 6.8 dB ~ 3 µV at 10 Hz were measured in the frequency region of the 1/f noise. It furthermore seemed

that the noise was pH independent between pH 1 and pH 13, this anomaly was attributed to the strengths of the respective liquids.

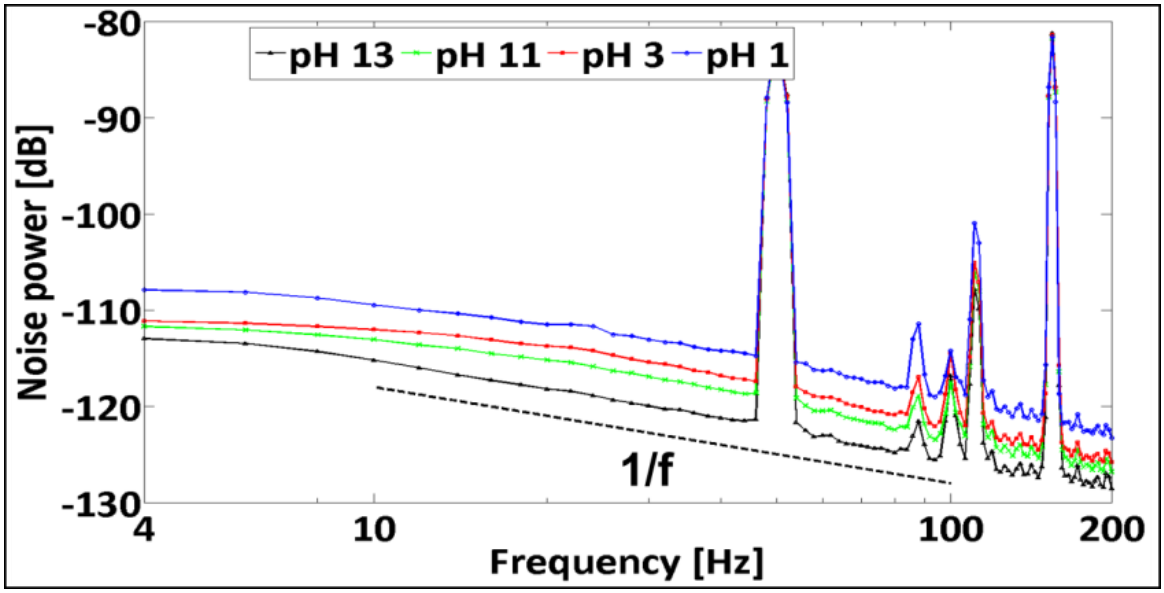

Figure 5.11 The pH sensitivity of the 1/f noise in an ISFET pixel is shown for the 4–200 Hz range. The results are shown in logarithmic–logarithmic scale. Results are in dBV.

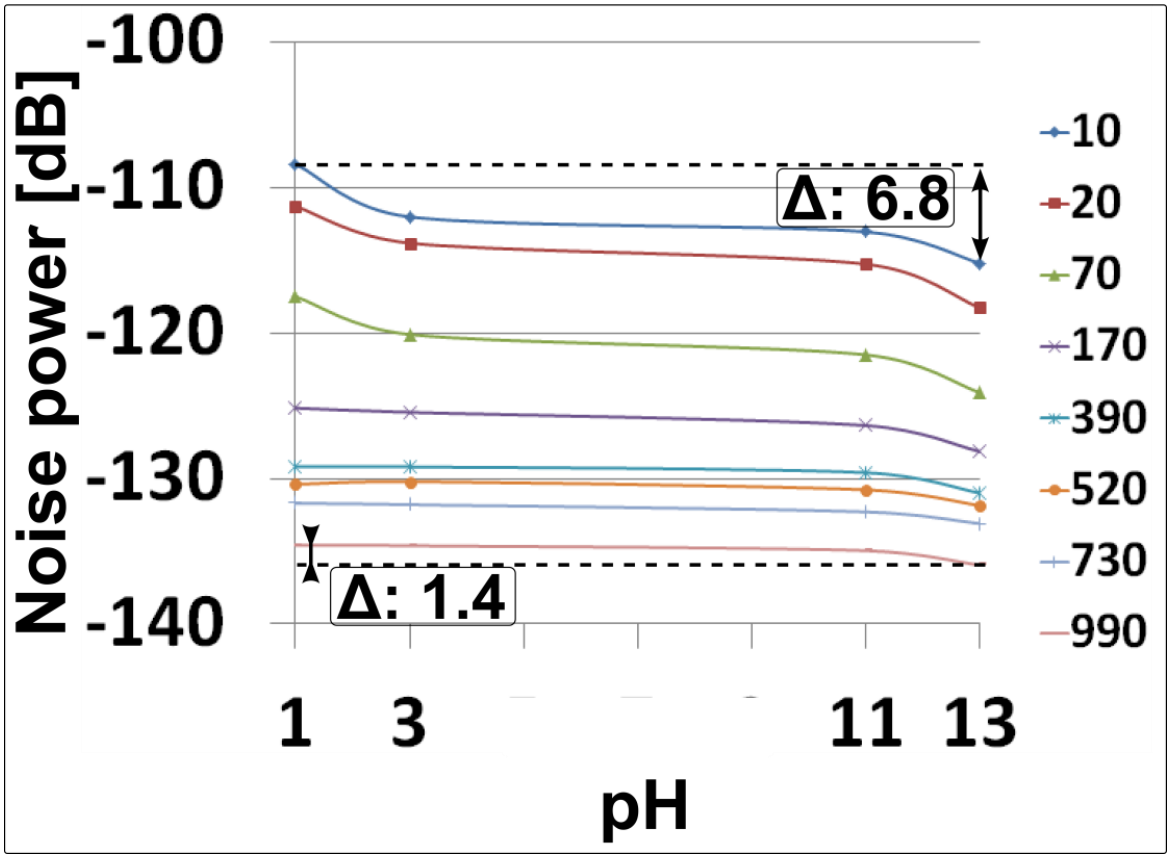

Figure 5.12 The image shows the pH dependent 1/f noise traces at selected frequencies. Results are in dBV.

5.6. H^+ flickering hypothesis

The demonstrated ability of influencing the level of the measured 1/f noise by changing the pH allows the hypothetical extension of the theory on its physical origin in analogy with the RTS phenomenon. It is assumed that a flickering effect occurs in the electrolyte on the surface of the ion–sensitive layer at a settled bias voltage and ionic concentration. At a stable pH level the fluctuations occur by binding H^+ and OH^- to the surface of the silicon nitride or dissolving it from the passivation layer into the electrolyte. The trapping and detrapping of H^+ and OH^- ions can therefore introduce a continuous and random voltage fluctuation across the double layer that develops at the interface of the nitride and electrolyte. This voltage fluctuation is then capacitively transferred to the transistor gate through intermediate vias and metal layers, hence it can affect the operation point of the device. As a consequence the flickering phenomena of the hydrogen and hydroxide ions can impose a direct effect on the transistor gate due to the capacitive coupling. It therefore can contribute to the developing fluctuation of the drain current across the channel and thus to the 1/f noise as well. It is discussed in Section 3.2.5 that the pH of the electrolyte and the drain current of the ISFET sensors are correlated substituting Equation (3.41) into Equation (3.39). It is therefore concluded that the continuous binding and de–binding of ions at the ion sensitive surface can influence the intrinsic noise of the sensors according to the H^+ flickering hypothesis.

The bias dependence of 1/f noise for small bias changes was reported by Nemirovsky [119] for 0.18 μm MOSFET devices. The transistors were characterised in the saturation operation region for 1.0 V, 1.3 V, 1.8 V gate voltages. Based on these results the it is expected that the small bias changes caused by the chemical reactions contribute to the overall 1/f noise for example in a similar form of the RTS noise.

The 64×64–pixel ISFET sensor array chip was surrounded by a MET4 ring that was in physical contact with the passivation layer. The metal ring was connected to an I/O pad in the padring through a buffer connected amplifier that limited the chances for experiments. The hypothesis of hydration dependent 1/f noise is planned to be confirmed as proof–of–concept using the second version of the 64×64–pixel ISFET array chip where the MET4 ring and the I/O pad are in direct connections. It enables the comparison of the arising 1/f noise spectra while the nitride is dry and hydrated by solutions with various pH levels.

5.7. Slime mould

The biological applicability of semiconductor based chips primarily depends on the materials used and their long and short term effects on the cultured biological specimens involved. The diffusion, solvation or outgassing of deposited or surrounding materials, e.g. not properly hardened encapsulants, might lead to fatal outcomes for cell–based living tissues. Therefore the appropriate selection of materials is important when a chip surface is brought into contact with living samples. The surfaces of semiconductor chips fabricated in an unmodified CMOS process are mostly suitable for integration in biological applications. On the one hand the silicon nitride passivation layer should not contaminate cultured biological systems and on the other hand the ion sensitive passivation is responsive to Na^+ and K^+. In human cell based applications there is an ion pumping mechanism, i.e. Na^+ and K^+ transport across the cell membrane. It affects the Si_3N_4, although the effects of the transport of individual ionic species cannot be probed due to the multiple ion sensitivity. Thus for human cells the aggregate effect of the total ionic transport is measureable using the factory default silicon nitride as the ion sensitive layer.

The slime mould, shown in Figure 5.13, was selected for analysis to demonstrate the ability of detecting low–level ionic activity and to tackle the concerns of the multiple ionic sensitivity. The slime mould, which is a large single–cellular and multi–nuclear organism, was a suitable choice because the living cell demonstrates a naturally synchronised and periodic activity. The pattern of changing the interior state in every 150–180 seconds was expected to be easily recognisable from the measurement results. Furthermore its activity occurs as a result of an intracellular oscillation in the concentration of Ca^{2+} which induces an extracellular variation in pH. Hence the slime mould is applicable with ISFET technology because it initiates extracellular pH fluctuations and extracellular ionic contributions other than protons have not been reported to date. The 64×64–pixel ISFET array chip was, therefore, used together with the slime mould and it was shown that the device was capable of observing a part of a complex cell culture in real–time.

The Physarum Polycephalum slime mould is a single cell organism that due to a lack of multiple connecting and interacting cells cannot be considered as a tissue. The single–cellular multi–nuclear characteristic ensures that the slime mould can demonstrate sufficient intelligence to react to external impact and recover from physical damage. In addition a slime mould is able to identify the best food source among multiple ones and can organise a coordinated flow of movements towards the target. The intracellular [Ca^{2+}]

fluctuations trigger the internal actin–myosin contraction and relaxation activity. This physiological activity is similar the one known in muscle tissues, e.g. peristaltic movements, because the observable synchronised activity spreads as propagated waves. Therefore the local thicknesses of the amoeba–shaped slime mould also periodically changes in correlation with the intracellular variation of the Ca^{2+} concentration.

The dynamic self–organisation of this primitive biosystem is based on a synchronous flow of movements that is interrupted if a part of the slime mould cell is exposed to environmental stimuli. As a consequence of the stimulation, e.g. finding food, exposure to light or cutting out a part of the cell, the localised part becomes desynchronised in comparison to the other parts of the cell. The slime mould then requires time to deliver a response, e.g. moving towards the food, escape from the light or start reintegration, which is followed by the recovery of the synchronised oscillatory behaviour. The utilised slime mould was cultured at the University of Glasgow in a laboratory environment. The growth of the slime mould was dependent on the humidity and therefore a moist environment was continuously maintained. The culturing of the cell was performed in Petri–dishes at ambient temperature that were placed into a sealable box to provide protection from light. The slime mould was nourished by commercial oat flakes during its culturing.

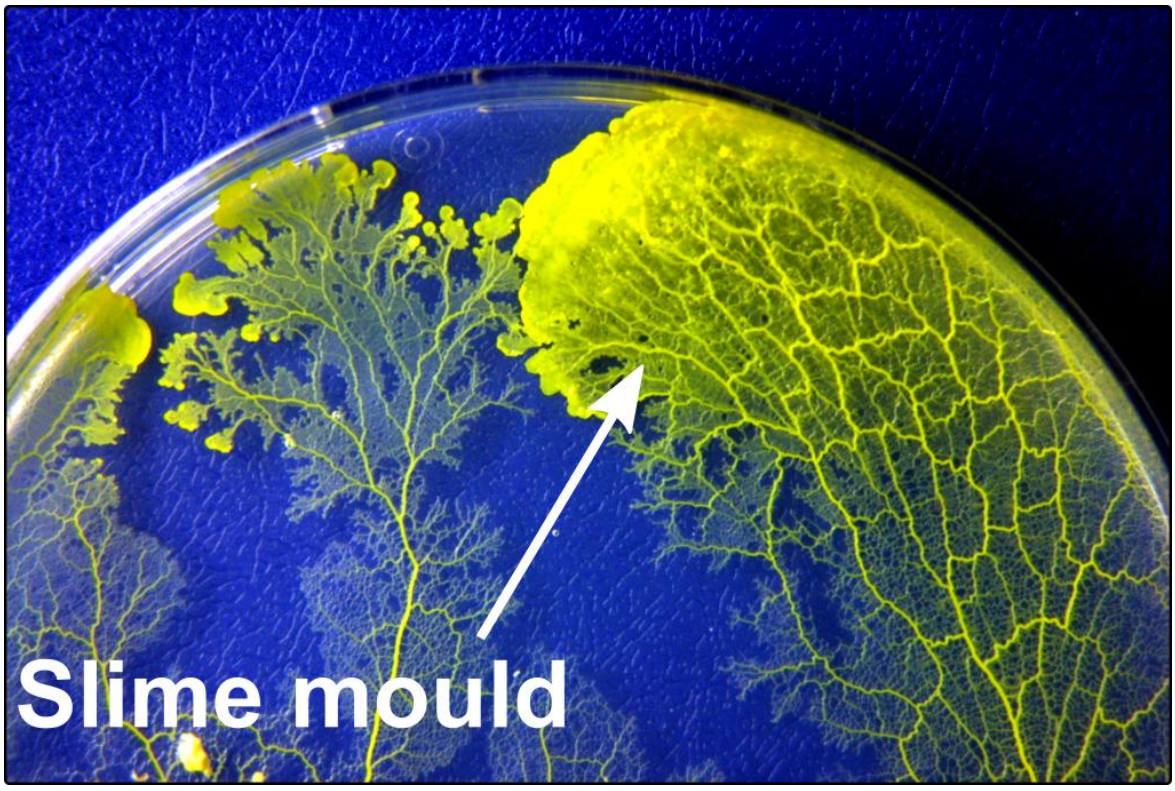

Figure 5.13 A Physarum Polycephalum slime mould growing on 1.5% agar gel.

Reported slime mould investigations involved the application of methods with invasive technique or cell freezing that were hazardous in terms of the health of the organism. The application of the 64×64–pixel ISFET sensor chip was a significant achievement because it enabled the in–situ analysis of the extracellular pH oscillations of the living slime mould cell without the risk of damaging the prepared sample.

The components of the measurement setup to detect the activity of the slime mould is shown in Figure 5.14a. The slime mould and agar gel were prepared in Petri–dishes in advance prior to the measurements. The cell was nourished once a day and it quickly grew around the glass container. It usually took 1.5–2 days culturing time to reach that extent. Epotek OE–145 epoxy was used for the chip encapsulation and a 15 ml Pyrex polypropylene centrifuge tube was fitted onto the ceramic chip carrier around the ISFET array chip. As demonstrated in Figure 5.14b, slime mould pieces were cut from the Petri–dish and deposited onto the surface of the silicon nitride. Before each measurement an agar gel disk was formed with a hole in its middle and placed into the polypropylene chamber on the top of the cell. The purpose of the agar gel was to keep the moist environment of the slime mould and the hole provided the cell access to the fresh air. Additional pieces of slime mould were cut and placed onto the already deposited one until the form shown in Figure 5.14b was achieved. As the last step of the preparations a BASi RE–6 reference electrode was brought into contact with the slime mould on the top of the agar gel. It was necessary to place the reference electrode onto the agar because its placement in the agar disk hole above the ISFET array would have blocked the air for the slime mould. The preparation of the measurements were finished by leaving the deposited slime mould for at least 30 minutes on the chip and agar surface to reintegrate into one single cell and to resume its synchronous biochemical oscillations.

Several 20 minutes–long data sets were acquired of the activity of the slime mould using the described measurement setup. Considering the temporal length and expected very slow changes in the extracellular pH the data acquisition rate was reduced from the maximum to 400 µs per pixel, 102.4 ms per sensor frame. This rate corresponded to an approximate 10 frame per second sampling speed. The initial expectations were to detect the pixel output voltage signal variations induced by the pH fluctuations. Amplitudes as low as 2–5 mV peak–to–peak and oscillation period of 150–180 seconds were expected. It was also assumed that any signal would appear in the 0.1–0.2 pH difference range. The signals which were extracted from the raw data set are shown in Figure 5.15a.

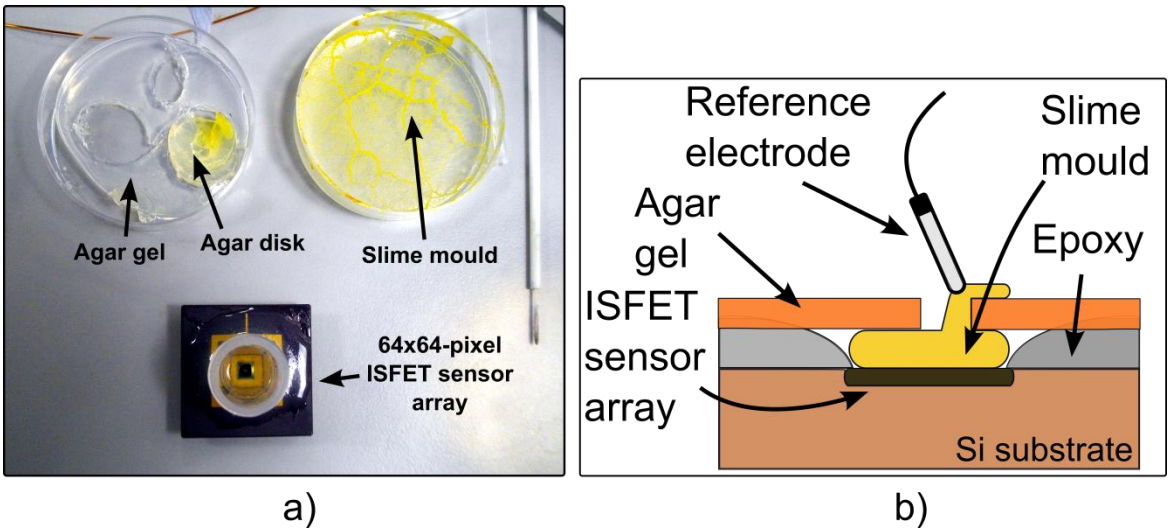

Figure 5.14 (a) shows the components of the measurement setup and (b) demonstrates a structural description of the measurement technique.

Figure 5.15a displays the extracted 20 minutes long data traces of 5 pixels which were selected from the four corners and one pixel from the middle of the sensor array. The results, shown in Figure 5.15a, demonstrate the expected periodic behaviour which was in correlation with the expectations. Thus the periodic response was attributed to the induced extracellular pH oscillations of the slime mould. The slime mould is acting in a chemically neutral environment hence the local pH oscillated around pH 7. The displayed data from 5 of the pixels shows similar characteristics which agrees with the size of the ISFET array chip to the prepared slime mould.

Although the ISFET chip detected the activity of distant pieces of the slime mould, the monitored area was small in comparison with the size of the cell therefore the recorded waves were consistent. The demonstration of propagation waves across the complete cell would have required multiple chips and an extended measurement setup. The data of the pixel in the middle of the ISFET array selected for analysis is shown in Figure 5.15b. The continuous oscillation showed stable period times in the range of 150 s ± 10 s. The peak–to–peak amplitudes of the pixel output voltage signal were in the approximate interval of 450 µV ± 70 µV. In the data trace in Figure 5.15b ripples were observed on the periodic signal which repeated at rate of nearly 10 s ± 2s. The origin of these ripples could not be reliably verified to date.

The observed 450 µV ± 70 µV peak–to–peak amplitude range indicates that the pH resolution of the system was better than 0.022 pH as described in Equation (3.44). This result is to be compared with the recent DNA sequencer chip [74] where 0.02 pH unit was

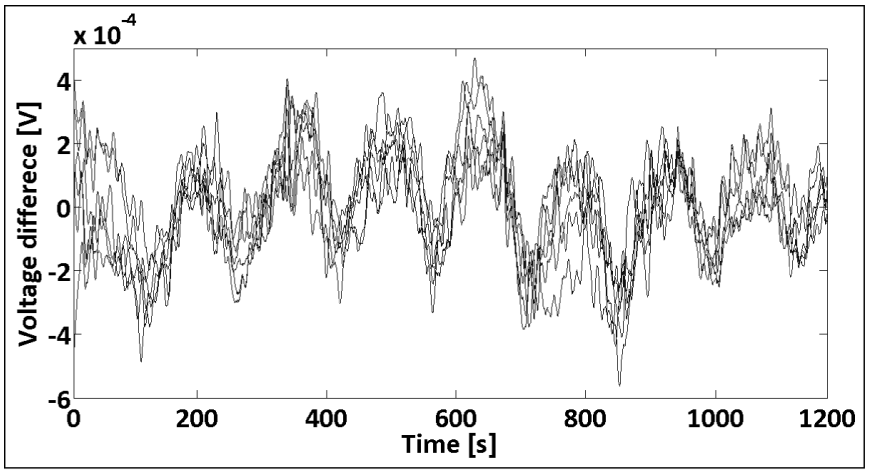

Figure 5.15 (a) demonstrates the 20 minute–long data traces of 5 pixels from the four corners and one from the middle of the array and (b) shows the response of the middle pixel.

reported to be the critical pH fluctuation value for detection of matching base pair. This high pH resolution of the standard factory default silicon nitride implies further potential for living cell–tissue based experimentation.

$$\Delta pH \cong \frac{\Delta V}{pH\ sensitivity} = \frac{450\mu V}{20\frac{mV}{pH}} = 0.022\,pH \qquad (3.44)$$

The observed pH oscillations were also compared to the measured intrinsic noise. The slime mould results were brought into relation with the results of Section 5.4 since the reference voltages 0 V and –1 V provided the highest noise level. Figure 5.7 showed that the level of the measured noise mostly stayed under the –100 dB limit thus this value, –100 dB, was considered as highest noise contribution. Using the relationship

$dBV = 20 \cdot \log_{10}\left(\frac{V_{pp}}{2\sqrt{2}}\right)$ the –100 dB ratio corresponded to a peak–to–peak voltage of 28.2 μV_{pp}. Hence if the maximum intrinsic noise was related to the observed 450 µV ± 70 µV peak–to–peak pH oscillation signal, a maximum noise contribution of 6.2 ± 1.2 % was calculable. The effect of the intrinsic 1/f noise could not be clearly identified from the acquired oscillating signal which was attributed to the extraction method and the application of moving averaging in Matlab.

5.8. Summary

This chapter presented the output response analysis of selected single ISFET pixels. The ionic sensitivity of the passivation layer to H^+ and Na^+ was shown which was followed by the discussion of noise sources and the operation range of an ISFET pixel. In addition the dependency of the measured 1/f noise on the reference bias and the pH was elucidated along with an RTS noise analogous hypothesis on H^+ flickering. The chip was shown to be capable of detecting ultra–low level pH oscillations and the acquired pH data was also related to the measured noise levels.

6. Real–time data acquisition based ionic imaging

The 64×64–pixel ISFET array chip could work as an ion camera device by performing real–time measurements and subsequent visualisations of localised ion concentration fluctuations. Corresponding to Section 4.6 the two NI PXIe–6358 measurement cards were the core of the applied data acquisition hardware. The software for data acquisition and data extraction was based on the LabVIEW environment and the data processing methods were implemented in Matlab. The extracted and processed data was also transformed into continuous video recordings showing the motion of the ions and associated complex chemical structures above the sensor array. The discussed experimental work was a cooperation between the Electronics Design Centre, School of Engineering and the Cronin Group, School of Chemistry, both from the University of Glasgow.

The described data extraction, Section 4.7, was used for multiple purposes besides the isolation of the fluctuating pH data during the data evaluation process. The data extraction method demonstrated advantages also in reducing the effects of trapped charges and physical imperfections in the ISFET array device. The distribution of charges that are

trapped in the passivation layer or in the gate oxide of the ISFET sensors is difficult to predict. It is assumed that the distribution of trapped charge is not uniform in the passivation layer of the ISFET array chip. This in turn indicates that the pixels of the ISFET based ion camera device have varying built–in charges that could be modelled as integral bias sources for each pixel. Therefore the output potentials of the pixels are expected to be different as well. The applied data extraction method counteracts this phenomenon by exploiting that the trapped charge induced bias differences should not change during the course of the measurements. Thus the imperfections can be considered to have a constant contribution to the acquired data set. Because of the built–in characteristics of the trapped charges each acquired data frame contains the steady signal of this imperfection. Therefore when the reference frame is subtracted from the data frames this source of disturbance is eliminated.

The main origin of the continuous signal fluctuation is the applied real–time data acquisition process along with the structure of the ISFET array chip was also found to demonstrate a noise contribution. The reason behind it is the sensor switching nature of the real–time data capturing. It was shown in Section 4.6 that the addressing of the ISFET pixels was controlled by delivering 14–bit long address words at the digital I/O port of the measurement cards. The first 8 bits of the address word were altered at a uniform pace and they were separated into row and column addresses. The 4–row blocks were scanned through sequentially which required that only the selected lines and columns, and therefore pixels, were activated and the rest of the components were inactivated. Each pixel in the sensor array was activated once in every 10.2 ms at a rate of 40 µs per pixel and one measurement data point was taken by the system. Therefore if an activated ISFET sensor did not return from the deactivated state into the exact same operation point as 10.2 ms before, an additive error value was generated which integrated into the acquired signal. In cases where this error value originating from the switching fluctuated from positive to negative or reversed, it resulted in a continuously fluctuating noise. This kind of dominating noise was visible in the 2 dimensional data representation when autoscaling was used and its maximum noise contribution was observed in the range of approximately ± 1 mV.

The measurements were carried out over a very short time range because the investigated electrochemical processes were fast, quickly ran out of flux and the biological exemplars showed activity for limited time. Hence gradual long term changes in the output voltages of the pixels were not considered. The required data acquisition time was typically less

than 5 minutes for the electrochemical experiments. The investigated ionic species included protons and sodium ions as a consequence of the applied materials.

The following sections describe the ISFET experimentation using the 64×64–pixel ISFET sensor array. It is shown that the ISFET array chip worked as an integrated ion camera device visualising the localised activity of moving polyoxometalate architectures, the Belousov–Zhabotinsky (BZ) reaction and the electrochemical response to acid injections. To the best knowledge of the author the ion camera chip with its high speed real–time data acquisition system is unique and it was the first time that self–assembly of polyoxometalate structures and the localised proton transport of the BZ reaction could be visualised by a single ISFET array chip in real–time.

6.1. Acid injections into alkali

The application of the 64×64–pixel ISFET array chip with aqueous substances was at first tested in relatively simple and controlled electrochemical measurements. The principal aims of the initial evaluation trials were to demonstrate that the ISFET array works as an integrated single–chip ion camera system by visualising the forced spread of substances on the surface of the sensor array. The compact example of injection of acidic substances into alkali was chosen to verify the electrochemical sensor functionality of the ISFET sensors and real–time suitability of the semiconductor chip. The packaging methodology of the Pyrex 15 ml centrifuge tube polypropylene chamber, Section 4.5, was applied and Epotek OE–145 epoxy was used for encapsulation. Contrary to fluid pump devices which release the required amount of liquid by applied mechanical forces, the principles of the fluid dispensing device used were based on the application of gaseous pressure. The used injection system consisted of four main parts that were the nitrogen gas source, the fluid dispensing device, the syringe and the semiconductor chip as shown in Figure 6.1. The gas for injections was provided from a standard nitrogen bottle at 6 bar pressure and the nitrogen bottle was in air tight connection with the fluid dispenser through plastic tubing. The Metcal DX–250 fluid dispenser used had the functionality of dispensing liquids as well as of sucking substances back from the container. The fluid sucking functionality was disabled during the measurements. The dispensing pressure was set to 0.5 bar and the gas pumping was triggered manually by pressing the control knob (not included in Figure 6.1).

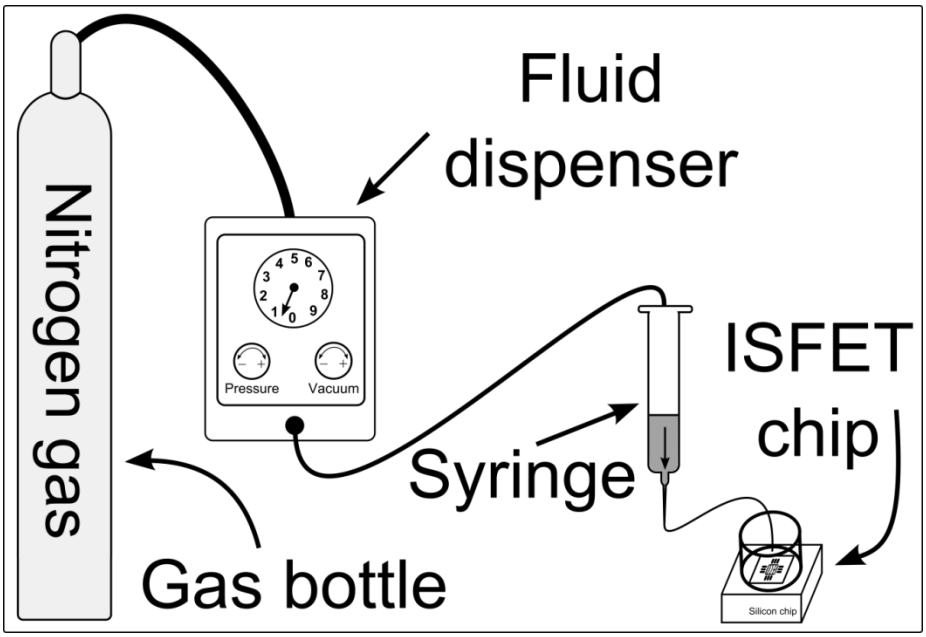

Figure 6.1 The image shows the repeatable technique for the acid injections.

The liquid to dispense was poured into a plastic syringe in advance and the syringe was in connection with the fluid dispenser device. If the gas pumping was triggered, the prepared fluid was forced through a plastic tubing with 0.5 mm inner diameter by the 0.5 bar nitrogen gas into the polypropylene chamber on the chip carrier. The placement of the end of the 0.5 mm inner diameter plastic tube was fixed during the measurements ensuring that the liquid was always injected from the same corner of the sensor array.

The repetitive data acquisition speed is critical when observing electrochemical processes because they can finish within a millisecond scaled time range. The effect of the acid injection into alkali was therefore initially tested by investigating the response of only one pixel to verify whether the applied real–time data acquisition system was able to provide sufficient temporal resolution for the measurements. The maximum data acquisition rate of 40 µs per pixel, 10.2 ms per sensor array was used, corresponding to a speed of approximately 100 frames per second. The measurement was carried out by depositing 1 ml of 0.1 M standard volume sodium hydroxide in the polypropylene chamber prior to the measurements. The injected substance was 1 ml of 0.2 M citric acid that was prepared by mixing 0.96 g of powdered citric acid and 25 ml of DI water. The pH level of the sodium hydroxide was pH 13 and the one of the citric acid solution was nearly pH 2. The results of an injection of citric acid are shown in Figure 6.2. The image Figure 6.2a demonstrates that the injection of 0.2 M citric acid into 0.1 M sodium hydroxide was carried out. The 0.5 bar pressure provided a sufficiently slow transition process in terms of electrochemical mixing as is shown in Figure 6.2b. The low pressure was critical because using a high pressure injection method the transition would be shown only as a rapid and immediate voltage

step. The curve of Figure 6.2a shows the fast pH change which is magnified in Figure 6.2b; each data point represents a time slot of 10.2 ms.

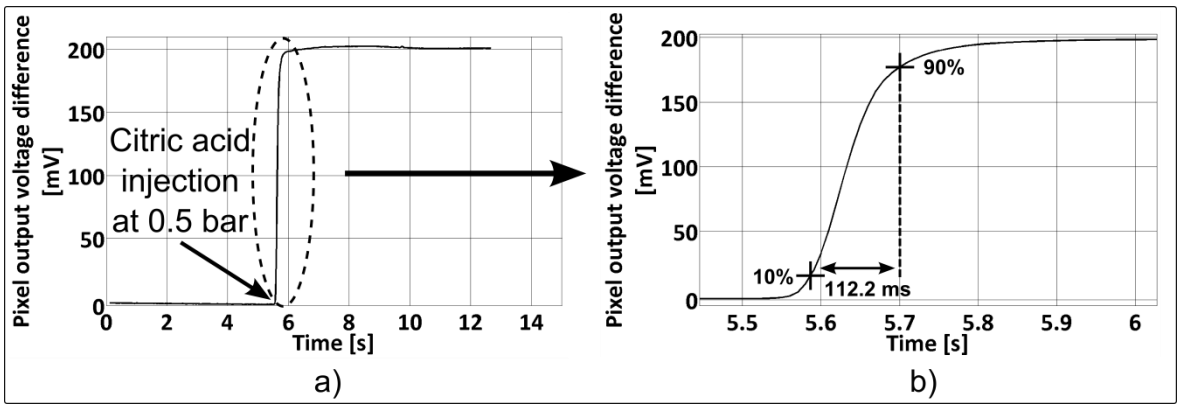

Figure 6.2 The images demonstrate (a) the injection of citric acid into sodium hydroxide and (b) the required rising time of the pixel output voltage signal between the initial equilibrium and resulting pH levels.

The rising time of the curve in Figure 6.2b was determined by calculating and marking the 10 % and 90 % points of the final voltage value. The intermediate data points were counted and the sum was multiplied by 10.2 ms, thus as a consequence 112.2 ms was taken as the required rising time from pH 13 to a nearly pH 3. The injection at 0.5 bar pressure was the one which caused the fastest rate of voltage change among all the discussed experiments. Therefore it was concluded that the developed real–time data acquisition system was capable of monitoring the dynamic behaviour of electrochemical processes.

The verification of the real–time capabilities of the data acquisition system was followed by mapping the acquired data of all the ISFET pixels included in the sensor array. Figure 6.3 demonstrates an experiment with the same parameters mapping the data of the sensors which was shown as a series of images by assigning a coloured scale to the measured voltage values. The displayed images are colour coded using the default colour scale of Matlab called jet. Matlab was also used to provide surface fitting interpolation for the extracted measurement results. In the images the blue colour represents the spots where alkali ions reside on the surface of the silicon nitride and the red colour shows the acidic regions. The images were also appended into a video format that showed the motion of ions across the chip surface; Figure 6.3 shows frames of a measurement result video. As indicated previously, it is demonstrated in Figure 6.3 that the acid injection consistently progressed from one corner of the array towards the opposite corner. The time scale of the measurement results of Figure 6.3 seems to contradict the ones in Figure 6.2. In the first case over 214 ms was required for the mixing while the latter case indicates an approximate 112 ms mixing time.

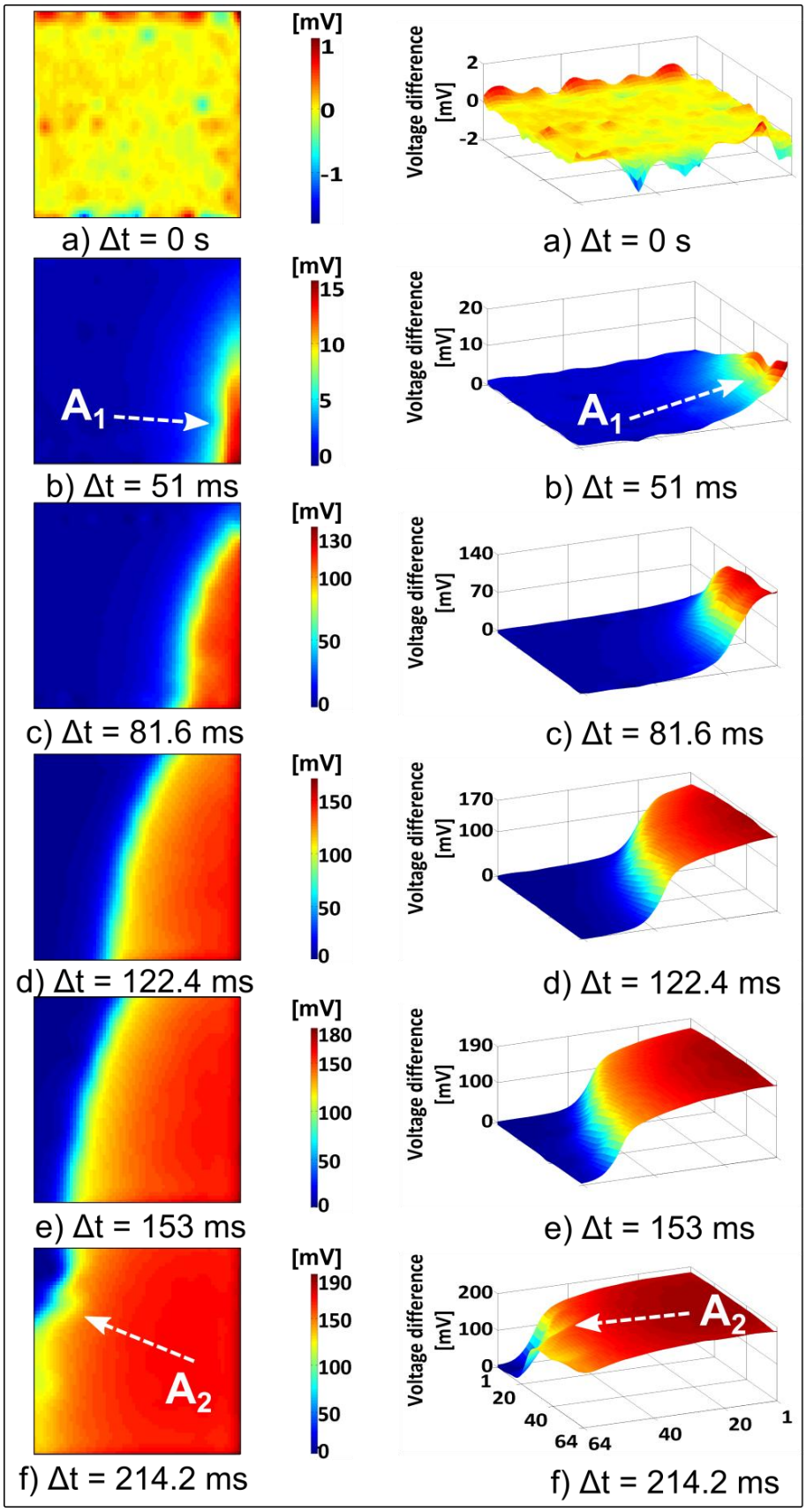

Figure 6.3 Two and three dimensional contour plots of the spread of citric acid over the 64×64–pixel ISFET array. The image shows the effect of injecting 1 ml 0.2 M citric acid into 1 ml 0.1 M sodium hydroxide. (a) before the acid injection, (b, c, d, e, f) the progress of the acid across the sensor surface. A_1 and A_2 show the anomalies in the ideal wave front shape which were attributed to turbulence originating from the forced injection. Blue shows less, red shows more, acidic areas.

It is important to notice that the signal rising time in Figure 6.2 was determined by taking the data values at the 10 % and the 90 % points of the maximum data value and in Figure 6.3 the complete mixing process is observed. Thus if the shown results are considered through the whole mixing process, the time scale of the data in Figure 6.2 are similar to Figure 6.3.

The resolution of this ionic imaging approach is observable from the images of Figure 6.3 which show that the pH level transition is displayed as a continuously progressing wave front with continuously rising pixel output voltage levels. It is shown that even neighbouring pixels can deliver slightly different output results therefore the imaging resolution of the ion camera device is the size of one ISFET pixel. The high imaging precision enables the display of minor details of mixing thus, for example, anomalies in the ideal wave front shape, as A_1 and A_2 in Figure 6.3b and f. The ripples observed in the continuous contours were attributed to the turbulence arising from the force of the injection of the citric acid into the alkali.

Corresponding to the description in Section 4.7, the imaging approach described is by nature a two dimensional visualisation method because the ISFET chip shows only the electrochemical events that occur on the surface of the chip. The 3 dimensional projections of the data were used to provide a better illustration for slight pH fluctuations, e.g. traces of turbulence. The three dimensional representation of the data can also give a very general estimation of the flow of the injected liquid in the vicinity of the nitride surface in the electrolyte bulk. The indexes of the x and y axes are the pixel indexes in the sensor array and the z dimension represents the extracted pixel output voltage levels.

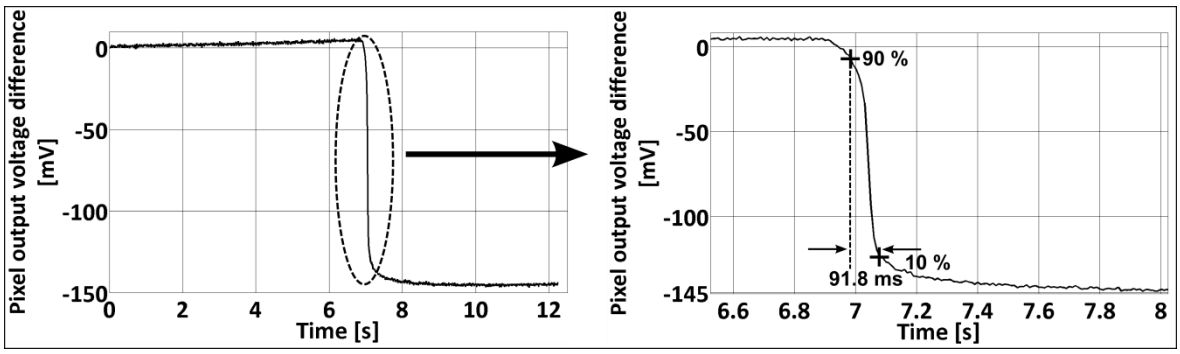

Figure 6.4 The images demonstrate (a) the manual injection of pH 12 into pH 7 buffer solution and (b) the measured falling time of the pixel output voltage signal between the initial equilibrium and resulting pH levels.

The presented approach for ionic imaging is also applicable when basic substance is injected over the sensor array. Figure 6.4 demonstrates the response of one pixel to the

sensor array to the manual injection of 1 ml 0.01 M sodium hydroxide (pH 12) into 1 ml pH 7 commercial buffer solution. It is shown that the fall time in pixel response was similar to the rise time shown in Figure 6.2. It is demonstrated in Figure 6.5 that the same visual representation method can be used to the signal sinking signals as well.

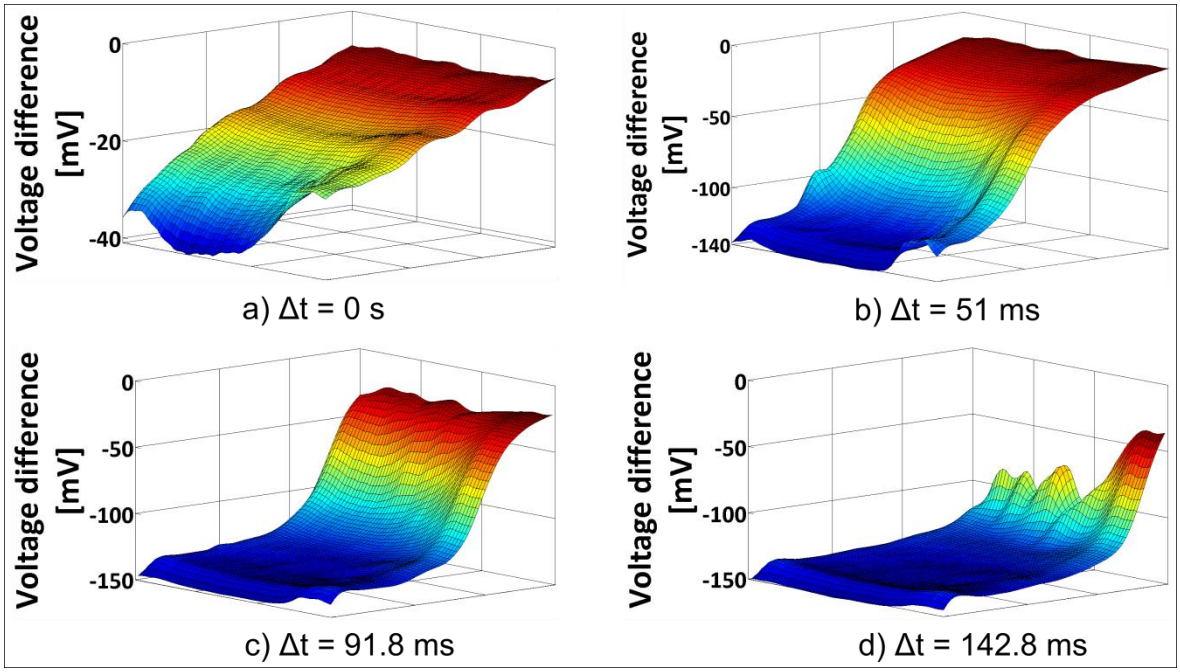

Figure 6.5 Three dimensional contour plots of the spread of citric acid over the 64×64–pixel ISFET array. The images (a, b, c d) shows the effect of the manual injection of 1 ml 0.01 M sodium hydroxide into pH 7 buffer solution. Blue shows less, red shows more, acidic areas.

6.2. Belousov–Zhabotinsky reaction

The electrochemical testing was continued by carrying out additional types of experiments to prove that the 64×64–pixel ISFET sensor array was also compatible with solutions that were not subject to external impacts, e.g. injection of substances. This was an essential step in the series of the scheduled measurement classes because experiments of this kind verified the ability of the ISFET chip to demonstrate the effect of chemical reactions originating from the electrolyte bulk. Corresponding to these requirements the Belousov–Zhabotinsky (BZ) reaction which was first introduced in the 1959 by Belousov [120] was selected for investigation. The BZ reaction belongs to a type of oscillating chemical reactions that deliver periodic reactions until the chemical fuel of the system runs out. It is of particular interest in terms of pH measurements because the internal state of the

electrolyte oscillates inducing repetitive fluctuations in the colour and the pH value of the liquid giving complex circular patterns. Thus the pH oscillation in the electrolyte bulk were expected to be visible in the output potential of the ISFET sensors.

The nature of the spontaneous oscillations in the case of the BZ reaction is based on the reduction and oxidation of transition metals, e.g. ferriin (Fe^{3+}) and ferroin (Fe^{2+}) as well as on the involvement of potassium bromate ($KBrO_3$), potassium bromide (KBr), malonic acid ($CH_2(COOH)_2$) and sulphuric acid (H_2SO_4) following the procedure of [121]. Due to the complexity of the BZ solution the required substances were prepared in advance at the School of Chemistry, University of Glasgow[2]. The following substances were included in the preparation of the required electrolyte: [$KBrO_3$] = 220mM, [KBr] = 28mM, [MA] = 64mM, and [H_2SO_4] = 200mM and [Ferroin indicator] = 250mM. The oscillating solution was prepared in two separate steps. At first the potassium bromate, potassium bromide, malonic acid and sulphuric acid were thoroughly mixed resulting in a solution that was called *pre–BZ solution*. Ferroin indicator was then subsequently added to the pre–BZ solution which triggered the pH oscillations with a random delay in the order of seconds. The BZ reaction was usually observable until the added malonic acid was consumed in the solution.

The measurements were carried out by washing the chip surface using DI water and depositing 5.5 ml of the pre–BZ solution onto the surface of the chip into the polypropylene chamber. The reference potential was provided by a BASi RE–6 glass reference electrode. The start of the data acquisition was followed by the addition of 1 ml of ferroin indicator to the pre–BZ solution. The data acquisition rate was set to 66 µs per pixel, 17 ms per pixel which corresponded to an approximate 58 frame per second sampling rate. The measured output voltage signal of the ISFET pixel (27; 31) is demonstrated in Figure 6.5. The data trace of Figure 6.5 shows that the curve of the pixel response steadily elevates during the course of the first 37 seconds. The elevation of the curve was attributed to the mixing process of the pre–BZ solution and the ferroin indicator solution, therefore to the increasing acidity level as a consequence of the combination of the two liquids. Baseline measurement was performed before triggering the BZ reaction which confirmed a continuous negative trend in the value of the pixel output voltage thus the curve elevation could be attributed to the chemical reactions. The spontaneous trigger

[2] The BZ solutions were initially prepared by Dr. Christoph Busche and Dr. Soichiro Tsuda

event occurred above the selected ISFET pixel at t = 37 s after the addition of ferroin indicator to the pre–BZ solution. As demonstrated in Figure 6.5 multiple spontaneous events were observed during the continuous measurement. However, contrary to the expected genuine oscillations in pH, spontaneous voltage steps were observed in the pixel response that indicated continuously increasing acidity as the occurring events progressed. The successive internal pH fluctuations were externally observable because of the induced changes in the colour of the electrolyte. The colour of the mixed liquid changed from dark red to light blue as a consequence of the first trigger event. Instead of falling back to the original state the substance changed its colour from light blue to light orange at the second trigger event. It was followed by another cycle to blue and back to orange.

The colour changes were increasingly less visible as the reaction progressed which could be the result of the reducing amount of malonic acid as the fuel of the reaction. The non–ideal colour changes corresponded to the non–ideal pH oscillations. Although the preparation of the BZ solution was attempted several times with various amounts of ingredients, the exact chemical reasons for the differences to the ideal BZ behaviour is still subject to further investigations.

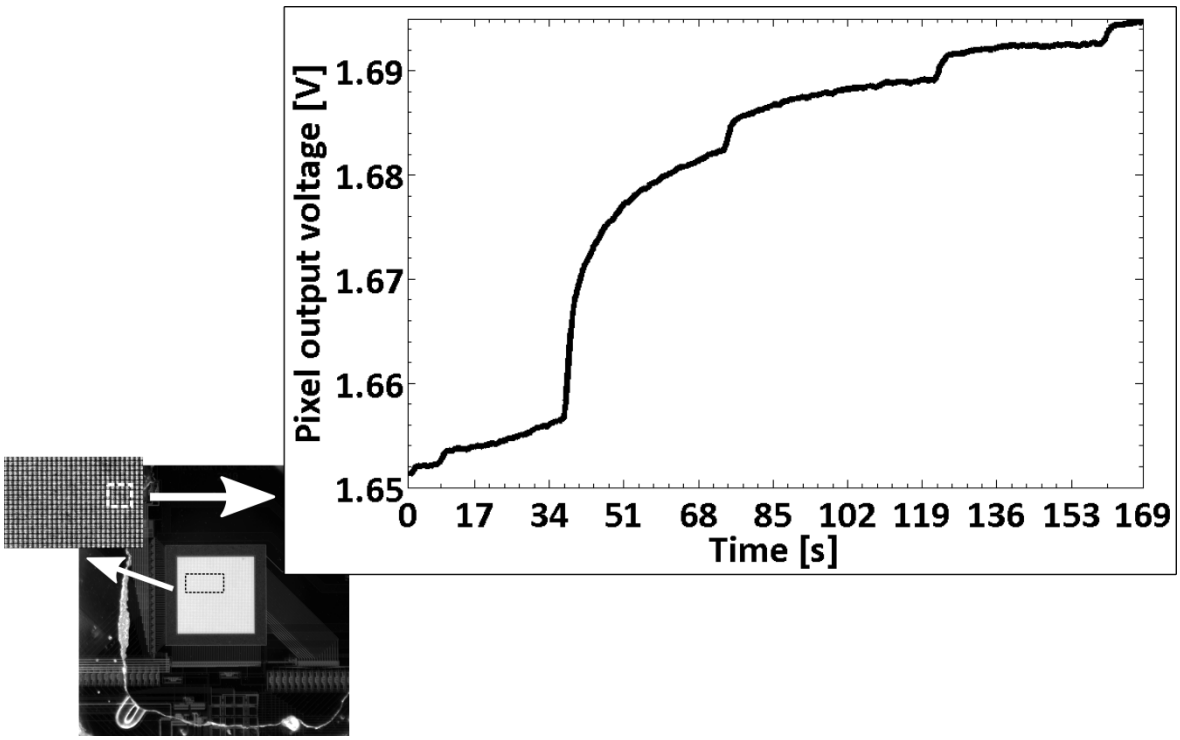

Figure 6.5 The image demonstrates the acquired output voltage response of the ISFET pixel (27; 31) during the BZ–reaction.

The flow of the reaction was similar in all the observed BZ processes which corresponded to the one displayed in Figure 6.5. In the experiment discussed the reaction triggered at t = 37 s above the selected array sensor initiating a large step in the output response of the investigated pixel. The progress of the reaction resulted in a decrease in the pH level of the electrolyte by 0.8 pH during the course of 10 seconds following the first trigger event. The subsequent trigger events causing the voltage steps in the signal occurred with decreasing amplitude. The correlation between the measured amplitudes of the voltage steps and the occurred pH change with respect to the 20 mV/pH sensitivity is shown in Table 6.1.

Corresponding to the decreasing amplitudes and pH changes it is apparent from the data of Table 6.1 that the speed of the reaction has also decreased. The more the reaction progressed, the longer was the time required for the transitions of the voltage steps. Although the parameters of the observed BZ–reaction showed it to be amplitude decreasing, the overall reaction maintained a regular period and the fluctuation events occurred at the expected 30–60 seconds time intervals.

The BZ–reaction was expected to occur in the form of a continuous waveform traveling across the sensor array at a constant flow speed. However, the observed reaction demonstrated different characteristics that are shown in Figure 6.6 and they were also correlated with the nonlinearity of the pH response in Figure 6.5.

Minor voltage steps	Approximate signal rising time [s]	Voltage increase [mV]	ΔpH
1.	2.4	3	0.15
2.	3.5	3	0.15
3.	4.5	1	0.05

Table 6.1 The table shows the correlation between the amplitudes of the observed voltage steps and the corresponding calculated pH fluctuations at 20 mV/pH sensitivity rate.

The utilised BASi RE–6 reference electrode was placed into the polypropylene chamber to the upper left corner of the 64×64–pixel ISFET array device. The reaction started to develop nearly 34 seconds after the addition of ferroin indicator and solution stirring. It was observed from the measurement results that each the reaction initiated from the corner where the reference electrode was located. It was especially apparent from the videos made of the extracted data that the ionic charge built up in the vicinity of the reference electrode and it was sharply released and the ionic wave spread across the sensor array.

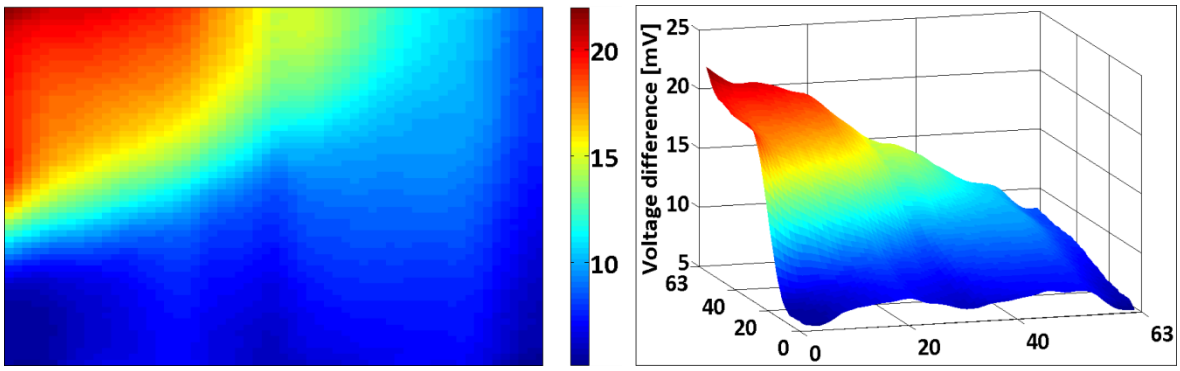

Figure 6.6 The image demonstrates the state of the first pH fluctuation during the BZ–reaction at the time slot of 37.4 seconds. The two dimensional image and its three dimensional projection show a data frame of the investigated BZ process. The sensor indexes provide the x and y dimensions and z dimension is represented by the acquired voltage values.

The results of Figure 6.6 comply with the result in Figure 6.5 because the investigated single pixel is almost in the geometrical centre of the sensor array and at t = 37.4 ms both images demonstrate matching results. The wave of triggered ionic fluctuations of the BZ–reaction usually required 10–14 seconds to travel across the sensor array, which accounts for an approximate wave propagation speed of between 71 µm/s and 50 µm/s (3–4 mm/min).Considering that this is a relatively slow propagation speed the data acquisition rate of the real–time data capturing was set to 400 µs per pixel, 102.4 ms per sensor array. This sampling rate also indicates that the sensor array was scanned nearly 10 times in one second thus the set data acquisition rate was sufficient to observe the oscillating reaction. The ion spreading process following the primary trigger event of the BZ–reaction is shown in Figure 6.7 with imaged area of 64×64 pixels.

The time slots of 34 s, 35.7 s, 36.8 s, 37.4 s, 39.7 s, 41.1 s and 43.3 s were selected to demonstrate the flow of the reaction indicating the acidic regions with red and the basic regions with blue colours. The build–up and release behaviour of the chemical process described is also shown in Figure 6.7; the build–up of ionic charges is shown in Figure 6.7a, b and c, and the phenomenon of release is observable Figure 6.7d, e, f and g. Figure 6.7a shows that the precision of the imaging process is very similar to the one discussed in Section 6.1. The ion camera chip could display the differences between two extremes of pH values within ~ 70 µm distance although the true spatial resolution of the imaging method was the size of one pixel because the neighbouring pixels consistently showed differently scaled pH values.

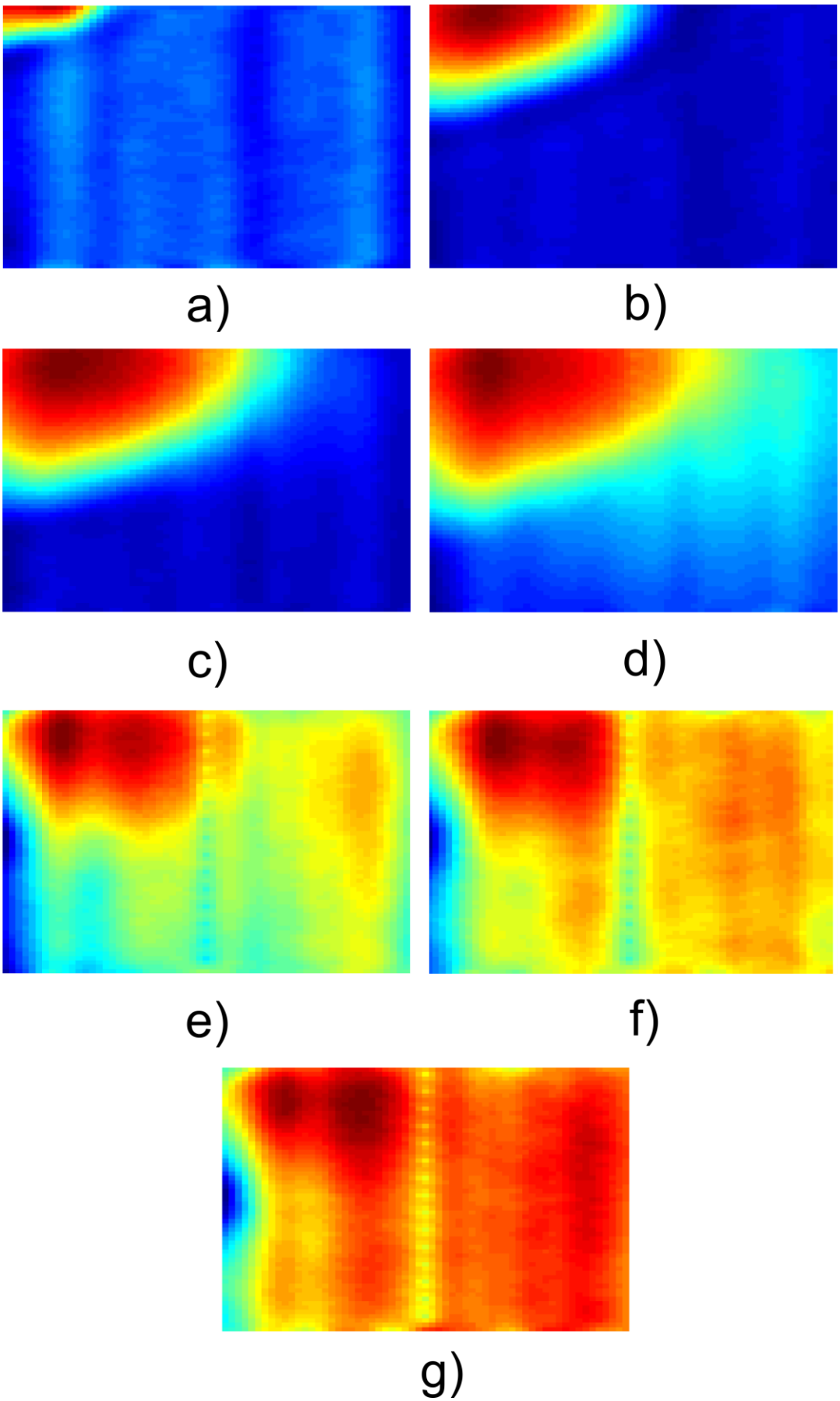

Figure 6.7 2D imaging of proton ion distributions over the 64×64–pixel (715.8×715.8μm) ISA of the trigger event in the BZ reaction at time slots of (a) 34s, (b) 35.7s, (c) 36.8s, (d) 37.4s, (e) 39.7s, (f) 41.1s, (g) 43.3s, red displays the highest and blue the lowest output potential.

The irregularities shown in the middle of Figure 6.7e, f and g are attributed to disruption in the delivery of the pixel address 96 (pixel 32 in the second line of each 4–row block) on the digital port. The irregularities are also present in Figure 6.7a, b, c and d, although due to the output voltage values of the surrounding pixels and the colour scaling of Matlab they are hardly visible. The results of multiple and spatially distant pixels were analysed to provide verification for the electrochemical imaging data shown in Figure 6.7. The pixels (1; 61), (3; 5), (30; 58), (30; 35), (29; 1), (62; 62) and (61; 9) were selected for investigations as they were located at the four corners and in the middle of the ISFET array. The data traces of each selected pixel was plotted and collected into one graph as shown in Figure 6.8a.

The pixel indexes are to be compared with the sensor array in Figure 6.8b; the pixel (1; 1) is the bottom–left corner of the device. The magnified representations of the primary trigger events of the pixels were emphasised by enclosing them into a dashed box. The results of Figure 6.8a comply with Figure 6.7 because pixel (1; 61) in the top–left corner of the array responds at first which is in the proximity of the reference electrode. It is followed by pixel (30; 58) and then (30; 35). The rest of the pixels, (3; 5), (29; 1), (61; 9) and (62; 62) respond later, almost at the same time as the reaction progresses. Thus Figure 6.8 and Figure 6.7 demonstrate the same progression paths for the experiment.

In addition, Figure 6.8 shows that large output voltage variations were observed in the pixel data, which were considered a consequence of the corrosiveness of the BZ–reaction.

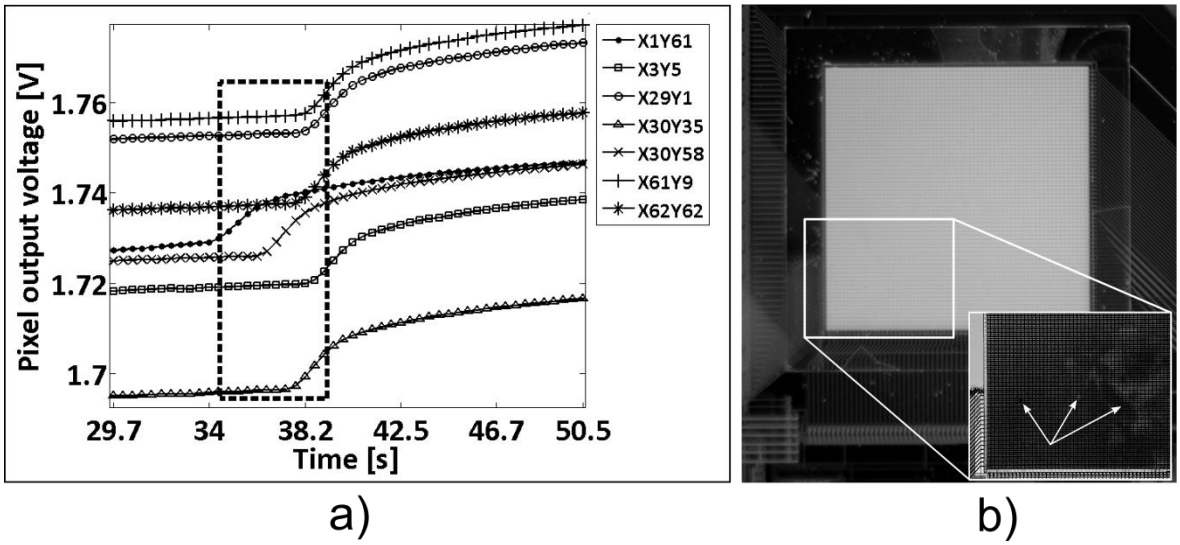

Figure 6.8 The images show (a) the primary trigger events of the selected (1; 61), (3; 5), (30; 58), (30; 35), (29; 1), (62; 62), (61; 9) pixels and (b) the traces of the corrosiveness of the BZ–reaction.

Various concentrations of the BZ reaction solution were found to have permanent destructive effects on the structure of some of the ISFET array chips used. The majority of the damage, displayed in Figure 6.8b, was observed in the MET4 metal ring around the sensor array and minor damage was observed above the array device. The applied BZ liquids were highly acidic solutions that became more acidic as the reaction progressed. The optical microscope image of Figure 6.8b shows that lighter coloured spots appeared on the surface of the chip which were concluded to originate from thinned silicon nitride and sensors were found to be damaged. Parts of the MET4 ring around the sensor array completely disappeared making the underlying MET3 tracks visible. Due to the destructiveness of the solutions to the sensor chips the investigation of the BZ–reaction was terminated.

6.3. Polyoxometalate Tubes And Membranes

The ion camera functionality of the 64×64–pixel ISFET sensor array was further investigated to show that on the one hand the true spatial resolution of the device is the area of one ISFET pixel. On the other hand it was important to show that the ion camera device was capable of imaging nearly nano–scaled architectures and that the obtained ion based images had excellent correlation with the ones taken by optical microscopes. Thus it was initially expected that this first prototype device would successfully provide a reference in the field of ionic imaging with sensor arrays. Therefore the further development of this sensor topology was planned to facilitate the examination of complex chemical structures.

The demonstration of pixel–sized spatial resolution demanded the extent of the investigated material to be comparable with the dimensions of an ISFET pixel. It was also required that the substance maintained ionic activity over a strongly limited area of the silicon nitride passivation layer. Locally confined ion fluxes were essential from the perspective of ion sensing because the ion camera chip detected the local *change* in the ionic concentration rather than the static ionic activity.

Polyoxometalate (POM) crystals, shown in Figure 6.9a, were selected for the experiments based on their suitable characteristics of small volume, reactivity with organic cations, H^+ and Na^+ ions, and the ability to grow low micrometre–sized tubular and membranous architectures. The solvated multi–atom polyoxometalates pass hydrogen ions therefore the pH change throughout the complete reaction with POM crystals was tested *a priori*. The

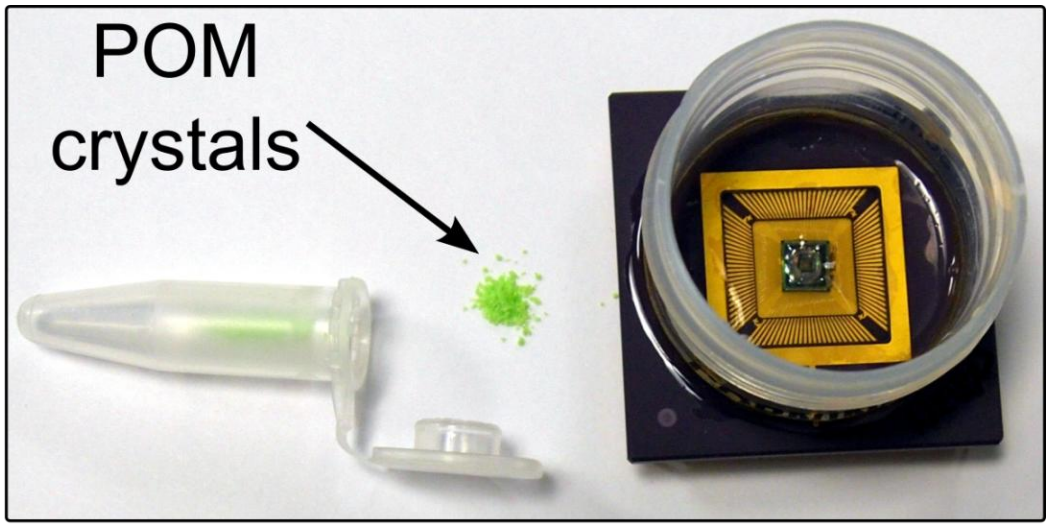

a)

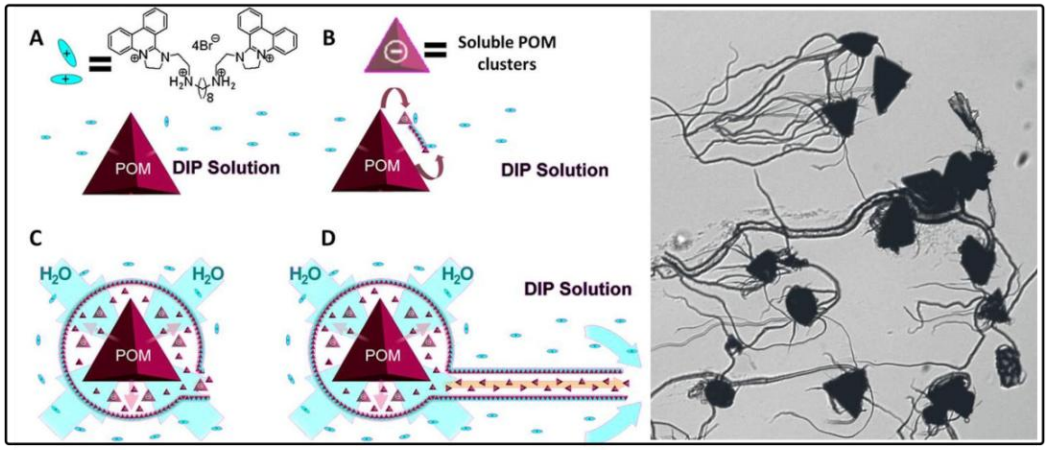

b)

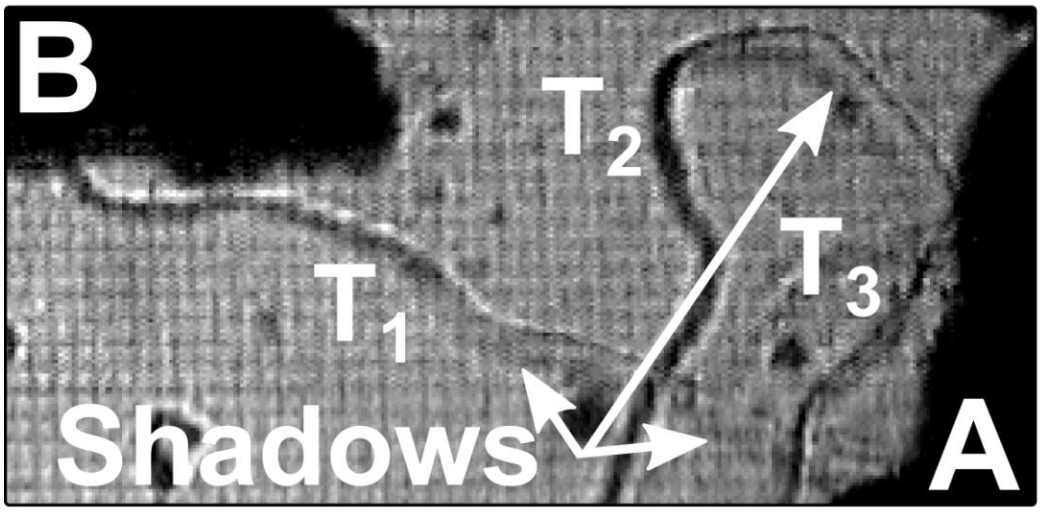

c)

Figure 6.9 The images show (a) the synthesised polyoxometalate crystals and the packaged and encapsulated chip with a silicon chamber, (b) the principles of the chemical reactions of the forming nearly nano–sized tubular architectures and optical microscope images of the formed structures [122], (c) shows the T_1, T_2 and T_3 POM tubes growing across the DIP solution and T_1, T_2 dropping shadows onto the chip surface.

test was carried out using a high–precision Mettler Toledo SevenMulti pH meter at ±0.01 pH accuracy settings. The pH meter failed to detect any pH change in the bulk solution during the solvation of the POM crystals. This undetectable pH change confirmed the initial assumption on the highly localised characteristics of the occurring ion fluxes which the pH meter would detect the pH change only at the utmost proximity of the event. The applied POM crystal structures from type of $Na_4H_3(C_6H_{11}N_2)_{13}[(SiW_{10}O_{36})_2(Ni_4O_6)]\cdot 12H_2O$ and average volume of 0.1 × 0.1 × 0.1 mm^3 were specifically synthesised before the physical experiments.

The chemical reactions which occurred, described later, were identical in terms of electrochemical principles. Furthermore each reaction consisted of four separate stages as shown in Figure 6.9b for the case of tubular structures. The POM crystals were at first manually immersed into *N,N´*–bis(5–phenanthridinium–5–yl–ethyl chloride)octane–1,8–diamine dihydrochloride (DIP), Figure 6.9bA. Thus a sparsely soluble organic cation in aqueous solution is brought into physical contact with the also sparsely soluble POM crystal. An ion exchange process follows, involving anions which are released from the POM crystal and counter cations from the organic DIP solution near to the electrolyte–solid interface. It was observed during measurements that the time rate of the reaction heavily depends on the concentration of the cation in the DIP solution. As a result of the interaction between the cations and anions which are present in the solution, a hollow membrane precipitates around the crystal structure, Figure 6.9bB. Because of the permeability of the membrane to water molecules there is a constant stream of water from the DIP solution into the membrane. As a consequence the continuously passing water molecules into the interior of the membrane give rise to the inner tension and thus to an osmotic pressure. Figure 6.9bC demonstrates that the membrane is able to withstand the pressure increase up to the critical stress level and exceeding it the rupture of the membrane occurs. The persisting inflow of water molecules forces the dissolving anions of the POM crystal through the opening in the membrane into the DIP solution. The forced and continuous flux of anions through the aperture in the membrane encounter the surrounding organic cations which results in an immediate precipitation, Figure 6.9bD. This constant outflow of anions prevents the opening from closing and forms a growing tubular structure. The described process continues until the system runs out of flux, thus when the driving osmotic pressure drops and the POM crystal stops delivering supporting ions. The termination of the growing phenomenon causes the end of the tubular structure to seal. The grown structures remained permanently on the chip surface after the end of the

reaction, and therefore the polypropylene chamber was thoroughly cleaned by DI water following each measurement trial.

The POM crystals were manually placed onto the chip surface so that they did not float on the surface of the electrolyte solution. It was essential to place the crystals onto the device surface because the tubes grew in three dimensions out of the shell of the hollow membrane. And as a consequence of the crystal placements the tubes grew *on the surface* of the ion camera chip with considerably increased probability. The ability of the tubes to grow in three dimensions in shown in Figure 6.9c. It is demonstrated that the growth of T_1 and T_2 tubes on the left hand side originated from the A POM crystal on the right–hand side of the image. The tubes then touched down onto the silicon nitride and continued their path on the chip surface. It is informative to observe that the T_1 and T_2 tubes dropped shadows on the chip surface while progressing towards the chip which proves the 3D growing characteristic. The data extraction method, described in Section 4.7, provided additional advantage during the several consecutive experiments performed. The precipitation of the tubes and membranes resulted in somewhat persistent structures on the chip surface that in some cases left ionic and physical stains even after the most thorough DI water wash. The advantage was that the selected reference frames contained the information of these contaminations which could be mostly subtracted from the acquired raw data.

6.3.1. Membranes

The molarity of the applied DIP solution was important during the growth of the various structures because the type of the growing composites was controllable by the concentration of DIP in the electrolyte. At low molarity of DIP the growing structures were usually membranous with slow growing rate characteristics. The expanding membrane firmly separated its ion–rich interior from the surrounding electrolyte at a steady expansion rate although damage, e.g. leakage through the membrane and membrane rupture, were often observed as well. The approach for growing polyoxometalate membranes contained several unpredictable parameters, e.g. start time of the membrane growth, type of damage, time duration of the growth process. However, despite these uncontrolled parameters the imaging of ionic concentration fluctuations could be successfully carried out using the 64×64–pixel ISFET sensor array.

The imaging approach for the growth of a membrane in case of a POM crystal immersed into 2.5 mM DIP solution is displayed in Figure 6.10. The images from the continuous live video recording optical microscope, Figure 6.10–left column, are compared with the recorded two and one dimensional imaging data of the ISFET chip, Figure 6.10–middle and right columns.

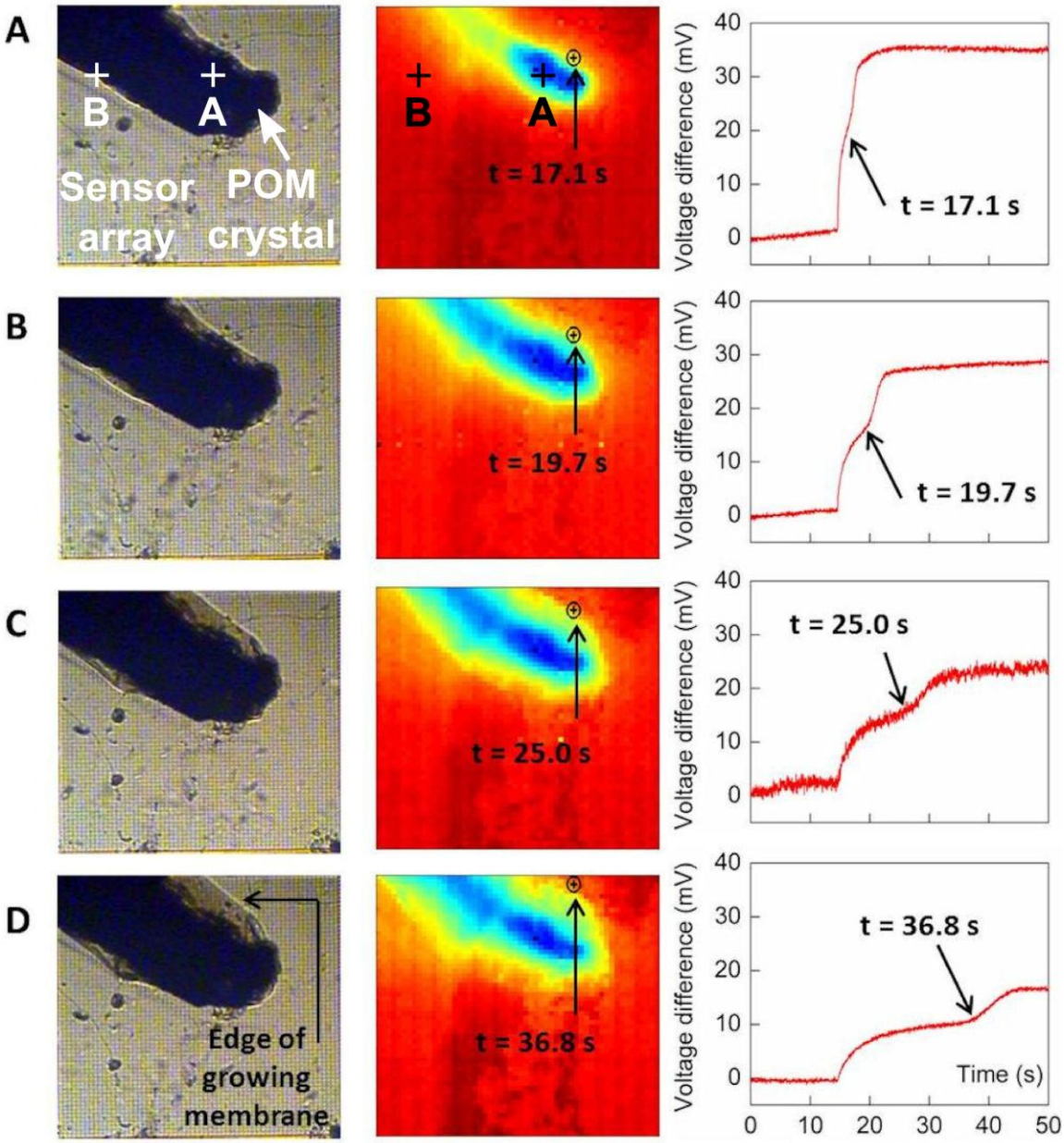

Figure 6.10 The growth of a membranous architecture is shown. The progress of growing is demonstrated by optical microscope (left column) and ion camera images (middle column) as well as by voltage difference vs. time graphs of the activities of selected pixels (right column). The panels show an area of 57 × 57 pixels.

The imaging data is presented separately in one and two dimensions because of the different information sets delivered regarding the membrane structure. The two dimensional data was used to follow the fluctuations in the intensity of the internal ion

concentration and the one dimensional data represented the physical movement of the membrane on the chip surface. The middle column in Figure 6.10 demonstrates the localised activity of Na^+ and H^+ ions (blue colour) and the DIP solution (red colour). The dissolving of the crystal surface was a continuous process that was visible only in the ion camera pictures (Figure 6.10A and B) if compared to the optical images. It is apparent from the right column image sequence of Figure 6.10, where the time domain responses of selected pixels were investigated, that the crystal immersion occurred at t = 14.6 s since all graphs show a clear edge at the referred time slot. The time t = 0 s is considered as the start of the real–time data acquisition at rate of 400 μs per pixel, 102.4 ms per array. The location of the edge of the POM membrane during the progression is observable in the data traces of the separate pixels. An inflexion was found in each plotted curve at the times (17.1 s, 19.4 s, 25 s, 36.8 s) when the edge of the membrane crossed above the respective pixel. The correlation of the inflexions is apparent when the one dimensional results are compared to the optical and ion camera images.

It is also informative to notice that the intensity of the ionic reactions in the interior of the membrane decreased with the distance from its centre, the POM crystal. The growth of the membrane also equally slowed down with the distance dependent decrease of the ionic flux. The middle column of Figure 6.10 represents the decaying intensity by the colour differences. In addition the decaying intensity is also observable from the single pixel responses by considering the decreasing response amplitudes and increased rising time of the curves as distance from the POM crystal increases.

Besides the movement of the polyoxometalate membrane, Figure 6.10 provides indication of the physical contact between the POM crystal and the surface of the ISFET array chip showcasing the differences between ion camera and optical images. The left column of Figure 6.10 shows the optical microscope images which suggest that the immersed crystal is in full contact chip surface. The optical images can show only the surface of the POM crystal due to the perpendicular position of the microscope lens to the chip surface. However, it is apparent from the ion camera images that only a part of the POM crystal was in contact with the silicon nitride. Two markers were placed in the images, A and B in Figure 6.10A, which represent a distance of ~27 pixels. It is demonstrated that the ion camera images show elevated ionic activity only at a narrow section of the ISFET array, around the A marker. The part of the crystal surrounding the B marker remained red suggesting that it does not touch the silicon nitride. Therefore it was concluded that only a very limited part of the POM crystal was in direct contact with the chip surface and that the

ion camera chip could also monitor the crystal activity when the optical images were obstructed. The velocity of the membrane expansion was a slow process as the pixels marked by the arrows indicate in middle column of Figure 6.10. The growing membrane expanded a distance of 10 pixels in the considered direction between the time slots of t_1 = 17.1 s and t_4 = 36.8 s. Since the distance between the centre points of two neighbouring pixels was 11.2 µm (10.2 µm pixel + 1µm gap on MET4 level) the total expansion distance was 10 × 11.2 = 0.11 mm. Hence the growth rate in the observed direction was calculated as $\frac{0.11mm}{(36.8-17.1)s} = 5.58\frac{\mu m}{s}$.

6.3.2. Tubes

The growth of tubular architectures was achieved by increasing the concentration of the cations in the applied electrolyte solution. The molarity of the DIP was increased to 10 mM which ensured a shorter reaction time. Although it was also experienced that the tube growth of the tested crystals were unpredictable even if they originated from identical samples and identical DIP solutions. The diameters of the growing tubes at a given molarity level were observed to be relatively consistent. Following the explanation of [122] the diameter parameter of the growing tubes was controllable by changing the concentration of cations since the ejected POM anions were required to travel less distance to encounter cations and precipitate.

The growing polyoxometalate tubes were in the diameter range of 10 µm which was apparent by microscopic observation as well because the thickness of the growing tubes in the 10 mM DIP solution matched the width of one square shaped ISFET array pixel. Similar to the membranous experiments, the growth of the tubular architectures was also subject to live optical video recording using the available optical microscopes. Due to the higher cation concentration the growth rate in the electrochemical cell was almost 20 times higher than in the membranous case. The stronger ionic flux thus demanded adjustment in the real–time data acquisition rate which was set to the maximum speed of 40 µs/pixel, 10.2 ms/array. It was expected in advance that even if the polyoxometalate tubes grew substantially faster than the membranes, the 100 complete array scans would provide sufficient information for the data evaluation.

The growth process of a thin polyoxometalate tube with outer diameter in the 10 µm range across the ISFET sensor array is shown in Figure 6.11. The displayed tube originates from

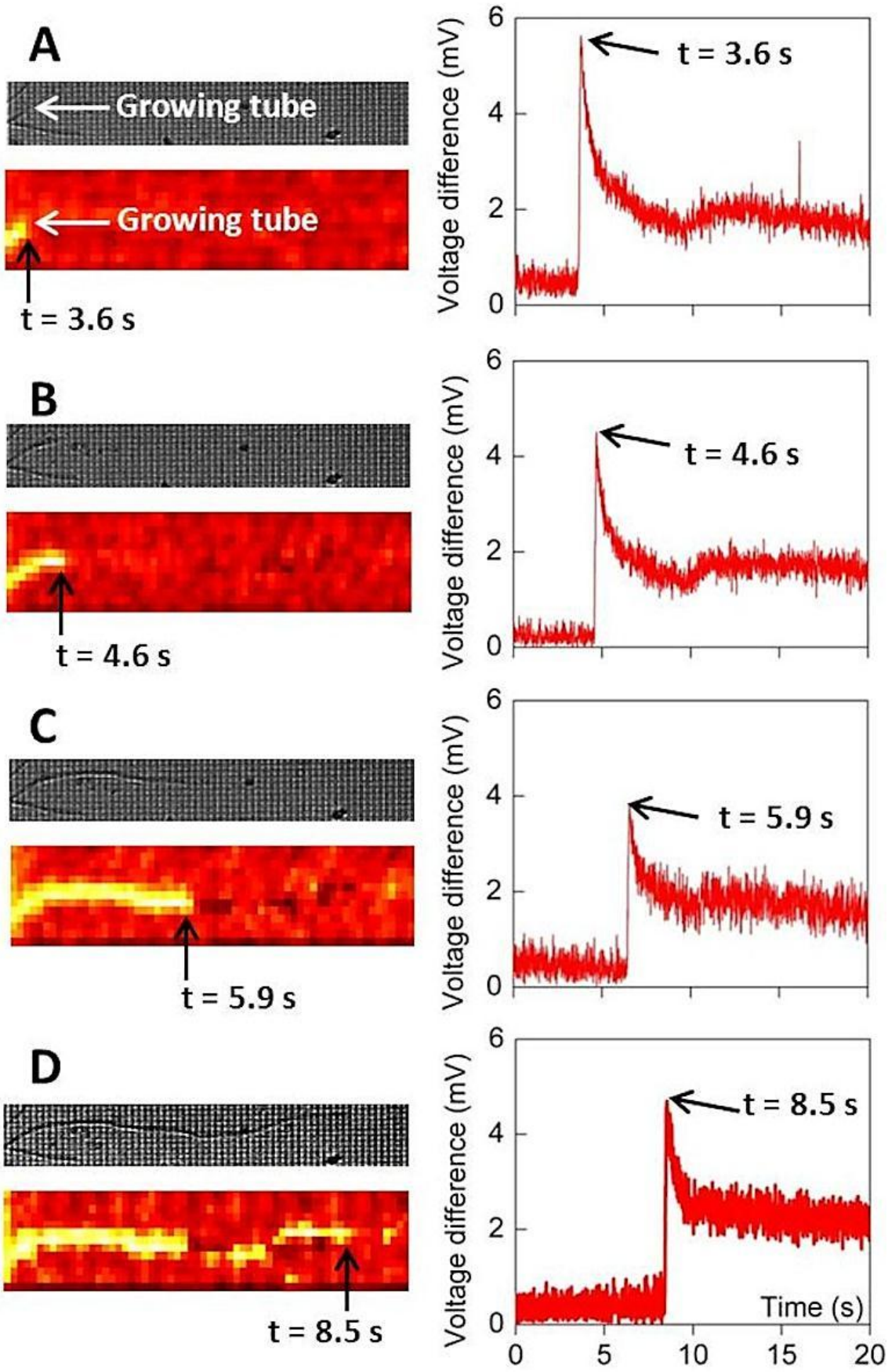

Figure 6.11 The images demonstrate a polyoxometalate tube travelling across the ISFET sensor array. The top panels in the left column show the optical microscope images, the bottom panels show the ion camera images. The right column shows the voltage difference vs. time responses of the selected pixels. The imaged area was ~64×11 pixels.

a POM crystal deposited outside the sensor array, from above the MET4 ring around the sensors. The left column of Figure 6.11 demonstrates the growth using both optical and ion camera representation on the top and bottom panels, respectively. The ion camera images are colour coded similarly to the representations of the membrane composition, the red colour shows low ionic concentration areas and the yellow colour shows the spots of high ionic flux. Red and yellow colours were preferred for the representation of this data to maintain the high contrast. The optical pictures show the parts of three different POM tubes however only the middle one is considered. At the time of the investigation the growth of the additional tubes was either already terminated or was outside the field of view. In the left hand column of Figure 6.11A it is shown that the growing tubular structure entered the area of the sensor array 3.6 s after the start of the measurement. The observed tube then travelled across the sensor array within the following 4.9 s, Figure 6.11B–D. It was apparent from the further image analysis that the total growing distance the tube achieved was approximately 56 pixels. Following the considerations of the previous section this number of pixels corresponds to a distance of 11.2 µm × 56 = 6.27 mm. As a consequence the calculated growth rate is 127 µm / s.

The images on the right hand side of Figure 6.11 show the recorded activity of single pixels in the path of the tube, the investigated pixels are marked by a black arrow on the bottom panels of the left hand column. The single pixel data demonstrates the effect of the over 20 times faster growing speed in comparison with the discussed membrane structures. In the voltage difference vs. time plots it is apparent that the baseline values are followed by a sharp rise in the voltage data which then decays to an intermediate voltage level. The observed behaviour of falling back to an intermediate voltage level between the peak of the spike and the baseline data values allowed the assumption that the remaining precipitated tube continuously maintains a local ion concentration difference with respect to the DIP solution. It is shown in Figure 6.11 that the displayed data curves showed good correlation with the imaged data in time and pixel location. The time shift is apparent among the voltage peaks that corresponds to the growth rate of the observed tube. Hence it was concluded that a peak of the recorded kind originates from the occurrence when a tube crosses the sensitive area of the pixel which initiates a short and pronounced change in the local ionic flux.

The characteristics of the growth of polyoxometalate tubular structures were extensively studied in order to demonstrate occurring tube joining events while the ionic flux is maintained. The extent of potential side diffusions of completely grown and already

precipitated tube composites was also analysed because arising side diffusions could blur the ion camera image and therefore lower the precision of the imaging. The data analysis was carried out for experiments with applied 10 mM DIP solution thus the diameters of tubes were expected to remain in the 10–20 µm range.

The growth of multiple POM tubes is represented in Figure 6.12 comparing the ion camera images with the pictures from the live video recording. The POM crystals shown in Figure 6.12 were deposited after the measurement started and the displayed growing tubular composites originated from the crystal on the right hand side of the images. The growth process of the tubes is demonstrated from the time slot when the first tube touched down to the silicon nitride, Figure 6.12a. Therefore the tube parts were marked by dashed–line rectangles only from the points from where they were in physical contact with the nitride passivation. Tubes travelling through the electrolyte bulk were discussed at Figure 6.9c. The applied 400 µs/pixel, 102.4 ms/sensor array scanning rate was sufficient to perform the electrochemical measurement. During the first second only the tube on the right touches the nitride surface shown in Figure 6.12a and b. The second one reaches the chip surface in 2 seconds from the start of the evaluation Figure 6.12, and grows under the crystal on the left hand side while the other tube continues progressing further, Figure 6.12d. The wall of the shell of the crystal on the right hand side ruptures at an additional location releasing another fast travelling tubular structure. At 5.7 s from the start the most recently formed tube joins into the path of the first one that is shown in Figure 6.12e.

The newly formed tube then exactly follows the path of the former one as displayed in Figure 6.12f. It was difficult to provide clear evidence on whether the referred tubes physically joined or only shared the same path during the measurement because on the one hand the optical microscope could deliver video recording only at a limited resolution. On the other hand the applied DIP solution made the very fine details of the images relatively blurred due to the diffraction of the light. It was concluded though that the first and last displayed tubes only shared the same channel because later they continued travelling on different paths before their ion flux ran out. Due to the later diversion in their growth and the relative rigidness of the precipitated skin of the low diameter tubes, channel sharing was believed more likely.

The phenomenon for the two tubes of sharing the identical channel paths and the side diffusion of the growing and precipitated tubes were also investigated as shown in Figure 6.13. Instead of taking the results from one single pixel, multiple pixels were selected for

simultaneous observation and comparison of their output data. Two observation vectors, OBS1 and OBS2, of 10 elements each were established in Matlab, that were in the path of the tubes in question, shown in Figure 6.13a. As demonstrated in Figure 6.13a, OBS1 contained the data of 10 pixels from an area where only one tube crossing occurred during the time of the investigation which was at 11 seconds. The OBS2 vector however collected the data of 10 pixels that encountered 2 separate tube crossings. The top graph in Figure 6.13b shows that the first displayed tube crossed the line of the vector at $\Delta t = 0$ and only the ion trace of the remaining tube is observable. The bottom graph of Figure 6.13b demonstrates that the first tube required 1.2 s time to reach from location of OBS1 to OBS2 and after crossing left a pronounced ionic trace. In addition the trace of the second, channel path sharing, tube is also visible which crosses the line of OBS2 vector 4.8 s later. From the results it is apparent that the peak of the second tube appeared exactly in line with the first one that supports the observation of sharing the same channel path. The 4.8 s time difference between the tube crossings is also compatible with the imaged data if Figure 6.12b and Figure 6.12e images are compared.

The first tube required 1.2 s time to arrive from OBS1 to OBS2 that are approximately 13 pixels away from each other in distance if we draw a line between the two observation vectors. Hence the growth rate of the first tube is calculable as $\frac{13 \times 11.2\,\mu m}{1.2\,s} = 121.3\frac{\mu m}{s}$

This result is similar to the tube experiment of Figure 6.11 which shows the repeatability of the system. The data analysis failed to reveal any side diffusions, as for example the leakage through the membrane in the case of 2.5 mM DIP, shown in the data plots of Figure 6.13. The data traces of the tubes demonstrated the paths of the tubes using only two pixels and this two pixel resolution generally applied to tube experiments at elevated DIP concentration.

.

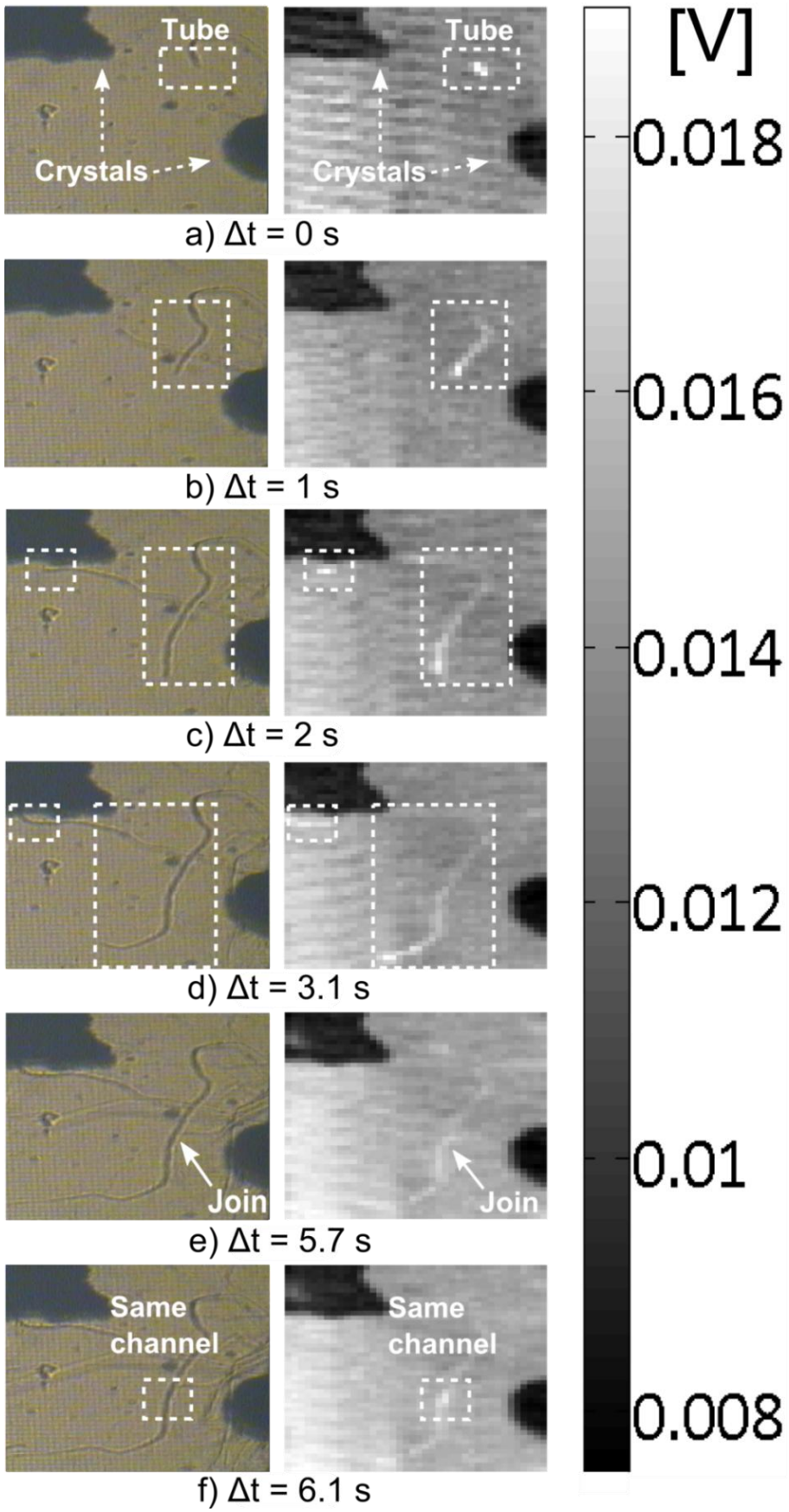

Figure 6.12 The ion camera and optical microscope images demonstrate the placement of two POM crystals and two growing tubes from the crystal on the right hand side. The images E and F show two tubes joining and sharing the same channel path. The voltage difference values are in Volts. The imaged area is ~43 × 48 pixels.

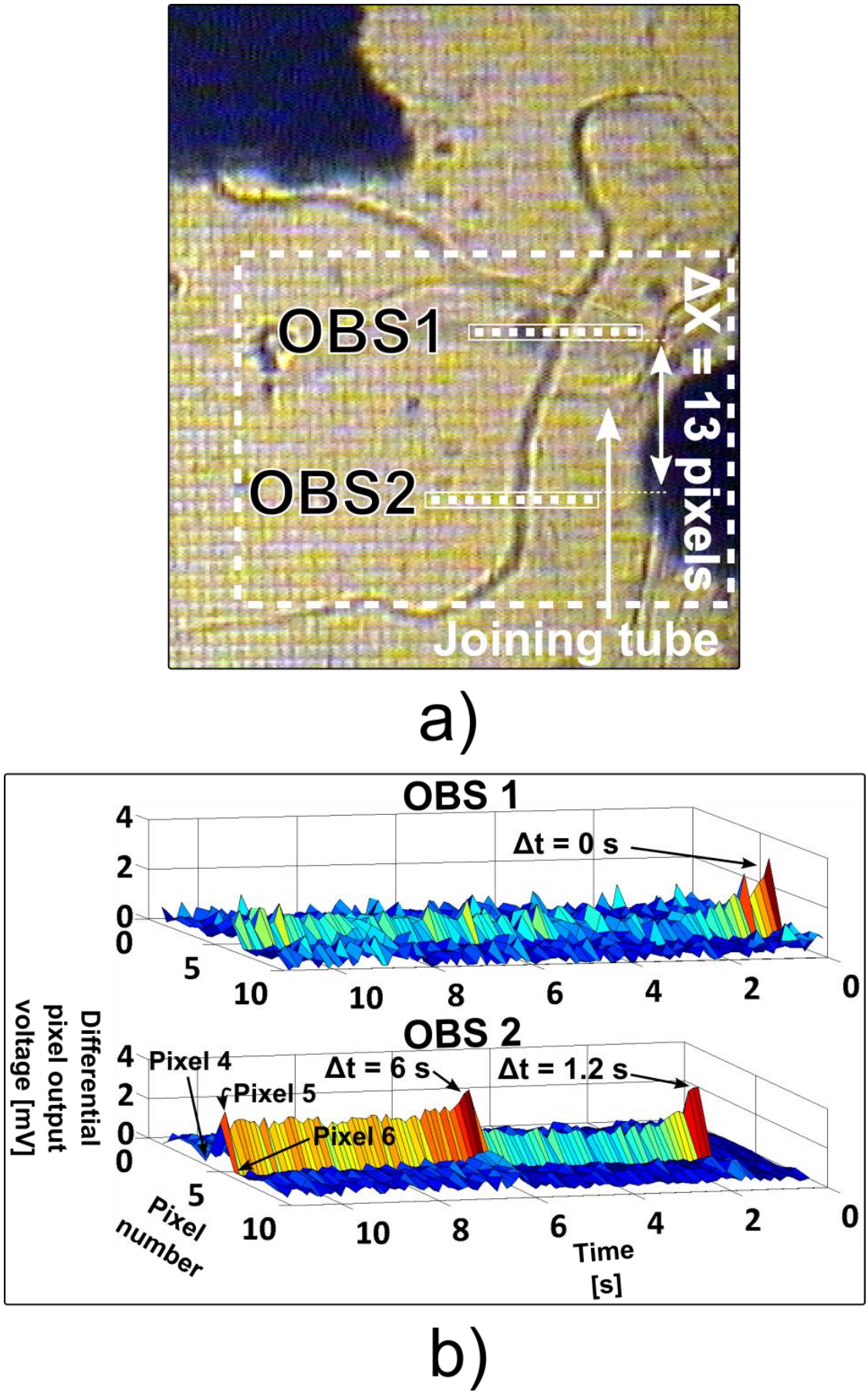

Figure 6.13 (a) presents optical image of the joined tubes and (b) shows the response differences between multiple–pixel OBS1, OBS2 observer vectors with one and two crossing tubes, respectively. The accuracy of the data representation is two pixels.

6.3.3. Ion camera without optical microscopes

The optical microscope was capable of taking live video recordings perpendicular to the chip surface keeping the ISFET sensor array in the centre of the image. Thus as indicated in Section 6.3.1 the optical images provided information only of the arrangement that was visible from the 90 degrees angle with respect to the chip surface. As a consequence the fields being covered by either residue floating on the surface of the electrolyte or the deposited POM crystal were out of scope for the microscope device. In case of this the ion camera chip could still continuously record the ionic exchange activities. The applied real–time data acquisition speed was 40 µs/pixel, ~100 frame per second.

The growth of tubular structures with larger outer diameter was also achieved using 5 mM DIP solution and similarly synthesised POM crystals as for Section 6.3.2. The tubes grew in 3 dimensions in the electrolyte solution although their growth direction strongly depended on the location of the rupture on the crystal shell. Thus it was also possible for the tubular composites to progress underneath the crystal bulk which was hidden from the optical observation as shown in Figure 6.14 and Figure 6.15. The point of the rupture was near to the chip surface from where a thick tube with diameter of 50–60 µm developed which is indicated in Figure 6.14a. It shows a tube growing that covers 5–6 pixels of the ISFET array. The lower DIP concentration in the electrolyte resulted in a physical motion of the tube which was considerably slower than ~127 µm/s at 10 mM molarity. The growth of the thick tube over the ISFET pixels required approximately 12.5 s time from the point when the fully developed tube touched the silicon nitride, Figure 6.14b – f. In the region of the tube the crystal covered a line of 21 pixels thus corresponding to a growth rate of 18.8 µm/s which is nearly 6.5 times slower in comparison with the 10 mM DIP electrolyte. The image series of Figure 6.14 show only the part of the POM crystal that was situated above the ISFET pixels, therefore the growing tube was optically visible only later when it completely left the cover of the crystal.

The ion camera chip could also record a rarely occurring event when a thick and slow tube encounters a thin and fast one underneath the crystal body maintaining the previous molarity conditions. The precipitated part of the thick tube and the quickly growing end of the thin structure is shown in Figure 6.15a. The thick tube grew at first on a circle from the top of the crystal towards the crystal middle and it continued growing remaining in the circle trace under the POM crystal. Contrary to Section 6.3.2 the growth rate of the thin tube was considerably lower as a consequence of the lower DIP concentration.

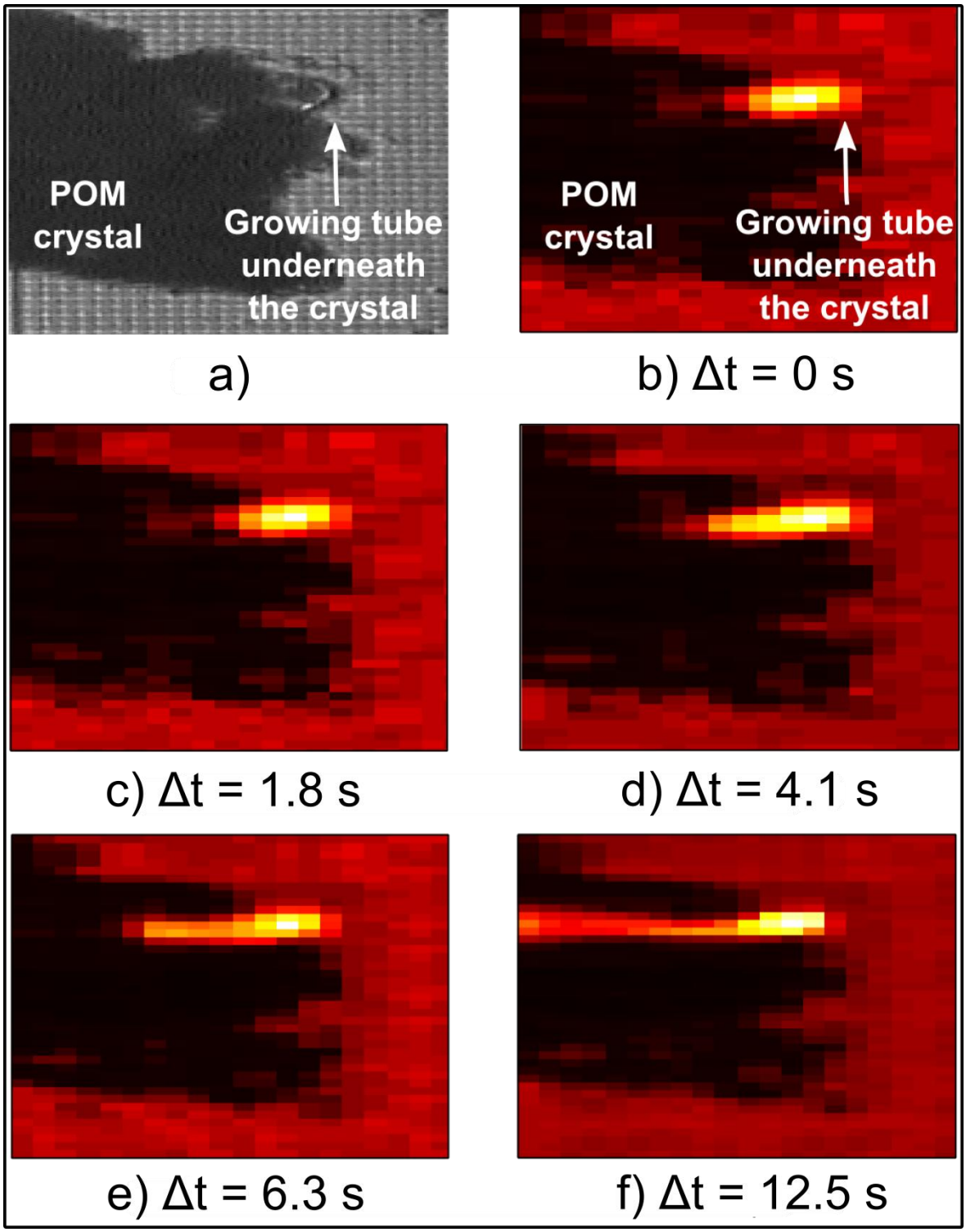

Figure 6.14 The images demonstrate a thicker tube growing underneath the deposited POM crystal outwards from the sensor array. The imaged area of the crystal is ~ 21×34 pixels.

The lower growth rate is observable from the time and path difference between Figure 6.15b and d. The thinner tube with rigid outer cover progressed towards the thicker one during 6 seconds travelling a distance of 10 pixels if we draw a line between the structures. Thus the thinner tube with an approximate travelling speed of 18.6 µm/s hit the wall of the thicker tube, Figure 6.15d. The growth of the tube with 50–60 µm outer diameter slowed down while growing underneath the crystal and having collided with the thin tube. The

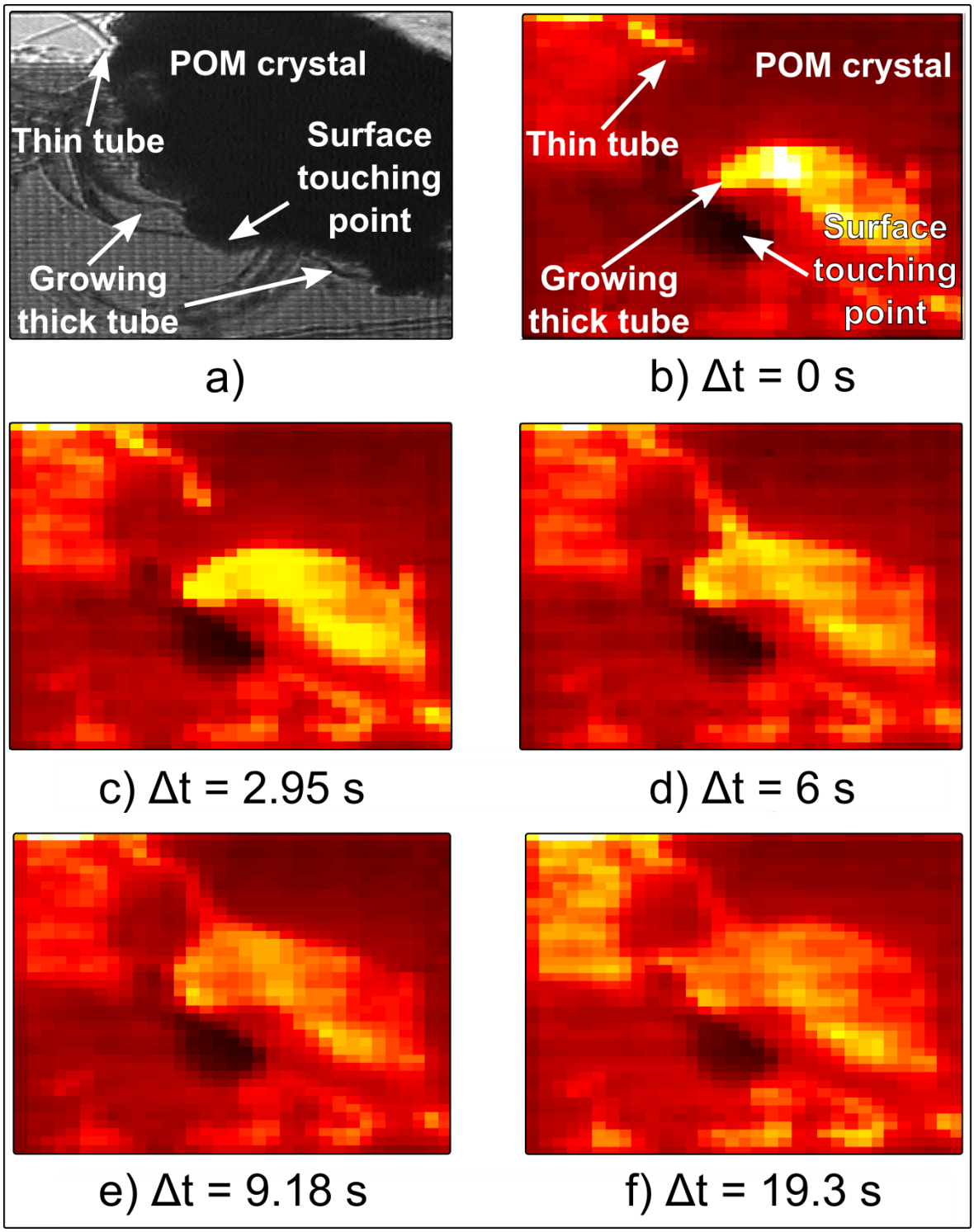

Figure 6.15 (a) shows an optical microscope image of a POM crystal, a thin tube and thicker tubes. The thin tube progresses fast, (b) and (c), under the deposited crystal and this collides with a tube of larger diameter (d) and the hit thicker tube expands (e) continuing also a very slow growing motion or burst (f). The imaged area of the crystal is ~ 32×38 pixels.

growth stopped shortly after the collision. The collision resulted in the local expansion of the thicker tube shown in Figure 6.15e and f. The POM crystal was manually moved once from the one side of the array to the other during the experiment. Therefore the red spot on

the left hand side of the images of Figure 6.15, besides the thin tube, was attributed to the ionic stain left by the crystal movement.

6.4. Summary

This chapter demonstrated that the 64×64–pixel ISFET array chip could be used as an integrated ion camera device. The ionic imaging and real–time data acquisition capabilities were tested by carrying out acid injections into alkali showing that the injected citric acid progressed as a wave front across the ISFET array surface. The ion camera chip was also exposed to complex and corrosive chemistry demonstrating that the chip device could follow the spontaneously occurring pH oscillations of the BZ–reaction. The real accuracy of the integrated imaging method was also verified by growing polyoxometalate structures on the surface of the chip. It was shown that the chip could visualise the growth of membranes and tubes as well as phenomena where optical recording was not possible. Thus the 64×64–pixel ISFET sensor array worked as a hardware–timed single–chip integrated ion camera system.

7. Conclusion and Future Work

7.1. Conclusion

This thesis presented the first prototype of the ion camera device that is of novelty as a system in the field of ISFETs. Although the results showed that the 64×64–pixel worked as an ion camera device, much research is still required to fully establish a versatile and embedded ion visualisation tool that is widely applicable in life sciences. The following sections, Section 7.1.1-7.1.5, present a brief summary and conclusion on the achieved results.

7.1.1. Measurement results

It was demonstrated in the discussion of testing results that the developed CMOS based ISFET chip could work as an ion camera device. The ISFET array of the chip was used to visualise the invisible ion fluxes on the surface of the silicon nitride. The ion sensitive passivation layer responded at an average 20 mV/pH and 9 mV/pNa rates to the electrochemical perturbations. Non–equilibrium chemical processes were applied to test the electronic system because the ISFET sensors detected the fluctuations in the surface ion concentrations. The measured results were reconstructed into coloured images that displayed the motion of mobile ions in the electrolyte. The capability of imaging ion fluxes was initially tested with reactions that provided gradual ion concentration changes over the sensor array. On the one hand citric acid was injected at 0.5 bar pressure showing the acid moving through the alkali as a wave front with eventual turbulences. On the other hand the self–oscillating BZ–reaction was triggered in the electrolyte and each event appeared as a voltage step at the output signal as well as the ionic front slowly progressed over the chip. The results showed a high spatial resolution of one pixel and a high real–time temporal resolution of maximum 40 µs per pixel, 10.2 ms per array. The precision of the imaging modality was also tested using chemical crystals that grew self–assembling micrometre–scaled inorganic tubular and membranous structures. The growing polyoxometalate trajectories on the ion camera images showed excellent correlation with the optical microscope recordings. In addition the ion camera chip could record signals of ion flux movements that the optical microscope was not able to because of limited optical view.

The 64×64–pixel ISFET sensor array chip was also able to detect the activity of mobile ions cell based biological exemplars, slime moulds, over the sensor array. Ultra–low, 0.022 pH, pH fluctuations were observed in a non–destructive manner was demonstrated using only chips with unmodified CMOS fabrication. This low level detection was believed to open the opportunity to explore the natural activity of additional biological systems in the extracellular space. The detected low level pH signals corresponded to a voltage fluctuation of 450 µV ± 70 µV peak–to–peak at the output of the selected ISFET pixels. The intrinsic noise of the ISFET devices was also observed since the ISFET sensors are CMOS based devices and thus they are affected by intrinsic, e.g. 1/f, noise. Measurements were taken to investigate the behaviour of the noise and its affect to the low level signals detected. The results showed that the level of the measured noise could be influenced by changing the applied reference bias potential or the electrolyte pH. The maximum noise contribution was approximated with –100 dB which corresponded a 28 µV peak–to–peak voltage value. This noise was brought into relation with the data of the slime mould which resulted in a 6.2 ± 1.2 % with respect to 20 mV/pH sensitivity. Furthermore it was hypothesised that a H^+ flickering effect could contribute to the overall noise of ISFET devices in analogy with the RTS noise.

The overall conclusion was drawn from these results that the developed ion camera chip technology could potentially be used for the analysis of human cells since the tissues produce ion currents. The necessary accuracy was demonstrated along with the critical ion sensitivities, thus it is expected that the device is capable for tissue analysis as well.

7.1.2. System architecture

It was shown that a dense array of ISFET sensors can be used imaging tool for non–equilibrium chemistry. The detection of ionic concentration fluctuations was carried out using the developed 4.2×4.3 mm large silicon based chip with the 715.8×715.8 µm ISFET sensor array located in the centre of the device. The developed ISFET sensor array contained 4096 sensors arranged into a square shaped architecture with a 1 µm separation gap among the sensors. Thus the maximum achievable spatial resolution of the developed imaging modality was the size of one pixel that corresponded to an area of 10.2×10.2 µm. Each sensor circuit contained 4 transistors including one PMOS ISFET device. The schematic and layout representations of the circuit components were designed using the HIT–Kit v3.70 design libraries supplied by austriamicrosystems. Only standard library

based components were used for the development of the complex chip circuit topology in order to maximise time efficiency and ensure that manufacturable modules were designed.

The applied ion sensitive layer was an LPCVD silicon nitride layer which was deposited as the final step of the selected AMS 0.35 µm 4–metal CMOS fabrication process. Based on the obtained measurement data the average sensitivity of the silicon nitride to H^+ was 20 mV/pH which was 9 mV/pNa to Na^+. The indicated sensitivities were sufficient to visualise the spontaneous or physically induced motion of ions across the sensor array as well as the ion fluxes of growing hybrid tubular and membranous polyoxometalate structures.

The pixels were required to be addressed to enable the measurement hardware to read out the analog output voltage response of the sensors. The sensor readout occurred upon a row and column addressing match which activated the sensor in question and kept it activated during a prescribed time interval. When activated, the pixels received a constant bias voltage of 1.2 V which produced approximately 16 µA in–pixel current. The row addressing process was carried out using 16 blocks of 1/4 demultiplexers on the input side of the sensor array and 16 blocks of 4/1 multiplexers on the output side. The column addressing was implemented by the incorporation of a 6/64 decoder circuit that sequentially activated and deactivated the columns along the sensor array. Corresponding to the number of demultiplexers and multiplexers the array structure was internally divided into 16 separate parts to enable parallelised operation.

The connection between the 95 I/O pads of the chip and the ISFET circuits in the sensor array was separated by buffer connected amplifiers. The buffers helped to separate the sensors from the output and to prevent damage of the pixels, e.g. faulty code delivery on digital output. The ion camera chip was designed with multiple operation modes to provide operational variability for the various applications. Due to the required synchronised operation principles the device was used only in fully external mode thus the components of the chip were driven by external hardware. Printed circuit boards were designed to maintain the interface between the semiconductor chip and the NI PXIe–6358 measurement cards and the NI PXI–4461 dynamic signal analyser card. The boards also contained several checkpoints to verify the incoming and outgoing potentials facilitating the debugging process for hardware or software issues.

7.1.3. Real–time data acquisition

The continuous monitoring of electrochemical and biological processes required a pipelined and hardware–timed sampling approach because of the fast diminishing signals as a result of the rapidly decaying ion fluxes. The developed real–time data acquisition system was capable of delivering a maximum 40 µs per pixel, 10.2 ms per sensor array, synchronised sampling rate. Additional sampling rates of 66 µs per pixel (17 ms per array) and 400 µs per pixel (102.4 ms per array) were also applied depending on the conditions of the actual experiment. Two PXIe–6358 measurement cards with chassis and controller, a custom–built RT–target desktop PC and a host computer were used to drive the real–time data acquisition process. In the maximum speed configuration the 64×64–pixel ISFET sensor frame was scanned approximately 100 times in each second. 100 fps provided sufficient time resolution for accurate monitoring of various chemical reactions including the spread of acidic substances in alkali by injections.

The large generated data volume demanded a high data throughput system that was able to handle large and continuous data streams therefore the PXI–Express platform was selected for the experimentation. The maximum data capturing rate produced a continuous byte stream of 1.56 MB/s (93.75 MB/min) which was transmitted from the RT–target to the host computer using the TCP/IP protocol and streamed out into the NI standard TDMS log file format. The crosstalk between active and inactive lines or pixels was a potential risk for compromising the acquired voltage levels during the operation. The inactive row and column addressing lines, as well as the unused output channels, were switched to power and ground potentials to minimize the possibility and effect of crosstalk.

7.1.4. Packaging and encapsulation

The ion camera chips were attached to holders to enable the straightforward exchange of the devices on the interface boards. Ceramic PGA–100 chip carriers were used because 95 I/O pads were required to be bonded and this type of chip carrier was a common industrial standard. Wire bonding of the chip to the carrier was carried out using a local facility at the University of Glasgow. Two component epoxies were deposited in multiple layers to prevent physical contact between the electrolyte and the electronics as well as bonding wires. The applied Epotek OE–145 and Epotek 302–3M resins were mixed with their hardeners and deposited manually, then dried at 80 ^{o}C in an environmental chamber and on a hotplate, respectively. Because of the explicitly low viscosity of the Epotek 302–3M

epoxy resin : hardener 40% : 60 % compound a chamber was formed around the sensor array on the surface of the chip using silicon rubber. This helped to prevent the deposited epoxy from running over the surface of the sensor array which would have completely damaged the device. Cut parts of polypropylene 25 ml and 50 ml Corning centrifuge tubes were fitted onto the surface of the chip carrier with epoxy and super glue. The purpose of attaching the centrifuge tube parts with screw caps was the storage of the chemical substances during and after the measurement sessions.

7.1.5. Interactive software system

The developed software system was designed with distributed architecture because the underlying hardware configuration consisted of 5 interacting modules; the host computer, the RT–target desktop computer, the NI PXIe–6358 X–series cards, the NI PXIe–1073 chassis and the ion camera chip. The LabVIEW environment with the Real–Time Module was utilised for programming and running the non–deterministic and real–time software codes. A Microsoft Windows based host computer was at the top of the communication chain and the controls were incorporated with hand–shaking characteristics to provide synchronisation points for the flow of the data acquisition. The operation flow was started by launching the non–deterministic software component on the host computer. It downloaded a list of digital output codes through the network using FTP protocol to the RT–target and deployed the RT project afterwards.

The real–time software design was built following the principles of the producer/consumer architecture that was critical for the pipelined process of data capturing. The producer loop was of high–priority and fired at each 40 μs time slot and delivered the gathered data in every 10.2 ms at the maximum sampling speed. In each hardware–timed cycle at first the digital data was provided which was followed by one synchronised analog voltage reading. Upon finished readout of all sensor devices the 1×4096 vector of data was asynchronously flattened and transmitted to the host computer using the TCP/IP protocol. Due to the non–deterministic characteristic of the TCP/IP protocol the synchronisation on the host computer was provided by performing actions only after the receipt of a complete data block of 16384 bytes. The data was then instantly streamed out into a TDMS file by generating a new channel at each cycle.

7.2. Future Work

Another chip version has been designed and submitted to continue experiments because the noise and ionic imaging experimentation required all the devices available. The second prototype of the ion camera chip with similar topology has been fabricated and is being prepared for complex electrochemical measurements. As discussed in the subsequent sections the individual pieces of the system can be subject to further improvements to enhance the overall performance.

7.2.1. Ultrasound

The demonstrated ion visualisation capability is scheduled to be tested using the 64×64–pixel ISFET array chip and an ultrasound device. The ultrasound device is mounted onto the surface of the chip carrier as shown in Figure 7.1. The ultrasound is expected to trap and move particles with uniform pattern in the electrolyte above the sensor chip. The particles which can induce local pH fluctuation should be detected by the ISFET pixels. This development is subject to further research.

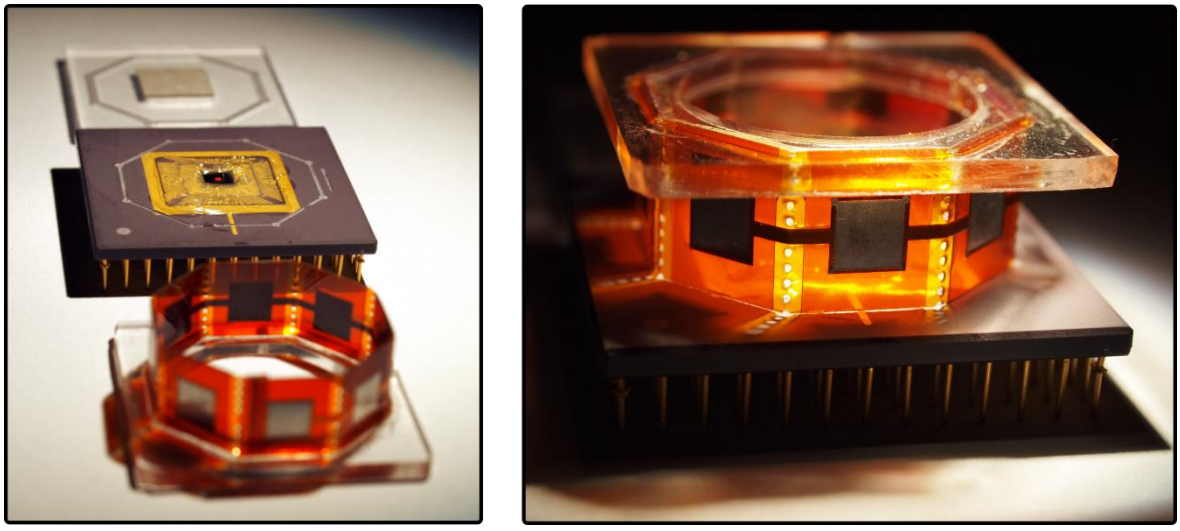

Figure 7.1 The image shows the first prototype of the joint development using the 64×64–pixel ISFET array chip and the ultrasound device developed by Dr. Anne Bernassau.

7.2.2. Deposition of additional ion sensitive layers

The silicon nitride deposited by the manufacturer was shown to respond efficiently to the concentration changes of several ionic species. As a consequence of the multiple ionic sensitivity, the ionic specificity is difficult to achieve with using only silicon nitride.

Therefore the 64×64–pixel ISFET sensor chip requires adjustments in the future if specific ionic currents are to be investigated. The adjustments can take place on the one hand as deposition of a supplementary layer completely covering the silicon nitride above the ISFET sensors. This solution indicates that the used material, e.g. PVC based layer, is fixed to the chip surface and permanently affects the acquired measurement results. It is mostly beneficial if the ionic activity of living biological tissues is investigated in the extracellular space. On the other hand it is also feasible to have several layers of chemical substances, e.g. polyoxometalates, deposited onto the chip surface that interact internally and demonstrate increased sensitivity to specific ions, e.g. K^+. The core advantage of the second solution is that the chemical layers can be removed from the chip surface by exposing them to solutions with high pH, e.g. pH 13.

7.2.3. 1/f noise measurements

The measurement technique of the 1/f noise of the ISFET pixels is subject to improvements in terms of applied substances and measurement setup. The chemicals used in the measurements were pH 13, pH 11, pH 3 and pH 1 where pH 11 and pH 3 were DI water dilutions of pH 13 and pH 1, respectively. It was observed that the silicon nitride behaved differently to the dilutions in comparison with the stock substances. This was attributed to the chemical strength difference of the solutions. It is therefore planned to repeat the experimentation with a changed set of chemicals of the same strength. Also, a repeatable way needs to be devised in order to produce solutions with exact pH 7. This was challenging because of the titration curve of the used alkali and acid substances.

The acquired noise contained several disturbances that were mainly attributed to the switched–mode power supply of the laptop computer which was necessarily located in the same room with the ISFET chip. Due to cabling and instrumentation problems another technique should be elaborated to provide an independent Faraday–cage for the devices under test. Hence it is expected that the superimposed disturbances are eliminated from the signal of interest enabling the measurement of the pure flicker noise of the ISFET pixels.

7.2.4. Quality of passivation

The 64×64–pixel sensor array was surrounded by a closed loop MET4 ring which was connected to an I/O pad through a buffer connected amplifier circuit. In the following prototypes of the ion camera chip the MET4 ring will be connected directly to an I/O pad

to obtain the full range of potential underneath the silicon nitride. The purpose of the directly connected MET4 ring will be to monitor the potential change under the passivation which is in correlation with the occurred change in pH and the pixel output voltage. The recorded potential change on the top metal ring on the one hand helps to determine whether the passivation layer delivers the theoretical Nernstian response. On the other hand it enables investigation into whether the sensitivity could be increased by thinning the nitride with HF etch in the case of sub–Nernstian response.

7.2.5. Data acquisition and video recording

The improvement of the developed data acquisition methods with respect to the experiences during the measurements is also planned for subsequent chip prototypes. The planned modifications in the data capturing process are focussed on the (i) interface board, (ii) measurement hardware, (iii) addressing and readout method.

The interface between the ion camera chip and the data acquisition hardware was based on an externally fabricated custom designed printed circuit board. The chip was connected using a PGA–100 socket in the middle of the board and the cables of the PXIe–6358 cards were linked on the sides of the board. The connecting cables made the placement of the board under the optical microscope difficult and inconvenient. In this connection configuration under the microscope the placement of the polyoxometalate crystals into the silicon chamber required considerable practice by the chemistry experts. Therefore future interface boards are planned to serve only the essential number of I/O pads which requires also a complete rearrangement of the connectors and their leads. The relocation of the SCSI connectors of the cables will also contribute to the design of a smarter board that is easier to handle.

The speed of the data acquisition is subject to adjustment by resolving obstacles in the simultaneous digital output and analog input operations for the PXIe–6358 cards. The rate of data capturing should be lowered up to 4 µs per pixel, ~1 ms per array, 250 kHz sampling frequency. Depending on the demands of future experimentation the hardware limitations may also be solved using the FPGA–based NI CompactRIO (cRIO) technology which would also increase the mobility of the experiments considering its compact size and portability.

The change in the pixel addressing technique is expected to facilitate the reduction of the overall measureable noise of the imaging results. The pixel addressing was carried out by repeatedly switching on the pixels when activated and switching them off when inactivated. It would be beneficial to address certain pixels while keeping them in continuous operation. This would eliminate the problem of pixels not returning to the exact same operation point as prior to activation. This planned modification requires changes in the circuit structure by unifying the input bias point of the pixels and using only the output multiplexers to select the respective channels while the pixels are sequentially addressed by the decoder.

The live video resolution and the placement of the optical camera were critical factors during the experimentation. The optical camera had limited resolution and the liquids that were deposited into the polypropylene chamber reduced the resolution of the optical pictures. In addition the camera was included into the probe station setup that fixed the distance between the chip and the optical camera device. Therefore it is scheduled to purchase a high–resolution optical camera that is mobile and its position is freely adjustable to the actual focus requirements.

7.2.6. Enhanced packaging and encapsulation

The packaging was carried out by using a PGA–100 standard ceramic chip carrier and fixing the silicon die into the open cavity. The further packaging methods are also subject to test without chip carrier because it would increase the portability of the application or the potential of incorporation into other applications.

The encapsulation was implemented using two component epoxies by manual handling and the quality of the used epoxy was controlled by the observed viscosity of the compound. This method was suitable for laboratory environment without the demand of the exact repeatability. Hence a steady and repeatable new method for encapsulation should be developed. The new technique might be based on the deposition of known materials, e.g. polyimide, that are patternable and thus provide a well–controlled encapsulation process.

7.2.7. Software modifications

The used software environment for data acquisition and related tasks were based on LabVIEW 2009. For practical purposes the data processing was accomplished using Matlab. In order to unify the processes they should be merged by using the features of the latest LabVIEW version. Thus the complete data processing flow is planned to be incorporated into the LabVIEW implementation which makes the ion camera system fully automatised and besides the real–time data acquisition it also enables the real–time imaging as well.

Appendix A

The schematics and layouts were designed using the Cadence Virtuoso environment with the HIT–Kit v3.70 definition kit supplied by austriamicrosystems. The following images present the schematics of the chip components discussed in this thesis.

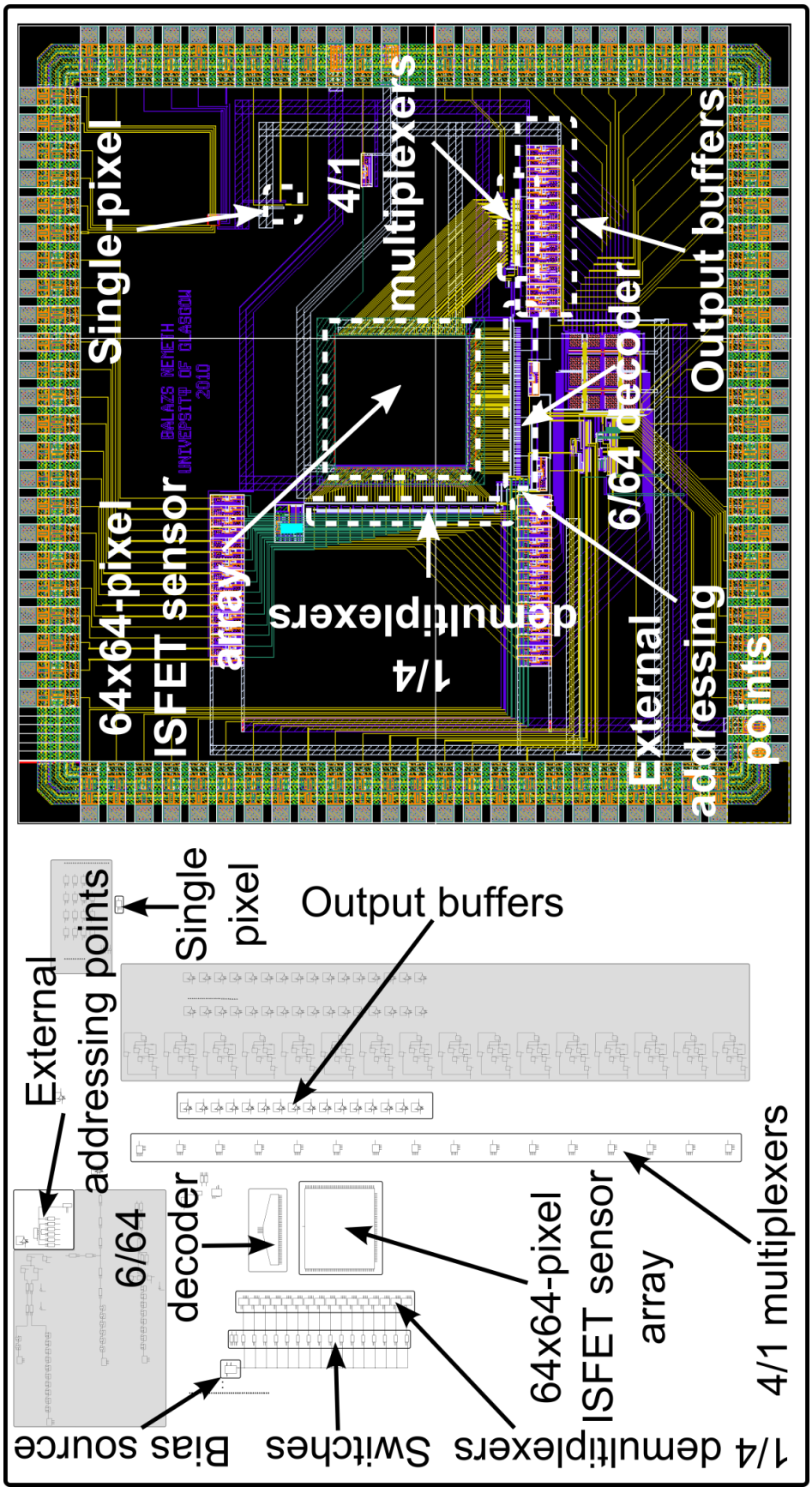

Figure A.1 Schematic and layout representation of the complete ion camera chip

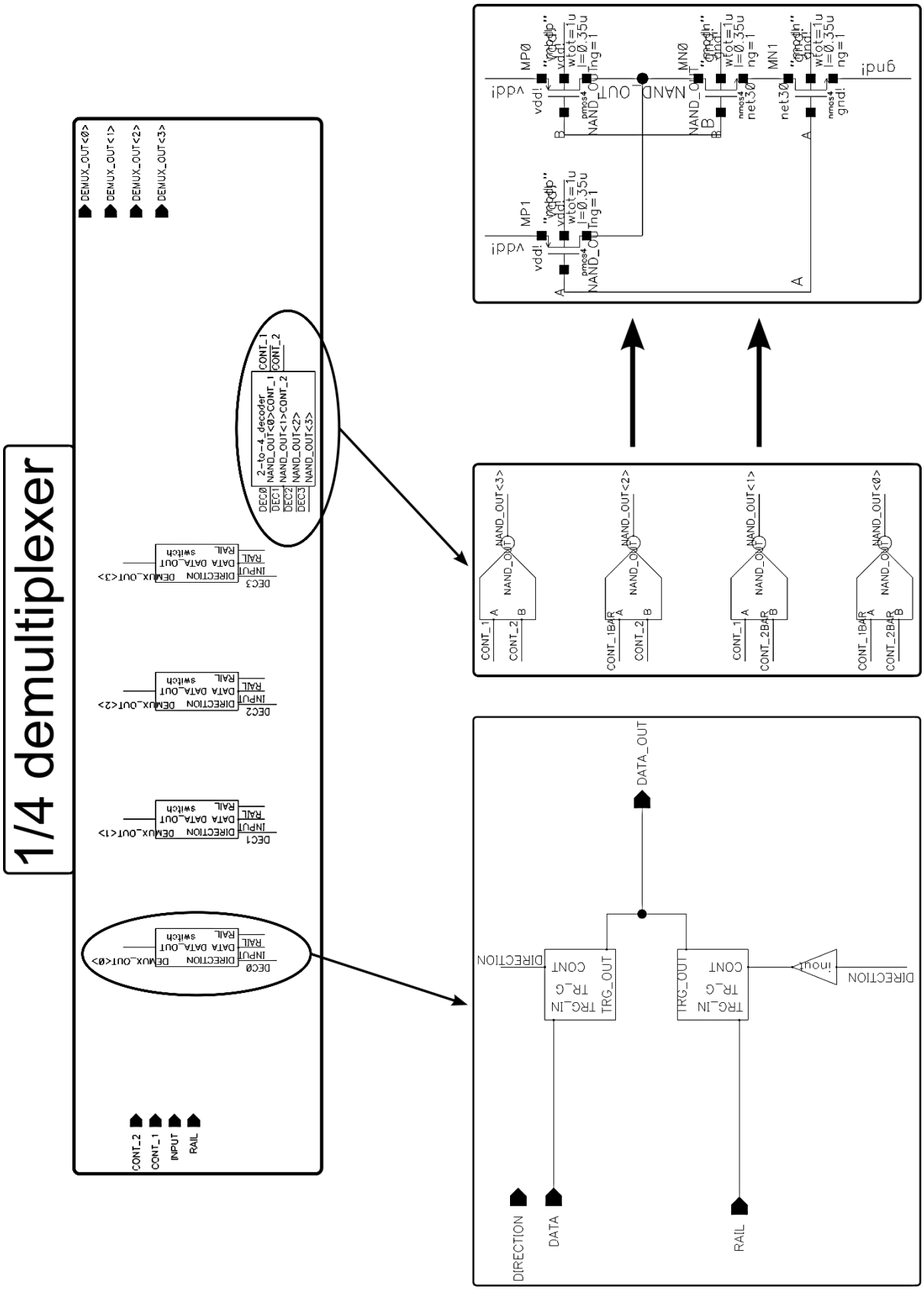

Figure A.2 Schematic representation of the 1/4 demultiplexer block

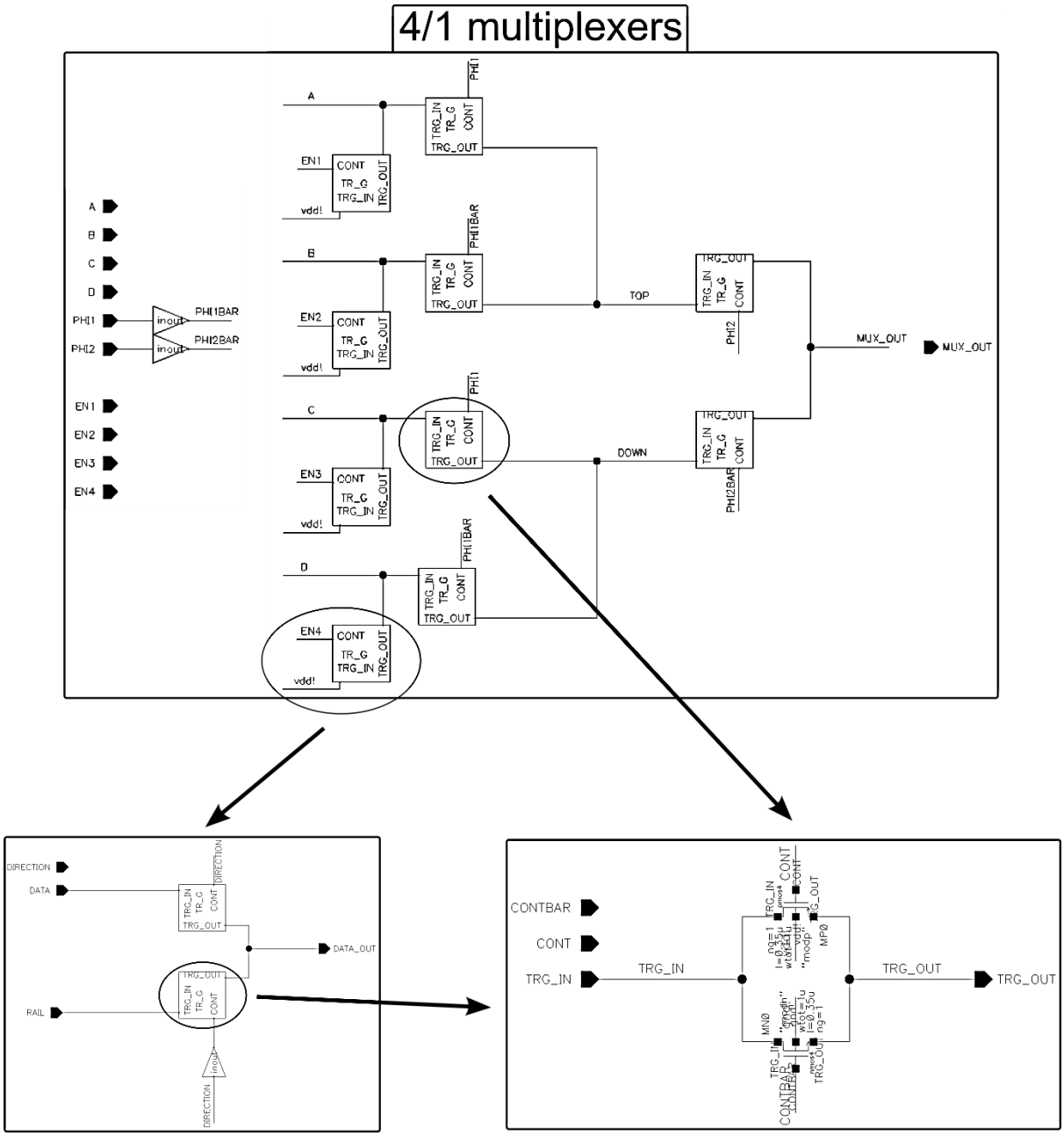

Figure A.3 Schematic representation of the 4/1 multiplexer block

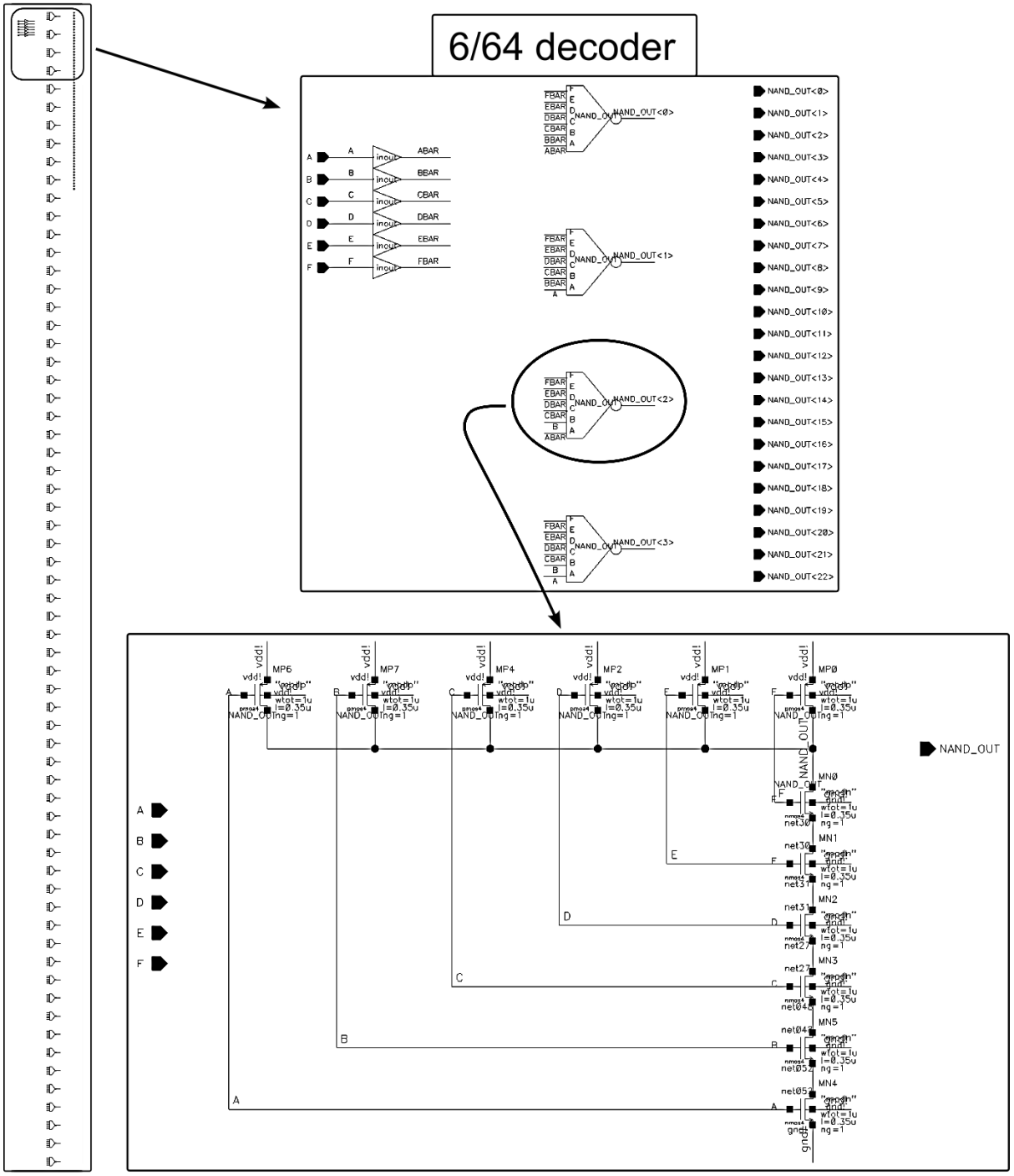

Figure A.4 Schematic representation of the 6/64 decoder block

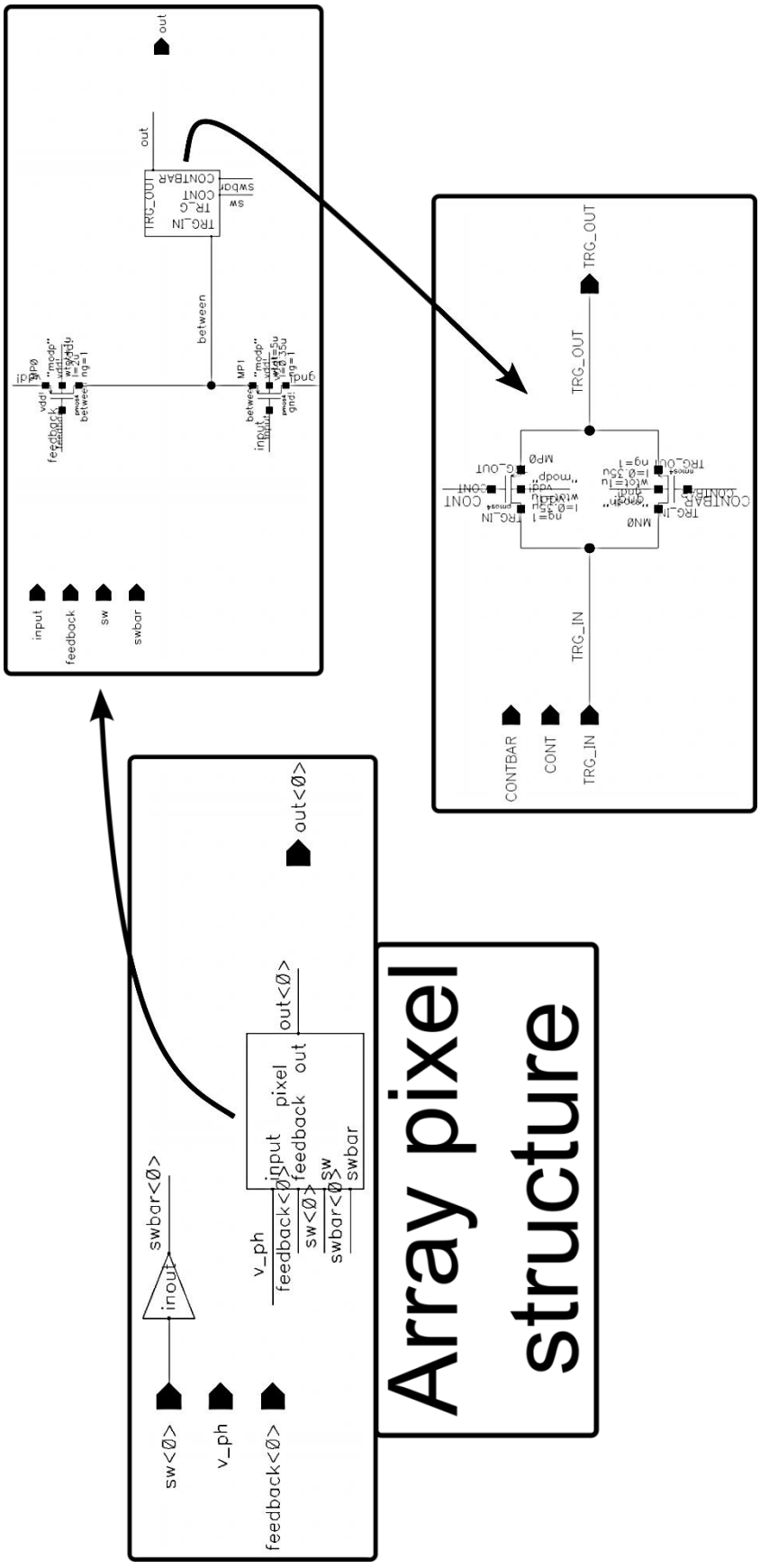

Figure A.5 Schematic representation of an ISFET array pixel

Appendix B

The software for data acquisition and extraction was based on the LabVIEW environment using also the Real–Time Module to provide deterministic and continuous analog readings as well as digital outputs. The subsequent images present snippets from the code of the real–time data acquisition cycle corresponding to the explanation of Section 4.6.

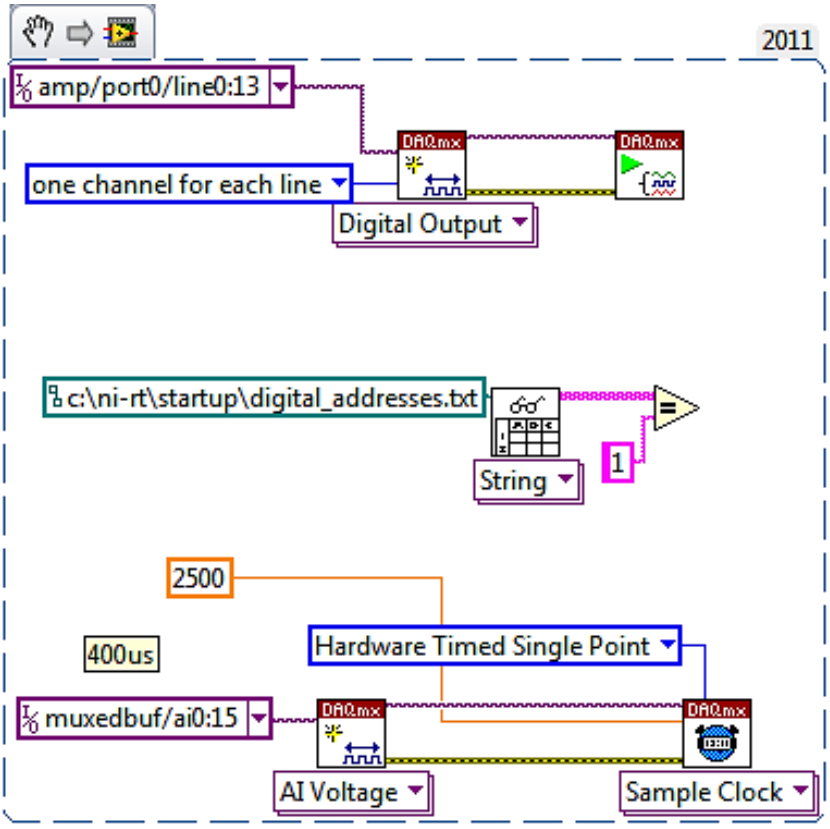

Figure B.1 The image demonstrates the parameters set for the hardware–timed analog readings and digital outputs.

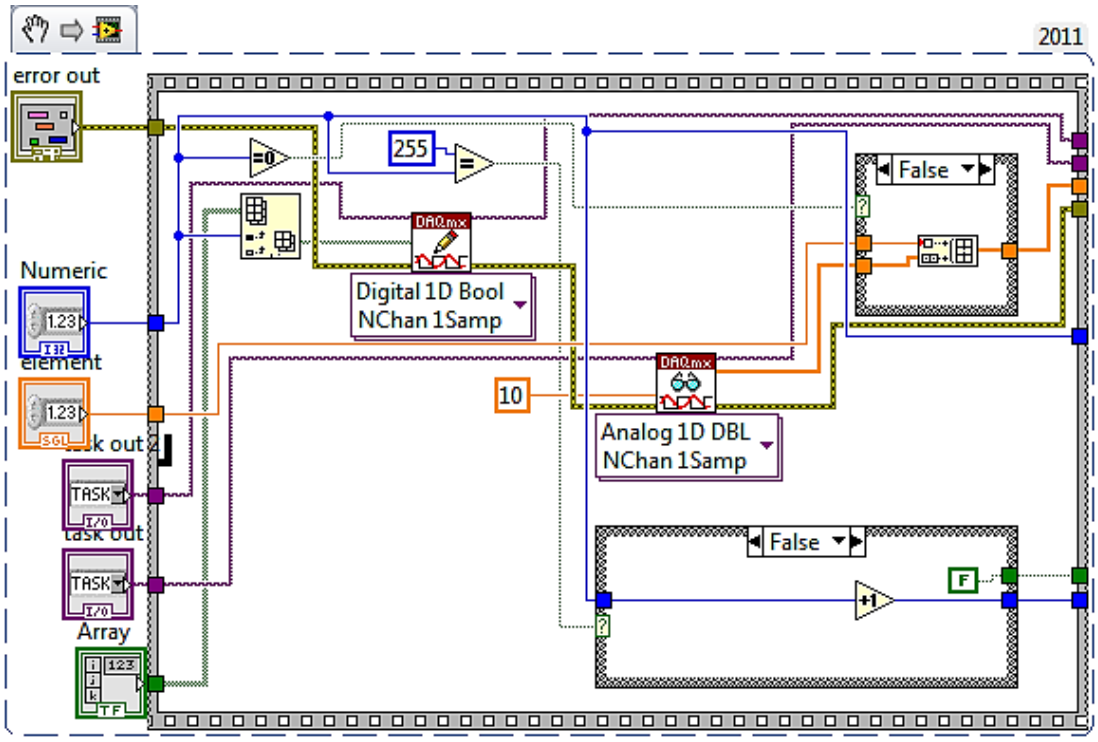

Figure B.2 It is shown that a data acquisition cycle finished when all the 256 pixels of the 4–row blocks were read out. The image also demonstrates the synchronisation method between analog reading and digital output.

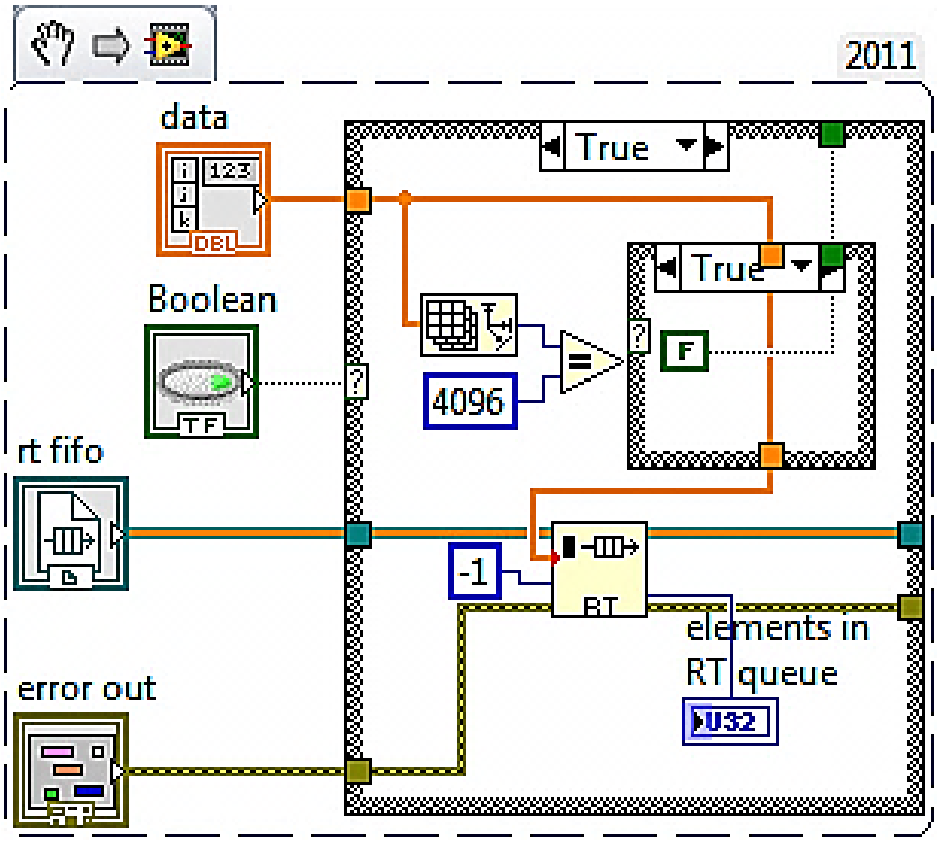

Figure B.3 This image displays the transmission of the data frames from the high–priority process to the asynchronous loop.

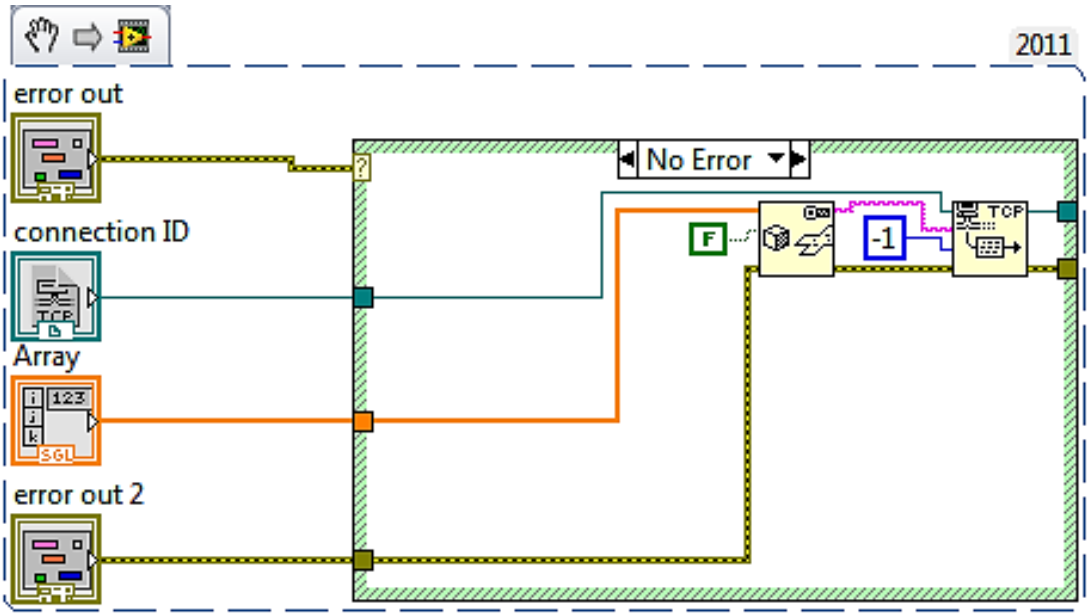

Figure B.4 Transmission of data frames over network using the TCP/IP protocol.

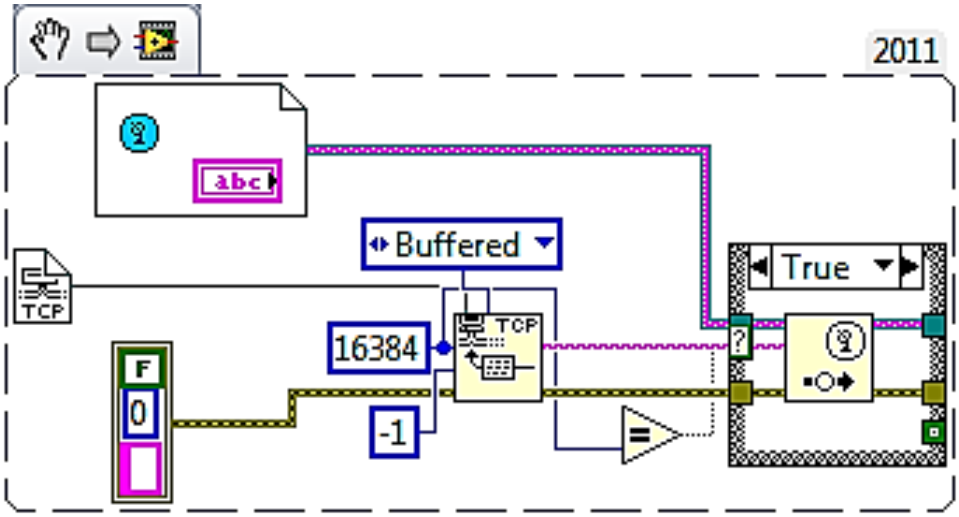

Figure B.5 The image shows that the transmitted data was streamed out into file upon receipt of 16384 bytes.

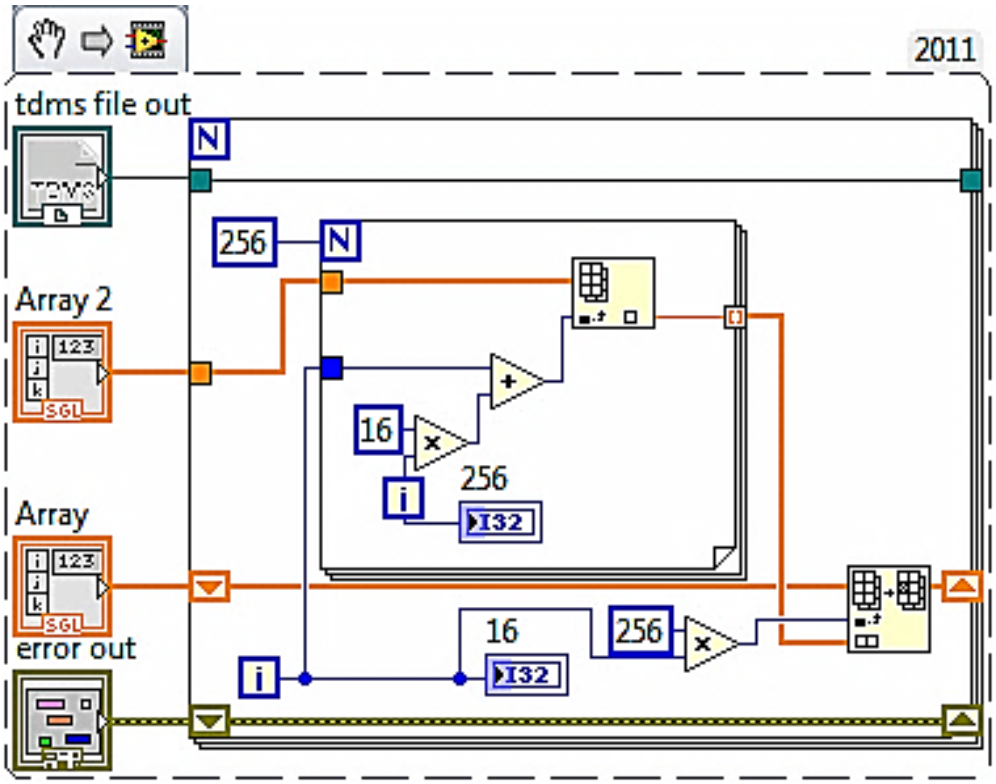

Figure B.6 The core of the data reconstruction method is displayed since the raw stored data was essential to be reconstructed.

References

[1] C. Toumazou and P. Georgiou, “Piet Bergveld - 40 years of ISFET technology: From neuronal sensing to DNA sequencing,” *Electronics Letters*, vol. 47, no. 26, p. S7, 2011.

[2] J. Bausells, J. Carrabina, A. Errachid, and A. Merlos, “Ion-sensitive field-effect transistors fabricated in a commercial CMOS technology,” *Sensors And Actuators*, vol. 57, pp. 56 - 62, 1999.

[3] T. B. Tang *et al.*, “Toward a Miniature Wireless Integrated Multisensor Microsystem for Industrial and Biomedical Applications,” *Sensors (Peterborough, NH)*, vol. 2, no. 6, pp. 628-635, 2002.

[4] P. Bergveld, “Development of an Ion-Sensitive Solid-State Device for Neurophysiological Measurements,” *IEEE TRANSACTIONS ON BIO-MEDICAL ENGINEERING,*, pp. 70-71, 1970.

[5] P. Bergveld, “Development , Operation , and Application of the Tool for Electrophysiology,” no. 5, pp. 342-351, 1972.

[6] T. Matsuo and K. D. Wise, “An Integrated Field-Effect Electrode for Biopotential Recording,” *IEEE Transactions on Biomedical Engineering*, vol. BME–21, no. 6, pp. 485-487, Nov. 1974.

[7] S. D. Moss, J. Janata, and C. C. Johnson, “Potassium ion-sensitive field effect transistor,” *Analytical Chemistry*, vol. 47, no. 13, pp. 2238-2243, Nov. 1975.

[8] P. McBride, J. Janata, P. Comte, S. Moss, and C. Johnson, “Ion-selective field effect transistors with polymeric membranes,” *Analytica Chimica Acta*, vol. 101, no. 2, pp. 239-245, Nov. 1978.

[9] M. Esashi and T. Matsuo, “Integrated micro multi ion sensor using field effect of semiconductor.,” *IEEE transactions on bio-medical engineering*, vol. 25, no. 2, pp. 184-92, Mar. 1978.

[10] T. Matsuo, M. Esashi, and H. Abe, “pH ISFET’s using Al2O3,Si3N4, and SiO2 gate thin films,” *IEEE Transactions on Electron Devices*, vol. 26, no. 11, pp. 1856-1857, Nov. 1979.

[11] P. Gimmel, B. Gompf, D. Schmeisser, H. D. Wiemhöfer, W. Göpel, and M. Klein, “Ta2O5-gates of pH-sensitive devices: Comparative spectroscopic and electrical studies,” *Sensors and Actuators*, vol. 17, no. 1–2, pp. 195-202, May 1989.

[12] A. Olszyna, W. Włosiński, D. Sobczyńska, and W. Torbicz, “A study of borazon-gate pH-sensitive field effect transistors,” *Journal of Crystal Growth*, vol. 82, no. 4, pp. 757-760, Apr. 1987.

[13] D. Sobczyńska and W. Torbicz, “ZrO2 gate pH-sensitive field effect transistor,” *Sensors and Actuators*, vol. 6, no. 2, pp. 93-105, Oct. 1984.

[14] J. A. Mihell and J. K. Atkinson, “Planar thick-film pH electrodes based on ruthenium dioxide hydrate,” *Sensors and Actuators B: Chemical*, vol. 48, no. 1–3, pp. 505-511, May 1998.

[15] Y.-L. Chin, J.-C. Chou, Z.-C. Lei, T.-P. Sun, W.-Y. Chung, and S.-K. Hsiung, “Titanium Nitride Membrane Application to Extended Gate Field Effect Transistor pH Sensor Using VLSI Technology,” *Japanese Journal of Applied Physics*, vol. 40, no. Part 1, No. 11, pp. 6311-6315, Nov. 2001.

[16] K. Tsukada, T. Kiwa, T. Yamaguchi, S. Migitaka, Y. Goto, and K. Yokosawa, “A study of fast response characteristics for hydrogen sensing with platinum FET sensor,” *Sensors and Actuators B: Chemical*, vol. 114, no. 1, pp. 158-163, Mar. 2006.

[17] W.-D. Huang, H. Cao, S. Deb, M. Chiao, and J. C. Chiao, “A flexible pH sensor based on the iridium oxide sensing film,” *Sensors and Actuators A: Physical*, vol. 169, no. 1, pp. 1-11, Sep. 2011.

[18] V. Jankovic and J. P. Chang, “HfO2 and ZrO2 - Based Microchemical Ion Sensitive Field Effect Transistor (ISFET) Sensors: Simulation & Experiment,” *Journal of The Electrochemical Society*, vol. 158, no. 10, p. P115-P117, Oct. 2011.

[19] P. D. van der Wal, M. Skowronska-Ptasinska, A. van den Berg, P. Bergveld, E. J. . Sudhölter, and D. N. Reinhoudt, “New membrane materials for potassium-selective ion-sensitive field-effect transistors,” *Analytica Chimica Acta*, vol. 231, pp. 41-52, 1990.

[20] T. Matsuo, M. Esashi, and H. Abe, “ISFET’s using inorganic gate thin films,” *IEEE Transactions on Electron Devices*, vol. 26, no. 12, pp. 1939-1944, Dec. 1979.

[21] A. Bouazizi, H. Maaref, N. Jaffrezic-Renault, R. B. Chaabane, M. Gammoudi, and G. Guillaud, “A study of ion sensitivity to sodium and cobalt for calixarene based sensors,” *Sensors and Actuators B: Chemical*, vol. 34, no. 1–3, pp. 487-489, Aug. 1996.

[22] S. Wakida, Y. Kohigashi, K. Higashi, and Y. Ujihira, “Chemically Modified Copper Ion-selective Field-effect Transistor With 7,7,8,8-tetracyanoquinodimethane,” in *Proceedings of the International Solid-State Sensors and Actuators Conference - TRANSDUCERS ’95*, 1995, vol. 2, pp. 925-927.

[23] L. Bousse, J. Shott, and J. D. Meindl, “A process for the combined fabrication of ion sensors and CMOS circuits,” *IEEE Electron Device Letters*, vol. 9, no. 1, pp. 44-46, 1988.

[24] H.-S. Wong and M. H. White, “A CMOS-integrated ‘ISFET-operational amplifier’ chemical sensor employing differential sensing,” *IEEE Transactions on Electron Devices*, vol. 36, no. 3, pp. 479-487, Mar. 1989.

[25] C. Cane, I. Gracia, A. Merlos, M. Lozano, E. Lora-Tamayo, and J. Esteve, “Compatibility of ISFET and CMOS technologies for smart sensors,” in *TRANSDUCERS ’91: 1991 International Conference on Solid-State Sensors and Actuators. Digest of Technical Papers*, pp. 225-228.

[26] T. C. W. Yeow, M. R. Haskard, D. E. Mulcahy, H. I. Seo, and D. H. Kwon, “A very large integrated pH-ISFET sensor array chip compatible with standard CMOS processes,” *Sensors and Actuators B: Chemical*, vol. 44, no. 1–3, pp. 434-440, Oct. 1997.

[27] J. Bausells, J. Carrabina, A. Errachid, and A. Merlos, “Ion-sensitive field-effect transistors fabricated in a commercial CMOS technology,” *Sensors And Actuators*, vol. 57, pp. 56 - 62, 1999.

[28] J. Johnson, “Thermal Agitation of Electricity in Conductors,” *Physical Review*, vol. 32, no. 1, pp. 97-109, Jul. 1928.

[29] H. Nyquist, “Thermal Agitation of Electric Charge in Conductors,” *Physical Review*, vol. 32, no. 1, pp. 110-113, Jul. 1928.

[30] M. V. Haartman and M. Östling, *Low-frequency noise in advanced MOS devices*. Springer, 2007, p. 216.

[31] W. Schottky, “Über spontane Stromschwankungen in verschiedenen Elektrizitätsleitern,” *Annalen der Physik*, vol. 362, no. 23, pp. 541-567, 1918.

[32] R. Sarpeshkar, T. Delbruck, and C. A. Mead, “White noise in MOS transistors and resistors,” *IEEE Circuits and Devices Magazine*, vol. 9, no. 6, pp. 23-29, 1993.

[33] P. Horowitz and W. Hill, *The art of electronics, Volume 816*. Cambridge University Press, 1989, p. 1125.

[34] B. K. Jones, “Low-frequency noise spectroscopy,” *IEEE Transactions on Electron Devices*, vol. 41, no. 11, pp. 2188-2197, 1994.

[35] M. J. Kirton and M. J. Uren, “Noise in solid-state microstructures: A new perspective on individual defects, interface states and low-frequency ($1/f$) noise,” *Advances in Physics*, vol. 38, no. 4, pp. 367-468, Jan. 1989.

[36] S. Machlup, “Noise in Semiconductors: Spectrum of a Two-Parameter Random Signal,” *Journal of Applied Physics*, vol. 25, no. 3, p. 341, Mar. 1954.

[37] K. Ralls et al., “Discrete Resistance Switching in Submicrometer Silicon Inversion Layers: Individual Interface Traps and Low-Frequency (1/f?) Noise,” *Physical Review Letters*, vol. 52, no. 3, pp. 228-231, Jan. 1984.

[38] K. K. Hung, P. K. Ko, C. Hu, and Y. C. Cheng, “Random telegraph noise of deep-submicrometer MOSFETs,” *IEEE Electron Device Letters*, vol. 11, no. 2, pp. 90-92, 1990.

[39] J. Johnson, “The Schottky Effect in Low Frequency Circuits,” *Physical Review*, vol. 26, no. 1, pp. 71-85, Jul. 1925.

[40] J. Chang, A. A. A. Abidi, and C. R. R. Viswanathan, “Flicker noise in CMOS transistors from subthreshold to strong inversion at various temperatures,” *IEEE Transactions on Electron Devices*, vol. 41, no. 11, pp. 1965-1971, 1994.

[41] M. von Haartman, “Low-frequency noise characterization, evaluation and modeling of advanced Si- and SiGe-based CMOS transistors.” Doctoral Thesis, KTH Royal Institute of Technology, 2006.

[42] A. L. McWhorter, “1/f noise and related surface effects in germanium,” *Semiconductor Surface Physics, University of Pennsylvania Press*, 1956.

[43] F. Hooge, “1/*f* noise is no surface effect,” *Physics Letters A*, vol. 29, no. 3, pp. 139-140, Apr. 1969.

[44] P. Dutta and P. Horn, “Low-frequency fluctuations in solids: 1f noise,” *Reviews of Modern Physics*, vol. 53, no. 3, pp. 497-516, Jul. 1981.

[45] M. Weissman, “1f noise and other slow, nonexponential kinetics in condensed matter,” *Reviews of Modern Physics*, vol. 60, no. 2, pp. 537-571, Apr. 1988.

[46] F. Hooge, “On the correlation function of 1/f noise,” *Physica B: Condensed Matter*, vol. 239, no. 3–4, pp. 223-230, Aug. 1997.

[47] A. Manz, N. Graber, and H. M. Widmer, “Miniaturized total chemical analysis systems: A novel concept for chemical sensing,” *Sensors and Actuators B: Chemical*, vol. 1, no. 1–6, pp. 244-248, Jan. 1990.

[48] P. Abgrall and A.-M. Gué, “Lab-on-chip technologies: making a microfluidic network and coupling it into a complete microsystem—a review,” *Journal of Micromechanics and Microengineering*, vol. 17, no. 5, p. R15-R49, May 2007.

[49] W. Baumann, “Microelectronic sensor system for microphysiological application on living cells,” *Sensors and Actuators B: Chemical*, vol. 55, no. 1, pp. 77-89, 1999.

[50] M. Lehmann et al., “Simultaneous measurement of cellular respiration and acidification with a single CMOS ISFET,” *Biosensors and Bioelectronics*, vol. 16, no. 3, pp. 195-203, May 2001.

[51] B. Palan, K. Roubik, M. Husak, and B. Courtois, “CMOS ISFET-based structures for biomedical applications,” in *1st Annual International IEEE-EMBS Special Topic Conference on Microtechnologies in Medicine and Biology. Proceedings (Cat. No.00EX451)*, pp. 502-506.

[52] L. Ravezzi, D. Stoppa, M. Corra, G. Soncini, G.-F. Dalla Betta, and L. Lorenzelli, “A CMOS ASIC for differential read-out of ISFET sensors,” in *ICECS 2001. 8th IEEE International Conference on Electronics, Circuits and Systems (Cat. No.01EX483)*, pp. 1513-1516.

[53] L. Lorenzelli, B. Margesin, S. Martinoia, M. . Tedesco, and M. Valle, “Bioelectrochemical signal monitoring of in-vitro cultured cells by means of an automated microsystem based on solid state sensor-array,” *Biosensors and Bioelectronics*, vol. 18, no. 5–6, pp. 621-626, May 2003.

[54] E. Lauwers, J. Suls, W. Gumbrecht, D. Maes, G. Gielen, and W. Sansen, “A CMOS multiparameter biochemical microsensor with temperature control and signal

interfacing," *IEEE Journal of Solid-State Circuits*, vol. 36, no. 12, pp. 2030-2038, 2001.

[55] T. B. Tang et al., "Toward a Miniature Wireless Integrated Multisensor Microsystem for Industrial and Biomedical Applications," *Sensors (Peterborough, NH)*, vol. 2, no. 6, pp. 628-635, 2002.

[56] L. Wang et al., "A programmable microsystem using system-on-chip for real-time biotelemetry.," *IEEE transactions on bio-medical engineering*, vol. 52, no. 7, pp. 1251-60, Jul. 2005.

[57] R. A. Rani and O. Sidek, "ISFET pH sensor characterization: towards biosensor microchip application," in *2004 IEEE Region 10 Conference TENCON 2004.*, vol. D, pp. 660-663.

[58] F. Flores, J. Artigas, J.-L. Marty, and F. Valdés, "Development of an EnFET for the detection of organophosphorous and carbamate insecticides.," *Analytical and bioanalytical chemistry*, vol. 376, no. 4, pp. 476-80, Jun. 2003.

[59] W.-Y. Chung, "ISFET-based sensor signal processor chip design for environment monitoring applications," in *Proceedings of SPIE*, 2004, vol. 5586, no. 1, pp. 18-25.

[60] P. A. Hammond, D. Ali, and D. R. S. Cumming, "Design of a Single-Chip pH Sensor Using a Conventional 0 . 6- m CMOS Process," *Sensors (Peterborough, NH)*, vol. 4, no. 6, pp. 706-712, 2004.

[61] D. T. Krick, P. M. Lenahan, and J. Kanicki, "Electrically active point defects in amorphous silicon nitride: An illumination and charge injection study," *Journal of Applied Physics*, vol. 64, no. 7, p. 3558, Oct. 1988.

[62] P. Georgiou and C. Toumazou, "A Silicon Pancreatic Beta Cell for Diabetes," *IEEE Transactions on Biomedical Circuits and Systems*, vol. 1, no. 1, pp. 39-49, Mar. 2007.

[63] T. R. Chay and J. Keizer, "Minimal model for membrane oscillations in the pancreatic beta-cell.," *Biophysical journal*, vol. 42, no. 2, pp. 181-90, May 1983.

[64] M. S.-C. Lu, "CMOS open-gate ion sensitive field effect transistors for femto-molar dopamine detection," in *2010 IEEE Sensors*, 2010, pp. 419-423.

[65] W. S. W. Zain, T. Prodromakis, and C. Toumazou, "A bulk-driven ISFET-based chemical mixer," in *2010 Biomedical Circuits and Systems Conference (BioCAS)*, 2010, pp. 134-137.

[66] K. Shitashima, "Evolution of compact electrochemical in-situ pH-pCO<inf>2</inf> sensor using ISFET-pH electrode," in *OCEANS 2010 MTS/IEEE SEATTLE*, 2010, pp. 1-4.

[67] L. Wang et al., "A programmable microsystem using system-on-chip for real-time biotelemetry.," *IEEE transactions on bio-medical engineering*, vol. 52, no. 7, pp. 1251-60, Jul. 2005.

[68] B. Eversmann et al., “A 128×128 cmos biosensor array for extracellular recording of neural activity,” *IEEE Journal of Solid-State Circuits*, vol. 38, no. 12, pp. 2306-2317, Dec. 2003.

[69] M. Lehmann et al., “Non-invasive measurement of cell membrane associated proton gradients by ion-sensitive field effect transistor arrays for microphysiological and bioelectronical applications,” *Biosensors and Bioelectronics*, vol. 15, no. 3–4, pp. 117-124, Jun. 2000.

[70] M. J. Milgrew, P. A. Hammond, and D. R. S. Cumming, “The development of scalable sensor arrays using standard CMOS technology,” *Sensors and Actuators B: Chemical*, vol. 103, no. 1–2, pp. 37-42, Sep. 2004.

[71] M. J. Milgrew, M. O. Riehle, and D. R. S. Cumming, “A large transistor-based sensor array chip for direct extracellular imaging,” *Sensors and Actuators B: Chemical*, vol. 111–112, pp. 347-353, Nov. 2005.

[72] M. J. Milgrew and D. R. S. Cumming, “A proton camera array technology for direct extracellular ion imaging,” in *2008 IEEE International Symposium on Industrial Electronics*, 2008, pp. 2051-2055.

[73] A. Hassibi and T. H. Lee, “A Programmable 0.18-µm CMOS Electrochemical Sensor Microarray for Biomolecular Detection,” *IEEE Sensors Journal*, vol. 6, no. 6, pp. 1380-1388, Dec. 2006.

[74] J. M. Rothberg et al., “An integrated semiconductor device enabling non-optical genome sequencing,” *Nature*, vol. 475, no. 7356, pp. 348-352, Jul. 2011.

[75] B. Nemeth et al., “Real-Time Ion-Flux Imaging in the Growth of Micrometer-Scale Structures and Membranes,” *Advanced Materials*, p. n/a, 2012. DOI:10.1002/adma.201104345.

[76] K. Sawada et al., “Novel CCD-based pH imaging sensor,” *IEEE Transactions on Electron Devices*, vol. 46, no. 9, pp. 1846-1849, 1999.

[77] K. Sawada, T. Shimada, T. Ohshina, H. Takao, and M. Ishida, “Highly sensitive ion sensors using charge transfer technique,” *Sensors and Actuators B: Chemical*, vol. 98, no. 1, pp. 69-72, Mar. 2004.

[78] T. Hizawa, K. Sawada, H. Takao, and M. Ishida, “Fabrication of a two-dimensional pH image sensor using a charge transfer technique,” *Sensors and Actuators B: Chemical*, vol. 117, no. 2, pp. 509-515, Oct. 2006.

[79] T. Hizawa et al., “32 x 32 pH Image Sensors for Real Time Observation of Biochemical Phenomena,” in *TRANSDUCERS 2007 - 2007 International Solid-State Sensors, Actuators and Microsystems Conference*, 2007, pp. 1311-1312.

[80] K. Nakazato, M. Ohura, H. Ozawa, and S. Uno, “E-6-3 A BioCMOS LSI circuit with extended-gate FET sensor array,” *Electronics*, no. 23, pp. 748-749, 2008.

[81] K. Nakazato, “An Integrated ISFET Sensor Array,” *Sensors*, vol. 9, no. 11, pp. 8831-8851, Nov. 2009.

[82] L. Bess, “A Possible Mechanism for 1f Noise Generation in Semiconductor Filaments,” *Physical Review*, vol. 91, no. 6, pp. 1569-1569, Sep. 1953.

[83] C. C. Enz and G. C. Temes, “Circuit techniques for reducing the effects of op-amp imperfections: autozeroing, correlated double sampling, and chopper stabilization,” *Proceedings of the IEEE*, vol. 84, no. 11, pp. 1584-1614, 1996.

[84] “http://www.mathworks.co.uk.” [Online]. Available: http://www.mathworks.co.uk/. [Accessed: 02-Dec-2011].

[85] D. Siprak, M. Tiebout, N. Zanolla, P. Baumgartner, and C. Fiegna, “Noise Reduction in CMOS Circuits Through Switched Gate and Forward Substrate Bias,” *IEEE Journal of Solid-State Circuits*, vol. 44, no. 7, pp. 1959-1967, Jul. 2009.

[86] F. Horng-Sen and S. Chih-Tang, “Theory and experiments on surface 1/f noise,” *IEEE Transactions on Electron Devices*, vol. 19, no. 2, pp. 273-285, Feb. 1972.

[87] G. Ghibaudo, “On the theory of carrier number fluctuations in MOS devices,” *Solid-State Electronics*, vol. 32, no. 7, pp. 563-565, Jul. 1989.

[88] A. S. Roy and C. C. Enz, “Critical discussion on the flat band perturbation technique for calculating low-frequency noise,” *IEEE Transactions on Electron Devices*, vol. 53, no. 10, pp. 2664-2667, Oct. 2006.

[89] G. Ghibaudo, O. Roux, C. Nguyen-Duc, F. Balestra, and J. Brini, “Improved Analysis of Low Frequency Noise in Field-Effect MOS Transistors,” *Physica Status Solidi (a)*, vol. 124, no. 2, pp. 571-581, Apr. 1991.

[90] F. N. Hooge, “1/f noise sources,” *IEEE Transactions on Electron Devices*, vol. 41, no. 11, pp. 1926-1935, 1994.

[91] E. Simoen, “On the flicker noise in submicron silicon MOSFETs,” *Solid-State Electronics*, vol. 43, no. 5, pp. 865-882, May 1999.

[92] F. N. Hooge, T. G. M. Kleinpenning, and L. K. J. Vandamme, “Experimental studies on 1/f noise,” *Reports on Progress in Physics*, vol. 44, no. 5, pp. 479-532, May 1981.

[93] A. Ohata, A. Toriumi, M. Iwase, and K. Natori, “Observation of random telegraph signals: Anomalous nature of defects at the Si/SiO2 interface,” *Journal of Applied Physics*, vol. 68, no. 1, p. 200, Jul. 1990.

[94] M. J. Kirton and M. J. Uren, “Capture and emission kinetics of individual Si:SiO2 interface states,” *Applied Physics Letters*, vol. 48, no. 19, p. 1270, May 1986.

[95] M. Uren, “The gate-voltage dependence of telegraph noise amplitudes in small MOSFET’s,” *Applied Surface Science*, vol. 39, no. 1–4, pp. 479-485, Oct. 1989.

[96] M. J. Kirton and M. J. Uren, “Noise in solid-state microstructures: A new perspective on individual defects, interface states and low-frequency ($1/f$) noise,” *Advances in Physics*, vol. 38, no. 4, pp. 367-468, Jan. 1989.

[97] L. Cohen, “The generalization of the Wiener-Khinchin theorem,” in *Proceedings of the 1998 IEEE International Conference on Acoustics, Speech and Signal Processing, ICASSP ’98 (Cat. No.98CH36181)*, vol. 3, pp. 1577-1580.

[98] D. R. Crow, *Principles and Applications of Electrochemistry*. Chapman and Hall, 1979, p. 230.

[99] A. J. Bard and L. R. Faulkner, *Electrochemical Methods: Fundamentals and Applications*. John Wiley & Sons, 1980, p. 736.

[100] W. M. Siu and R. S. C. Cobbold, “Basic properties of the electrolyte-SiO2-Si system: Physical and theoretical aspects,” *IEEE Transactions on Electron Devices*, vol. 26, no. 11, pp. 1805-1815, Nov. 1979.

[101] M. Waleed Shinwari, M. Jamal Deen, and D. Landheer, “Study of the electrolyte-insulator-semiconductor field-effect transistor (EISFET) with applications in biosensor design,” *Microelectronics Reliability*, vol. 47, no. 12, pp. 2025-2057, Dec. 2007.

[102] C. M. A. Brett and A. M. O. Brett, *Electrochemistry: Principles, Methods, and Applications (Oxford Science Publications)*. OUP Oxford, 1993, p. 456.

[103] H. Helmholtz, “Studien über electrische Grenzschichten,” *Annalen der Physik und Chemie*, vol. 243, no. 7, pp. 337-382, 1879.

[104] M. Gouy, “Sur la constitution de la charge électrique à la surface d’un électrolyte,” 1910.

[105] D. L. Chapman, “LI. A contribution to the theory of electrocapillarity,” *Philosophical Magazine Series 6*, vol. 25, no. 148, pp. 475-481, Apr. 1913.

[106] D. Andelman, “Electrostatic properties of membranes: the Poisson-Boltzmann theory,” *Handbook of biological physics*, vol. 1, pp. 603 - 642, 1995.

[107] O. Stern, “Zur Theorie der elektrolytischen Doppelschicht,” *Z. Elektrochem.*, no. 30, pp. 508–516, 1924.

[108] D. C. Grahame, “The Electrical Double Layer and the Theory of Electrocapillarity.,” *Chemical Reviews*, vol. 41, no. 3, pp. 441-501, Dec. 1947.

[109] J. O. Bockris, M. A. V. Devanathan, and K. Muller, “On the Structure of Charged Interfaces,” *Proceedings of the Royal Society A: Mathematical, Physical and Engineering Sciences*, vol. 274, no. 1356, pp. 55-79, Jun. 1963.

[110] D. E. Yates, S. Levine, and T. W. Healy, “Site-binding model of the electrical double layer at the oxide/water interface,” *Journal of the Chemical Society, Faraday Transactions 1*, vol. 70, p. 1807, Jan. 1974.

[111] D. L. Harame, L. J. Bousse, J. D. Shott, and J. D. Meindl, “Ion-sensing devices with silicon nitride and borosilicate glass insulators,” *IEEE Transactions on Electron Devices*, vol. 34, no. 8, pp. 1700-1707, Aug. 1987.

[112] S. Mezzasalma, “Characterization of Silicon Nitride Surface in Water and Acid Environment: A General Approach to the Colloidal Suspensions,” *Journal of Colloid and Interface Science*, vol. 180, no. 2, pp. 413-420, Jun. 1996.

[113] F. L. Riley, “Silicon Nitride and Related Materials,” *Journal of the American Ceramic Society*, vol. 83, no. 2, pp. 245-265, Dec. 2004.

[114] C. D. Fung, P. W. Cheung, and W. H. Ko, “A generalized theory of an electrolyte-insulator-semiconductor field-effect transistor,” *IEEE Transactions on Electron Devices*, vol. 33, no. 1, pp. 8-18, Jan. 1986.

[115] D. A. Fiedler, “An ESR-Electrochemical Cell Which Can Be Used in High and Low Dielectric Solvents Over Wide Ranges of Temperature and Time Domain,” *Journal of The Electrochemical Society*, vol. 142, no. 3, p. 862, Mar. 1995.

[116] P. Bergveld, “Thirty years of ISFETOLOGY,” *Sensors and Actuators B: Chemical*, vol. 88, no. 1, pp. 1-20, Jan. 2003.

[117] P. E. Allen, D. R. Holberg, and Allen, *CMOS Analog Circuit Design*. Oxford University Press, USA, 2002, p. 250.

[118] R. E. G. van Hal, J. C. T. Eijkel, and P. Bergveld, “A novel description of ISFET sensitivity with the buffer capacity and double-layer capacitance as key parameters,” *Sensors and Actuators B: Chemical*, vol. 24, no. 1–3, pp. 201-205, Mar. 1995.

[119] Y. Nemirovsky, D. Corcos, I. Brouk, A. Nemirovsky, and S. Chaudhry, “1/f noise in advanced CMOS transistors,” *IEEE Instrumentation & Measurement Magazine*, vol. 14, no. 1, pp. 14-22, Feb. 2011.

[120] A. Zhabotinsky, “Belousov-Zhabotinsky reaction,” *Scholarpedia*, vol. 2, no. 9, p. 1435, Sep. 2007.

[121] W. Jahnke and A. T. Winfree, “Recipes for Belousov-Zhabotinsky reagents,” *Journal of Chemical Education*, vol. 68, no. 4, p. 320, Apr. 1991.

[122] G. J. T. Cooper et al., “Osmotically driven crystal morphogenesis: a general approach to the fabrication of micrometer-scale tubular architectures based on polyoxometalates.,” *Journal of the American Chemical Society*, vol. 133, no. 15, pp. 5947-54, Apr. 2011.